Modelling Bladder-Collapse Flow

Marios Tziannaros

Department of Mathematics

University College London

A thesis submitted for the degree of

Doctor of Philosophy

Supervisor:

Prof. F. T. Smith F.R.S.

January 2011

I, Marios Tziannaros, confirm that the work presented in this thesis is my own. Where information has been derived from other sources, I confirm that this has been indicated in the thesis.

Abstract

The thesis is concerned with the modelling of urinary motion during bladder collapse and is mathematically based. The bladder model as a collapsing vessel is developed as a step towards complementing use of nomograms. Urine motion inside is taken as unsteady flow of incompressible fluid, while the dimensions and collapse rate of the vessel are prescribed using data which is close to realistic biological values. Evolutions of velocities, volume flow rates and effects of the collapse rate are examined. An introduction is made which includes lower urinary tract urodynamics as well as the unique feature that the bladder changes shape and size substantially compared with other vessels. An investigation of simple two-dimensional shapes takes place in chapter two, along with limiting cases for thin vessels. Chapter three analyses simple axisymmetric shapes especially the sphere because of its relevance in addition to its fundamental nature. Development of a numerical scheme is addressed in the next chapter to tackle more complex shapes through the boundary element method and an iterative finite difference scheme with emphasis on flexibility of approach. An extension to more advanced structures of the vessel is constructed in chapter five by means of a concise boundary condition and shape definition. Chapter six takes the work a step further as the approach is applied to axisymmetric configurations. While in an appendix, an extension to implement full viscous effects is then inspected. Finally, further work is discussed in the conclusion.

Acknowledgements

I cannot adequately express my deep gratitude to my supervisor, Professor Frank T. Smith FRS, for his constant help, advice, and patient support throughout my research and subsequent preparation of this thesis. My thanks go wholeheartedly to him.

I must also thank my second supervisor Professor Alan Cottenden and his son David, for all their specialist advice and discussions. I would also like to thank everyone from the Medical Modelling Group at UCL as well as my friend George and colleagues Stephen and Hannah. In particular, I would like to thank the Engineering and Physical Sciences Research Council (EPSRC) as well as the Cooperative Awards in Science and Engineering (CASE) through Astellas Pharma Ltd for their financial support.

On a more personal note, I would like to express my sincere indebtedness to my fiancee, Isidora, for her continual patience, kindness and love. Last, but not least, I would like to thank my parents, Angela and Antonis, as well as my brothers, Solon and Joseph, and sister Antonia who are there for me always.

Contents

1 Introduction **21**

1.1 Aims and Motivations 21

1.2 The Lower Urinary Tract 23

1.2.1 The bladder 24

1.2.2 The urethra 26

1.3 Medical Background 28

1.3.1 Nervous Control 28

1.3.2 Pathology 29

1.3.3 Urodynamics 31

1.4 Mechanics of the Bladder 33

1.4.1 Pressures 33

1.4.2 Filling and Evacuation Phases 35

1.5 Medical Modelling 38

1.5.1 General 38

1.5.2 Lower Urinary Tract Modelling 39

1.6 Numerical Schemes Used in the Thesis 41
1.6.1 Iterative Finite Difference Method 41
1.6.2 Boundary Element Method 41
1.7 Thesis Summary 42
1.7.1 Background 43
1.7.2 Chapter Review 46
1.8 Non-Dimensionalisation 47

2 Analysis of Two-Dimensional Shapes 48

2.1 Analytical Solution for Fluid Flow in a Circular Bladder with a Point Discontinuity 52
2.1.1 Use of Poisson Integral Formula 52
2.1.2 Use of Complex Functions 58
2.2 Analysis for Elliptical Thin Two-Dimensional Shapes of Vessel 65
2.2.1 Thin Horizontal Vessel 65
2.2.2 Thin Vertical Vessel 72
2.2.3 Euler/Laplace Region 78
2.3 Summary & Results 87

3 Analysis of Axisymmetric Shapes 91

3.1 Axisymmetric Shapes 91
3.1.1 Ideas and Set-up 91
3.1.2 Formulation for the Sphere Problem 94
3.2 Thin or Slender Axisymmetric Shapes 100

3.3 Summary & Results 101

4 Numerical Solutions for Simple Two-Dimensional Shapes 103

4.1 Methodology 104

4.2 Circular and Horizontal/Vertical Elliptical Shapes using an Iterative Finite Difference Method 107

4.2.1 Background 107

4.2.2 Finite Difference Method with Dirichlet Conditions 107

4.2.3 Convergence 109

4.2.4 Boundary Interpolation 110

4.2.5 Numerical Results 115

4.2.6 Steady Ellipses 118

4.2.7 Results & Comments 131

4.3 Collapsing of Circular Shape to Flat Elliptical Shape 134

4.3.1 Circle Collapsing into Flat Ellipse 134

4.3.2 Results 136

4.4 Circular Shape using Boundary Element Method 143

4.4.1 Boundary Integral Formulation 143

4.4.2 Numerical Implementation 146

4.4.3 Numerical Solutions 150

4.4.4 Results & Comments 153

4.5 Summary 155

5 Numerical Solutions for More Complex Two-Dimensional Shapes 156

5.1 Cardioidal Shapes 156
5.1.1 Analysis of Boundary Condition 157
5.1.2 Validation 159
5.1.3 Construction of Shapes 161
5.1.4 Implementation of the Numerical Scheme 162
5.2 Results 163
5.3 Summary 171

6 Numerical Solutions for Axisymmetric Shapes 173
6.1 Numerical Solution for Axisymmetric Sphere 174
6.1.1 Numerical Scheme using Finite Difference Method 175
6.1.2 Boundary Interpolation 177
6.1.3 Numerical Results 182
6.2 Numerical Solutions for More Complex Axisymmetric Shapes 190
6.2.1 Axisymmetric Cardioidal Shapes 190
6.2.2 Construction of shapes 192
6.2.3 Implementation of the Numerical Scheme 193
6.3 Results 200
6.4 Summary 201

7 Concluding Remarks 202
7.1 Overview 202
7.2 Summary Discussions for Each Section 204
7.3 Suggestions for Future Work 206

Appendices **208**

A Navier-Stokes Effects **209**

A.1 Ideas/Notation 209

A.2 Numerical Scheme 210

A.2.1 Finite Difference Scheme 210

A.2.2 Applications 211

A.3 Verification through Driven Cavity 212

A.4 More Complex Two-Dimensional Shapes 217

A.5 Summary 230

B Evaluation of Poisson Integral **231**

List of Figures

1.1 Diagram [112] of sections through the urinary tract and more specifically the ureters, parts of the bladder and the urethra. 22

1.2 Sagittal section of the male pelvis [45]. The bladder, the peritoneum, the prostate and other parts around the area of concern are shown. . . 25

1.3 Diagram [112] of the lower urinary tract. Urine is formed in the kidneys and passes through the ureters to end up in the bladder where it is stored. When the time comes for micturition, urine is excreted to the outside world by the urethra. 28

1.4 Graph of the actual representative normal flow rate during micturition. 32

1.5 Starting shapes of bladder, taken by a Voiding Cystourethrogram (a) [34], (b) [85], (c) [92]. The bladder is the light circular patch in the middle. Also visible around it are bones and in (b) the ureters can be seen coming down. See also Figure 1.6. 43

1.6 Shapes of different bladders later on during micturition, taken by a Voiding Cystourethrogram (a) [27], (b) [29] , (c) [27], (d) [92]. Once again the light patch in the middle is the bladder. Also visible are the bones and in some instances like in (c) and (d) we can see the right ureter. . . 44

2.1 Simple circular structure for the vessel showing the prescribed normal velocity condition (the "squeeze") at the vessel wall, the Cartesian and polar reference coordinates and the sink. The radius of the vessel here is $F(t)$ at time t. 50

2.2 Ellipse-shaped vessel, the major and minor axes, the sink (at the origin) and the lower and upper halves of the ellipse for future reference. . . . 55

2.3 Analytical result: the two-dimensional streamlines in the vessel derived by the Poisson Integral Formula. Streamlines are of course not normal to the wall as there is usually tangential velocity as well. Also plotted are the horizontal (b) and vertical (c) velocity along the horizontal centreline. 59

2.4 Simple circular structure for the vessel showing the positions of the sink C and effective source O as well as the Cartesian and polar reference points. Cartesian axes are centred at the urethra as shown. The squeeze velocity at the boundary and the sink also apply here in the same way as Figure 2.1 (see arrows). 62

2.5 Analytical result for the two-dimensional flow in a circular vessel derived by the complex function analysis showing the streamlines. Also plotted are the horizontal (b) and vertical (c) velocity along the horizontal centreline. 64

2.6 Thin horizontal (left) and thin vertical (right) elliptical vessels. Mathematical analysis for the two cases is performed in the text. The so-called Euler region in black is shown. Incoming flows induced outside that region are also shown. See section 2.2.3. 66

2.7 Plot of the velocity U (vertical axis) against x (horizontal axis) at time $t = 0$ for initial conditions $a = 12$, $b = 4$ (implies $a' = -3$, $b' = -1$). See also section 2.2.3. 70

2.8 Plot of the velocity U (vertical axis) against x (horizontal axis) at time $t = 3$ with initial conditions $a = 12$, $b = 4$ (implies $a' = -3$, $b' = -1$). This looks similar to Figure 2.7 but in a shorter scale due to the vessel collapse. See section 2.2.3. 71

2.9 Contours of the streamfunction $\Psi \approx \Psi_0$ at time $t = 0$ with initial conditions $a = 1$, $b = \frac{1}{100}$. The streamlines are all directed towards the centre $x = 0$. Concerning the shaded area in the middle, see Figure 2.15 for the solution closer to $x = 0$. 72

2.10 Plot of the induced fluid velocity V at time $t = 0$ for initial conditions $a = 4$, $b = 12$ with $a' = -\frac{1}{3}$, $b' = -1$. See section 2.2.3 concerning the region near the bottom of the vessel. 75

2.11 Plot of the induced fluid velocity V at time $t = 3$ for initial conditions $a = 4$, $b = 12$ with $a' = -\frac{1}{3}$, $b = -1$. See section 2.2.3 concerning the region near the bottom of the vessel. 76

2.12 Contour of the streamfunction or streamlines $\Psi \approx \hat{\Psi}_0$ at time $t = 0$ inside the majority of the vertical thin ellipse with initial conditions $a = \frac{1}{100}$, $b = 1$. The streamlines here are all directed downwards towards the sink at the origin. Concerning the shaded area see Figure 2.18 for the solution closer to $y = 0$. 77
2.13 Plot of the local flow problem in both the z-plane and the ζ-plane. . . . 79
2.14 Computational streamlines of the flow for the thin horizontal Euler/Laplace local case shown in Figure 2.13. A close-up view of this computed solution is presented in the next figure. 81
2.15 Analytical (a) and computational (b) streamlines of the two-dimensional flow for the horizontal Euler/Laplace local case shown in Figure 2.13. The streamlines are directed towards the origin. Also plotted are the horizontal (c) and vertical (d) velocity along the horizontal centreline for both the computational (small circles) and analytical (line) results. . . 82
2.16 Set-up for the local Euler flow region in the thin vertical vessel; compare Figure 2.13. 83
2.17 Computational streamlines of the flow for the thin vertical Euler/Laplace case of Figure 2.16. See also the zoom-in in the following figure. 85
2.18 Analytical (a) and computational (b) streamlines of the two-dimensional flow for the vertical Euler/Laplace local case shown in Figure 2.16. The streamlines are directed towards the origin. Also plotted are the horizontal (c) and vertical (b) velocity along the horizontal centreline for both the computational (small circles) and analytical (line) results. 86

3.1 Spherical and cylindrical reference points for a simple axisymmetric spherical structure. 93
3.2 Set-up of the formulation for determining the flow inside the sphere. See also Figures 2.1 and 2.4. 96
3.3 Contour plot of the streamlines inside the spherical vessel. The flow directions are all associated with downward motion (downward arrows). Also plotted are the horizontal (b) and vertical (c) velocity along the horizontal centreline. The sphere here is shifted up so that the urethra is at the origin. 99

4.1 Diagram of the Yin-Yang grid [76]. 105
4.2 Example of 5-point stencil on our grid. 108
4.3 Example of a possible elliptical boundary in our grid. The nodes are generally separated by a distance h. Yet, near the boundary this is not always the case. As you can see in the figure, $h_{i+1} = h_{i-1} = h_{j-1} = h$. This is not the case with h_{j+1} which is smaller. We therefore employ the formula (4.2.7) for this point P. In the case of the point Q on its right, we will have two points which will be smaller than h. The formula (4.2.7) tackles this case too. 111
4.4 Plots of the horizontal (a) and vertical (b) velocity along the horizontal centreline for both computational - without the boundary interpolation - (small circles) and analytical (line) results. The boundary condition used is $\Psi_B = \theta - \sin(\theta)$. 115

4.5 Contour plot for computational results (a) and analytical results (b) using the boundary condition $\Psi_B = \theta - \sin(\theta)$. Streamlines are of course not normal to the wall as we also have tangential velocity. Also plotted are the horizontal (c) and vertical (d) velocity along the horizontal centreline for both computational (small circles) and analytical (line) results. 117

4.6 Contour plots for computational results using the boundary condition $\Psi_B = \theta - \sin(\theta)$. Also plotted are the horizontal and vertical velocity along the horizontal centreline. The testing of the code efficiency is demonstrated through the showing of more coarse grids. First a 4x4 (contour plot (a), horizontal velocity (b) and vertical velocity (c)), then an 8x8 ((d)-(f)), 16x16 ((g)-(i)), 32x32 ((j)-(l)) and 64x64 ((m)-(o)) grid are presented respectively. 123

4.7 Contour plot for an ellipse with major axis to minor axis ratio of 3 using the boundary condition from (4.2.24). Also plotted are the horizontal (b) and vertical (c) velocity along the horizontal centreline. 124

4.8 Contour plot for an ellipse with major axis to minor axis ratio of 5 using the boundary condition from (4.2.24). Also plotted are the horizontal (b) and vertical (c) velocity along the horizontal centreline. 125

4.9 Contour plots for computational results for an ellipse with major axis to minor axis ratio of 3 using the boundary condition from (4.2.24). The assessment of code efficiency is demonstrated here through the showing of more coarse grids. Also plotted are the horizontal and vertical velocity along the horizontal centreline. First a 4x4 - in a 1x1 xxy grid - (contour plot (a), horizontal velocity (b) and vertical velocity (c)), then an 8x8 ((d)-(f)), 16x16 ((g)-(i)), 32x32 ((j)-(l)) and 64x64 ((m)-(o)) grid are presented respectively. 130

4.10 Contour plot for an ellipse with major axis to minor axis ratio of 0.5 using the boundary condition from (4.2.24). Also plotted are the vertical velocity along the horizontal centre line (b) and the vertical centre line (c). 132

4.11 Contour plot for an ellipse with major axis to minor axis ratio of 0.2 using the boundary condition from (4.2.24). Also plotted are the vertical velocity along the horizontal centre line (b) and the vertical centre line (c). 133

4.12 Shapes taken by the vessel at different times before it collapses to a thin flat ellipse. 135

4.13 Contour plots of the flow inside the collapsing bladder described in section 4.3. Also plotted are the horizontal and vertical velocity along the horizontal centreline. Times for the parts are 0 (contour plot (a), horizontal velocity (b) and vertical velocity (c)), then 3((d)-(f)), 6((g)-(i)), 9((j)-(l)), 12((m)-(o)) and 16((p)-(r)) respectively. 142

4.14 The collapsing circle model showing the sink, general internal point P and polar coordinates r and θ based at the centre of the vessel of diameter F(t). Cartesian coordinates x and y are horizontal and vertical in turn with the sink as the origin. 151

4.15 A basic test. Contour plot of exact streamfunction values (a) and numerical values (b) in a circle. Also plotted are the horizontal (c) and vertical velocity (d) along the horizontal centreline. 152

4.16 Contour plot of exact streamfunction values (a) and numerical values (b) in a circle with a point discontinuity at the base. Also plotted are the horizontal (c) and vertical velocity (d) along the horizontal centreline. . 154

5.1 Constructions of basic triangles used for the calculations. 158

5.2 Shapes that the vessel takes at different times as it collapses with a cardioidal-like shape, in the model of section 5.1. Horizontal x, vertical y. 164

5.3 Contour plots of the fluid motion within the modeled collapsing vessel. Also plotted are the horizontal and vertical velocity along the horizontal centreline. Times for the parts are 0.01 - just after the start of micturition - (contour plot (a), horizontal velocity (b) and vertical velocity (c)), then 8((d)-(f)), 12((g)-(i)), 15((j)-(l)) and 16.8 - just before the end of micturition - ((m)-(o)) respectively. 169

6.1 Example of 5-point stencil on our grid. 176

6.2 Example of a possible elliptical boundary within our grid. The nodes are generally separated by a distance h. Near the boundary though this is not always the case. As you can see in the figure, $h_{i+1} = h_{i-1} = h_{j-1} = h$. This is not the case with h_{j+1} which is smaller. We therefore employ formula (6.1.10) for this point P. In the case of the point Q on its right, we have two points which are smaller than h. The formula (6.1.10) tackles this case as well. Horizontal R(t), vertical z(t). 178

6.3 Contour plot of exact streamfunction values (a) and numerical values (b) for the sphere using the boundary condition $\Psi = (1 + \cos\theta) - \frac{1}{2}\sin^2\theta$. Also plotted are the horizontal (c) and vertical (d) velocity along the horizontal centreline. 184

6.4 Contour plot for computational results for the sphere using the boundary condition $\Psi = (1 + \cos\theta) - \frac{1}{2}\sin^2\theta$. Here, the demonstration of the code efficiency is through the showing of more coarse grids. Also plotted are the horizontal and vertical velocity along the horizontal centreline. First a 4x4 grid (contour plot (a), horizontal velocity (b) and vertical velocity (c)), then we have an 8x8 ((d)-(f)), 16x16 ((g)-(i)), 32x32 ((j)-(l)) and 64x64 ((m)-(o)) grid respectively. Again the urethra is at the origin. . 189

6.5 Constructions of triangles used for the calculations. 191

6.6 Shapes that the axisymmetric vessel takes at different times as it collapses with a cardioidal-like shape. Horizontal axis is R, vertical is z. . 194

6.7 Contour plots of the fluid motion within the modeled collapsing vessel. Also plotted are the horizontal and vertical velocity along the horizontal centreline. Times for the parts are 0.01 -just after the start of micturition- (contour plot (a), horizontal velocity (b) and vertical velocity (c)), then 8((d)-(f)), 13((g)-(i)), 15((j)-(l)) and 16.8 -just before the end of micturition- ((m)-(o)) respectively. 199

A.1 Example of 5-point stencil on our grid. 212

A.2 Contour plot of numerical streamfunction plots (a) and numerical vorticity plots (b) for the driven cavity problem with the scheme developed for Reynolds number of 1. The upper wall has a velocity of unity from left to right. 214

A.3 Contour plot of numerical streamfunction plots (a) and numerical vorticity plots (b) for the driven cavity problem with the scheme developed for Reynolds number of 100. 215

A.4 Contour plot of numerical streamfunction plots (a) and numerical vorticity plots (b) for the driven cavity problem with the scheme developed for Reynolds number of 400. 216

A.5 Plot of the shapes the vessel takes near time zero (a) and also the velocity profiles of v (b). Here, y, v are in the vertical direction and x, u (or shifted x as time increases) are in the horizontal direction. 222

A.6 Plot for a shape which evolves slightly faster in time towards a non-circular form. Here, the corresponding velocity profiles v are again presented and are somewhat more involved than the previous ones of Figure A.5. The temporal decay is nevertheless quite similar to that observed in the previous figure. 226

A.7 Plot (a) shows a more bladder-like evolution of the cross-sectional shape which is in keeping with those studied in earlier chapters of the thesis. The numbers shown on the shapes in the figure refer to entry numbers in the associated time-marching data file and hence are a scaled measure of time t. The velocity results v for the case of (a) are given in (b) and (c) and these include results for different grids, namely, 51x51, 76x76 and 101x101 in terms of $x \,\mathrm{x}\, y$. 229

Chapter 1

Introduction

1.1 Aims and Motivations

This thesis project concentrates on moving towards a quantitative model for the human bladder, part of the lower urinary tract [48]. Another main part which is the urethra is also examined in a thesis by Glavin [43]. The bladder model addressed here is simply a reservoir with a small outlet and the urethra model is a narrow tube. The present thesis project is very specific to the lower urinary tract application for which, more broadly and for the longer term, it aims to help with increased understanding of symptoms such as incontinence [3], [23]. The ageing population and people's demand for a better quality of life mean that the number of Stress Urinary Incontinence patients who need to be cured is increasing [63].

Around 15% of women and 7% of men suffer from incontinence while benign prostatic

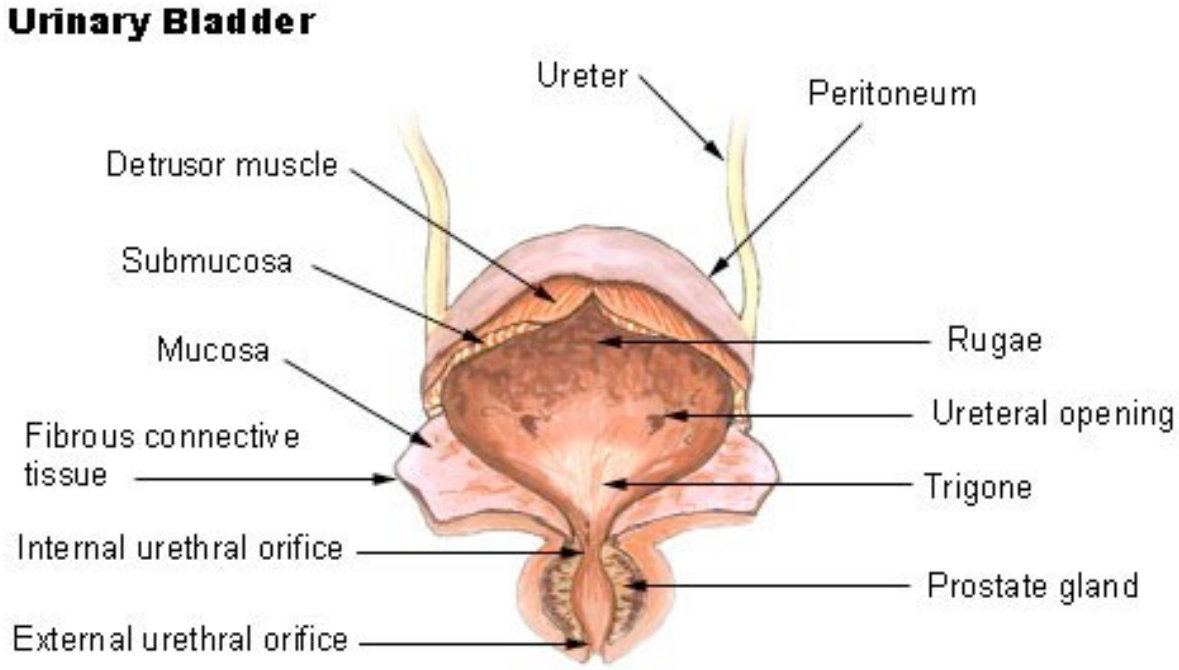

Figure 1.1: Diagram [112] of sections through the urinary tract and more specifically the ureters, parts of the bladder and the urethra.

hyperplasia occurs in more than 80% of men aged 75 [1]. Therefore, diagnosing and curing problems of the lower urinary tract is vital. This is the aim of urodynamics. Indeed in urodynamics, examination measurements such as pressure in various regions of the lower urinary tract, volume of urine and flow rate are taken and then used to indicate underlying pathologies. It is important to understand the physical properties of the tract and its contained flow of urine as several pathologies can exhibit similar symptoms. Developing a mathematical tool is potentially important in this regard as it could be used to check or validate current tests and measurements. It can also indicate further predictive tests that may prove useful in diagnosis by providing a better

understanding of the mechanics of the lower urinary tract. The complexity of a system such as the bladder means that a lot of important properties could be taken into account and hence investigated.

1.2 The Lower Urinary Tract

The urinary tract consists of a system of tubes, valves and reservoirs that guide and propel urine from the kidneys to the outside world [48] (see Figure 1.3). Urine in the kidneys is continuously formed in order to maintain the body's fluid and chemical balance. The kidneys are connected to the ureters passing the urine to the bladder. The ureters are mostly closed, apart from when every few seconds a bolus of urine passes along it towards the bladder. This is pushed through by a wave of muscular contraction in the ureteral wall. This is how urine is accumulated in the bladder. The bladder is connected on the other end by a tube called the urethra which passes the urine to the outside world. Apart from the time of micturition, the urethra is kept shut by muscular contraction. The modelling of many aspects of the lower urinary tract is done and it ranges from effects in ureteric stents in urine flow [30] to crystal aggregation and deposition in the catheterised lower urinary tract [6].

When a considerable volume of urine is accumulated in the bladder (normally between $350 - 500\,ml$), it is sensed by the nervous system and when socially convenient micturition occurs. The muscular walls of the bladder contract acting as a pump that expells the urine through the relaxed urethra to the outside world. Outflow is at a rate of about $25\,ml/s$. Backflow into the ureters is normally prevented by a non-return valve at the

junction of each ureter with the bladder. When the bladder empties, its wall relaxes and starts storing urine from the kidneys again. Therefore, the urethra closes.

1.2.1 The bladder

The urinary bladder is located immediately behind the pubic bones within the pelvis [102] as shown in Figure 1.2. The bladder, which is the part of the urinary tract that this thesis aims to model, is approximately a hollow sphere with an internal radius of about $5\,cm$. (The approximation as a sphere is rather a simplification since the bladder shapes vary hugely from person to person as described later on.) This muscular balloon shaped organ has two functions. It first collects the urine from the kidneys, thus acting as a reservoir, and then, during micturition by the use of the detrusor muscle, - an explanation of detrusor follows - it expels the urine out into the urethra. As far as we are aware, it appears that usually there is no air in the bladder. The bladder consists of a tissue which has a constant volume. Hence, the more the bladder fills the thinner the wall becomes. The thickness of it is typically just a few millimetres. The spherical shape of the bladder is preserved as long as it has more than about $100\,ml$. Anything below these levels makes the shape to fold up. At the end of micturition, the bladder usually remains with about $2\,ml$ of urine.

The bladder wall consists mainly of a smooth muscle called the detrusor (see Figure 1.1). It has two slits where the ureters are connected to it and a third one where the urethra starts. The muscle of the bladder is different between the three slits. It is anatomically different from the detrusor and is called the trigone. This is a smoother surface than

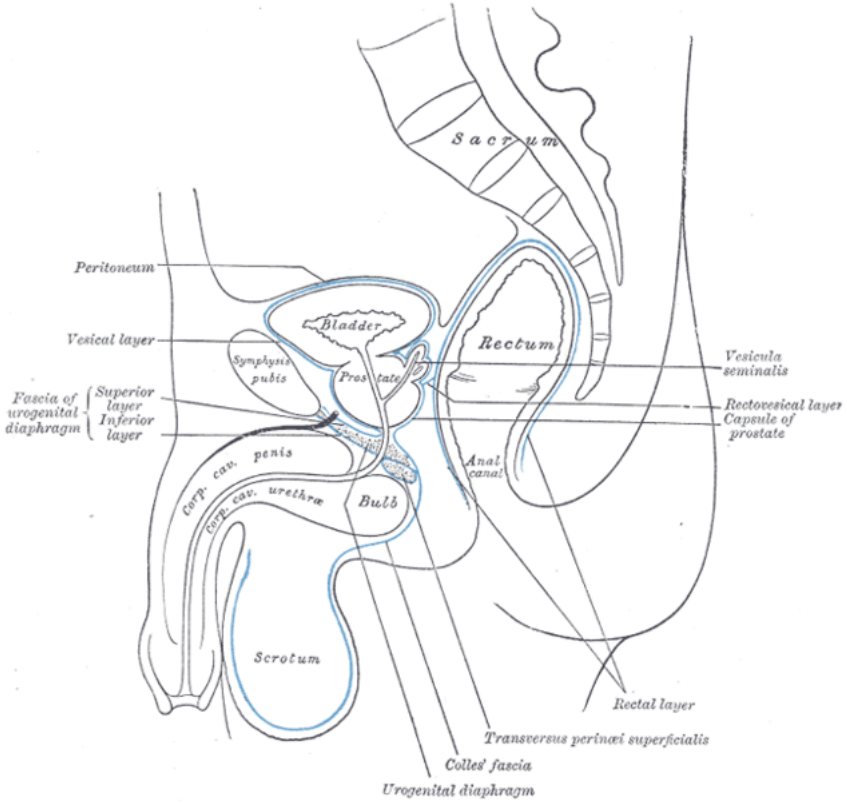

Figure 1.2: Sagittal section of the male pelvis [45]. The bladder, the peritoneum, the prostate and other parts around the area of concern are shown.

the rest of the bladder wall. However, the mechanical properties of the bladder are essentially those of the detrusor. Its fibres are visible and when they contract, they apply an approximately uniform surface tension within the bladder which generates a uniform pressure within the spherical modelled bladder. Near the urethra, the fibres of the detrusor along with those of the trigone and the urethra form the bladder neck.

The bladder is a special vessel as regards its shape. It alters in shape massively. Naturally, the quantity of urine in it is one of the reasons for the shape. When the bladder

empties, it collapses creating folds as mentioned earlier. On top of the bladder is the peritoreum as seen in Figure 1.2. This covers the bladder from the vertex to the line where the ureters enter the bladder. It is movable over the bladder and forms a transverse reserve fold which straightens out when the bladder is full. If it is filled to capacity, the vertex of the bladder ascends between the abdominal wall and the peritoneum [69]. Thus, folding and different shapes at all times are very common, posing considerable difficulty in terms of creating a useful tractable model. A large prostate can also affect the capacity of the bladder as well as its shape [48].

1.2.2 The urethra

The urethra is an output tube for the bladder and is used during micturition. The urethra is different for the two sexes. In particular, the male one is longer. Yet, in both cases it is a distensible, partly muscular, curved tube. At rest the walls are folded up and the urethra is closed [48]. Its cross sectional shape varies throughout its length and it is not plain circular. It even has different shapes at different parts of itself. It has an approximate diameter of $5\,mm$ but this varies throughout the length of the urethra. Indeed, it can be thicker at some parts than others.

Female Urethra

The female urethra is about $3.8\,cm$ long [103]. It starts from the neck of the bladder to the external meatus where it opens into the vestibule approximately $2\,cm$ below the clitoris. At the sides of the external meatus there are some small openings called the

paraurethral glands [103]. Much of the inner part of the wall is composed of smooth muscle with fibres running in a longitudinal direction and with a thin outer layer of circular fibres. This muscle is surrounded by a layer of grooved muscle fibres running in a circular direction within the urethral wall [48]. These grooved muscles exert a sustained contraction. This can be used to shut the urethra in order to hinder undesired leakage if the bladder should involuntarily contract. The periurethral sphincter is also responsible for this.

Male Urethra

The male urethra is about $20\,cm$ long and extends from the neck of the bladder to the external meatus on the glans penis [103]. It is divided into three parts, the prostatic urethra ($3\,cm$ in length), the membranous urethra ($1.5\,cm$ in length) and the penile urethra ($15.5\,cm$ in length). The prostatic urethra is the widest and the most dilatable part of all. The membranous urethra is surrounded by the urethral sphincter and is the least dilatable. The external meatus (the end lips of the urethra) of the penile urethra is the narrowest part of the whole urethra [103]. The penile urethra is mainly non-muscular during micturition [48].

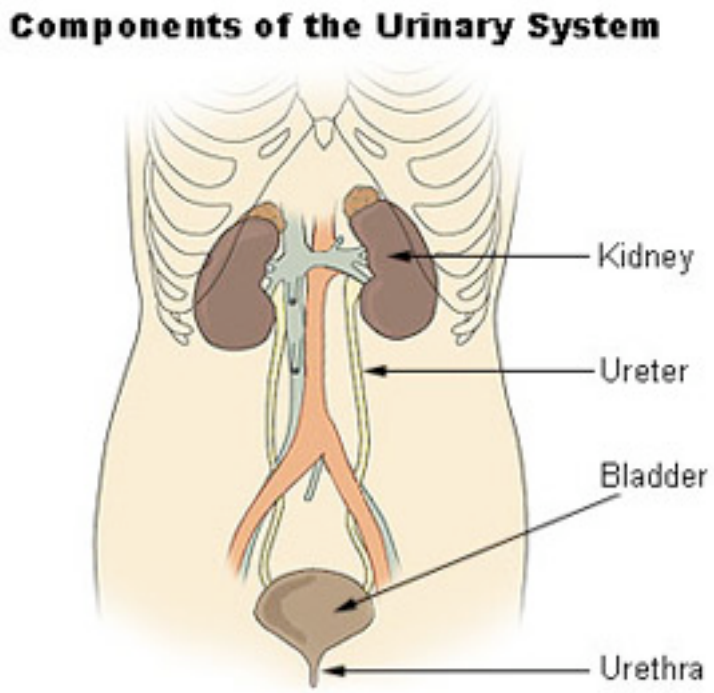

Figure 1.3: Diagram [112] of the lower urinary tract. Urine is formed in the kidneys and passes through the ureters to end up in the bladder where it is stored. When the time comes for micturition, urine is excreted to the outside world by the urethra.

1.3 Medical Background

1.3.1 Nervous Control

The muscles of the bladder and the urethra are controlled by the nervous system. The co-ordinated contraction associated with micturition is produced by stimulation of the detrusor. This happens due to motor impulses from the pelvic nerves which run from the lowest part of the spine to the bladder (parasympathetic branch). At the same

time, some of the urethral and peri-urethral muscles relax allowing fluid to pass more easily. This simultaneous contraction and relaxation is called a micturition reflex and is co-ordinated at the micturition centre in the sacral part of the spinal chord. The feedback input tending to trigger the reflex is believed to be an afferent signal in the pelvic nerve originating from the receptors in the bladder wall stimulated as the bladder fills with urine. If this were all then micturition would occur automatically at a certain bladder volume. Indeed, this may be the case in babies and people with certain types of spinal injury. However, the spinal centre that co-ordinates the reflex is also subject to learned voluntary control, descending from the brain via the spinal cord. As such, the trigger level can be voluntarily adjusted and the bladder volume at which micturition occurs can be controlled, within limits, at will. The bladder and urethra are also influenced by the sympathetic branch of the autonomic nervous system via the hypogastric nerves which originate from the middle part of the spinal cord. Sympathetic efferent signals inhibit contraction of the detrusor between micturitions and keep the urethra shut by stimulation of the urethral muscle. Finally, the peri-urethral sphincter can be consciously stimulated to contract by the somatic nervous system via the pudendal nerves which originate from the sacral part of the spine [48].

1.3.2 Pathology

The symptoms of the lower urinary tract are divided into three categories [23]. Here the description of [23] is adopted in a slightly modified form. As the name suggests, the storage symptoms are experienced during the storage phase in the bladder. The voiding

symptoms take place during the voiding phase while the post micturition symptoms happen straight after micturition.

The storage symptoms are the following:

- Increased daytime frequency - This is when the patient feels that he voids too often.
- Nocturia - This is when the patient has to wake up at night to void.
- Urgency - The patient has a sudden strong desire to void.
- Urinary incontinence - Involuntary leakage by the patient.

The voiding symptoms are as follows:

- Slow stream - Reduced flow rate.
- Splitting or spraying - The patient experiences splitting or spraying of the urine.
- Intermittent stream (intermittency) - Urine flow that starts and stops several times during micturition.
- Hesitancy - Difficulty to initiate micturition when ready to pass urine.
- Straining - Muscular effort used to initiate, maintain or improve the stream.
- Terminal dribble - Prolonged final part of micturition when flow has slowed.

The post micturition symptoms are as follows:

- Feeling of incomplete emptying

- Post micturition dribble - Involuntary loss of urine straight after finishing from the toilet.

For all the above symptoms there is a variety of causes that are split into three categories:

- Simple mechanical defect in the urinary tract (i.e. obstruction or mechanical weakness of the bladder).
- Malfunctioning of the neuromuscular control system.
- Both of the above at the same time.

Mechanical problems in the bladder tend to relate to low or high compliance of the detrusor muscle tissue. Medics often refer to a floppy bladder (high compliance) as being hypotonic and a stiff bladder (low compliance) as being hypertonic.

1.3.3 Urodynamics

An excellent description of urodynamics is given by [48] and others. Urodynamics is a group of diagnostic procedures (as hinted at the beginning of this chapter) that are performed to evaluate disorders related to the bladder and the urethra. The parameters which are measured during a urodynamic procedure mainly include pressure and flow rate. Figure 1.4 shows a normal flow rate plot against time taken from both academic and experimental results found in [1] and [98]. Thus far, procedures have been relatively insufficient in suggesting treatments for the problems involved. Developments in treatments depend to a large extent on understanding the behaviour of the system. The

present research aims at addressing mathematically part of that behaviour by tackling the mechanical behaviour of the bladder and its contained fluid. The high distensibility of the system in parallel with the large disturbances in the shape make this task quite hard to tackle and tend to put it outside the range of previous modelling as far as we know [115], [116]. It is very hard to understand the mechanical behaviour of the bladder due to its complex anatomy. Hence, in order to make any progress in tackling urodynamic problems, a grasp of the purely mechanical behaviour is vital [48].

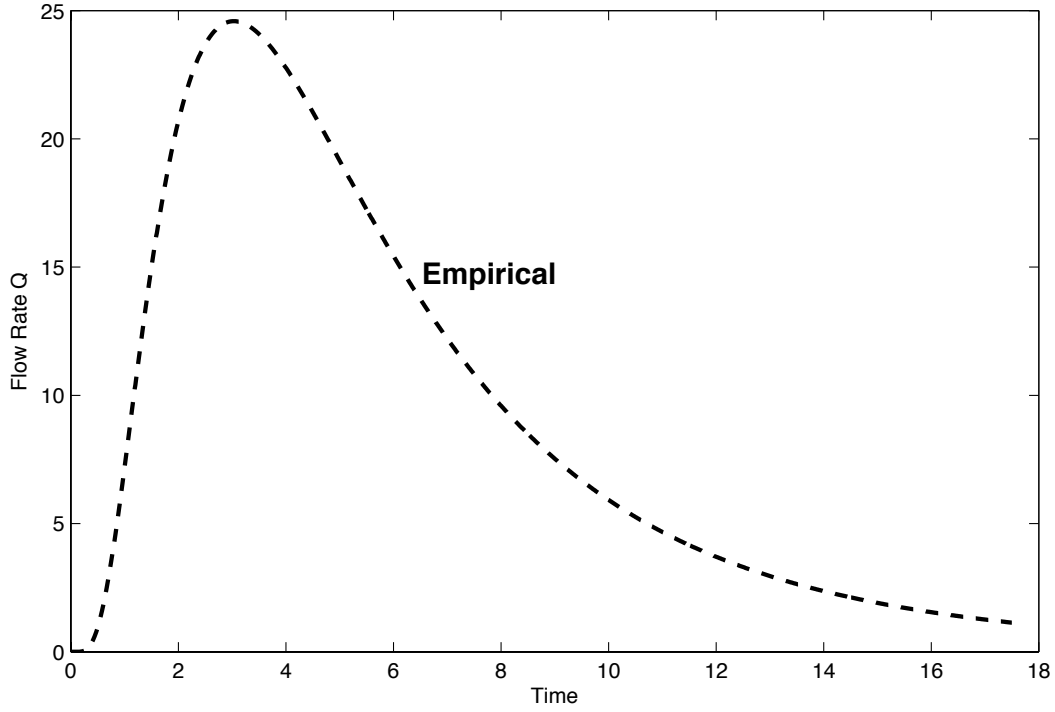

Figure 1.4: Graph of the actual representative normal flow rate during micturition.

1.4 Mechanics of the Bladder

1.4.1 Pressures

We will begin with the pressure relation that holds in the bladder as described and explained in [48],

$$p_{det} = p_{ves} - p_{abd}, \tag{1.4.1}$$

where p_{det} is the detrusor pressure due to forces in the bladder wall, p_{abd} is the abdominal pressure due to forces outside the bladder and p_{ves} is the intravesical pressure, namely, the pressure within the bladder. p_{ves} exists when a bladder is full and static, and is also uniform and measurable from point to point. It is therefore a purely hydrostatic pressure. Now, since p_{abd} is defined as the contribution to p_{ves}, it seems only sensible to define p_{det} and p_{abd} as purely hydrostatic pressures averaged over the bladder. However, measuring p_{abd} is difficult or almost impossible and as a result we cannot calculate p_{det}. Now, the stresses caused by p_{abd} are likely to be non-uniform and have shear components which are to be removed by averaging. To avoid this difficulty, clinicians measure in practice the hydrostatic pressure within a second cavity inside the abdomen and close to the bladder. The intrinsic contribution to the pressure from the cavity walls is neglected so that the measured piezometric pressure is the same as p_{abd} for the cavity [48].

When in equilibrium, urine has a vertical gravitational pressure gradient implying that pressures must be referred to a particular level. Since p_{ves} is the pressure in the bladder with respect to atmospheric pressure measured at the top of the bladder, a difference exists. However, the relevant differences are only minor, in fact quite small, compared

with the micturition bladder pressures. Micturition bladder pressures range from $20 - 100\,cm\,H_2O$, whereas gravitational pressures tend to be only a few $cm\,H_2O$ [48].

A quick estimate can be measured from the pressures at the top of the bladder to the bottom of the bladder near the urethra. Hence, the pressure at the urethra p_{ur} is

$$p_{ur} \approx \rho u^2 \approx \rho(300)^2, \tag{1.4.2}$$

where ρ is the urine density and u the speed of the fluid exiting the bladder. A value of $300\,cm/s$, which is perhaps a relatively high estimate for the speed, is taken. On the other hand, the pressure p_{gr} at the highest position of the spherical bladder, the hydrostatic one, is

$$p_{gr} \approx \rho g h \approx \rho(981)(10), \tag{1.4.3}$$

where g is the gravitational acceleration taken as $981\,cm/s^2$ and h is the bladder height taken to be $10\,cm$ (twice the radius of the bladder). Taking a ratio of the two gives

$$\frac{p_{gr}}{p_{ur}} \approx 0.1, \tag{1.4.4}$$

which is reasonably small. On the other hand, a relatively low estimate [48] of $100\,cm/s$ for the speed yields a pressure ratio of about 1. In any case, we decide to omit the gravity effect for now.

1.4.2 Filling and Evacuation Phases

Filling

This section starts with a discussion of the filling (storage) phase. Typically the ureters fill the bladder at the combined rate of approximately $1\,ml/min$ - about $1.5\,L/day$ - depending, obviously, on the recent fluid intake. By making the oversimplification that the bladder behaves like a thin-walled sphere, the detrusor pressure p_{det} due to forces in the bladder wall can then be expressed as [52]

$$p_{det} = \frac{F}{\pi R^2}, \tag{1.4.5}$$

where R is the bladder radius and $F = F(t)$ is the total force (tension) [48] depending on time t acting over the bladder circumference.

As the bladder is filled, the wall becomes gradually more stretched and so the force F increases. In addition, the radius R increases since the bladder gets larger. Now, looking at the above equation, it is seen that any increases in F and R^2 can cancel each other out, so that p_{det} normally remains quite low and nearly constant until the bladder is really full. At low volumes the bladder folds up. As mentioned before, this folding effect makes the modelling of the bladder rather difficult since it is in effect almost possible for the bladder to take any shape. The force F and therefore the detrusor pressure p_{det} also depend on the rate of bladder filling. During fast filling, higher detrusor pressures are recorded. This is obviously an oversimplification and it only applies when the bladder is spherical. However, as mention above, it is still hugely simplified.

Evacuation

Finally, the voiding (evacuation) phase is considered. The voiding is described by two entirely separate mechanical concepts:

- The detrusor pressure strength.
- The urethral resistance.

The detrusor pressure is not by itself a complete measure of the strength of the detrusor contraction since an adequately contracting detrusor can either produce a high detrusor pressure and low flow rate or a low pressure and high flow rate, depending on the urethral resistance [52]. This trade-off relation (bladder output relation) between the pressure generated and the flow rate produced is a consequence of the force/speed of the shortening relation, characteristic of any contracting muscle [48], [49].

One way to measure the detrusor contraction strength is by interrupting the stream during voiding and using the isovolumetric values of the detrusor pressure. Yet, this method is not suitable for following changes in contraction strength as the bladder empties.

A better way to measure the strength of the contraction is by using a variable WF (Watts Factor) [52], coming from the fundamental force/velocity law. This law is similar to the bladder power but has a near constant value for each trade-off curve and does not vary too widely during the normal bladder emptying [50], [51]. For any point during the void, the variable WF represents the power of the bladder during shortening and is calculated from p_{det}, the flow rate and the bladder volume [120]. Even though

it requires no additional manoeuvres to be performed by the patient, it is hard to calculate [16]. This allows measurement of the contraction strength without disturbing the micturition.

WF/volume plots can be used to predict both the contraction strength and dysfunctions during voiding by having in mind the following:

- The contraction does not diminish and probably becomes stronger until the bladder is essentially empty.
- If WF remains high until zero volume, meaning that the bladder is empty, then this corresponds to normal voiding.
- If WF goes to zero before the volume is zero, leaving the urine residual, this corresponds to malfunction of voiding i.e. obstruction, thickened bladder wall preventing complete collapse.

However, trying to model the detrusor contraction simply by using one variable (WF), no matter how complex that is, involves a large degree of approximation [52]. As such, a more sophisticated description might be more suitable sometimes according to [47], [119].

1.5 Medical Modelling

1.5.1 General

In recent years, a desire for a faster or more assured pace of development in medicine has (it seems) called for the involvement of modelling and more specifically mathematical modelling [19]. In order to be able to understand certain features relating to the human body and the various dynamics involved, a more mathematical approach has been felt to be of potential benefit, depending on what part or aspect of the body is of interest. This perceived need for medical modeling though had apparently an affect in mathematical developments as well. For example, the immersed boundary method [90] was developed by Peskin and McQueen [88] in order to model the human heart. Since then, the method has come a long way in terms of the applications [73], [93] it has tackled and most of all in medical modelling [62]. Other computational methods such as [17] have also been developed as a result of medical modelling challenges concerned with shape.

The progress of medical understanding in league with mathematical modelling has been considerable. Now, if not all, many parts of the body, from the skin down to the smallest cell have been or are modelled, . The numerous advances in computing power mean that numerical schemes can be used in order to model an ever-increasing variety of phenomena and processes. Many numerical schemes that will be used in this thesis and also others are mentioned later on.

1.5.2 Lower Urinary Tract Modelling

In recent years, modelling of medical issues that improve the quality of life is an area that has seen high demand. Even though the mechanics of the lower urinary tract have been modelled for a long time (see [47] D.J. Griffiths), the complex features of the bladder and its complex mechanics with respect to its obscure collapse mean that, in relative terms, not a lot of progress has been made. Currently, most models that are used for patient evaluation use statistical data. There is no direct or predictive model for the bladder collapse and the urethra response in order to aid their evaluation.

Currently, many researches study the pelvic floor dysfunction due to the decreasing biomechanical properties of the supporting tissue in the pelvic floor [33], [104]. Angiography and dynamic MRI examination during micturition were compared by Gufler et al [55]. The results showed that when the pelvic floor is functioning, there is no statistical difference in the position of bladder neck, urethral angle, bladder-urethra posterior angle and the position of vaginal vault through urinary bladder.

The development of non-invasive diagnoses by previous researchers in the area of the measurement of the bladder wall thickness, the prostatic size, the prostatic resistant index and the use of an inflatable penile cuff are some of the issues tackled in the past [7], [53], [72], [118]. Measurements by ultrasound visualisation is another tool that is recently used to get accurate results of bladder wall thickness and to diagnose prostatic hyperplasia. The detrusor muscle hypertrophy process is caused by the increase of the lower urinary tract obstruction [56], [66], [78]. The use of ultrasound visualisation means that the results are fast and effortless but they are not accurate.

Uroflowmetry is currently the representative non-invasive method for the diagnosis of the lower urinary tract symptoms and is used to measure the strength of uroflow. If the maximum uroflow rate is less than $10\,ml/s$, then there is a 90% possibility of obstruction (abnormal). If we get a value between $10\,ml/s$ to $15\,ml/s$, there is a 65% possibility of obstruction (equivocal). Finally, if the reading is higher than $15\,ml/s$, then the possibility of obstruction is 30% (normal). However, it is difficult to identify a lower bladder obstruction and detrusor contractile dysfunction [2], [57].

Computer technology means however that it is possible to utilise three-dimensional numerical methods to model bladder and urethra dynamics. Research also takes place on animal bladders such as for the cat [70]. In addition, a lot of simple models are developed [21], [117] but these are not very accurate since they cannot be applied to individual cases and hence they have no (or no direct) application in the clinical world. At the same time, there is a lot of three-dimensional research concerning the pelvic floor [4] and the urethra [84], [89]. Nonetheless, to date there is no realistic model around. A recent attempt to model the bladder and urethra dynamics is in [65] but even though flow is modelled using incompressible Navier-Stokes equations, the wall is treated as a rigid body ignoring its elastic characteristics. Other attempts were also made to model micturition based on urodynamic recording [113], [114] using the computational fluid dynamics method of [89].

The above then suggest that little progress has been made in recent years regarding the modelling of the lower urinary tract. Moreover, most of the studies involved cannot be used in clinical situations or even if they can, they are rather too oversimplified. Thus, it seems that a lot more progress needs to be made.

1.6 Numerical Schemes Used in the Thesis

1.6.1 Iterative Finite Difference Method

The main numerical scheme (see also the next section) that this thesis will widely use is the iterative finite difference method. This well established method is used extensively here but is modified in such a way that it is made more efficient around the boundary of the model shapes of interest. The conceptual and mathematical simplicity of this method make it more or less ideal to tackle the very enormously altered shapes of the containing vessels that will be examined here provided the issues of accuracy and flexibility are dealt with. The main disadvantage of the method is usually the fact that it is not very efficient around arbitrary curves and is more suitable for simple geometries [86]. However, the modification that is added on this method makes it in principle more accurate than without it and sufficiently flexible for the task of calculating fluid flows in a wide range of odd-shaped vessels. This method will be widely used here due to its simplicity.

1.6.2 Boundary Element Method

Another numerical scheme briefly used in this thesis is the boundary element method. This powerful numerical technique has many advantages for solving elliptic partial differential equations such as Laplace's equation, which is of concern to the work in the thesis. The strength of the method is in principle derived from its ability to solve efficiently and accurately problems in domains with complex and possibly evolving ge-

ometry where traditional methods can be inefficient or unreliable [91]. The boundary element method is also very efficient from a computational point of view in the sense that for the same level of accuracy, similar to other methods, it uses fewer nodes and elements. This results in less computer time and storage. It is also easy to define and vary the boundary elements. Its main disadvantages include fully or dense blockwise populated matrices, the difficulty in handling non-linear and inhomogeneneous problems [41], [54] and the fact that it requires the knowledge of a suitable fundamental solution. Furthermore, it is still perhaps a relatively recent method not very well known amongst users [41]. This method is more appropriate for problems with complex geometries such as the bladder but implementing the numerical scheme fully proves complex. We therefore develop and use this method up to a certain level.

1.7 Thesis Summary

The thesis at heart is interdisciplinary involving medical modelling and applied mathematics at the very least. The particular area of study concerning the human bladder and its contained fluid dynamics is in many senses a new area and that leads to a novel set of questions to be addressed. The complexity of the shapes that the bladder can take during its collapse make this task rather awkward and a unique aspect of the study. The main task though is to provide for a good mathematical basis to tackle shapes like the ones shown in the cystourethrograms in Figures 1.5 and 1.6.

The background of the thesis and a review of the chapters that follow are presented next.

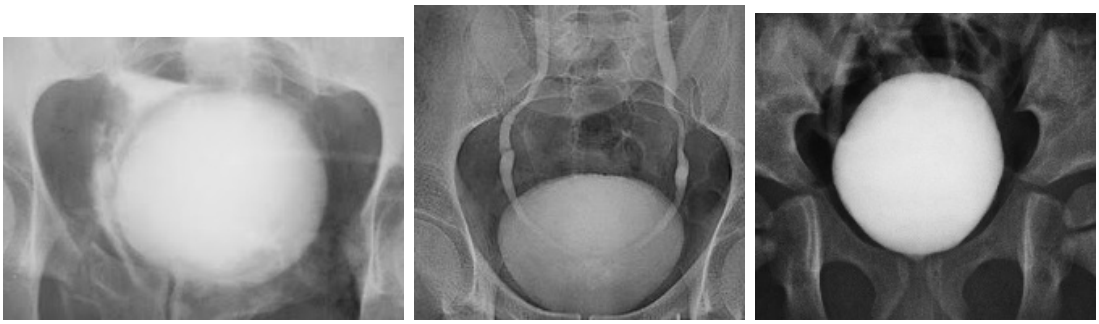

(a) (b) (c)

Figure 1.5: Starting shapes of bladder, taken by a Voiding Cystourethrogram (a) [34], (b) [85], (c) [92]. The bladder is the light circular patch in the middle. Also visible around it are bones and in (b) the ureters can be seen coming down. See also Figure 1.6.

1.7.1 Background

This thesis therefore will use a simple and quite basic approach to construct and address a first model for the bladder collapse in order to aid the understanding of the associated medical processes. The complex shape of the bladder, the consequent lack of knowledge regarding its mechanics and the large changes in the vessel shape are central problems here. The aim is to tackle the task both numerically to examine the massive changes in the vessel shape and analytically to aid or direct its numerical aspects.

As mentioned in section 1.6, two methods will mostly be used to tackle the vessel collapse; a modified iterative finite difference method and, to a lesser extend, a boundary element method. Other methods might also have been appropriate for such modelling, subject to the comments in the previous section.

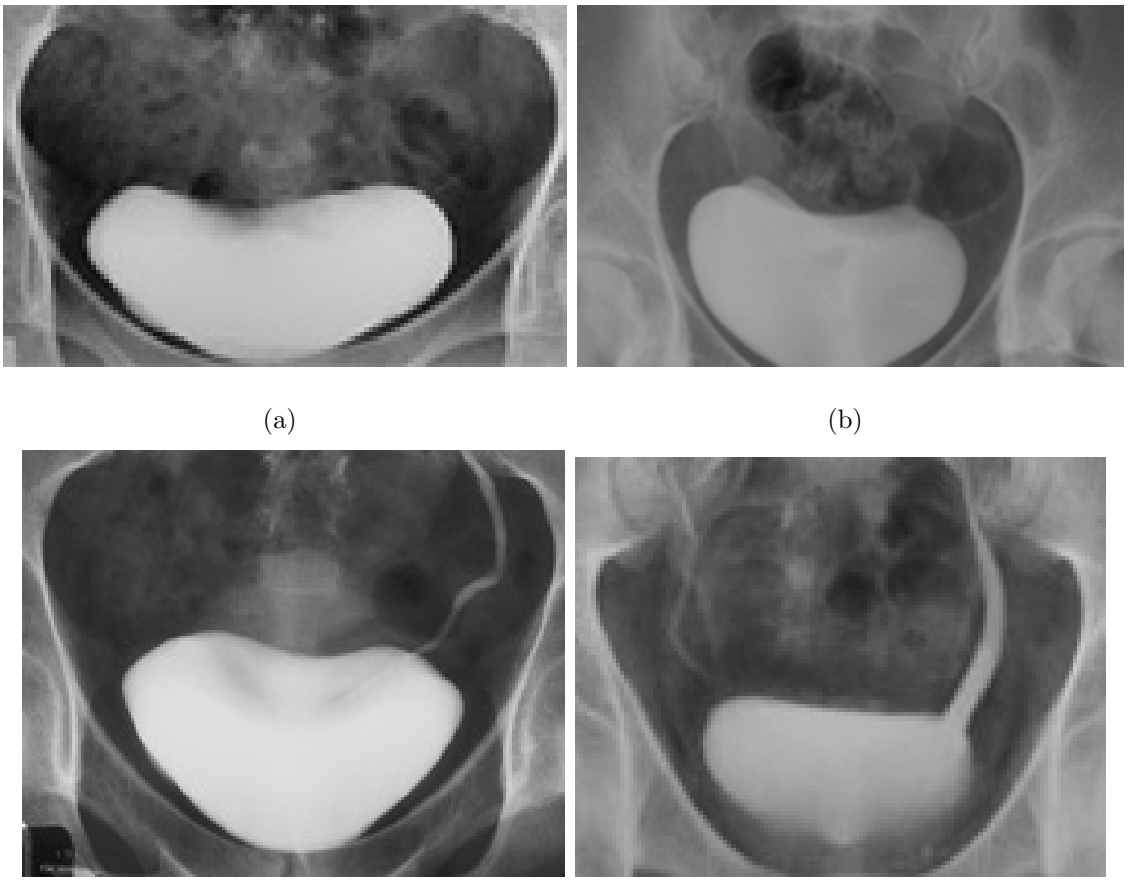

(a) (b)

(c) (d)

Figure 1.6: Shapes of different bladders later on during micturition, taken by a Voiding Cystourethrogram (a) [27], (b) [29] , (c) [27], (d) [92]. Once again the light patch in the middle is the bladder. Also visible are the bones and in some instances like in (c) and (d) we can see the right ureter.

As a matter of fact we have considered using conformal mappings [97] in order to tackle the two-dimensional models in the thesis. The feature that this method is very well established for solving Laplace's and related equations in two dimensions, is counterbal-

anced by the disadvantage that the method is in reality applicable only in two spatial dimensions. Obviously, the plan of the present thesis is to use a flexible method that can be built on and taken easily from two to three dimensions. Another disadvantage of conformal mapping is the fact that the grid density is not controlled readily in the physical domain [36].

Another possibility would be using a volume of fluid (VOF) method [106]. This would be achieved by discretizing the volume fraction of one of the fluids in a two-fluid context say by using a conservation law to capture the motion on the interface for the volume fraction and the Navier-Stokes equations simultaneously. The need for mass conservation would also be imposed. In addition, the difficulty in computing accurate local curvature from volume fraction due to the sharp transition in volume fraction near the interface means that probably it would not be the ideal technique to tackle vessel collapse of such distorted shapes [126] as those of concern here.

The level set method is also another method that could possibly be used. The fact that this method uses an implicit approach makes the tackling of topological changes easy to handle. The approach can also be extended to higher dimensions with relative ease [18]. However, its computational complexity and comparatively more difficult implementation make this method unattractive on the whole here [107].

Another possibility that is increasingly popular is the immersed boundary method [90]. This method is designed to work with moving interfaces on fixed meshes. It uses extra delta-function approximations near the boundary to account for interface conditions and then a standard finite difference stencil. The simplicity of the method makes it

very attractive but the findings are only first order accurate [107], [12], by the Dirac delta function approximation. Also the method apparently is not able to produce reliable gradients at the interface which has a certain drawback regarding its application here [107].

This thesis in contrast explores a simple approach which stems in detail from that developed by Tadjfar and Smith (2004) [108] and Bowles, Ovenden and Smith (2008) [17] and which, like theirs, has the advantage of being rather flexible in terms of the types of shapes it can handle. It is clear that this flexibility is potentially important in the context of bladder modelling especially since the variety of shapes that bladders can take from person to person are remarkably extensive [32], [48], [83], [127]. The flexibility is believed to extend in principle also to covering complicated three-dimensional geometries and folding processes of the kind mentioned previously. The simple approach just mentioned refers to a numerical methodology developed in the thesis, namely, a finite difference treatment. Nevertheless, analysis methodology is also adopted in many parts of this study, as remarked earlier on, and is proved very helpful in providing test cases and independent comparisons for the numerical methodology.

1.7.2 Chapter Review

The main body of the thesis is split into five chapters. Chapters 2 and 3 describe the analytical work. In particular, chapter 2 tackles two-dimensional problems and chapter 3 axisymmetric problems. The analysis here is for rather simple shapes for both the two-dimensional and axisymmetric cases. This work though is significant for

the latter parts of the thesis as they provide the backbone of the numerical work that is undertaken in chapters 4-6. Chapter 4 tackles simple two-dimensional models and is mostly used to validate the numerical scheme with respect to the analysis performed in chapter 2. Chapter 5 extends the method to tackle more complex shapes using the scheme from [17]. Chapter 6 deals with the extension of the numerical method used and developed in the previous chapters in order to use it for axisymmetric geometries.

1.8 Non-Dimensionalisation

Throughout this thesis, non-dimensional terms will be used. Hence, strictly no units will be used. It is a simple matter however to extract the predictions below in physical dimensional form, as is done in several parts of the presentation. Laplace's equation does not need any special treatment in that regard.

Chapter 2

Analysis of Two-Dimensional Shapes

The concern in this chapter is with setting the initial scene for the thesis by means of certain two-dimensional models involving particular shapes, for each of which direct analytical progress proves possible. In terms of application and motivation, it is noted that in reality bladders especially do indeed take many different shapes and sizes. The phenomenon of bladder-expansion or contraction is rather like that for a balloon, a subject where the compressibility of the contained fluid (air) can play an important role. However, in our setting the fluid (urine or water say) is incompressible. In terms of analysis, it should be mentioned that some solutions below (see for example (2.1.22)) represent exact solutions and others are results obtained from the use of matched asymptotic expansions.

The bladder is special in terms of its evolving shape; it deforms a great deal, more so than perhaps any other major vessel in the human body over the particular time scales involved. Tackling such a complex problem as the collapse of the human bladder could entail careful consideration of many factors. However, it makes sense to start with a simple model in the form of a two-dimensional circular vessel or "bladder" as in Figure 2.1 in order to try to obtain an analytical solution and hence some basic insight. The extraction of the fluid is through the sink at the bottom of the vessel which is taken to be a point. The flow is modelled within such a vessel which is collapsing inwards. The vessel has a well prescribed shape (a circle for example) in two dimensions where the point sink at the bottom of the vessel represents the opening of the urethra. The mass flux Q into the point sink can be determined directly from a total mass conservation balance if, as in the present study, the squeeze velocity (in the normal direction) at the vessel walls displayed in Figure 2.1 is assumed given. The work in this thesis however is intended to also determine the flow streamlines and velocities produced inside the vessel.

The nondimensionalisation applied here is based on a representative velocity of the fluid U^* say and a length scale L^* such as the typical effective bladder diameter. The Reynolds numbers $\frac{U^*L^*}{\nu^*}$ of concern have generally large values (see the next paragraph), where ν^* is the kinematic viscosity of the fluid, and as a first approximation these act to justify the use of inviscid modelling. The pressure is made nondimensional with respect to ρ^*U^{*2} where ρ^* is the fluid density, while the time scale T^* may be estimated as $\frac{L^*}{U^*}$ or conversely the velocity scale may be defined as $\frac{L^*}{T^*}$ for a given time scale T^*. However, many of the results found below can be immediately applied in dimensional

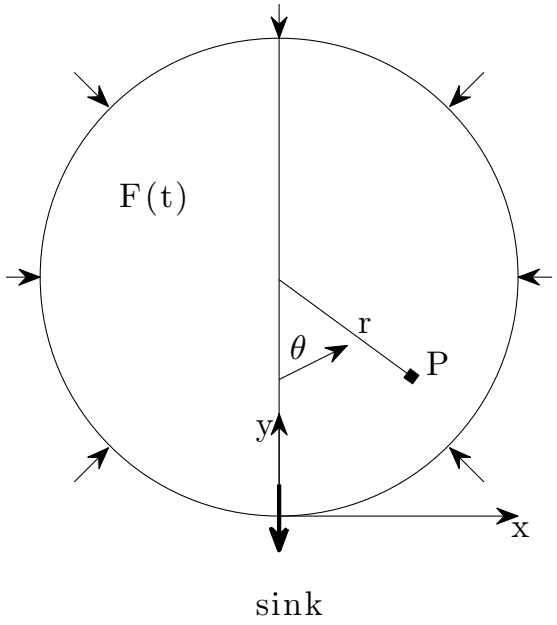

Figure 2.1: Simple circular structure for the vessel showing the prescribed normal velocity condition (the "squeeze") at the vessel wall, the Cartesian and polar reference coordinates and the sink. The radius of the vessel here is $F(t)$ at time t.

terms as it will become apparent.

Generally the Reynolds numbers for the collapsing bladder have quite large values. When the bladder is full it has an approximately spherical shape with a diameter of about 0.1 m. The representative speed of urine during micturition at the urethra is between 1-4 m/s [48]. As an estimate based on two-dimensional mass conservation and taking the thickness of the urethra to be 0.005 m, the speed of the urine in the bladder is between 0.05-0.2 m/s. Taking the kinematic viscosity of urine [77], [99], [122] at body temperature of 37^oC to be approximately 0.7x10^{-6} m^2/s, we end up with a

Reynolds number of 7142 (using a velocity of 0.05 m/s). In cases where the speed of the flow is higher, the Reynolds number becomes even larger of course. In cases where the bladder has a small diameter, for example when near the end of its collapse say at 0.02 m (the bladder does reduce much more than this), the Reynolds number is still the same at 7142 (since two-dimensional mass conservation then gives an increased speed in the bladder of 0.25-1 m/s). As a consequence, the flow may be taken to be unsteady, incompressible and irrotational, and as such the governing equation of the streamfunction within the domain is

$$\nabla^2 \Psi(x, y, t) = 0 \tag{2.0.1}$$

where $\nabla^2 = \frac{\partial^2}{\partial x^2} + \frac{\partial^2}{\partial y^2}$ is the Laplacian operator, Ψ is the streamfunction, t denotes time and x, y are the Cartesian co-ordinate axes as in Figure 2.1. This partial differential equation is Laplace's equation in two dimensions. The streamfunction is a scalar field which is related, as below, to the fluid velocity $\mathbf{v}$ in order to satisfy continuity, in other words $\nabla \cdot \mathbf{v} = 0$. It is also suitable to mention at this point the potential function, a scalar field often written as Φ and also related to $\mathbf{v}$, in order to satisfy irrotationality, that is $\nabla \times \mathbf{v} = 0$. Laplace's equation (2.0.1) is equivalent here to this irrotationality condition.

The aim is to determine the streamfunction at every interior point of the domain D, the inner part of the vessel, and then find the velocity $\mathbf{v} = (u, v)$ using

$$u = \frac{\partial \Psi}{\partial y}, \qquad v = -\frac{\partial \Psi}{\partial x}, \tag{2.0.2}$$

where u is the horizontal velocity of the flow in the x direction and v the vertical in the y direction. This will be done here by first finding an analytical solution for the

streamfunction at any point inside the vessel, and then using (2.0.2) to calculate the velocities of the flow at any point inside.

2.1 Analytical Solution for Fluid Flow in a Circular Bladder with a Point Discontinuity

2.1.1 Use of Poisson Integral Formula

Use will be made of the Poisson Integral Formula [20], [46], [64] applied within a disk. Let $f(\theta)$ be a real valued function that is bounded and may be either continuous or piecewise continuous for $-\pi < \theta < \pi$. Then, when the integral exists, the function

$$\psi(r,\theta) = \frac{1}{2\pi}\int_0^{2\pi} \frac{(R^2 - r^2)f(\phi)d\phi}{R^2 - 2rR\cos(\phi - \theta) + r^2} \tag{2.1.1}$$

is harmonic inside the disk $0 \leq r \leq R$, and on the boundary of the disk $r = R$. This assumes that the boundary condition $\psi(R,\theta) = f(\theta)$ wherever $f(\theta)$ is continuous or piecewise continuous.

An attempt is made to evaluate this integral in the case where $f(\phi) = \phi - \sin(\phi)$ (see below), and for convenience substitute ϕ with $\hat{\theta}$. This boundary condition includes a sink at the required point (in our case the origin). Also, for simplicity and without loss of generality, we assume that $R = 1$, hence $0 \leq r \leq 1$. Substituting into (2.1.1), we have

$$\psi(r,\hat{\theta}) = \frac{1 - r^2}{2\pi}\int_0^{2\pi} \frac{\hat{\theta} - \sin(\hat{\theta})}{1 - 2r\cos(\hat{\theta} - \theta) + r^2}d\hat{\theta}. \tag{2.1.2}$$

The function describing $f(\theta)$ here arises from the kinematic boundary condition (see equation (2.1.16) in the next section) on the vessel which in this case is circular. Therefore (2.1.2) gives us the analytical formula for the streamfunction in the vessel in terms of an integral which is studied in the following subsections.

Kinematic Boundary Condition for a Circle or an Ellipse

In order to ensure that in the normal direction the fluid at the wall of the vessel is moving with the same velocity as the vessel wall, as shown in Figure 2.1, we need to embed in our mathematical formulation the kinematic boundary condition [9]. The fluid is as if inviscid in the present setting. At an impermeable boundary, the flow of fluid relative to the boundary must be tangential to it. The sink is at the bottom of the setup and it remains fixed with the vessel collapsing towards it. If the boundary is fixed in space, this means that the component of fluid normal to the boundary must be zero. However, if the boundary is moving (as in our case), then the normal component of the fluid flow velocity must be equal to the velocity of the boundary normal to itself.

So, if $F(\mathbf{x}, t) = 0$ is the equation of the bounding surface, always consisting of the same particles, then

$$\frac{DF}{Dt} = 0 \quad \text{on} \quad F = 0, \tag{2.1.3}$$

where $\frac{D}{Dt} = \frac{\partial}{\partial t} + \mathbf{u}.\nabla$ is the material derivative. This is the kinematic boundary condition and expresses the fact that a bounding surface is a fluid material surface, at all points on the surface. Therefore, for the two-dimensional case

$$\frac{\partial F}{\partial t} + v\frac{\partial F}{\partial y} + u\frac{\partial F}{\partial x} = 0. \tag{2.1.4}$$

From the fact that $u = \frac{\partial \Psi}{\partial y}$, $v = -\frac{\partial \Psi}{\partial x}$ the kinematic boundary condition becomes

$$\frac{\partial F}{\partial t} - \frac{\partial F}{\partial y}\frac{\partial \Psi}{\partial x} + \frac{\partial F}{\partial x}\frac{\partial \Psi}{\partial y} = 0. \tag{2.1.5}$$

To begin with, the vessel here is modelled using the shape of an ellipse, that includes the circle as a special case. In other words,

$$F(x, y, t) = \frac{x^2}{a^2} + \frac{(y-b)^2}{b^2} - 1, \tag{2.1.6}$$

with $a = a(t)$ and $b = b(t)$ denoting the lengths of the semi-major and semi-minor axis respectively and in general being time dependent. The ellipse is placed in such a way that its lowest point lies at the origin as in Figure 2.2. Now, differentiating F with respect to t, x and y,

$$\frac{\partial F}{\partial t} = -\frac{2x^2 a'}{a^3} - \frac{2b'(y-b)}{b^2} - \frac{2b'(y-b)^2}{b^3}, \quad \frac{\partial F}{\partial x} = \frac{2x}{a^2} \quad \text{and} \quad \frac{\partial F}{\partial y} = \frac{2(y-b)}{b^2}. \tag{2.1.7}$$

Here $a' = \frac{\partial a}{\partial t}$ and $b' = \frac{\partial b}{\partial t}$.

Parametric co-ordinates are used to describe the ellipse which is shown in Figure 2.2 where θ and r are measured from the centre of the ellipse as shown in Figure 2.1 with the urethra at the bottom. Namely,

$$\frac{x}{a} = r\sin(\theta) \quad \text{and} \quad \frac{y-b}{b} = -r\cos(\theta). \tag{2.1.8}$$

This of course satisfies $F(x, y, t) = 0$ in our case as we take $r = 1$ in this setup. This implies the need to use the following chain rules

$$\frac{\partial \Psi}{\partial x} = \frac{\partial \Psi}{\partial r}\frac{\partial r}{\partial x} + \frac{\partial \Psi}{\partial \theta}\frac{\partial \theta}{\partial x}, \quad \frac{\partial \Psi}{\partial y} = \frac{\partial \Psi}{\partial r}\frac{\partial r}{\partial y} + \frac{\partial \Psi}{\partial \theta}\frac{\partial \theta}{\partial y}, \tag{2.1.9}$$

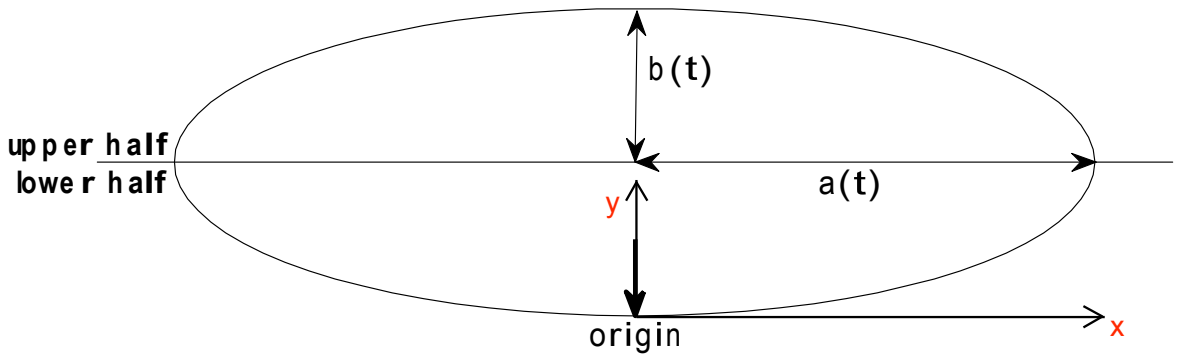

Figure 2.2: Ellipse-shaped vessel, the major and minor axes, the sink (at the origin) and the lower and upper halves of the ellipse for future reference.

in order to change from Cartesian to parametric coordinates. Thus, we need to work out $\frac{\partial r}{\partial x}$, $\frac{\partial r}{\partial y}$, $\frac{\partial \theta}{\partial x}$, $\frac{\partial \theta}{\partial y}$ by converting equations (2.1.8) in order to have an equation for r dependent on just x and y and similarly θ dependent only on x and y. This is done in order to evaluate the partial derivatives. Doing that we have

$$r = \sqrt{\left(\left(\frac{x}{a}\right)^2 + \left(\frac{y-b}{b}\right)^2\right)}, \theta = \arctan\left(\frac{-xb}{a(y-b)}\right). \tag{2.1.10}$$

Working out $\frac{\partial r}{\partial x}$, $\frac{\partial r}{\partial y}$, $\frac{\partial \theta}{\partial x}$ and $\frac{\partial \theta}{\partial y}$ and substituting in (2.1.9) yields

$$\frac{\partial \Psi}{\partial x} = \frac{\sin(\theta)}{a}\frac{\partial \Psi}{\partial r} + \frac{\cos(\theta)}{ar}\frac{\partial \Psi}{\partial \theta}, \tag{2.1.11}$$

and

$$\frac{\partial \Psi}{\partial y} = -\frac{\cos(\theta)}{b}\frac{\partial \Psi}{\partial r} + \frac{\sin(\theta)}{br}\frac{\partial \Psi}{\partial \theta}. \tag{2.1.12}$$

Now, substituting in (2.1.5) yields

$$\left(-\frac{1}{ab}\right)\frac{\partial\Psi}{\partial\theta} = -\frac{a'(\sin(\theta))^2}{a} + \frac{b'\cos(\theta)}{b} - \frac{b'(\cos(\theta))^2}{b}, \tag{2.1.13}$$

which upon rearrangement becomes

$$\frac{\partial\Psi}{\partial\theta} = ba'(\sin(\theta))^2 - ab'\cos(\theta) + b'a(\cos(\theta))^2. \tag{2.1.14}$$

The derivatives of Ψ with respect to r cancel out. The result (2.1.14) for an ellipse-shaped vessel is subsequently used in the thesis.

In the case of a circle, $a = b$ and $a' = b'$. Hence, (2.1.14) becomes

$$\frac{\partial\Psi}{\partial\theta} = aa'(1 - \cos(\theta)), \tag{2.1.15}$$

which implies that, to within an arbitrary constant,

$$\Psi_B = aa'(\theta - \sin(\theta)), \tag{2.1.16}$$

where Ψ_B is the stream function at the boundary. This is in keeping with the form written in the previous subsection and more specifically in equation (2.1.2). As we have observed previously, a and a' are only dependent on time t and thus can be regarded as constant when it comes to the integral of interest (2.1.2). The working here helps to derive equation (2.1.2) and more specifically $f(\theta)$ which is part of it.

The Integral for the case of a Circle

Focusing specifically on the circle, we now address (2.1.2) for the circular shape in detail in order to determine the exact explicit solution for the circular vessel, which will enable

us to compare with numerical results later on in chapter 4. To start with, we split the integral into two parts such that

$$\frac{1-r^2}{2\pi}\int_0^{2\pi}\frac{\hat{\theta}-\sin(\hat{\theta})}{1-2r\cos(\hat{\theta}-\theta)+r^2}d\hat{\theta}$$
$$=\frac{1-r^2}{2\pi}\left(\underbrace{\int_0^{2\pi}\frac{\hat{\theta}}{1-2r\cos(\hat{\theta}-\theta)+r^2}d\hat{\theta}}_{\text{(A)}}-\underbrace{\int_0^{2\pi}\frac{\sin(\hat{\theta})}{1-2r\cos(\hat{\theta}-\theta)+r^2}d\hat{\theta}}_{\text{(B)}}\right). \quad (2.1.17)$$

We first attempt to integrate part (A) of (2.1.17),

$$A=\int_0^{2\pi}\frac{\hat{\theta}}{1-2r\cos(\hat{\theta}-\theta)+r^2}d\hat{\theta}, \quad (2.1.18)$$

through various integration techniques. The step by step full solution of the integral can be found in Appendix B. Hence, we obtain the following result

$$\frac{1-r^2}{2\pi}\int_0^{2\pi}\frac{\hat{\theta}}{1-2r\cos(\hat{\theta}-\theta)+r^2}d\hat{\theta}$$
$$=\begin{cases}\theta+\pi-2\arctan\left(\frac{(1+r)\tan(\frac{\theta}{2})}{(1-r)}\right) & \text{for } 0\leqslant\theta<\pi\ ,\\ \theta-\pi-2\arctan\left(\frac{(1+r)\tan(\frac{\theta}{2})}{(1-r)}\right) & \text{for } \pi\leqslant\theta<2\pi\ .\end{cases} \quad (2.1.19)$$

Next, we attempt to integrate part (B), namely,

$$B=-\int_0^{2\pi}\frac{\sin(\hat{\theta})}{1-2r\cos(\hat{\theta}-\theta)+r^2}d\hat{\theta}. \quad (2.1.20)$$

Once again this is shown in full detail in the Appendix B, and we have

$$\frac{1-r^2}{2\pi}\int_{-\theta}^{2\pi-\theta}\frac{\sin(\varphi+\theta)}{1-2r\cos(\varphi)+r^2}d\varphi=r\sin(\theta). \quad (2.1.21)$$

Therefore, adding together parts (A) and (B), we have

$$\begin{aligned}\psi(r,\hat{\theta}) &= \frac{1-r^2}{2\pi}\int_0^{2\pi}\frac{\hat{\theta}-\sin(\hat{\theta})}{1-2r\cos(\hat{\theta}-\theta)+r^2}d\hat{\theta} \\ &= \begin{cases} \theta - r\sin(\theta)+\pi-2\arctan\left(\frac{(1+r)\tan(\frac{\theta}{2})}{(1-r)}\right) & \text{for } 0\leqslant\theta<\pi\ , \\ \theta - r\sin(\theta)-\pi-2\arctan\left(\frac{(1+r)\tan(\frac{\theta}{2})}{(1-r)}\right) & \text{for } \pi\leqslant\theta<2\pi\ . \end{cases}\end{aligned} \tag{2.1.22}$$

This is the analytical result for the stream function value at any point inside the circle dependent on r and θ. Plotting this result on $Matlab$, we end up with Figure 2.3.

2.1.2 Use of Complex Functions

Another way to tackle analytically the two-dimensional problem described in section 2.1.1 is using complex functions. This will be another way to double check our result and provide a foundation for future work since a similar method can be used in axisymmetric flows.

Let there be once again an irrotational flow of incompressible inviscid fluid. Then, it satisfies the irrotationality and incompressibility conditions, namely,

$$\frac{\partial u}{\partial y}-\frac{\partial v}{\partial x}=0, \quad \frac{\partial u}{\partial x}+\frac{\partial v}{\partial y}=0. \tag{2.1.23}$$

In this context, x and y denote the usual position vectors whereas u and v the horizontal and vertical velocities respectively. As it is common, the velocity can be written in terms of a scalar potential in order to satisfy identically the irrotationality condition, and also in terms of the stream function in order to satisfy the incompressibility condition.

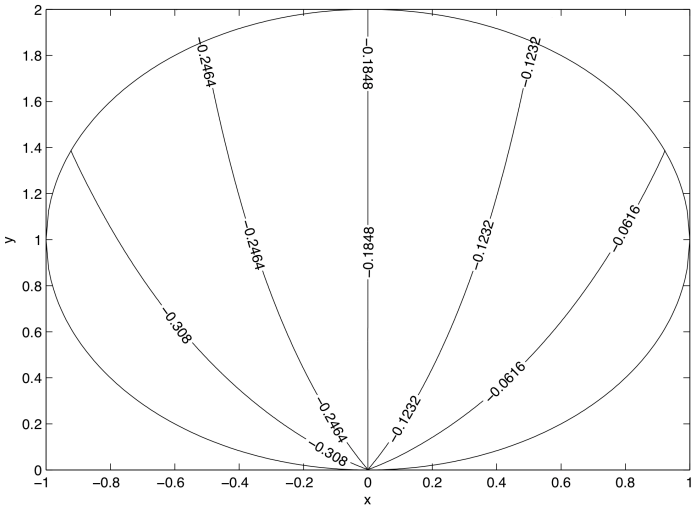

(a)

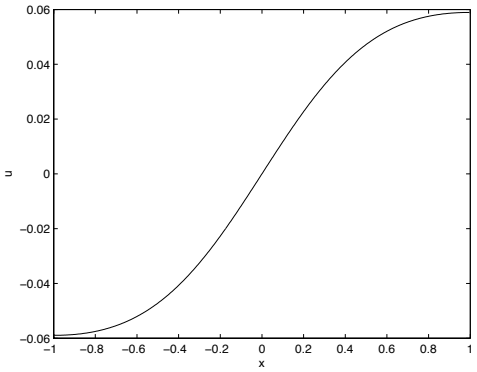

(b)

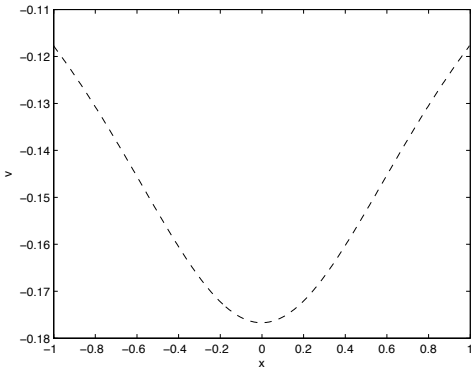

(c)

Figure 2.3: Analytical result: the two-dimensional streamlines in the vessel derived by the Poisson Integral Formula. Streamlines are of course not normal to the wall as there is usually tangential velocity as well. Also plotted are the horizontal (b) and vertical (c) velocity along the horizontal centreline.

Hence, the flow that satisfies equations (2.1.23) has the property that

$$u = \frac{\partial \Phi}{\partial x} = \frac{\partial \Psi}{\partial y}, \quad v = \frac{\partial \Phi}{\partial y} = -\frac{\partial \Psi}{\partial x}. \tag{2.1.24}$$

Once again Φ is the velocity potential and Ψ the stream function.

Considering the complex function defined by

$$\omega = \Phi(x, y) + i\Psi(x, y), \tag{2.1.25}$$

i.e. the complex potential, the real and imaginary parts of ω also satisfy the Cauchy-Riemann equations. Hence, ω is also analytic and can only be written as a function of the complex position z, namely $\omega = \omega(z)$.

Now, let $f(z)$ be the complex potential of a flow with no rigid boundaries and with no singularities within a distance a from the origin. Then, by introducing an impermeable circular cylinder into the flow field, we are led by the method of images [9] into forming the complex potential

$$\omega(z) = f(z) + \bar{f}\left(\frac{a^2}{z}\right), \tag{2.1.26}$$

where the overbar denotes the complex conjugate. This is the circle theorem. The proof is simple. Since $|z|^2 = z\bar{z} = a^2$ on the boundary of the circle, equation (2.1.26) becomes

$$\omega(z) = f(z) + \bar{f}\left(\bar{z}\right). \tag{2.1.27}$$

It follows that $\omega(z)$ is real-valued on $|z| = a$ and hence gives zero stream function as required on the boundary. This methodology forms the basis for the approach developed below.

Formulation of the Present Problem

The solution for the circular problem of current concern is obtained as follows. Bear in mind three main features which are: the sink at the urethra, the squeeze velocity at the moving boundary and the fact that the urethra position remains fixed throughout. See Figure 2.1. We first allow for a flow due to a point source in the centre of a circle (a sink at the origin will be added in subsequently to cancel out that source). From [80] and [82] we know that the complex potential for a source is

$$\omega(z) = m \ln(z - z_0), \tag{2.1.28}$$

where m is the source strength and is equal to the volumetric discharge from the source per unit length into the plane of the flow. Also, $z_0 = (x_0, y_0)$ is the point where the source is placed in the complex plane. Define the source at O as having complex potential

$$\omega_1(z) = m_1 \ln(z), \tag{2.1.29}$$

with m_1 the volumetric flow at O as shown in Figure 2.4. We also define a sink directly below it at C in Figure 2.4, namely,

$$\omega_2(z) = -m_2 \ln(z + i), \tag{2.1.30}$$

with m_2 the volumetric flow at C. We then add the corresponding two images arising from the circle theorem (2.1.26), obtaining the image term

$$\omega_3(z) = m_1 \ln(\frac{1}{z}) \tag{2.1.31}$$

from equation (2.1.29), and also from equation (2.1.30) the image term

$$\omega_4(z) = -m_2 \ln(\frac{1}{z} - i), \tag{2.1.32}$$

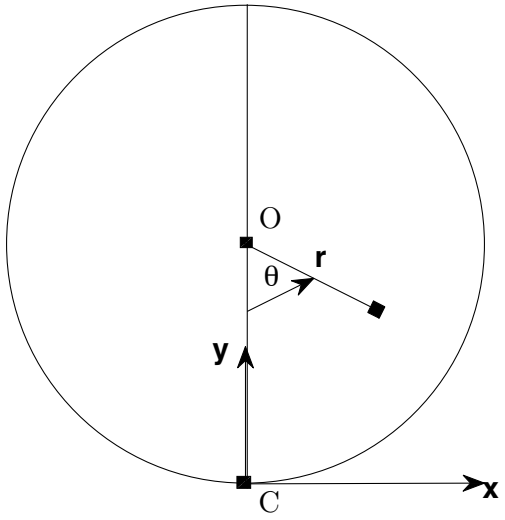

Figure 2.4: Simple circular structure for the vessel showing the positions of the sink C and effective source O as well as the Cartesian and polar reference points. Cartesian axes are centred at the urethra as shown. The squeeze velocity at the boundary and the sink also apply here in the same way as Figure 2.1 (see arrows).

with m_1 and m_2 as defined above.

The next step is to put together the source at O of (2.1.29) and the sink at C of (2.1.30) along with their images in (2.1.31), (2.1.32) and admit a sink at the origin (as mentioned in the previous paragraph) to cancel out the source at the origin, thereby allowing for the normal squeeze velocity at the boundary of the circle. Finally, we add a uniform downward flow in order to keep the urethra position of our vessel fixed while squeezing takes place. Adding up all the terms and canceling out accordingly, we have

simply

$$\omega(z) = -m(2\ln(z+i) + iz), \tag{2.1.33}$$

where the second term on the right hand side of (2.1.33) is due to the uniform downward flow. Now, using equation (2.1.25), equation (2.1.33) is split into real and imaginary parts ending with

$$\Phi = -my - m\ln(x^2 + (1+y)^2), \quad \Psi = mx - 2m\tan^{-1}[x, 1+y], \tag{2.1.34}$$

where $\tan^{-1}[y, x]$ gives elements that lie in the closed interval $[-\pi, \pi]$. As we have been working with the stream function thus far, we will continue to do so and proceed to plot this.

Use is made of the same parametric coordinates as before in order to describe the circle with the urethra at the bottom, namely,

$$x = r\sin\theta, \quad y = -r\cos\theta, \tag{2.1.35}$$

with r being the radius of the circle and θ the angle measured from the bottom vertical as shown in Figure 2.4. Hence, substituting these coordinates in the second equation of (2.1.34), we find

$$\Psi = mr\sin\theta - 2m\tan^{-1}[r\sin\theta, 1 - r\cos\theta]. \tag{2.1.36}$$

Plotting on *MatLab*, we obtain Figure 2.5. The results here make good physical sense in terms of the streamlines and their shapes as fluid is squeezed inward (pushed) at the vessel wall and drawn down (pulled) by the sink at the lowermost position.

Comparing Figure 2.3 with Figure 2.5, it is seen that the two results are identical and hence the analyses performed are equivalent. The analysis using complex variables is

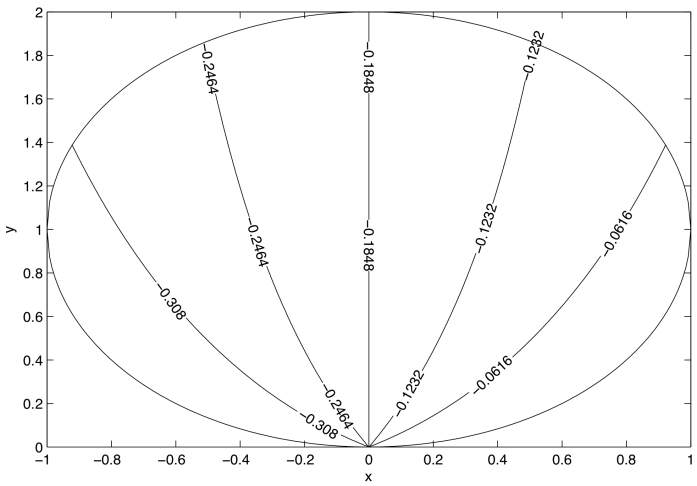

(a)

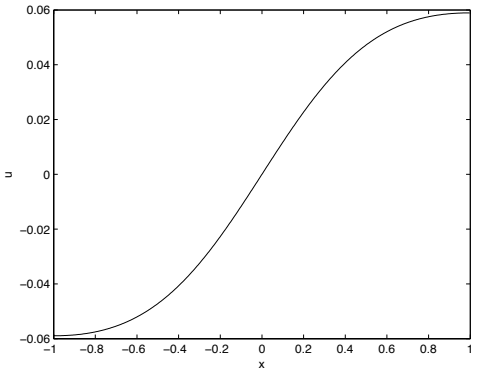

(b)

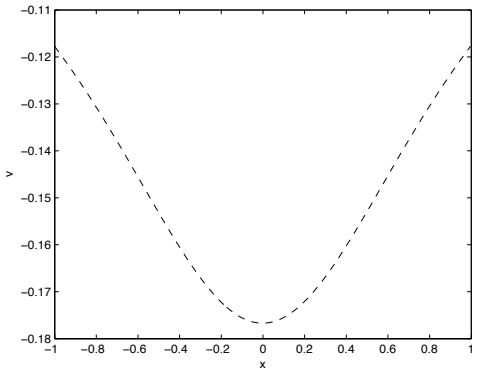

(c)

Figure 2.5: Analytical result for the two-dimensional flow in a circular vessel derived by the complex function analysis showing the streamlines. Also plotted are the horizontal (b) and vertical (c) velocity along the horizontal centreline.

especially useful later in the thesis as we can apply a similar analysis for axisymmetric flow. Therefore, it is encouraging to see that the result from the Poisson integral also matches the complex variable flow result.

2.2 Analysis for Elliptical Thin Two-Dimensional Shapes of Vessel

We now examine the flow solution for thin elliptical shapes of the vessel, further to the work on the kinematic boundary condition earlier in the chapter. Of course the analysis carried out here is for extreme cases with the shape being extremely thin. However, this gives us values and directions of the flow in order to make comparisons with our computational results later on. The work on thin vessels is similar to that on fluid guns [101] and on free surfaces with small gravity effects [60], [100], [111].

As with the circular shape, the flow is initially modeled within a vessel of a well prescribed shape (an ellipse in this case) in two dimensions. The vessel collapses inwards with a point sink at the bottom of the ellipse.

2.2.1 Thin Horizontal Vessel

Considering Laplace's equation (2.0.1) once again in two dimensions and taking $x \sim 1$ but $y = h\bar{y}$, with $\bar{y}$ of O(1) but the thickness parameter h small, we have

$$\Psi_{xx} + \frac{\Psi_{\bar{y}\bar{y}}}{h^2} = 0. \tag{2.2.1}$$

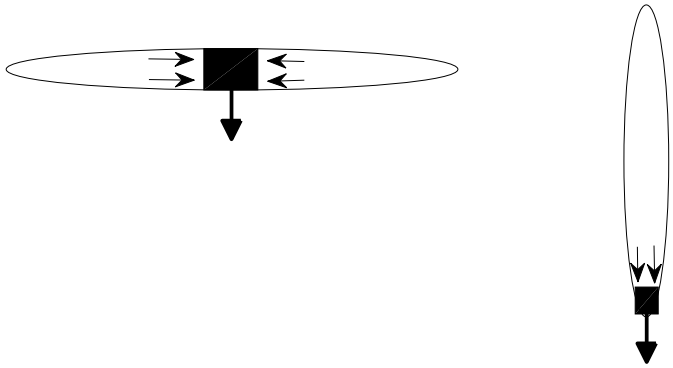

Figure 2.6: Thin horizontal (left) and thin vertical (right) elliptical vessels. Mathematical analysis for the two cases is performed in the text. The so-called Euler region in black is shown. Incoming flows induced outside that region are also shown. See section 2.2.3.

An asymptotic expansion can now be set up for the solution Ψ in terms of powers of h in the majority of the flow field; thus, we have

$$\Psi = \Psi_0(x, \bar{y}) + \dots . \tag{2.2.2}$$

Since h is small the governing equation of the streamfunction within the domain is to leading order simply

$$\Psi_{\bar{y}\bar{y}} = 0 \quad (\text{or more strictly } \Psi_{0\bar{y}\bar{y}} = 0), \tag{2.2.3}$$

for any thin vessel, including the case of a thin horizontal ellipse. We refer here to Figure 2.6 and we also refer forward to section 2.2.3 for consideration of the small Euler region which is also present. Using the kinematic boundary condition of (2.1.4), (2.1.5)

in the form

$$F_t + u\frac{\partial F}{\partial x} + \bar{v}\frac{\partial F}{\partial y} = 0, \tag{2.2.4}$$

the prescribed shape now has $F(x, y, t) = y - f(x, t)$ say. Hence,

$$\frac{\partial F}{\partial t} = -f_t, \quad \frac{\partial F}{\partial x} = -f_x, \quad \frac{\partial F}{\partial y} = 1. \tag{2.2.5}$$

Substitution in (2.2.4) thus leads to another traditional form,

$$\bar{v} = f_t + uf_x, \tag{2.2.6}$$

where $y = f(x, t)$ is the prescribed vessel shape.

For a general thin ellipse, (2.2.3) implies that

$$\Psi = A(x, t)y + B(x, t), \tag{2.2.7}$$

where $A(x, t)$, $B(x, t)$ are effectively constants of integration. Therefore

$$u = \frac{\partial \Psi}{\partial y} = A(x, t)\,,\ \bar{v} = -\frac{\partial \Psi}{\partial x} = -A_x(x, t)y - B_x(x, t). \tag{2.2.8}$$

Taking $B(x, t) = 0$ for now for simplicity, we obtain from equation (2.2.6) the equation

$$f_t = -(uf_x + fu_x). \tag{2.2.9}$$

This is one of the classical slender-flow or shallow water equations as expected [31], [95].

In particular, we now take $y = f_1(x, t) = \frac{ba+b\sqrt{a^2-x^2}}{a}$ being the upper half of the ellipse and $y = f_2(x, t) = \frac{ba-b\sqrt{a^2-x^2}}{a}$ the lower half, where $a = a(t)$ and $b = b(t)$. Now, the kinematic boundary condition at the top wall of the ellipse is $\bar{v} = (f_1)_t + u(f_1)_x$ and at the bottom wall $\bar{v} = (f_2)_t + u(f_2)_x$. In general, $B(x, t) \neq 0$; so we end up with

$$-u_x f_1 + B_x = (f_1)_t + u(f_1)_x, \tag{2.2.10}$$

and

$$-u_x f_2 + B_x = (f_2)_t + u(f_2)_x. \tag{2.2.11}$$

Subtracting the two equations from each other, we have

$$-u_x \mathscr{F} = \mathscr{F}_t + u\mathscr{F}_x, \tag{2.2.12}$$

where $\mathscr{F} = f_1 - f_2$ is the scaled width of the ellipse.

Thus, we see in effect that the kinematic boundary condition can be written here as

$$\mathscr{F}_t + (U\mathscr{F})_x = 0, \tag{2.2.13}$$

where $u = U(x,t)$ is unknown and

$$\mathscr{F} = \frac{2b\sqrt{a^2 - x^2}}{a}. \tag{2.2.14}$$

Integrating in x then gives

$$U(x,t) = -\frac{1}{\mathscr{F}}\left(\int \mathscr{F}_t \, dx + c(t)\right), \tag{2.2.15}$$

where $c(t)$ is a constant of integration.

Substituting (2.2.14) into (2.2.15), yields the form

$$U(x,t) = -\frac{a}{2b\sqrt{a^2 - x^2}} \left((b'a - a'b)\frac{x}{a^2}\sqrt{a^2 - x^2} + (b'a + a'b)\arcsin\left(\frac{x}{a}\right) + c(t)\right). \tag{2.2.16}$$

We then use the end conditions $U = \pm a'$ at $x = \pm a$ to find $c(t)$ and hence our equation for $U(x,t)$. In doing so, we find

$$c(t) = \begin{cases} (ba' + b'a)\frac{\pi}{2} & \text{for } 0 < x < a\ , \\ -(ba' + b'a)\frac{\pi}{2} & \text{for } -a < x < 0. \end{cases} \tag{2.2.17}$$

Hence, the induced velocity is

$$U(x,t) =$$
$$\begin{cases} -\frac{a}{2b\sqrt{a^2-x^2}}\left((b'a-a'b)\frac{x}{a^2}\sqrt{a^2-x^2}+(b'a+a'b)\left(\arcsin\left(\frac{x}{a}\right)-\frac{\pi}{2}\right)\right) & \text{for } 0<x<a\ , \\ -\frac{a}{2b\sqrt{a^2-x^2}}\left((b'a-a'b)\frac{x}{a^2}\sqrt{a^2-x^2}+(b'a+a'b)\left(\arcsin\left(\frac{x}{a}\right)+\frac{\pi}{2}\right)\right) & \text{for } -a<x<0. \end{cases} \tag{2.2.18}$$

We will now assume that the vessel contracts inwards with its sides collapsing at the same rate as the top but the bottom remaining fixed. We then use the following for $a(t)$ and $b(t)$ as a simple representation,

$$a(t) = a_0 - \frac{a_0}{b_0}t,\ b(t) = b_0 - t, \tag{2.2.19}$$

where a_0 and b_0 are the initial values of a and b respectively. Hence,

$$\frac{b}{a} = \frac{b_0}{a_0} \quad \text{for all } t. \tag{2.2.20}$$

In order to demonstrate the above form of $U(x,t)$, we substitute numerical values for a and b. We let $a_0 = 12$, $b_0 = 4$ which implies that $a' = -3$, $b' = -1$. We first examine the case where $t = 0$ which implies that $a = a_0$ and $b = b_0$. Hence, we obtain

$$U(x,t) = \frac{36}{\sqrt{144-x^2}}\left(\arcsin\left(\frac{x}{12}\right)+\frac{\pi}{2}\right), \qquad -12<x<0, \tag{2.2.21}$$

and

$$U(x,t) = \frac{36}{\sqrt{144-x^2}}\left(\arcsin\left(\frac{x}{12}\right)-\frac{\pi}{2}\right), \qquad 0<x<12. \tag{2.2.22}$$

Plotting the above on *MatLab* produces Figure 2.7. It is noticeable that the induced horizontal velocity is directed inwards towards the vessel centre, which is not surprising

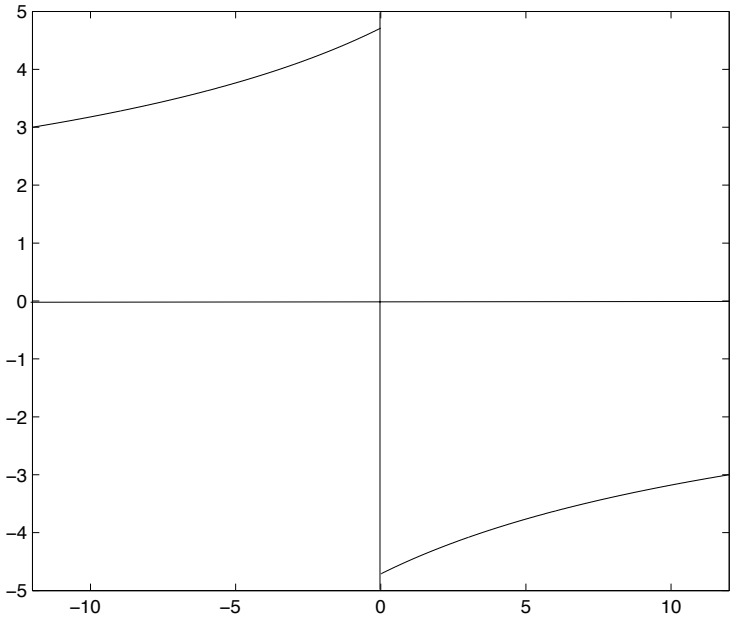

Figure 2.7: Plot of the velocity U (vertical axis) against x (horizontal axis) at time $t = 0$ for initial conditions $a = 12$, $b = 4$ (implies $a' = -3$, $b' = -1$). See also section 2.2.3.

in view of the overall squeeze effect taking place. Moreover, the fluid speed increases towards the centre leaving a discontinuity there on the present length scales.

Similarly, we can plot the same graph for the same initial conditions but at $t = 3$, where $a = 3$ and $b = 1$, giving

$$U(x,t) = \frac{9}{\sqrt{9-x^2}}\left(\arcsin\left(\frac{x}{3}\right) + \frac{\pi}{2}\right), \qquad -3 < x < 0, \tag{2.2.23}$$

and

$$U(x,t) = \frac{9}{\sqrt{9-x^2}}\left(\arcsin\left(\frac{x}{3}\right) - \frac{\pi}{2}\right), \qquad 0 < x < 3, \tag{2.2.24}$$

yielding a similar graph as shown in Figure 2.8. Comments similar to those at the end of the previous paragraph apply here as well.

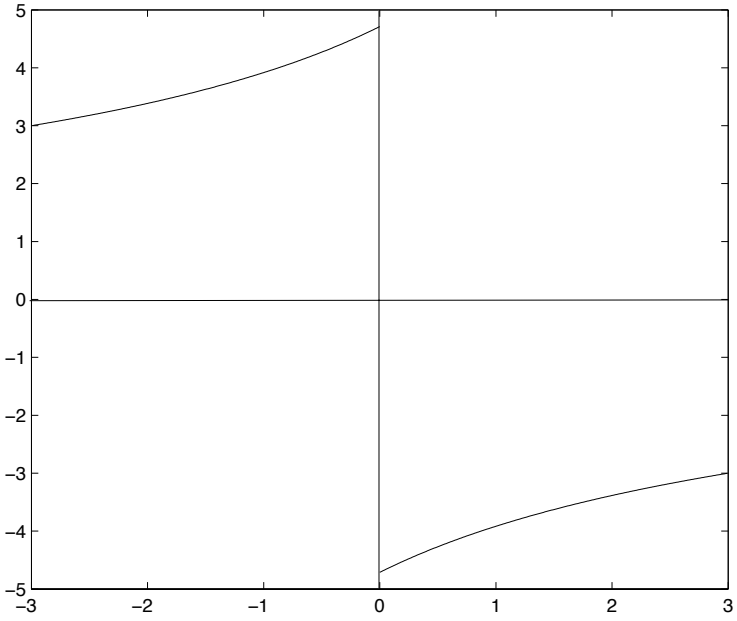

Figure 2.8: Plot of the velocity U (vertical axis) against x (horizontal axis) at time $t = 3$ with initial conditions $a = 12$, $b = 4$ (implies $a' = -3$, $b' = -1$). This looks similar to Figure 2.7 but in a shorter scale due to the vessel collapse. See section 2.2.3.

For the streamlines of this flow, the relationship $u(x,t) = \frac{\partial \Psi}{\partial y} \Rightarrow \Psi = uy$ is used to

within an additive function of x. As a result, we use (2.2.18) to find

$$\Psi = \begin{cases} -(b'a - a'b)\frac{xy}{2ab} - \frac{ay(b'a+a'b)\left(\arcsin\left(\frac{x}{a}\right)-\frac{\pi}{2}\right)}{2b\sqrt{a^2-x^2}} & \text{for } 0 < x < a\ , \\ -(b'a - a'b)\frac{xy}{2ab} - \frac{ay(b'a+a'b)\left(\arcsin\left(\frac{x}{a}\right)+\frac{\pi}{2}\right)}{2b\sqrt{a^2-x^2}} & \text{for } -a < x < 0. \end{cases} \tag{2.2.25}$$

Plotting once again on *Matlab* results in Figure 2.9. Again, we refer forward to section 2.2.3 as regards matters of length scale.

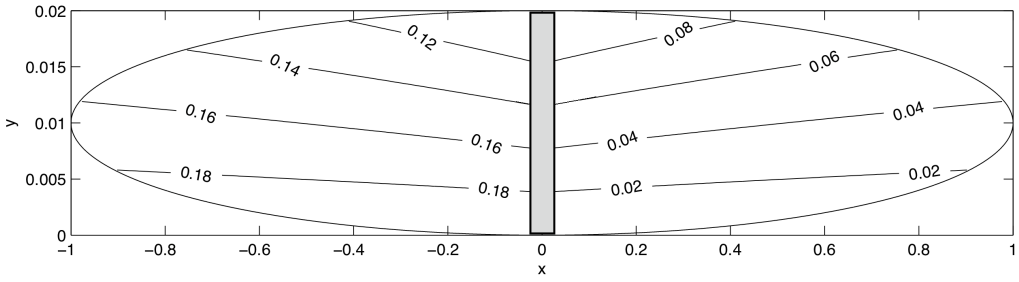

Figure 2.9: Contours of the streamfunction $\Psi \approx \Psi_0$ at time $t = 0$ with initial conditions $a = 1$, $b = \frac{1}{100}$. The streamlines are all directed towards the centre $x = 0$. Concerning the shaded area in the middle, see Figure 2.15 for the solution closer to $x = 0$.

2.2.2 Thin Vertical Vessel

A similar analysis to the one carried out above can be performed for an ellipse that is vertically thin, a case which is shown in Figure 2.6. As before, the flow is taken to be unsteady, incompressible and irrotational. Using Laplace's equation and asymptotic expansions once again and taking in this case $y \sim 1$ and $x = k\bar{x}$, with k very small, we

have

$$\Psi_{yy} + \frac{\Psi_{\bar{x}\bar{x}}}{k^2} = 0, \tag{2.2.26}$$

and thus the expansion in powers of k develops in the form

$$\Psi = \hat{\Psi}_0(\bar{x}, y) + \dots, \tag{2.2.27}$$

(see also Euler region later in section 2.2.3). Now, since k is small, we obtain the governing equation of the streamfunction within the domain as

$$\Psi_{\bar{x}\bar{x}} = 0 \quad \text{(or more strictly } \hat{\Psi}_{0\bar{x}\bar{x}} = 0), \tag{2.2.28}$$

for a thin vertical ellipse. Now, we also use the kinematic boundary condition, namely,

$$\frac{DF}{Dt} = \frac{\partial F}{\partial t} + u \cdot \nabla F = 0, \tag{2.2.29}$$

and therefore for two dimensions it takes the form

$$F_t + \bar{u}\frac{\partial F}{\partial x} + v\frac{\partial F}{\partial y} = 0. \tag{2.2.30}$$

In our case, the prescribed shape has an equation of the form $F(x, y, t) = x - f(y, t)$. Differentiating with respect to x, y and t and substituting in (2.2.30), we end up with

$$\bar{u} = f_t + v f_y, \tag{2.2.31}$$

where $x = f(y, t)$ is the prescribed shape of the vessel. Using similar calculations to the thin horizontal shape, we obtain

$$f_t = -(v f_y + f v_y). \tag{2.2.32}$$

In this case, we will take $x = f_1(y,t) = \frac{a\sqrt{2yb-y^2}}{b}$ being the left half of the ellipse and $x = f_2(y,t) = -\frac{a\sqrt{2yb-y^2}}{b}$ the right half where $a = a(t)$ and $b = b(t)$. In other words, we define our shape as an ellipse centred at $(0,b)$ once again but now our major axis is b. Following a similar analysis to section 2.2.1, we have a similar result of the form

$$-v_y F = F_t + vF_y, \tag{2.2.33}$$

where $F = f_1 - f_2$ is the scaled width of the ellipse, and hence

$$V(y,t) = -\frac{1}{F}\left(\int F_t\, dy + c(t)\right), \tag{2.2.34}$$

where $F = \frac{2a\sqrt{2yb-y^2}}{b}$. Differentiating F with respect to t, substituting in equation (2.2.34) and integrating, we end up with the result

$$V(y,t) = -\frac{b}{2a\sqrt{2by-y^2}} \left(\left(\frac{(a'b-b'a)(y-b)}{b^2} - \frac{2ab'}{b}\right)\sqrt{2by-y^2} + (a'b+b'a)\left(\arccos\left(\frac{b-y}{b}\right) - \pi\right)\right), \tag{2.2.35}$$

with the constant arriving from the initial conditions at $y = 2b$ where $V = -b'$ to find $c(t)$ and hence our equation for $V(y,t)$. We also take the same assumptions as in the horizontal case about the rate of collapse, so (2.2.20) is used.

To generate some insight for the above equation for $V(y,t)$, we substitute specific numbers in (2.2.19) for a and b that also satisfy (2.2.20). We let $a = 4$, $b = 12$ which implies $a' = -\frac{1}{3}$, $b = -1$ and $t = 0$. Hence, we have

$$V(y,t) = -1 + \frac{12}{\sqrt{24y-y^2}}\left(\arccos\left(\frac{12-y}{12}\right) - \pi\right), \qquad 0 < y < 24. \tag{2.2.36}$$

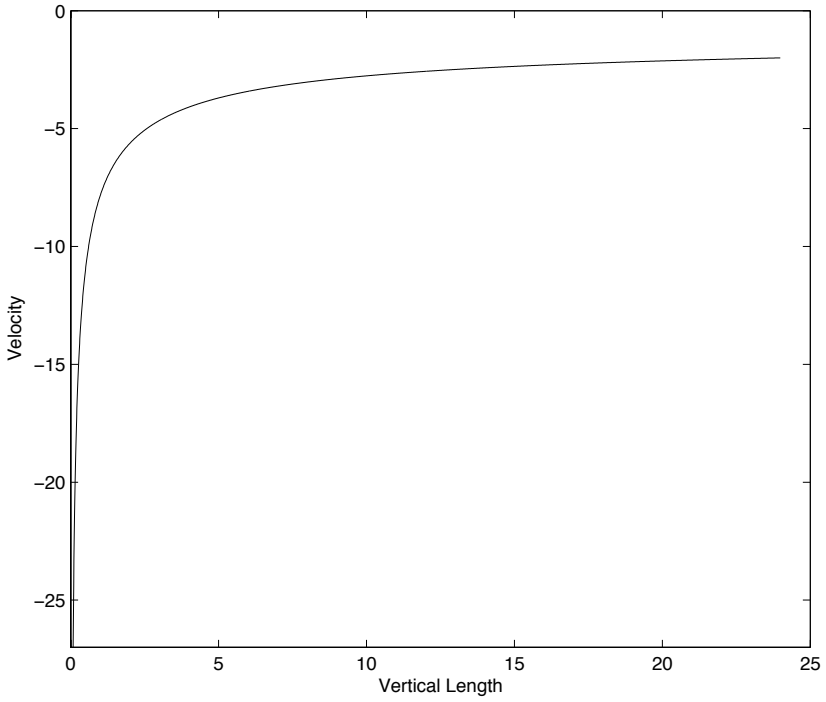

Figure 2.10: Plot of the induced fluid velocity V at time $t = 0$ for initial conditions $a = 4$, $b = 12$ with $a' = -\frac{1}{3}$, $b' = -1$. See section 2.2.3 concerning the region near the bottom of the vessel.

Plotting the above on $MatLab$, we obtain the graph shown in Figure 2.10. Similarly, we can plot the same graph for the same initial conditions at $t = 3$. Doing so gives

$$V(y,t) = -1 + \frac{9}{\sqrt{18y - y^2}} \left(\arccos\left(\frac{9-y}{9} \right) - \pi \right), \qquad 0 < y < 18, \qquad (2.2.37)$$

leading to a similar graph as is shown in Figure 2.11. In both cases of the figures, the fluid velocity inside the vessel is plainly seen to be directed downwards towards the lowermost position (the sink) and to significantly increase in magnitude there. Indeed,

there is a change of scale in velocity as well as in typical lengths as an Euler region is centered close to the sink. This is discussed in the next subsection.

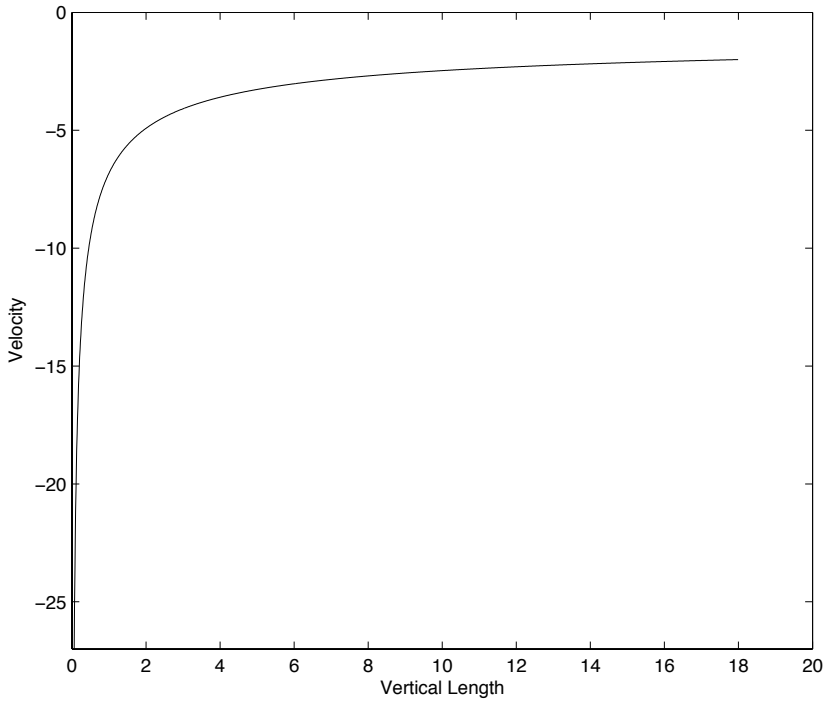

Figure 2.11: Plot of the induced fluid velocity V at time $t = 3$ for initial conditions $a = 4$, $b = 12$ with $a' = -\frac{1}{3}$, $b = -1$. See section 2.2.3 concerning the region near the bottom of the vessel.

It is also helpful to examine the streamlines of this flow. In other words, using the relationship $v = -\frac{\partial \Psi}{\partial x}$ implies $\Psi = -vx$ to within an additive function of y; therefore,

we use equation (2.2.35) and find

$$\Psi = \frac{(a'b - b'a)(y-b)x}{2ab} - b'x + \frac{b(a'b + b'a)x}{2a}\left(\frac{\arccos\left(\frac{b-y}{b}\right) - \pi}{\sqrt{2by - y^2}}\right). \tag{2.2.38}$$

Plotting on *Matlab* gives Figure 2.12.

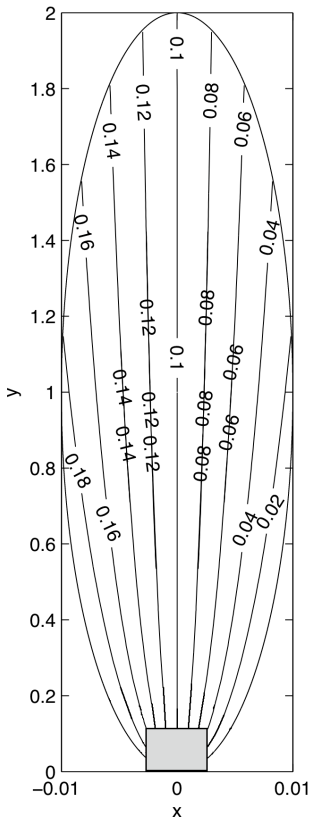

Figure 2.12: Contour of the streamfunction or streamlines $\Psi \approx \hat{\Psi}_0$ at time $t = 0$ inside the majority of the vertical thin ellipse with initial conditions $a = \frac{1}{100}$, $b = 1$. The streamlines here are all directed downwards towards the sink at the origin. Concerning the shaded area see Figure 2.18 for the solution closer to $y = 0$.

2.2.3 Euler/Laplace Region

We now consider the part of the vessel that is shown in Figure 2.6 on the left and is shaded in black. This is an Euler/Laplace region of size O(h) by O(h) in which the full Euler equations still hold at leading order when h is small, leading to the entire Laplace equation in our setting of zero vorticity. This localised region occurs in the middle of the thin horizontal ellipse on the left and at the bottom end of the thin vertical ellipse on the right in Figure 2.6, thereby surrounding the urethra position at the origin. It requires the use of a new expansion of the stream function and of matching with the bulk of the flow solution in the ellipse. The new expansion is

$$\Psi = \bar{\Psi}(\bar{x}, \bar{y}) + ..., \tag{2.2.39}$$

with both x and y now being of O(h), specifically $(x, y) = h(\bar{x}, \bar{y})$ so that $\bar{x}$, $\bar{y}$ are of O(1). Substitution into (2.0.1) shows of course that $\bar{\Psi}$ satisfies Laplace's equation in terms of $\bar{x}$, $\bar{y}$. As far as the boundary conditions are concerned, matching requires

$$\bar{\Psi}(\bar{x}, \bar{y}) \to \Psi_0(0\pm, \bar{y}) \quad \text{as} \quad \bar{x} \to \pm\infty, \tag{2.2.40}$$

in view of the scalings involved in (2.2.2) and (2.2.39) while $\bar{\Psi}$ must remain constant along the walls $\bar{y} = a \sim 1$ for all $\bar{x}$, $\bar{y} = 0$ for $\bar{x} < 0$ and $\bar{y} = 0$ for $\bar{x} > 0$, taking different values there because of the sink embedded at the origin. The walls here are parallel to leading order. The matching in (2.2.40) accommodates exactly the incoming uniform streams that are induced by the larger-scale behaviour as indicated in Figures 2.6-2.9. (An analogous matching condition applies in the thin vertical case which brings the $\hat{\Psi}_0$ effect into play.) The localised solution can be written down explicitly: see under the

headings “Horizontal Vessel” and “Vertical Vessel” below. Moreover, there is general application here in the sense that this local flow structure surrounding the urethra applies to inviscid flows with or without vorticity and to any vessel shape provided the vessel is thin.

Horizontal Vessel

For the horizontal setting we use the classical complex-variable result from [82] concerning the flow into a channel through a narrow slit in the wall. However, in our case the flow is reversed as depicted in Figure 2.13. The channel has an O(1) breadth of $\bar{b}$. The fluid moves from the vessel out of it through the slit (sink) at O, which is placed at the origin in the z-plane where $z = \bar{x} + i\bar{y}$; we drop the overbars here for convenience to leave $z = x + iy$ and likewise write Ψ instead of $\bar{\Psi}$. The far-upstream or far-downstream points A, B, C, D are mapped conformally onto the real axis of a ζ-plane as indicated in Figure 2.13. Here, B and C are taken to be coincident. The map opens out the

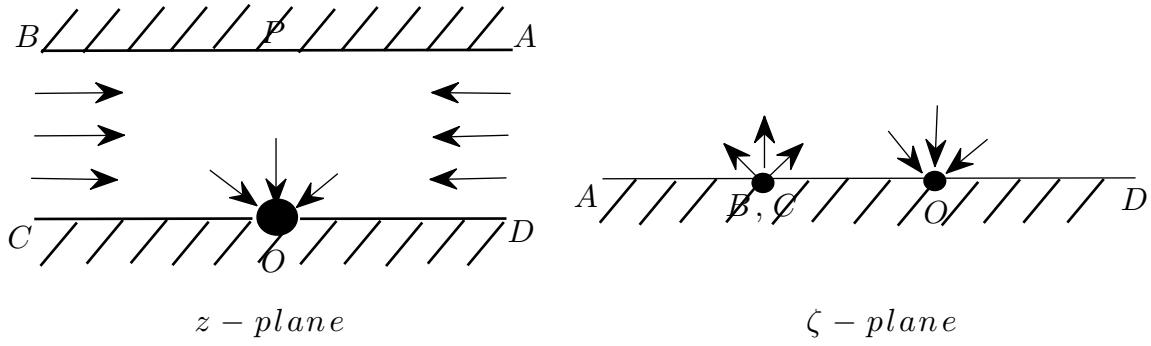

Figure 2.13: Plot of the local flow problem in both the z-plane and the ζ-plane.

walls into the real axis of the ζ-plane so that B and C become the origin $\zeta = 0$. We now have a sink at $\zeta = 1$ at the point marked O and a source at $\zeta = 0$ corresponding to B, C. Thus we obtain a complex potential which is

$$\omega = \phi + i\psi = m \log \sinh \frac{\pi z}{2\bar{b}}. \tag{2.2.41}$$

Separating the complex potential into its real and imaginary parts, we find the velocity potential ϕ and the stream function ψ,

$$\phi = \frac{1}{2} m \log \left(\cosh \left(\frac{\pi x}{2\bar{b}} \right)^2 \sin \left(\frac{\pi y}{2\bar{b}} \right)^2 + \cos \left(\frac{\pi y}{2\bar{b}} \right)^2 \sinh \left(\frac{\pi x}{2\bar{b}} \right)^2 \right), \tag{2.2.42}$$

and

$$\psi = m \arctan \left(\sin \left(\frac{\pi y}{2\bar{b}} \right) \cosh \left(\frac{\pi x}{2\bar{b}} \right), \sinh \left(\frac{\pi x}{2\bar{b}} \right) \cos \left(\frac{\pi y}{2\bar{b}} \right) \right). \tag{2.2.43}$$

Now, $\arctan(y, x)$ gives elements that lie in the closed interval $[-\pi, \pi]$. As in the previous sections, we work with the stream function ψ and we plot this result on $MatLab$, yielding Figure 2.15 (a).

These analytical results are very helpful as we can use them in order to compare, once again, with numerical results. Thin cases can be very tricky for numerical codes as accuracy can easily become elusive in these cases.

A direct computational approach based on finite differences similar to that adopted later in chapter 4 was also applied as a numerical scheme here using simple boundary conditions in order to describe the outer boundary of the z-plane in Figure 2.13. We apply the following normalised boundary conditions for the vessel

- $\psi = 0$, along OD,

- $\psi = y$, along DA,
- $\psi = \bar{b}$, along AB,
- $\psi = 2\bar{b} - y$, along BC,
- $\psi = 2\bar{b}$, along CO,

where the constant $\bar{b} = 0.1$, and then implement Laplace's equation inside the thin horizontal rectangular region. This produces Figure 2.14. Zooming-in to its middle square for a close-up view of the solution gives us Figure 2.15 (b) which is seen to be virtually identical to the analytical result shown in Figure 2.15 (a). We can also compare between its vertical and horizontal velocities which are also identical showing good numerical agreement as displayed in Figures 2.15 (c), (d).

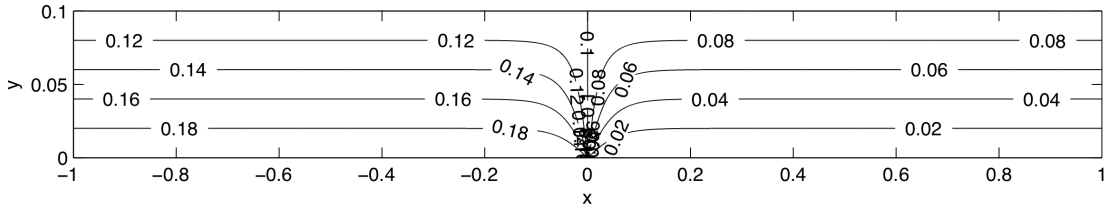

Figure 2.14: Computational streamlines of the flow for the thin horizontal Euler/Laplace local case shown in Figure 2.13. A close-up view of this computed solution is presented in the next figure.

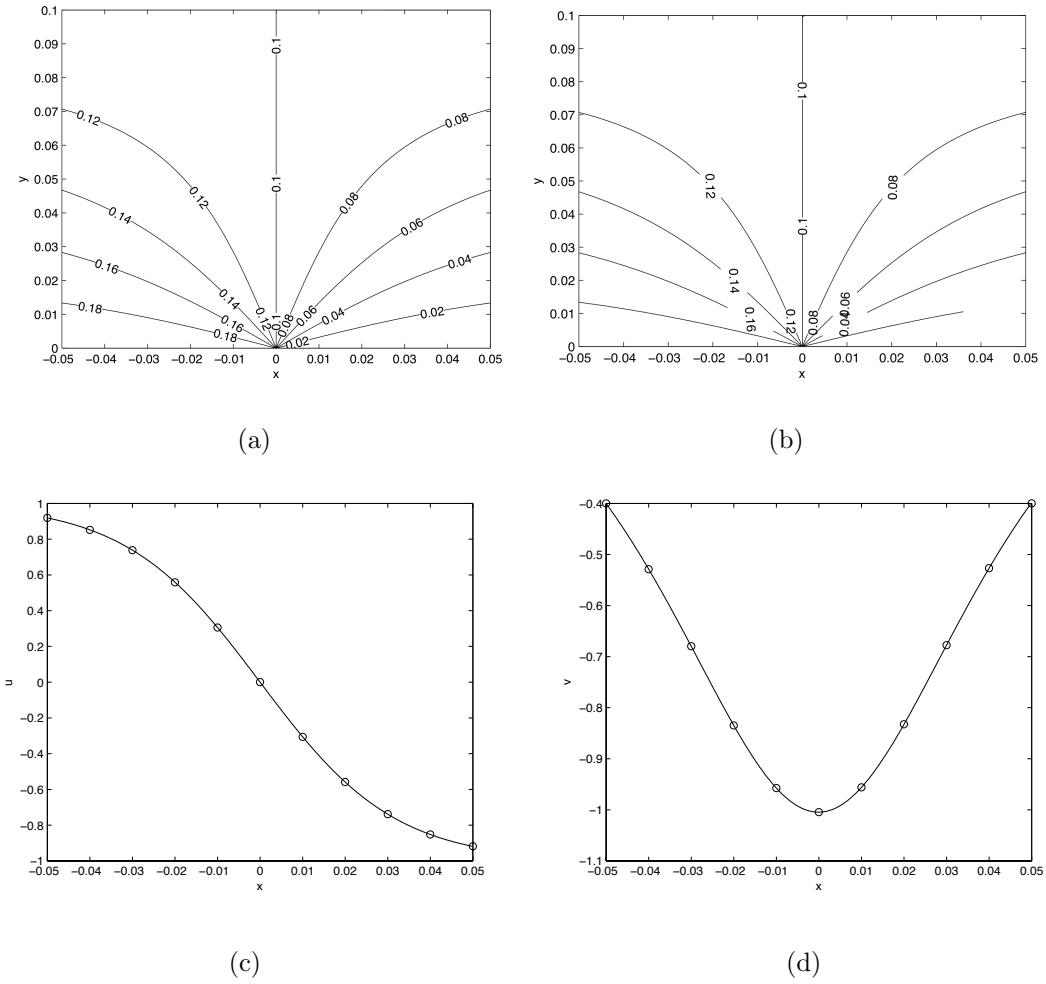

Figure 2.15: Analytical (a) and computational (b) streamlines of the two-dimensional flow for the horizontal Euler/Laplace local case shown in Figure 2.13. The streamlines are directed towards the origin. Also plotted are the horizontal (c) and vertical (d) velocity along the horizontal centreline for both the computational (small circles) and analytical (line) results.

Vertical Vessel

As with the horizontal case just studied, a local Euler analysis also applies to the vertical case. A slight alteration that will be discussed soon makes the present case essentially the same case but with the channel splitting from the point of symmetry, and rotated together to form the configuration drawn in Figure 2.16. As a result of that, the stream function is the same with only the axis rotated. Essentially, we find

$$\psi = m \arctan\left(\cos\left(\frac{\pi x}{2\bar{a}}\right)\sinh\left(\frac{\pi y}{2\bar{a}}\right), \cosh\left(\frac{\pi y}{2\bar{a}}\right)\sin\left(\frac{\pi x}{2\bar{a}}\right)\right). \tag{2.2.44}$$

Here $\bar{a}$ is an $O(1)$ constant. Plotting on $MatLab$ gives us the result shown in Figure

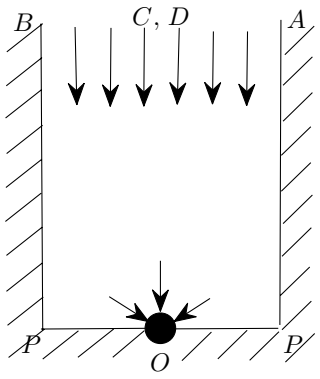

Figure 2.16: Set-up for the local Euler flow region in the thin vertical vessel; compare Figure 2.13.

2.18 (a). The stream lines are all directed towards the sink lying at the origin. A direct computational approach similar to the one of the horizontal vessel is also applied here. We apply the following normalised boundary conditions for the vessel

- $\psi = 0$, along OP,
- $\psi = 0$, along PA,
- $\psi = 2\bar{a} - x$, along AB,
- $\psi = 2\bar{a}$, along BP,
- $\psi = 2\bar{a}$, along PO.

Applying the code for the thin vertical case to satisfy Laplace's equation in the thin rectangle, we produce Figure 2.17. Zooming-in to its middle square for a close-up view of the solution gives us Figure 2.18 (b) which is seen to be virtually identical to the analytical result shown in Figure 2.18 (a). We can also compare in Figure 2.18 (c), (d) the vertical and horizontal velocities which are also identical showing good numerical agreement.

The slight alteration mentioned just before equation (2.2.44) concerns the fact that strictly the Euler region for the vertical vessel is bounded by parabola-shaped walls. The scaled velocity therefore decreases in magnitude towards zero as the distance from the sink increases matching asymptotically with equation (2.2.35) and Figures 2.10 and 2.11. However, the flow features can be expected to resemble those in Figures 2.17 and 2.18.

We can clearly see from Figure 2.18 that the computational results agree with the analytical ones, which is very encouraging, and they give us at the same time some guidance on the flow for certain vessel shapes. The insight is mainly as to what to expect from the flow in the vessels near the sink and near the vessel walls. Obviously,

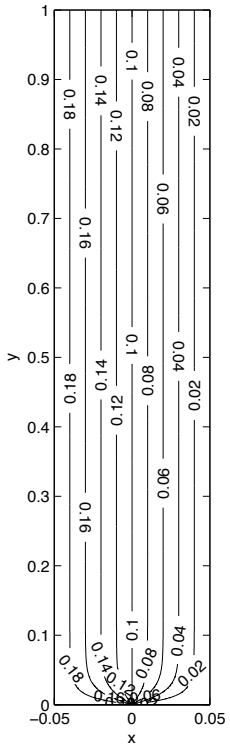

Figure 2.17: Computational streamlines of the flow for the thin vertical Euler/Laplace case of Figure 2.16. See also the zoom-in in the following figure.

there are more physical aspects to consider alongside this but the analytical findings also provide helpful and clear results. These results will be especially useful when it comes to comparing with computational results later in the thesis.

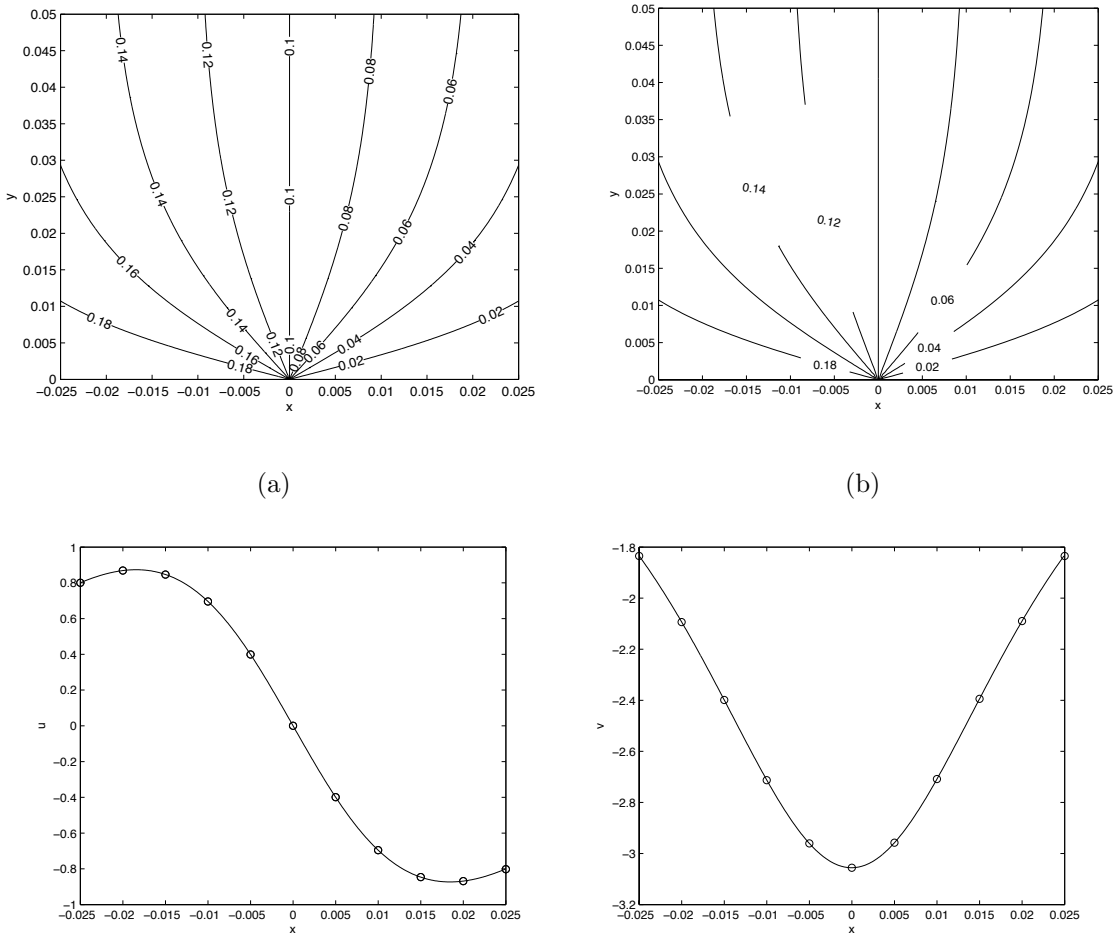

Figure 2.18: Analytical (a) and computational (b) streamlines of the two-dimensional flow for the vertical Euler/Laplace local case shown in Figure 2.16. The streamlines are directed towards the origin. Also plotted are the horizontal (c) and vertical (b) velocity along the horizontal centreline for both the computational (small circles) and analytical (line) results.

2.3 Summary & Results

This chapter has presented mostly analytical and certain numerical findings for certain basic shapes, namely the circle and also thin horizontal and vertical shapes. The Euler/Laplace region for the thin shapes was also studied. These findings will be used for comparison purposes with numerical results later in the thesis, specifically in chapter 4. The findings are extended to more realistic axisymmetric shapes in the following chapter.

The results of section 2.1, even though useful in being analytical, are far from completely realistic when it comes down to the collapse of the human bladder. The bladder shape does not remain circular throughout its collapse. It is though realistic to say that the bladder, when full and during the start of micturition, has a vessel shape which is approximately circular. The results are of course very important as they provide the basis for our numerical scheme. The simple boundary condition allowed us to solve analytically using a Poisson integral for the flow inside a circular vessel. The same problem is then solved in section 2.1.2 by use of complex functions. Apart from the fact that this result confirms the solution of section 2.1.1 (see and compare Figures 2.3 and 2.5), it also allows us to extend this method in a similar way to tackle axisymmetric cases. This analysis is performed in chapter 3.

It is also appropriate to mention that the value for the horizontal velocity on the boundary at $x = -1$ is $-\frac{1}{17} = a'(t)$, where $a(t)$ is the value of the horizontal axis at each

time step for our circular or elliptical vessel as shown in Figure 2.2. Therefore,

$$a(t) = a_0 - k\frac{a_0}{b_0}t \;\Rightarrow\; a'(t) = -k\frac{a_0}{b_0} = -k \quad \text{as} \quad a_0 = b_0 = 1. \tag{2.3.1}$$

Similarly for the case at $x = +1$, $a'(t) = \frac{1}{17}$. We also apply at the top a vertical velocity also depending on the vertical axis of our elliptical vessel

$$b(t) = b_0 - kt \;\Rightarrow\; b'(t) = -k. \tag{2.3.2}$$

Notice here that the vertical velocity in Figures 2.3 (c) and 2.5 (c) has a value of $v = 2k \approx 0.118$ at $x = \pm 1$ and $v = 3k \approx 0.176$ at $x = 0$, where $k = \frac{1}{17} \approx 0.0588$.

Section 2.2 is also of importance. The analytical results in the thin areas of the vessel are examined in sections 2.2.1 and 2.2.2. The non-thin areas (Euler/Laplace regions) are examined in section 2.2.3 (see shaded areas of Figures 2.9 and 2.12.)

With regard to the thin areas we can see the representative plots of vessels in Figures 2.7 and 2.8. The horizontal velocity is low near the extremes of the vessel and increases nearer the middle of the vessel and more specifically around the urethra. We add that Figure 2.7 is near the start of the collapse and Figure 2.8 at a later stage of the collapse but with the ratio of major to minor axis remaining the same (three). The horizontal velocity during these two stages of the collapse remains similar. This is mostly due to the fact that the ratio of major to minor axis is constant. Similar comments apply for the thin vertical case about Figures 2.10, 2.11 and 2.12. In this case, the vertical velocity plotted in Figures 2.10 and 2.11 is similar once again and we can see a high velocity value near $y = 0$ - vertical length in Figures 2.10 and 2.11 - (urethra).

The Euler/Laplace region which is shown in the shaded rectangles in Figures 2.9 and

2.12 (these are not to scale and are actually squares) is considered in section 2.2.3. With regard to the thin horizontal vessel the analytical representative streamlines are plotted in Figure 2.15 (a). In order to assess the numerical scheme that we will be using in later chapters, a basic problem has been set here in the form of a thin rectangle to which we have applied some basic boundary conditions that are similar to what we might expect for our vessel. The aim here though is once again to check the validity of the numerical scheme later as sometimes thin grids have convergence problems. The result that we obtain when applying the boundary conditions is shown in Figure 2.14. In this case we have used a major axis of one and a minor axis of one tenth. This is only representative as mentioned before, and any value significantly smaller than the length of the horizontal axis could have been applied. A zoom-in of Figure 2.14 is shown in Figure 2.15 (b), along with comparisons of their centre line velocities (both the vertical and horizontal, Figure 2.15 (c) and (d)). These are compared between the numerical and analytical results and are seen to be virtually identical. We can also compare the results of Figure 2.15 (c) with Figures 2.7 and 2.8. We can see that the outer results (thin-vessel results in Figures 2.7 and 2.8) and the thin Euler/Laplace region results of Figure 2.15 (c) show continuity/matching with each other. Similar comments apply for the vertical case.

It is also worth comparing the results of the two Euler/Laplace cases. Notice especially the higher values of the vertical velocity for the thin vertical case in Figure 2.18 (d) compared with Figure 2.15 (d). On the other hand, the horizontal velocities of both cases shown in Figures 2.15 (c) and 2.18 (c) have closely similar values. These high velocities could potentially be harmful in practice when the bladder takes such shapes.

This is of course on cases where the bladder works dysfunctionally as thin vertical shapes for the vessel are rare. Further discussions on the results and especially for thin elliptical cases take place in later chapters where more findings are presented.

Chapter 3

Analysis of Axisymmetric Shapes

3.1 Axisymmetric Shapes

This part of the investigation concerns axisymmetric shapes and most notably the sphere, for which an exact analytical solution is found. Yet, the features involved here carry over to a large extent to other more general three-dimensional shapes.

3.1.1 Ideas and Set-up

We now move on to an axisymmetric case that requires modelling using some of the conclusions from the flow studies for the two-dimensional case. In this case, we will model the bladder as an axisymmetric sphere. This is another well prescribed and basic shape.

Our task now is to solve the potential flow equations holding in the interior of the sphere subject to boundary conditions corresponding to a constant inward squeeze. Let us begin however with the axisymmetrical irrotational flow of incompressible inviscid fluid with no rigid boundaries. This is characterised by the stream function $\Psi_0(r,\theta)$ say all of whose singularities are at a distance greater than a from the origin and $\Psi_0 = O(r^2)$ at the origin. If the rigid sphere $r = a$ is then introduced into the appropriate flow, the stream function becomes

$$\Psi(r,\theta) = \Psi_0 - \Psi_0^* = \Psi_0(r,\theta) - \frac{r}{a}\Psi_0\left(\frac{a^2}{r},\theta\right). \tag{3.1.1}$$

This is Butler's theorem which makes use of "images" applied in the current axisymmetrical configuration [80], [82]. As a check, we need to show that the stream function given by (3.1.1) satisfies the following properties:

(i) the irrotationality condition,

(ii) has a constant value on the sphere surface $r = a$,

(iii) is nonsingular inside the sphere ($r \leq a$),

(iv) approaches the same flow as $\Psi_0(r,\theta)$ at infinity with zero net mass flow rate.

The above can be proved relatively quickly but, before we do so, we need to mention that it is common for axisymmetric flows to be described in either axisymmetric spherical coordinates (r,θ) or axisymmetric cylindrical polar coordinates (R,z). The two systems are related by $R = r\sin\theta$ and $z = r\cos\theta$ and have their reference points for our context as shown in Figure 3.1. The condition of irrotationality is now

$$\frac{\partial u_r}{\partial\theta} - \frac{\partial}{\partial r}(ru_\theta) = 0, \tag{3.1.2}$$

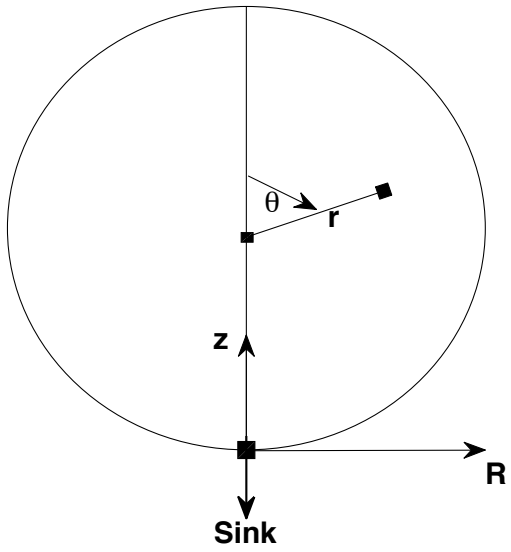

Figure 3.1: Spherical and cylindrical reference points for a simple axisymmetric spherical structure.

with r and θ as above. By introducing the Stokes stream function ψ as inferred from the continuity equation for the incompressible fluid and as defined by

$$u_r = \frac{1}{r^2 \sin\theta} \frac{\partial \Psi}{\partial \theta}, \quad u_\theta = -\frac{1}{r \sin\theta} \frac{\partial \Psi}{\partial r}, \tag{3.1.3}$$

we can then substitute (3.1.3) into (3.1.2) which gives the governing partial differential equation for the stream function, namely,

$$\frac{\partial}{\partial r}\left(\frac{1}{\sin\theta}\frac{\partial \Psi}{\partial r}\right) + \frac{1}{r^2}\frac{\partial}{\partial \theta}\left(\frac{1}{\sin\theta}\frac{\partial \Psi}{\partial \theta}\right) = 0. \tag{3.1.4}$$

Here (3.1.4) is not the Laplace equation, meaning that the stream function is not a harmonic function in the present axisymmetric potential flows.

Now, in order to prove the four points, we start with condition (i). We proceed there

by substituting the second term of equation (3.1.1) into (3.1.4). Making the change of variables $\xi = a^2/r$, we find

$$\xi^2 \frac{\partial^2}{\partial \xi^2} \Psi_0(\xi, \theta) + \sin\theta \frac{\partial}{\partial \theta} \left(\frac{1}{\sin\theta} \frac{\partial}{\partial \theta} \right) \Psi_0(\xi, \theta) = 0, \tag{3.1.5}$$

which has the same form as equation (3.1.4) acting on Ψ_0. Hence, the modified flow given by (3.1.1) is irrotational if the original flow is irrotational. Condition (ii) is satisfied by the proposed condition since at $r = a$, $\Psi(a, \theta) = 0$. At the same time condition (iii) is satisfied since r and a^2/r are inverse points with respect to a sphere of radius a, if $r > a$, then $a^2/r < a$ and vice versa. Therefore, (iii) requires that all singularities of $\Psi_0(r, \theta)$ are inside the sphere, and hence the singularities of $\Psi_0(a^2/r, \theta)$ are outside the sphere. Condition (iv) is proved in a similar way. In other words, we use the idea of image points. If $\Psi_0(r, \theta) = O(r^2)$ as $r \to 0$, then $\Psi_0(a^2/r, \theta) = O(1/r^2)$ as $r \to \infty$. From (3.1.3) we can see that the velocity induced by the second term of the right hand side of (3.1.1), which arises from the presence of the sphere, must vary as $O(1/r^3)$ as $r \to \infty$.

3.1.2 Formulation for the Sphere Problem

The exact solution for the spherical case in the present setting is constructed in a similar way to the two-dimensional case described in section 2.1.2. We consider three main features which are: the sink at the urethra, the squeeze velocity at the moving boundary and the fact that the urethra position remains fixed throughout. Let there be a flow due to a point source at the centre O of the axisymmetric sphere (a sink at the origin will be added in subsequently to cancel out that source), as in Figure 3.2.

From [67] we know that the stream function due to the point source is

$$\Psi = -\frac{Q}{4\pi}(1+\cos\theta), \tag{3.1.6}$$

where Q is equal to the volumetric flow rate emitted from the source and θ is the horizontal angle with respect to the point P. Defining the source at O as

$$\Psi_1 = -\frac{Q_1}{4\pi}(1+\cos\theta_1), \tag{3.1.7}$$

with Q_1 the volumetric flow at O and θ_1 as shown in Figure 3.2 with respect to point P, we also define a sink directly below it at C, namely,

$$\Psi_2 = -\frac{Q_2}{4\pi}(1+\cos\theta_2), \tag{3.1.8}$$

with Q_2 the volumetric flow at C and θ_2 as shown in Figure 3.2 with respect to P.

The next step involves placing P and C on the sphere leading to the property that

$$\theta_2 = \frac{1}{2}\theta_1, \tag{3.1.9}$$

where θ_1 is the angle measured from the vertical axis in the middle of the sphere and the line OP and similarly θ_2 with the line CP. This property is used a little later.

We then proceed by adding the images arising from Butler's theorem (3.1.1) yielding

$$\Psi_3 = \frac{Q_1 r}{4\pi a}(1+\cos\theta_1), \tag{3.1.10}$$

where Ψ_3 is the stream function term arising by applying the theorem to (3.1.7) and then similarly, by applying Butler's theorem to (3.1.8), we obtain

$$\Psi_4 = \frac{Q_2 r}{4\pi a}(1+\cos\theta_2), \tag{3.1.11}$$

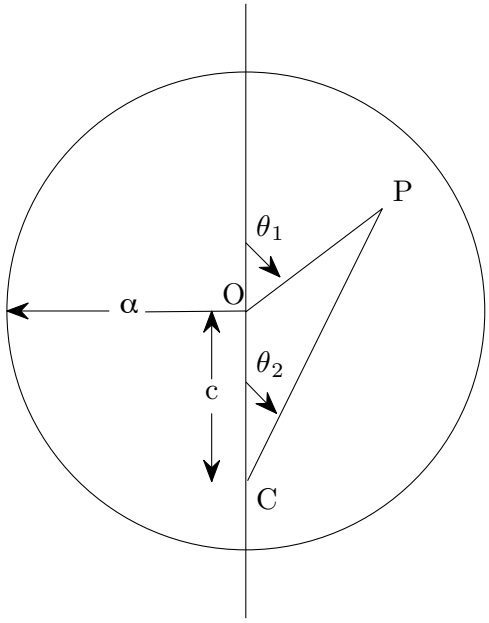

Figure 3.2: Set-up of the formulation for determining the flow inside the sphere. See also Figures 2.1 and 2.4.

with Q_2 and θ_2 as above, r the radius at any point relative to O, and a the radius of the sphere. In order to make the argument more understandable, we convert all expressions into terms of the angle θ_1. Using angle relationships as well as a few trigonometric identities, we find the following relationship

$$\cos\theta_2 = \frac{\left(\frac{c}{r} + \cos\theta_1\right)}{\left(\frac{c^2}{r^2} + \frac{2c}{r}\cos\theta_1 + 1\right)^{\frac{1}{2}}}. \tag{3.1.12}$$

The next step is to put together the source at O of (3.1.7), the sink at C of (3.1.8), their images in (3.1.10), (3.1.11) as well as a vertical downward flow stream D_s say in the vessel to keep the urethra position fixed (i.e. the bottom of the sphere fixed) while squeezing takes place. Then, we admit a sink at the origin (as previously mentioned) to

cancel out the source at the origin, thereby allowing for the normal squeeze velocity at the moving boundary of the sphere. Adding up all terms and canceling appropriately, we obtain the solution

$$\Psi = \frac{Q_1 r}{4\pi a}(1+\cos\theta) - \frac{Q_2}{4\pi}\left(1 + \frac{\frac{a}{r}+\cos\theta}{\left(\frac{a^2}{r^2}+\frac{2a}{r}\cos\theta+1\right)^{\frac{1}{2}}}\right) + \frac{Q_2 r}{4\pi a}\left(1 + \frac{\frac{r}{a}+\cos\theta}{\left(\frac{r^2}{a^2}+\frac{2r}{a}\cos\theta+1\right)^{\frac{1}{2}}}\right) + D_s, \qquad 0<\theta<\pi. \quad (3.1.13)$$

where $\theta = \theta_1$ and we have let $c \to a$.

Now, on the sphere $r = a$ and also $\theta_2 = \frac{1}{2}\theta_1$ as mentioned before. Hence, using also the trigonometric identity $\cos 2\theta = 2\cos^2\theta - 1$, we find that

$$\Psi_{r=a} = \frac{Q_1}{4\pi}(1+\cos\theta) + (D_s)_{r=a}. \quad (3.1.14)$$

Since the radial velocity on the sphere is $u_r = \frac{1}{r^2\sin\theta}\frac{\partial\Psi}{\partial\theta}$, on the sphere at $r = a$, we have

$$u_r = \frac{1}{a^2\sin\theta}\frac{Q_1}{4\pi}(-\sin\theta) = -\frac{Q_1}{4\pi a^2}, \quad (3.1.15)$$

which is a constant, as required for the inward squeeze, and gives the squeeze velocity as

$$V = \frac{Q_1}{4\pi a^2}. \quad (3.1.16)$$

This result makes good sense physically in terms of the surface area $4\pi a^2$ of the sphere.

Now, to determine the constant Q_2, we consider Ψ on the vertical axis (the z-axis). Above O, see Figure 3.2, the fact that $\theta_1 = \theta_2 = 0$ implies that $\Psi = \frac{Q_2}{4\pi}\left(-2 + \frac{2r}{a}\left(\frac{Q_1}{Q_2}+1\right)\right)$.

Below O, $\theta_1 = \pi$, $\theta_2 = 0$ implies that $\Psi = \frac{Q_2}{2\pi}$. Since there is no singularity at O, the above means that $Q_2 = -Q_1$.

We note that at the top of the sphere, see once again Figure 3.2, $\Psi = \frac{Q_1}{2\pi}$ if we exclude the D_s contibution for now. At the same time, we know that above and below O the value $\Psi = \frac{-Q_2}{2\pi}$ holds and the very bottom has $\Psi = 0$. The above confirms that $Q_2 = -Q_1$ to make the solution smooth at the top whereas at the bottom (modelling the urethra) we see a discontinuity consistent with a sink. In other words, $\Psi = 0$ on the sphere there but $\Psi = -\frac{Q_2}{2\pi}$ on the vertical axis.

Finishing this off, we are left with the downward stream flow D_s to determine. Hence, we use

$$\Psi_{stream} = \frac{1}{2} U r^2 \sin^2\theta, \tag{3.1.17}$$

where U is the velocity component along the axis of symmetry and r and θ are as defined previously. Canceling out the inward-squeeze velocity effect V in equation (3.1.16) at the bottom, we find that $U = -V$. This leaves us with the overall analytical result for the flow in a sphere as

$$\begin{aligned}\Psi = arV\left(1+\cos\theta\right) + a^2V\left(1+\frac{\frac{1}{r}+\cos\theta}{\left(\frac{1}{r^2}+\frac{2}{r}\cos\theta+1\right)^{\frac{1}{2}}}\right)\\ - arV\left(1+\frac{r+\cos\theta}{\left(r^2+2r\cos\theta+1\right)^{\frac{1}{2}}}\right) - \frac{r^2V}{2}\sin^2\theta, \qquad 0<\theta<\pi.\end{aligned} \tag{3.1.18}$$

Plotting the result (3.1.18) on *MatLab*, we obtain the solution curves of Figure 3.3. The results seem to make reasonable sense.

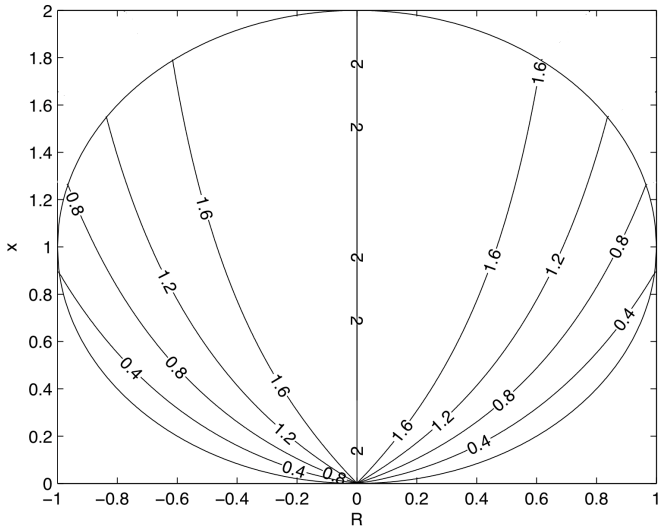

(a)

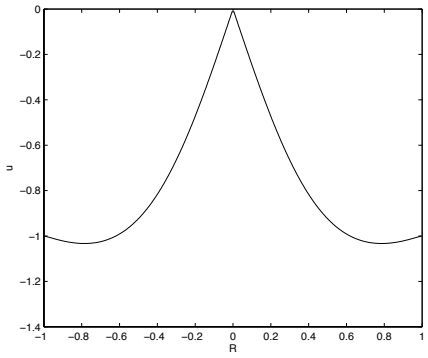

(b)

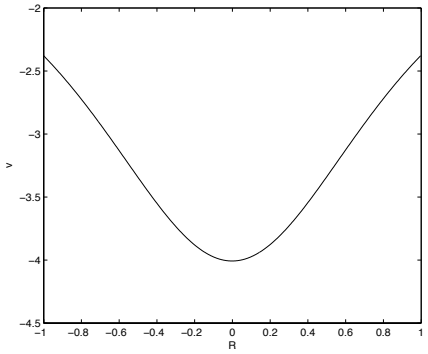

(c)

Figure 3.3: Contour plot of the streamlines inside the spherical vessel. The flow directions are all associated with downward motion (downward arrows). Also plotted are the horizontal (b) and vertical (c) velocity along the horizontal centreline. The sphere here is shifted up so that the urethra is at the origin.

It is also good to comment here on the negative value of the radius R in Figure 3.3 and any other figures where axisymmetric results are plotted (chapter 6). The positive side of the radius takes the value of $\phi = 0$ and the negative value of R takes the value $\phi = \pi$, where ϕ is the angle as starting from the positive side of the radius R perpendicular to the page and coming round the negative R side and back $2\pi\,(= 0)$.

We now convert (3.1.13) into axisymmetric cylindrical polar coordinates. This gives

$$\Psi = aV\left(\sqrt{R^2+z^2}+z\right) + a^2V\left(1+\frac{z+1}{(R^2+z^2+2z+1)^{\frac{1}{2}}}\right) - aV\left(\sqrt{R^2+z^2}+\frac{z+R^2+z^2}{(R^2+z^2+2z+1)^{\frac{1}{2}}}\right) - \frac{V}{2}R^2, \quad (3.1.19)$$

where $R = r\sin\theta$ and $z = r\cos\theta$. Again a quick check shows that this also satisfies the irrotationality condition where in axisymmetrical cylindrical coordinates

$$u_R = \frac{1}{R}\frac{\partial\Psi}{\partial z}\,, \qquad u_z = -\frac{1}{R}\frac{\partial\Psi}{\partial R}. \quad (3.1.20)$$

We will be using these results later in the thesis in order to compare with results from our numerical scheme for axisymmetric flows. It is felt to be potentially useful to have an exact foundation as these analytical results, even though axisymmetric, form a beginning for the three-dimensional modelling.

3.2 Thin or Slender Axisymmetric Shapes

The idea and subsequent working of section 2.2 for thin two-dimensional vessels can be extended to axisymmetric shapes.

For a thin horizontal axisymmetric vessel, for example, the controlling equation of (3.1.4) becomes in the majority of the vessel

$$\frac{\partial}{\partial\theta}\left(\frac{1}{\sin\theta}\frac{\partial\Psi}{\partial\theta}\right)=0, \tag{3.2.1}$$

$$\text{i.e.} \qquad \frac{\partial^2\Psi}{\partial z^2}=0, \tag{3.2.2}$$

to leading order since θ is close to $\pi/2$. Hence, $\Psi = A(R,t)z + B(R,t)$ and so on. A significant non zero (in fact increasing) inward motion is again left over on the approach to the origin here. This leads to a non-uniformity locally which brings into play a square or cube of full Laplace/Euler motion. This surrounds the actual sink or urethra position in similar fashion to that in Figure 2.15.

Likewise, for a slender vertical axisymmetric vessel the dominant effect of (3.1.4) is to produce

$$\frac{\partial^2\Psi}{\partial R^2}-\frac{1}{R}\frac{\partial\Psi}{\partial R}=0. \tag{3.2.3}$$

This and its implications are directly analogous to the working for the thin vertical case in section 2.2, together with the non-uniformity near the urethra where the flow velocities are considerably enhanced.

3.3 Summary & Results

The analytical results described in this chapter are once again potentially significant; even though axisymmetric. Apart from that, these results will provide a helpful check

when it comes to developing our numerical scheme for axisymmetric configurations in chapter 6.

The results of section 3.1 are analytical but they are once again not very realistic when it comes down to the collapse of the human bladder. The analytical model here is similar to the analytical case described in section 2.1 for the two-dimensional case. Similarly, here the shape of the bladder preserves its spherical form as it collapses. As with the two-dimensional results though, they are also significant as they provide the basis for the numerical scheme described later in the thesis. The result of section 2.1.2 for the two-dimensional case was performed and checked with the result of section 2.1.1 (see once again Figures 2.3 and 2.5). The same analysis that was performed in two dimensions in section 2.1.2 is applied here in section 3.1. The result is checked numerically later in the thesis in chapter 6 as it satisfies $E^2\Psi = 0$ where $E^2 = \frac{\partial^2}{\partial R^2} - \frac{1}{R}\frac{\partial}{\partial R} + \frac{\partial^2}{\partial z^2} = 0$. This is also defined in chapter 6. Similarly to the two-dimensional thin cases described in section 2.2, we also touched on the thin slender axisymmetric shapes briefly in section 3.2. They are not pursued further though as we expect results similar to the two-dimensional case.

Chapter 4

Numerical Solutions for Simple Two-Dimensional Shapes

The preceding chapters focused on analytical modeling of the vessels and their contained flows. We now move onto solving some of the fundamental problems numerically. The analytical solution for the flow inside a circular vessel from (2.1.22) will be used to verify our computational results. We first tackle the flow in a circular vessel using an iterative finite difference method. We then tackle elliptical shapes for the vessel. Finally, a simple model of a circular vessel collapsing in time to a flat ellipse is examined. We also evolve a boundary element method to tackle the flow in a circular vessel.

4.1 Methodology

As mentioned in the introduction and more specifically in section 1.6, the main numerical schemes that are used in this thesis are the boundary element method and the finite difference method. The boundary element method is a boundary-detailing method and the finite difference method a boundary-accommodating method. Both methods are praiseworthy. Other boundary-detailing methods include contour dynamics [79], [80], conformal mapping methods [97] and boundary element approaches [41], [54]. They are usually very accurate and elegant. The boundary-accommodating methods include Cartesian based methods with boundary interpolation. These are rather similar to those of the successful and widely used VOF (Volume of Fluid) techniques [106] applied in impacting droplet motions. They are also similar to the work of Tadjfar and Smith [108] and Bowles et al [17] who used simple in-out boundary conditions to accommodate quite complicated boundary shapes.

The boundary-accommodating approach is very flexible, is readily extendable to three spatial dimensions, requires relatively sparse information about the boundary and it can even cope with complicated topology and changes in topology fairly easy. Coping with large changes and varied complicated shapes is required in the context of bladder squeezing and closure; just as it is required in droplet-motion calculations. The option of boundary-accommodation methodology was chosen for the studies in this thesis and this appeared to work well, although we should immediately add that other methodologies could also work or have worked well of course.

The boundary element method was also used to tackle the problem and it is further

described in this chapter. As mentioned above the method is very elegant and extremely accurate with complex geometries. It is a very well established method and the results we obtained from a first scheme are very promising. This method can also be used to further develop a model for the collapsing vessel.

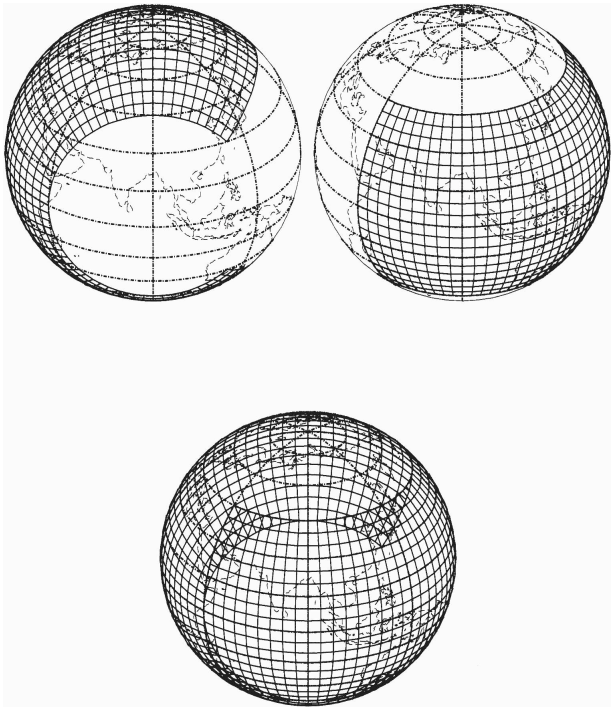

Figure 4.1: Diagram of the Yin-Yang grid [76].

Grids are again now a 'hot topic' in the field of numerical weather predication - the UK Met office have a so-called 'Lat-Lon' grid [22] which uses just latitudes and longitudes on the sphere - this has unpleasant CFL (Courant-Friedrichs-Lewy) problems at the pole. The CFL stability condition states that an explicit time stepping scheme for a convention-type equation cannot be stable if the geometric shape of the stencil is

such that information cannot propagate sideways as fast as it does in the governing equation. Therefore, this implies an upper limit of k/h, where tiny values of the spatial step size h near the poles severely restrict the time steps k that can be used [38]. Thus, in order to overcome this problem, several constructions have been proposed with the most popular being the Yin-Yang grid. This represents an overset gridding method [68] meaning that two different grids are composed to construct a mesh covering the whole sphere. The Yin-Yang grid is constructed of two rotated partial 'Lat-Lon' grids as in Figure 4.1. The two top spheres of Figure 4.1 are a rotation of each other. The problem with this method is the overlapping that can be viewed again in Figure 4.1 when the two grids are put together in the bottom sphere. There are several methods that tackle this problem either minimizing or eliminating the overlap. Aerodynamics is also an area where grids have always been crucial as in [96]. It is also seen in [96] that a special arrangement can also be made in order to accommodate the boundary.

The boundary-accommodating methods of Tadjfar and Smith [108] and Bowles et al [17] turn out to be of direct relevance for the shape-effect studies that will be described later in the thesis. Those two studies showed close agreement both with analysis and with alternative computational techniques. The present problem is also tackled by the boundary element method for which details are given later in the chapter. This method is very elegant and accurate. However, the accuracy of the Cartesian based grid method as well as its simplicity both in using and understanding made us decide to further extend it. (The boundary element method could in principle also be used to apply the work of this thesis.)

4.2 Circular and Horizontal/Vertical Elliptical Shapes using an Iterative Finite Difference Method

4.2.1 Background

The limiting cases of the previous chapters are used as guidance for this chapter. In fact, they are compared with the results that come out from the next part of the research. We use a finite difference method here to solve the Laplace equation numerically. Solving the equation in a domain with this method requires, as with the boundary element method, a boundary condition of course. It can be either a Dirichlet condition, when the function itself is specified on the boundary, or a Neumann condition, when the normal derivative of the function is specified on the boundary. In this next part, we have a Dirichlet condition on the boundary.

4.2.2 Finite Difference Method with Dirichlet Conditions

We convert Laplace's equation into a linear system of algebraic equations and write them in matrix notation. We solve this problem in a standard iterative way instead of inverting the whole matrix.

Now, consider the stencil from Figure 4.2 and for simplicity assume that the grid size is h. Since we want to satisfy Laplace's equation,

$$\frac{\partial^2 \psi_{(i,j)}}{\partial x^2} + \frac{\partial^2 \psi_{(i,j)}}{\partial y^2} = 0, \tag{4.2.1}$$

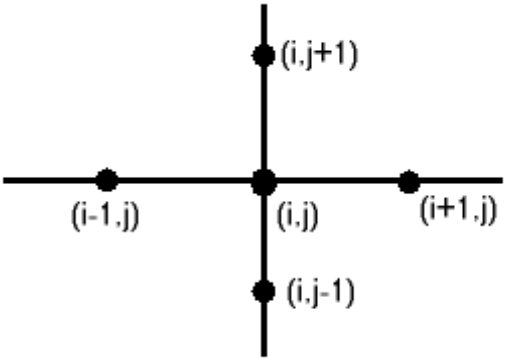

Figure 4.2: Example of 5-point stencil on our grid.

and hence using central finite difference approximation of the second derivatives of ψ with respect to x and y, we have

$$\frac{\psi_{(i+1,j)} - 2\psi_{(i,j)} + \psi_{(i-1,j)}}{h^2} + \frac{\psi_{(i,j+1)} - 2\psi_{(i,j)} + \psi_{(i,j-1)}}{h^2} = 0. \tag{4.2.2}$$

Now, upon rearranging, we obtain the following iterative formula [26], [61],

$$\psi(i,j) = \frac{1}{4}\left(\psi_{(i+1,j)} + \psi_{(i-1,j)} + \psi_{(i,j+1)} + \psi_{(i,j-1)}\right), \tag{4.2.3}$$

which is the resulting equation for calculating the streamfunction at any point inside our ellipse (or other shape of vessel).

The method is standard and relatively straightforward. Furthermore, we define the required vessel shape on a Cartesian grid and approximate it simply on that grid. We define the boundary conditions and then the code calculates the flow inside the vessel or approximated vessel satisfying Laplace's equation. Further refinements on the method are shown and discussed later on.

4.2.3 Convergence

The method used in order to accelerate the convergence of the iterative procedure is also conventional, known as successive over-relaxation [35], [40], [61]. We show how we apply this for the present scheme by modifying the iterative equation as follows,

$$\tilde{\psi}(i,j) = \frac{1}{4}\left(\psi(i+1,j) + \psi(i-1,j) + \psi(i,j+1) + \psi(i,j-1)\right), \tag{4.2.4}$$

which calculates an intermediate value $\tilde{\psi}(i,j)$ for $\psi(i,j)$. Then, the following equation determines the new converged values of the streamfunction $\psi(i,j)$,

$$\psi(i,j)^{(N)} = (1-\omega)\psi(i,j)^{(O)} + \omega\tilde{\psi}(i,j). \tag{4.2.5}$$

This is a weighted combination of the intermediate value $\tilde{\psi}(i,j)$ and the old one $\psi(i,j)^{(O)}$, where for any rectangular grid $m \,\mathrm{x}\, n$ the optimum relaxation value factor ω is given by [40], [61],

$$\omega = \frac{4}{2 + \sqrt{4 - \left(\cos(\frac{\pi}{n-1}) + \cos(\frac{\pi}{m-1})\right)^2}}. \tag{4.2.6}$$

This greatly increases the rate of convergence by using over-relaxation. Since in our case we have a rectangular region with Dirichlet boundary conditions, ω is estimated from (4.2.6), where $n-1$ is the number of spatial increments in the x direction and $m-1$ the number of spatial increments in the y direction. The formula assumes for convenience a grid aspect ratio of 1.

4.2.4 Boundary Interpolation

This aspect is non-standard. Accuracy on the boundary is very important as this is the place where most of the computational error of the above iteration occurs after comparing the analytical results of the circle with the results for our scheme without this refinement (see Figure 4.4). In order to minimise the error, we embed into our numerical scheme a boundary interpolation. The interpolation is done by relatively accurate means at the boundary.

In Figure 4.3 which shows an elliptical vessel in a grid, we can clearly see that most of those nodes that are just inside the boundary have part of their stencil outside the boundary but still on the grid. Now, since we are only interested in solution values inside and on the boundary and not outside, this feature needs to be tackled. Boundary interpolation is adopted.

The general formula for the nodes described and shown in Figure 4.3 satisfies the following equation

$$\left(\frac{2}{h_{i+1}h_{i-1}}+\frac{2}{h_{j+1}h_{j-1}}\right)\Psi(i,j) = \frac{2\Psi_{j+1}}{h_{j+1}(h_{j+1}+h_{j-1})}+\frac{2\Psi_{i+1}}{h_{i+1}(h_{i+1}+h_{i-1})} + \frac{2\Psi_{j-1}}{h_{j-1}(h_{j-1}+h_{j+1})}+\frac{2\Psi_{i-1}}{h_{i-1}(h_{i-1}+h_{i+1})}, \quad (4.2.7)$$

with h_{i+1}, h_{i-1}, h_{j+1}, h_{j-1} denoting the distances between the nodes. Each of these distances can have a value of either h or smaller depending on the boundary and as depicted in Figure 4.3.

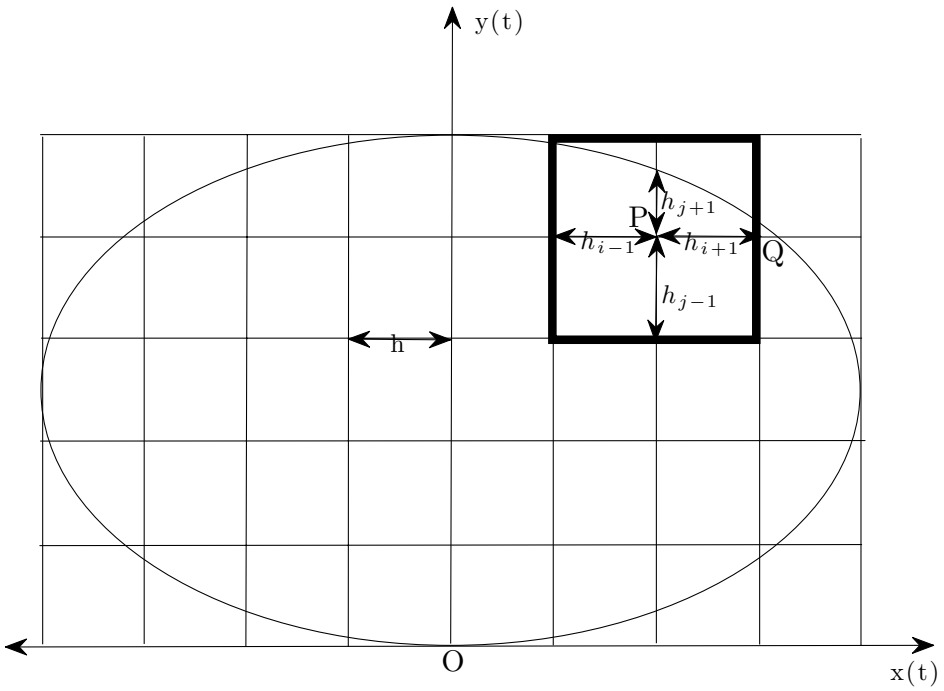

Figure 4.3: Example of a possible elliptical boundary in our grid. The nodes are generally separated by a distance h. Yet, near the boundary this is not always the case. As you can see in the figure, $h_{i+1} = h_{i-1} = h_{j-1} = h$. This is not the case with h_{j+1} which is smaller. We therefore employ the formula (4.2.7) for this point P. In the case of the point Q on its right, we will have two points which will be smaller than h. The formula (4.2.7) tackles this case too.

It is possible to have one, two or even three points of our stencil outside the grid. Therefore, depending on the position of the stencil inside the shape, different points of the stencil will be outside of the vessel and hence the above formula will vary accordingly.

For the case where we have one point of the stencil outside the shape, and more specifically the point $(i, j+1)$, then the iterative equation is as follows:

$$\Psi_0 = \frac{1}{(D_{j+1}+h)^2}\left(\frac{D_{j+1}(D_{j+1}+h)}{2}(\Psi_{i-1}+\Psi_{i+1}) + h^2\Psi_B + hD_{j+1}\Psi_{j-1}\right), \quad (4.2.8)$$

where h is the distance between stencil points, D_{j+1} the new distance between Ψ_0 and the boundary in the $(j+1)$ direction, and Ψ_B the value of Ψ on the boundary. Similarly, for the other three directions, we derive the following three equations. For the bottom one we have

$$\Psi_0 = \frac{1}{(D_{j-1}+h)^2}\left(\frac{D_{j-1}(D_{j-1}+h)}{2}(\Psi_{i-1}+\Psi_{i+1}) + h^2\Psi_B + hD_{j-1}\Psi_{j+1}\right), \quad (4.2.9)$$

for the left one we have

$$\Psi_0 = \frac{1}{(D_{i-1}+h)^2}\left(\frac{D_{i-1}(D_{i-1}+h)}{2}(\Psi_{j-1}+\Psi_{j+1}) + h^2\Psi_B + hD_{i-1}\Psi_{i+1}\right), \quad (4.2.10)$$

and for the right one

$$\Psi_0 = \frac{1}{(D_{i+1}+h)^2}\left(\frac{D_{i+1}(D_{i+1}+h)}{2}(\Psi_{j-1}+\Psi_{j+1}) + h^2\Psi_B + hD_{i+1}\Psi_{i-1}\right). \quad (4.2.11)$$

Similarly, for the case where we have two points of the stencil outside our shape, and more specifically $(i, j+1)$ and $(i+1, j)$, then the iterative equation is as follows:

$$\Psi_0 = \frac{1}{(D_{j+1}+D_{i+1})(D_{j+1}+h)(D_{i+1}+h)}$$
$$\left(D_{j+1}(D_{j+1}+h)(h\Psi_B + D_{i+1}\Psi_{i-1}) + D_{i+1}(D_{i+1}+h)(h\Psi_B + D_{j+1}\Psi_{j-1})\right), \quad (4.2.12)$$

where the notation is as in the case of one stencil point outside the shape. Similarly, there are three more cases with two points of the stencil outside the shape. For the

case where the points $(i+1, j)$ and $(i, j-1)$ are outside the stencil, we have

$$\Psi_0 = \frac{1}{(D_{j-1} + D_{i+1})(D_{j-1} + h)(D_{i+1} + h)}$$
$$\Big(D_{j-1}(D_{j-1} + h)(h\Psi_B + D_{j+1}\Psi_{j-1}) + D_{i+1}(D_{i+1} + h)(h\Psi_B + D_{j-1}\Psi_{j+1}) \Big), \quad (4.2.13)$$

for $(i, j-1)$ and $(i-1, j)$ we have

$$\Psi_0 = \frac{1}{(D_{j-1} + D_{i-1})(D_{j-1} + h)(D_{i-1} + h)}$$
$$\Big(D_{j-1}(D_{j-1} + h)(h\Psi_B + D_{i-1}\Psi_{i+1}) + D_{i-1}(D_{i-1} + h)(h\Psi_B + D_{j-1}\Psi_{j+1}) \Big), \quad (4.2.14)$$

and finally for $(i-1, j)$ and $(i, j+1)$

$$\Psi_0 = \frac{1}{(D_{j+1} + D_{i-1})(D_{j+1} + h)(D_{i-1} + h)}$$
$$\Big(D_{j+1}(D_{j+1} + h)(h\Psi_B + D_{i-1}\Psi_{i+1}) + D_{i-1}(D_{i-1} + h)(h\Psi_B + D_{j+1}\Psi_{j-1}) \Big). \quad (4.2.15)$$

Finally for the case where three points of the stencil are outside the shape, the following cases apply. In the event that $(i, j+1)$, $(i+1, j)$ and $(i, j-1)$ are outside the vessel shape, the iterative equation is as follows:

$$\Psi_0 = \frac{hD_{j+1}D_{i+1}D_{j-1}}{(D_{j+1}D_{j-1} + hD_{i+1})}$$
$$\left(\frac{\Psi_B}{D_{j+1}(D_{j+1} + D_{j-1})} + \frac{\Psi_B}{D_{i+1}(D_{i+1} + h)} + \frac{\Psi_B}{D_{j-1}(D_{j+1} + D_{j-1})} + \frac{\Psi_{i-1}}{h(h + D_{i-1})} \right), \quad (4.2.16)$$

for the case where $(i+1, j)$, $(i, j-1)$ and $(i-1, j)$ are outside the vessel shape we

have

$$\Psi_0 = \frac{hD_{i-1}D_{i+1}D_{j-1}}{(hD_{j-1} + D_{i+1}D_{i-1})} \left(\frac{\Psi_{j+1}}{h(h + D_{j-1})} + \frac{\Psi_B}{D_{i+1}(D_{i+1} + D_{i-1})} + \frac{\Psi_B}{D_{j-1}(h + D_{j-1})} + \frac{\Psi_B}{D_{i-1}(D_{i-1} + D_{i+1})} \right), \tag{4.2.17}$$

for the case where $(i, j+1)$, $(i, j-1)$ and $(i-1, j)$ are outside the vessel shape we have

$$\Psi_0 = \frac{hD_{j+1}D_{i-1}D_{j-1}}{(D_{j+1}D_{j-1} + hD_{i-1})} \left(\frac{\Psi_B}{D_{j+1}(D_{j+1} + D_{j-1})} + \frac{\Psi_{i+1}}{h(D_{i-1} + h)} + \frac{\Psi_B}{D_{j-1}(D_{j+1} + D_{j-1})} + \frac{\Psi_B}{D_{i-1}(h + D_{i-1})} \right), \tag{4.2.18}$$

and for the case where $(i+1, j)$, $(i, j+1)$ and $(i-1, j)$ are outside the vessel shape we have

$$\Psi_0 = \frac{hD_{i-1}D_{i+1}D_{j+1}}{(hD_{j+1} + D_{i+1}D_{i-1})} \left(\frac{\Psi_B}{D_{j+1}(h + D_{j+1})} + \frac{\Psi_B}{D_{i+1}(D_{i+1} + D_{i-1})} + \frac{\Psi_{j-1}}{h(h + D_{j+1})} + \frac{\Psi_B}{D_{i-1}(D_{i-1} + D_{i+1})} \right). \tag{4.2.19}$$

Equation (4.2.7) and the twelve conditions that are derived from it and have been employed (equations (4.2.8)-(4.2.19)) make the code more memory intensive than without them but a lot more accurate around the boundary. In the event that this interpolation is not employed in the boundary, the numerical scheme is less accurate if the same number of grid points is used. It can be seen in Figure 4.4 that, in the event of a

128x128 grid, the accuracy of the results is not as accurate as those in Figure 4.5. It can be seen that nearer to the boundary the error is slightly higher than in the middle. Nevertheless, it is quite clear that the interpolation on the boundary reduces the error and increases the accuracy.

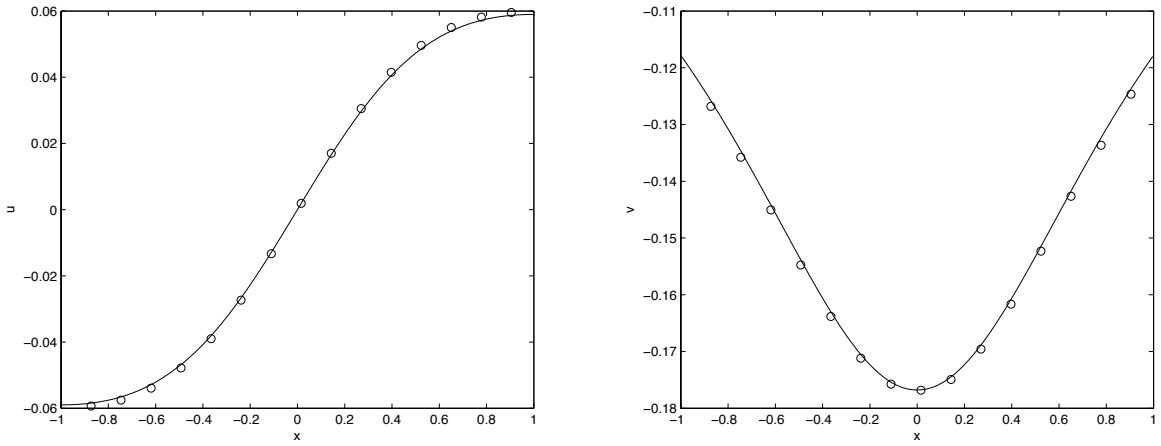

(a) (b)

Figure 4.4: Plots of the horizontal (a) and vertical (b) velocity along the horizontal centreline for both computational - without the boundary interpolation - (small circles) and analytical (line) results. The boundary condition used is $\Psi_B = \theta - \sin(\theta)$.

4.2.5 Numerical Results

We apply the numerical scheme described in section 4.2 in order to develop a numerical scheme on *MatLab*. The scheme can be used to examine numerical solutions for many different shapes and different rates of collapse for the vessel that will be tackled in the next chapters.

For the circle in particular, we first use the usual condition on the boundary for a circular vessel with a point discontinuity at the bottom. In other words

$$\Psi_B = \theta - \sin(\theta), \tag{4.2.20}$$

is to be used to test the validity of the Cartesian-based code. Using condition (4.2.20) on the boundary, then the analytical solution at any point inside the vessel is

$$\Psi = \theta - r\sin(\theta) - 2\arctan\left(\frac{(1+r)\tan\left(\frac{\theta}{2}\right)}{(1-r)}\right) + \pi, \qquad 0 < \theta < \pi, \tag{4.2.21}$$

and

$$\Psi = \theta - r\sin(\theta) - 2\arctan\left(\frac{(1+r)\tan\left(\frac{\theta}{2}\right)}{(1-r)}\right) - \pi, \qquad \pi < \theta < 2\pi, \tag{4.2.22}$$

with r and θ as above.

Plotting the results of both the numerical and analytical approaches, we obtain the plots in Figure 4.5. Comparing the two plots, we can clearly see that the computational results appear to be very accurate. The grid used here has 128x128 points in unitary xxy dimension of the grid (1x1). In fact, the error in the computational results is significantly less than half a percent. We define our error as the percentage difference between our analytical results (equations (4.2.21) and (4.2.22)) and the computational results. In order to see the efficiency of the scheme we compare the results for several coarse grids. These are shown in Figure 4.6. As we can see, the general flow structure of configuration remains intact but most of the error takes place down at the urethra. This makes sense as the discontinuity at the urethra makes it more vulnerable to errors. As such, the error at the urethral point is much higher than elsewhere, especially with

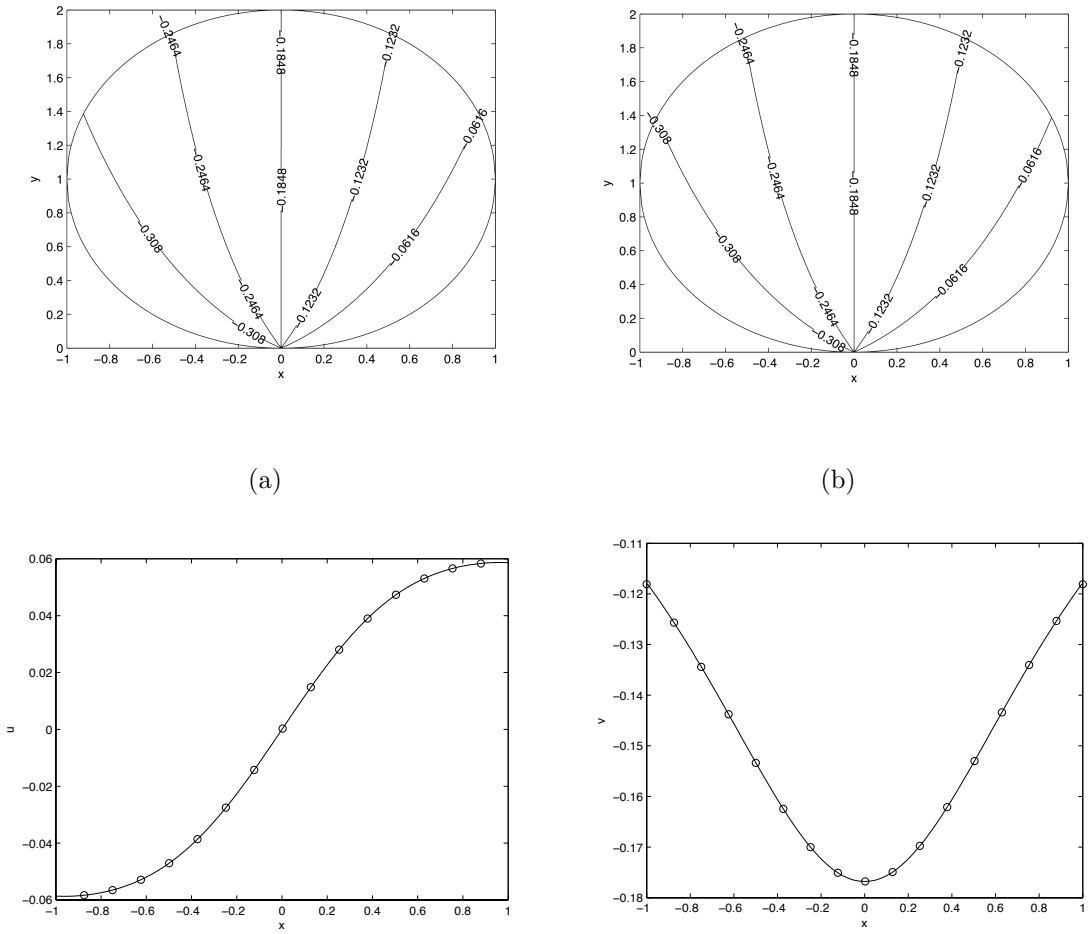

Figure 4.5: Contour plot for computational results (a) and analytical results (b) using the boundary condition $\Psi_B = \theta - \sin(\theta)$. Streamlines are of course not normal to the wall as we also have tangential velocity. Also plotted are the horizontal (c) and vertical (d) velocity along the horizontal centreline for both computational (small circles) and analytical (line) results.

these coarse grids. The apparent error decreases consistently if we investigate the grid refinements as Figure 4.6 shows.

4.2.6 Steady Ellipses

We move on to apply the numerical scheme to the case of elliptical shapes. We can also fairly easily compare these results with the analytical thin shape results of section 2.2.

We use the kinematic boundary condition (2.1.14),

$$\frac{\partial \Psi_B}{\partial \theta} = ba'(\sin(\theta))^2 - ab'\cos(\theta) + b'a(\cos(\theta))^2. \tag{4.2.23}$$

Integrating this with respect to θ and rearranging we end up with

$$\Psi_B = \left(\frac{b'a + ba'}{2}\right)\theta + \left(\frac{b'a - ba'}{2}\right)\sin(2\theta) - ab'\sin(\theta). \tag{4.2.24}$$

Rearranging our code and implementing in the numerical scheme all the above, we derive the following contour plots for different ellipses. These can be seen in Figures 4.7 and 4.8. It is important to mention here that we have kept our stencil the same as before (same distance horizontally and vertically). In order to assess the efficiency of the numerical scheme for the case of the ellipses, we once again present results from more coarse grids in Figure 4.9. We have used as an example the case where the ratio of the major axis to the minor one is 3. The apparent error once again decreases with the grid refinements. The general flow structure though remains intact but most of the error takes place down at the urethra as is seen especially with these coarse grids.

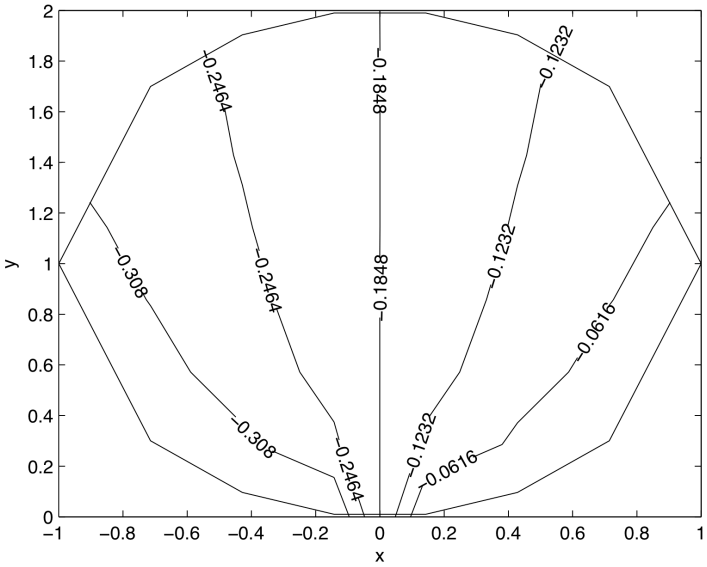
y
x
−0.2464
−0.1848
−0.1232
−0.308
−0.2464
−0.1848
−0.1232
−0.0616
−0.308
−0.2464
−0.1232
−0.0616

(a)

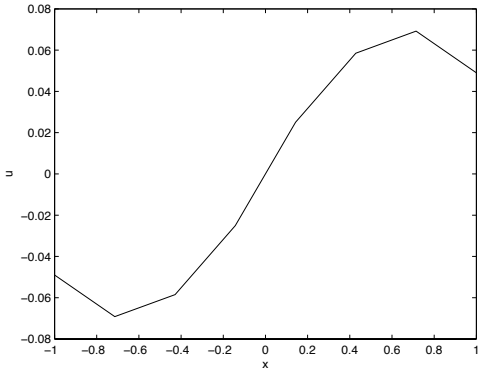
u
x

(b)

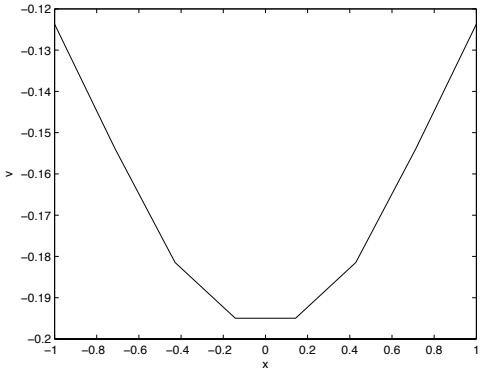
v
x

(c)

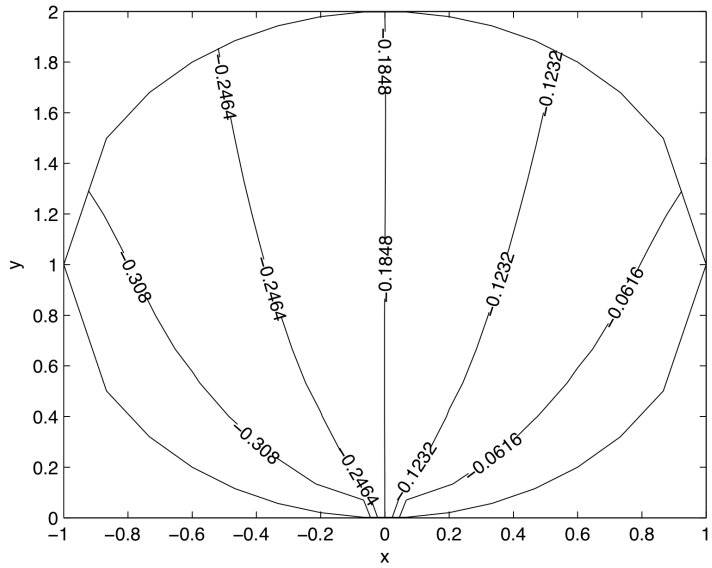

(d)

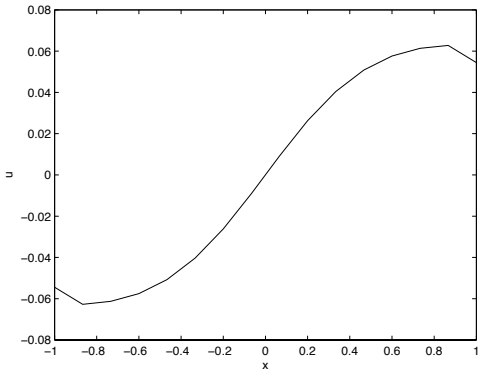

(e)

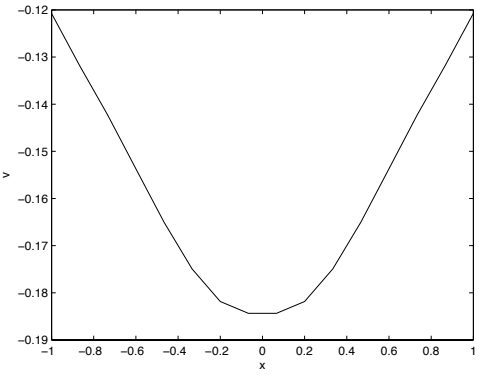

(f)

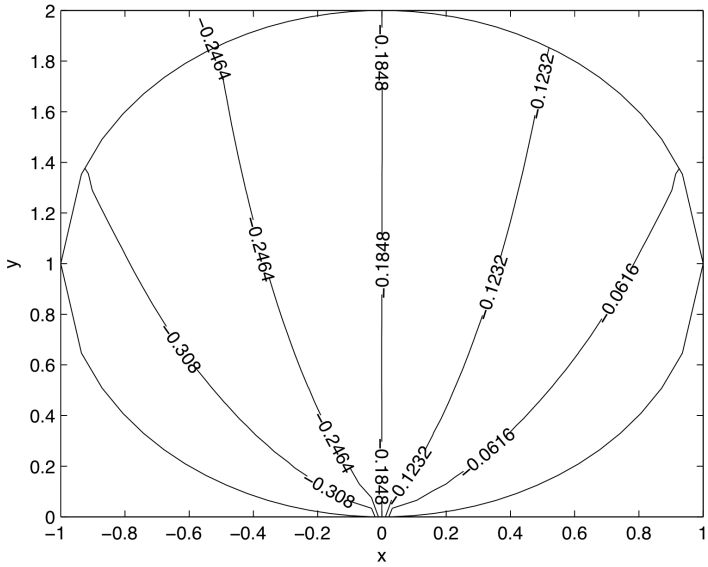
-0.2464
-0.1848
-0.1232
-0.2464
-0.1848
-0.1232
-0.0616
-0.308
-0.2464
-0.1848
-0.1232
-0.0616
-0.308
y
x

(g)

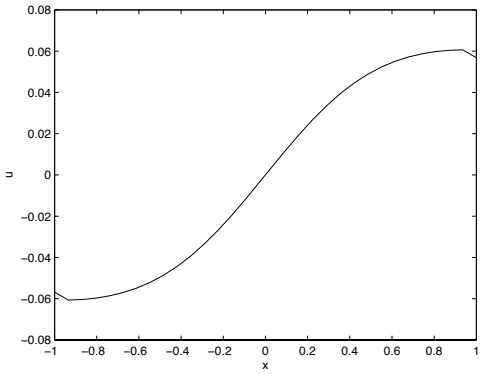
u
x

(h)

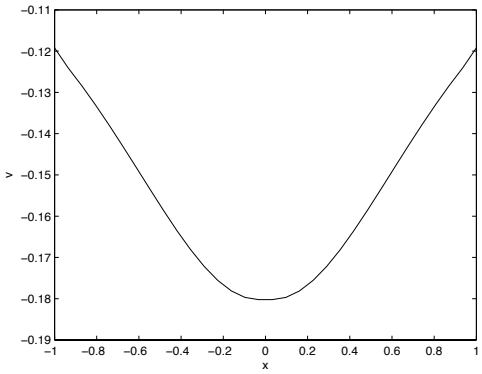
v
x

(i)

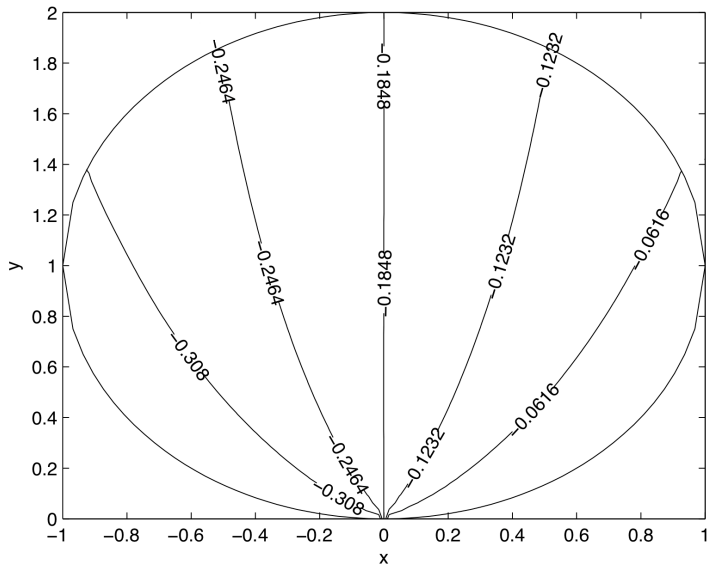

(j)

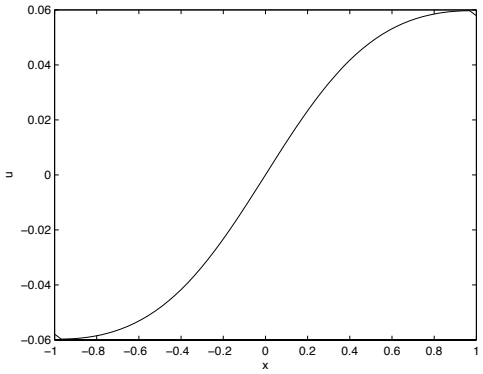

(k)

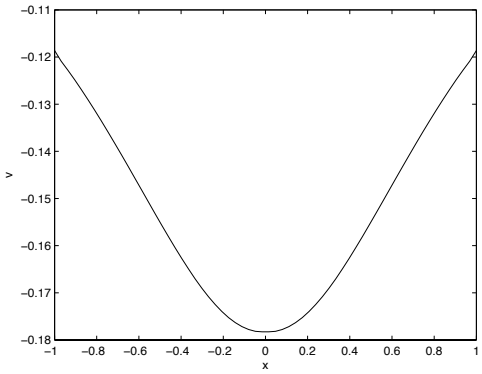

(l)

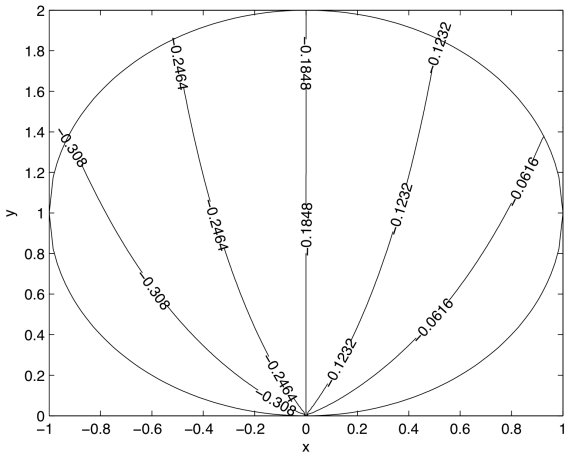

(m)

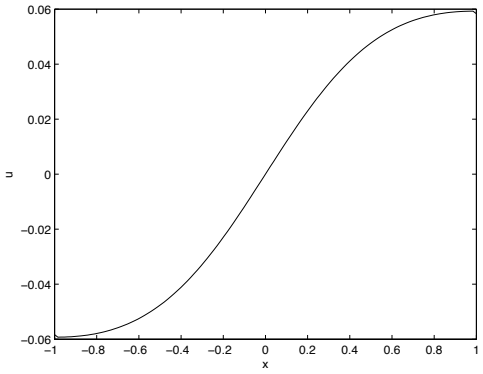

(n)

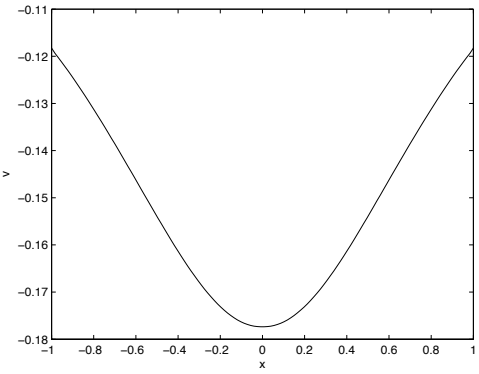

(o)

Figure 4.6: Contour plots for computational results using the boundary condition $\Psi_B = \theta - \sin(\theta)$. Also plotted are the horizontal and vertical velocity along the horizontal centreline. The testing of the code efficiency is demonstrated through the showing of more coarse grids. First a 4x4 (contour plot (a), horizontal velocity (b) and vertical velocity (c)), then an 8x8 ((d)-(f)), 16x16 ((g)-(i)), 32x32 ((j)-(l)) and 64x64 ((m)-(o)) grid are presented respectively.

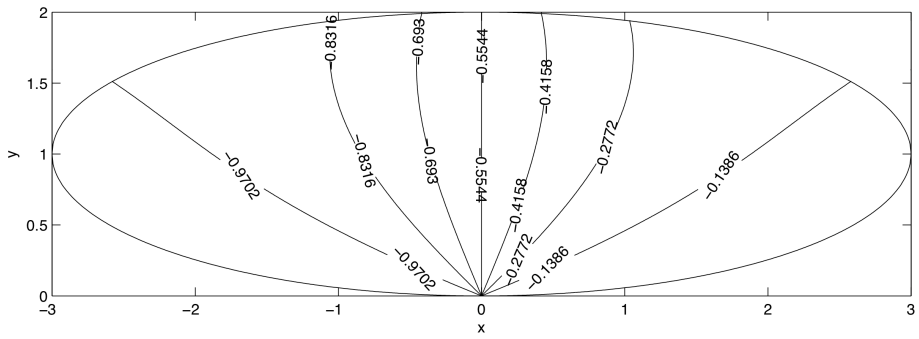

(a)

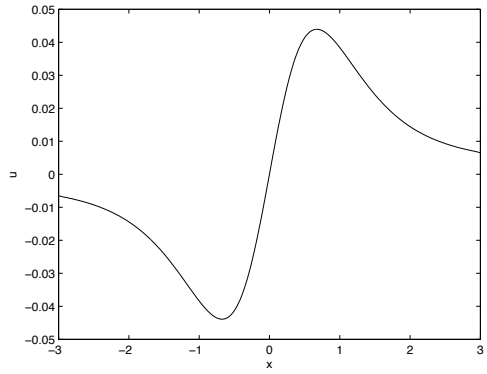

(b)

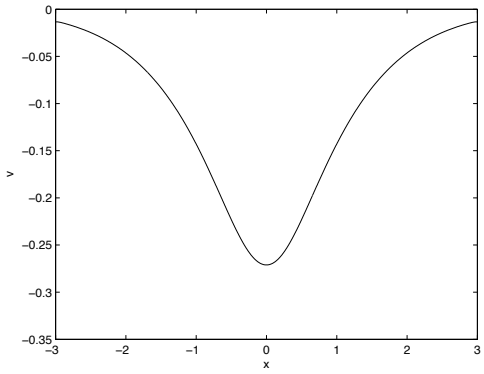

(c)

Figure 4.7: Contour plot for an ellipse with major axis to minor axis ratio of 3 using the boundary condition from (4.2.24). Also plotted are the horizontal (b) and vertical (c) velocity along the horizontal centreline.

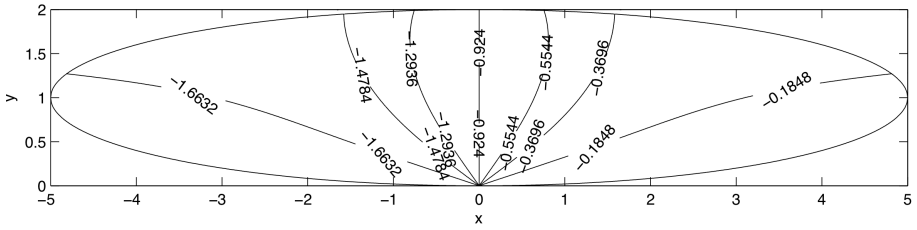

(a)

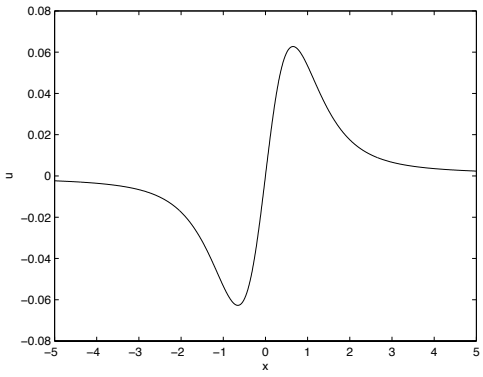

(b)

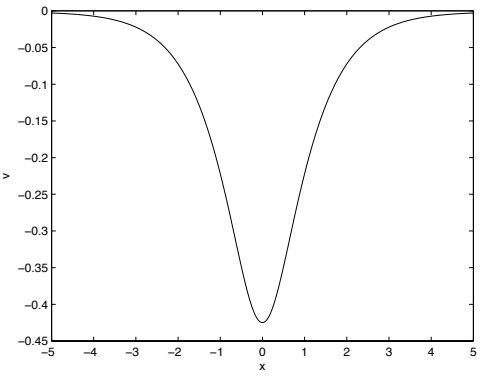

(c)

Figure 4.8: Contour plot for an ellipse with major axis to minor axis ratio of 5 using the boundary condition from (4.2.24). Also plotted are the horizontal (b) and vertical (c) velocity along the horizontal centreline.

We can see here that the two plots from the horizontal elliptical-shaped vessels follow the trend of the analytical results shown in section 2.2, specifically in Figure 2.9. The streamlines away from the centre have a similar flow.

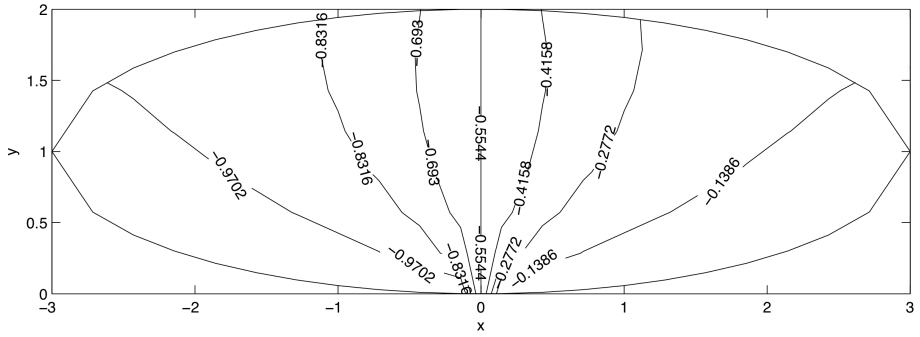

(a)

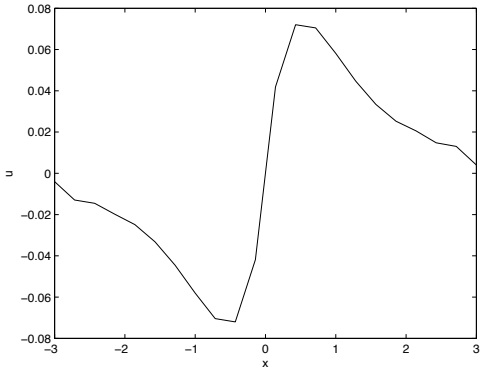

(b)

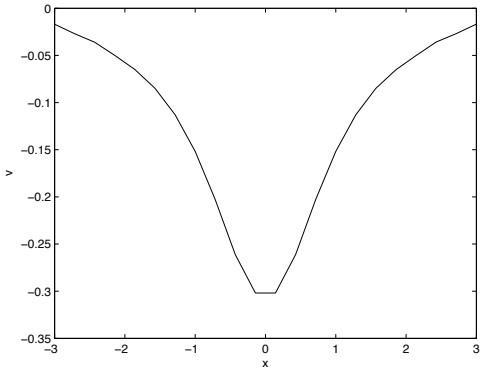

(c)

We take a similar approach with vertical elliptical-shaped vessels and also compare with the vertical thin elliptical-shaped vessels of section 2.2. Similarly to the previous results from the horizontal elliptical-shaped vessels case, we can also see that these plots follow

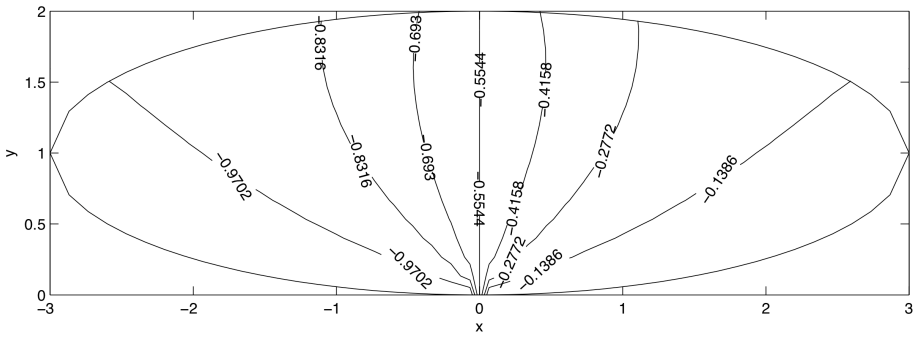

(d)

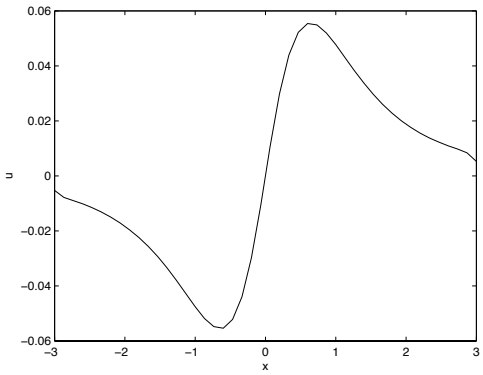

(e)

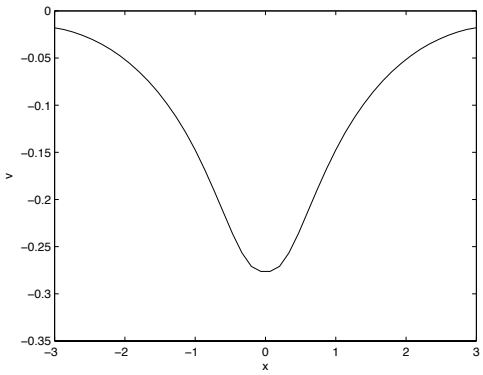

(f)

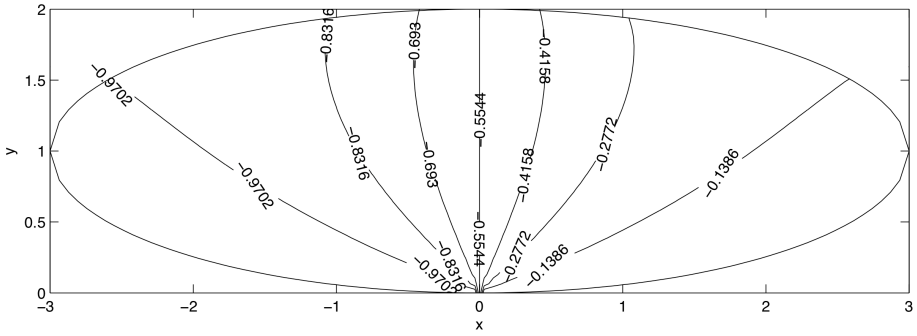

(g)

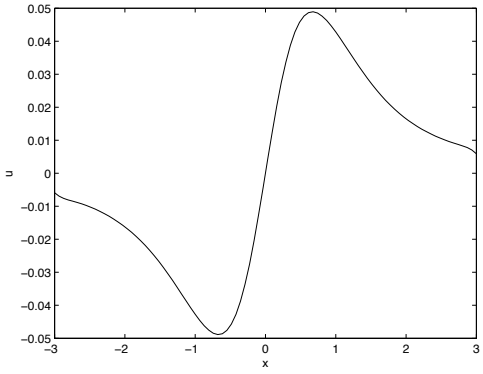

(h)

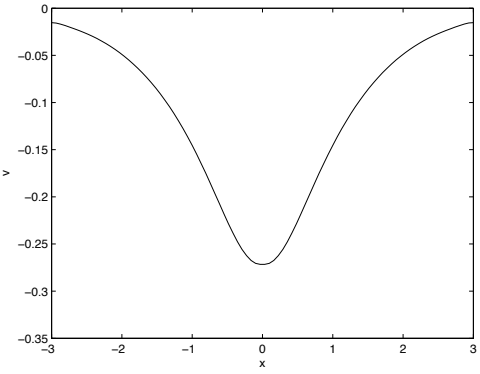

(i)

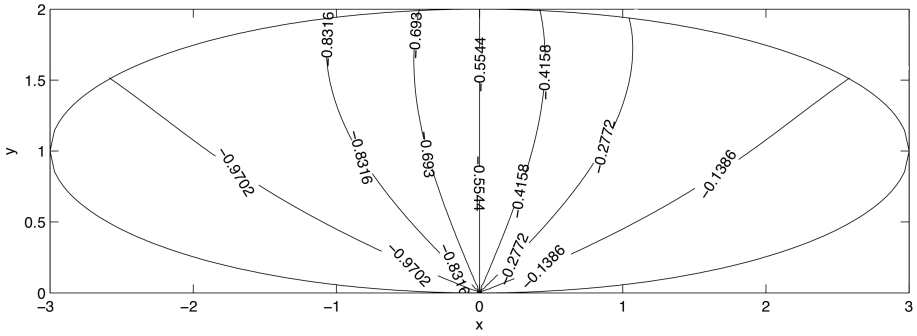
−0.8316
−0.693
−0.5544
−0.4158
−0.2772
−0.1386
−0.9702
−0.8316
−0.693
−0.5544
−0.4158
−0.2772
−0.1386
−0.9702
x
y

(j)

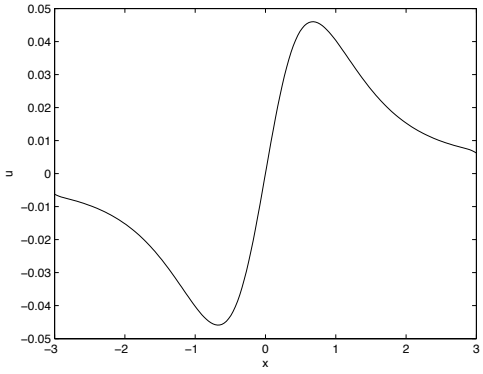
u
x

(k)

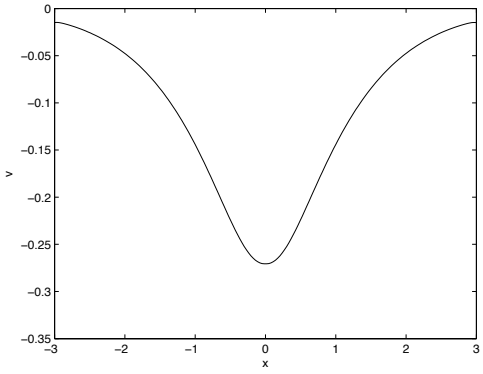
v
x

(l)

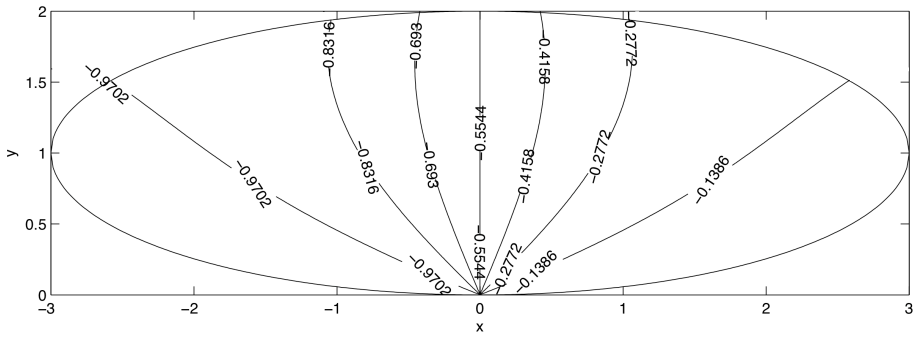

(m)

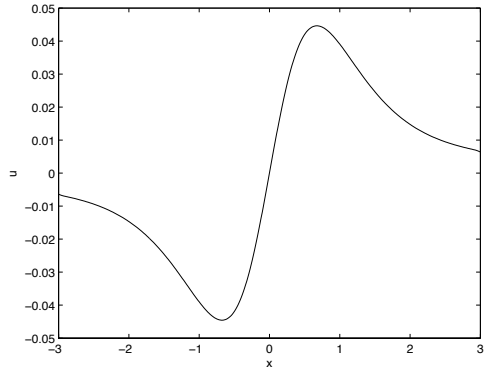

(n)

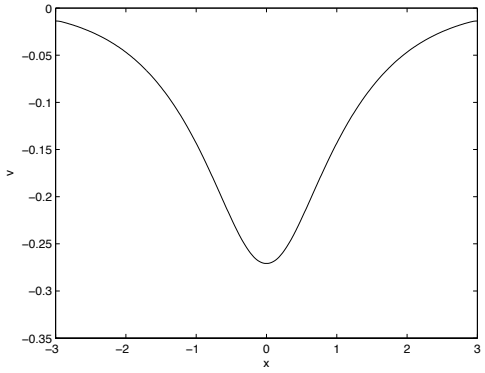

(o)

Figure 4.9: Contour plots for computational results for an ellipse with major axis to minor axis ratio of 3 using the boundary condition from (4.2.24). The assessment of code efficiency is demonstrated here through the showing of more coarse grids. Also plotted are the horizontal and vertical velocity along the horizontal centreline. First a 4x4 - in a 1x1 xxy grid - (contour plot (a), horizontal velocity (b) and vertical velocity (c)), then an 8x8 ((d)-(f)), 16x16 ((g)-(i)), 32x32 ((j)-(l)) and 64x64 ((m)-(o)) grid are presented respectively.

closely the trend of the analytical results for thin elliptical-shaped vessels as described in section 2.2, Figure 2.12.

4.2.7 Results & Comments

In this section, we set the ground work for our numerical scheme using a modified iterative finite difference scheme. Notice in Figures 4.4 and 4.5 that comparing the same number of grid points and more specifically a 128x128 grid, with regard to the accuracy between a standard iterative finite difference method (shown in Figure 4.4) and our modified iterative finite difference method (see Figure 4.5), the accuracy is improved. The boundary interpolation around the boundary of the vessel improves the accuracy at those points making the scheme more refined than a standard iterative finite difference scheme.

It is seen from the plots of section 4.2.6 that as the shape thins, the results for the elliptical shapes move closer to those of the thin-vessel analysis mentioned in chapter 2. This adds confidence in the validity of our numerical scheme to further extend it. Looking at Figure 4.8 and more specifically part (b), we can see that the horizontal velocity moves towards the thin-vessel results and it is comparable to the figures plotted in chapter 2 (see Figure 2.7 for the outer thin region and Figure 2.15 (c) for the Euler/Laplace region near $-1 \leq x \leq 1$). It is also worth seeing the vertical velocity of the vertical ellipses along the vertical centre line and more specifically Figure 4.11 (c) (the vertical velocity) as it also moves towards the results of the thin analysis results shown in Figure 2.10.

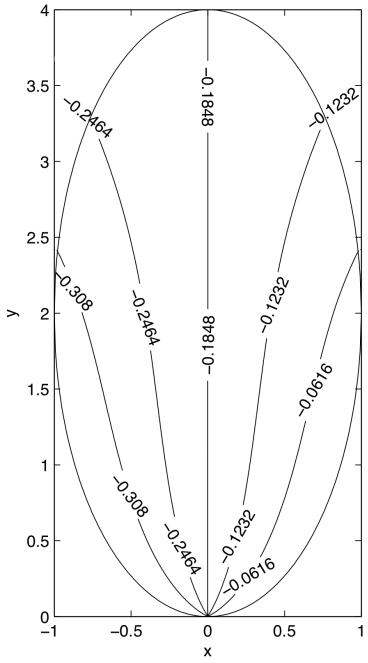

(a)

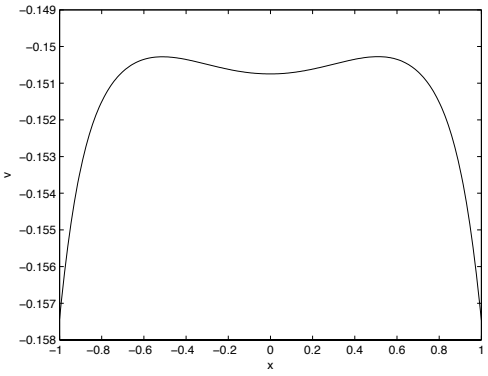

(b)

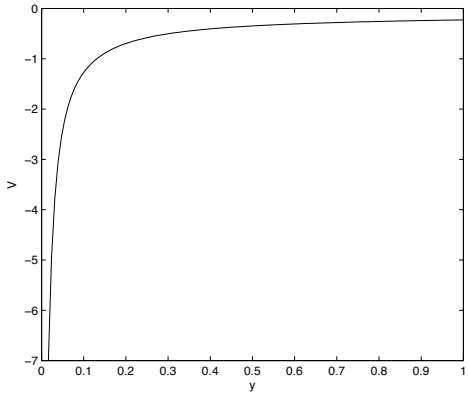

(c)

Figure 4.10: Contour plot for an ellipse with major axis to minor axis ratio of 0.5 using the boundary condition from (4.2.24). Also plotted are the vertical velocity along the horizontal centre line (b) and the vertical centre line (c).

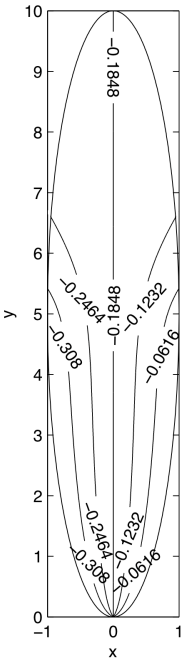

(a)

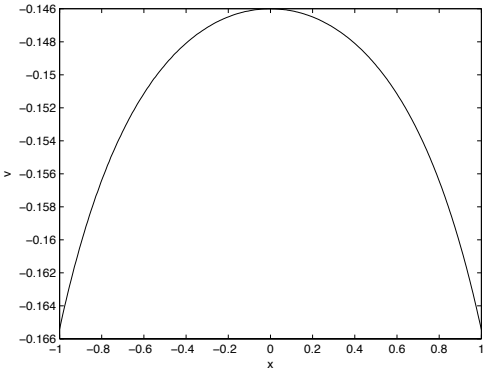

(b)

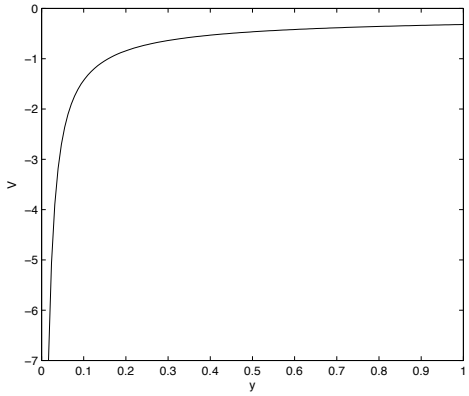

(c)

Figure 4.11: Contour plot for an ellipse with major axis to minor axis ratio of 0.2 using the boundary condition from (4.2.24). Also plotted are the vertical velocity along the horizontal centre line (b) and the vertical centre line (c).

Notice that Figures 4.7 (b) and 4.8 (b) resemble the results of both the thin horizontal analysis and the Euler/Laplace region as discussed in section 2.2. For $x > 1$ and $x < -1$, in both figures the thin-vessel analysis results are noticed. The Euler/Laplace region appears in the range $-1 < x < 1$ and also resembles the analysis. These results are comparable with the results in section 2.2 and more specifically Figures 2.7 and 2.15 (b). It is also worth noticing the high vertical velocities in those cases as seen in Figures 4.7 (c) and 4.8 (c). Similar comments also apply for the case of the thin vertical analysis. Notice the results of Figure 4.10 (c) and 4.11 (c) showing the vertical velocity at the vertical centre line y. It is also worth noticing the dip effect in Figure 4.10 (b).

4.3 Collapsing of Circular Shape to Flat Elliptical Shape

4.3.1 Circle Collapsing into Flat Ellipse

The results in this chapter are now assembled to create a reasonably realistic model or first model for the collapsing of the vessel at different time steps. We will assume that the circumference of our vessel remains the same at all stages. We start with a circle and by applying downward force at the top and outward force at the two sides we deform the circle into an ellipse. We once again use the boundary condition from (4.2.24). This also applies for the starting circle as when $a = b$ we retrieve (4.2.20). A

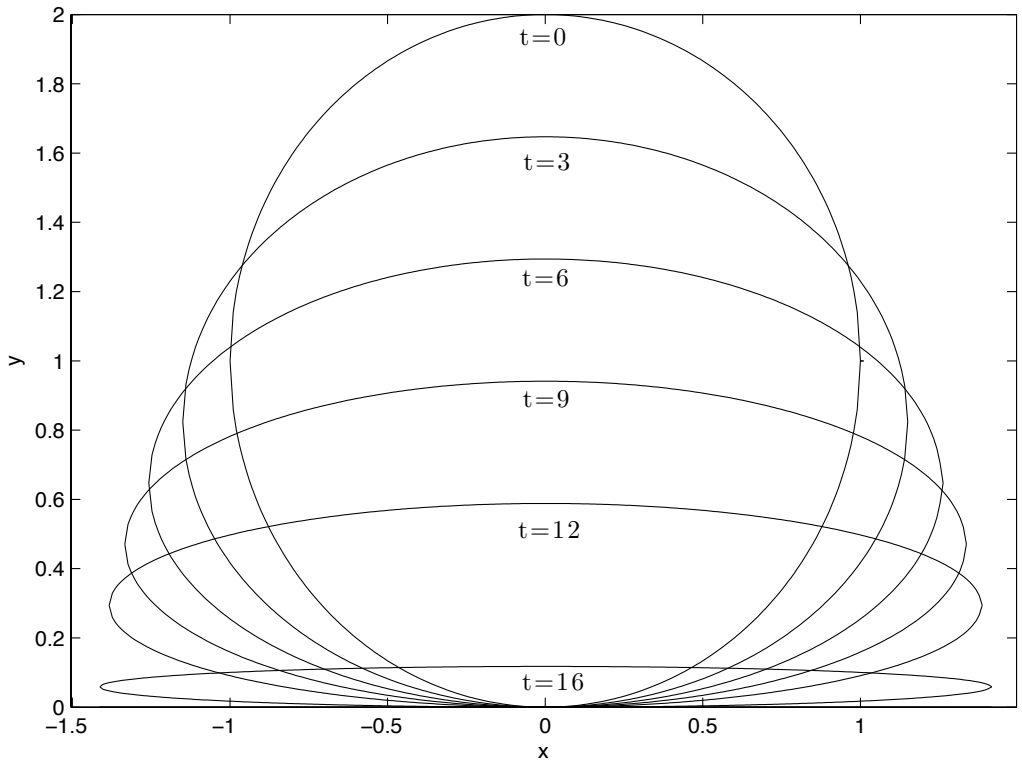

Figure 4.12: Shapes taken by the vessel at different times before it collapses to a thin flat ellipse.

variety of times are chosen, as displayed in Figure 4.12, in order to show the streamlines for the evolving shape as given in Figure 4.13. For this particular case, we have used values for $a(t)$ and $b(t)$ that are dependent on each other. More specifically,

$$a(t) = \sqrt{2 - (b_0 - kt)^2} \quad \text{and} \quad b(t) = b_0 - kt, \tag{4.3.1}$$

where a_0 and b_0 are the initial values for a and b, t is the time in seconds for micturition and also k is a parameter adjusting the time in terms of the total time for micturition.

In this case, the total time is taken to be 17 units of time (it can strictly be converted to seconds) rounding down our result that was previously used (17.5 seconds). This does not make any difference at all as any value can be inputed into the numerical scheme. Hence, $k = \frac{1}{17}$ is used to indicate that the vessel will collapse in 17 units of time. The changes in the streamlines in this model with time can be clearly seen. As we can see over time as the circular vessel collapses into an ellipse, most of the flow is in the middle. This is consistent with our thin analysis from section 2.2.

4.3.2 Results

The results shown in Figure 4.13 are for the first model of a collapsing vessel as defined in section 4.3.1. The model tries to incorporate some of the features of a collapsing vessel in general and at the same time it gives us some insight into and from our analytical results. In contrast with our earlier analytical results which must keep to a circular shape, we can see that the starting circle in these cases collapses into an ellipse. The horizontal velocity plots are odd about $x = 0$ and similarly the vertical velocities even about $x = 0$ as expected by symmetry. It is especially interesting and encouraging to see the horizontal velocity plot in Figure 4.13 (q) which clearly moves closer towards the thin-vessel analysis results of Figures 2.7 and 2.15 (b). Observe the apparent counterpart of an Euler/Laplace area near the region $-0.08 < x < 0.08$ approximately. It is also worth noticing the relatively high vertical velocities of the plot in Figure 4.13 (r) which is near the urethra.

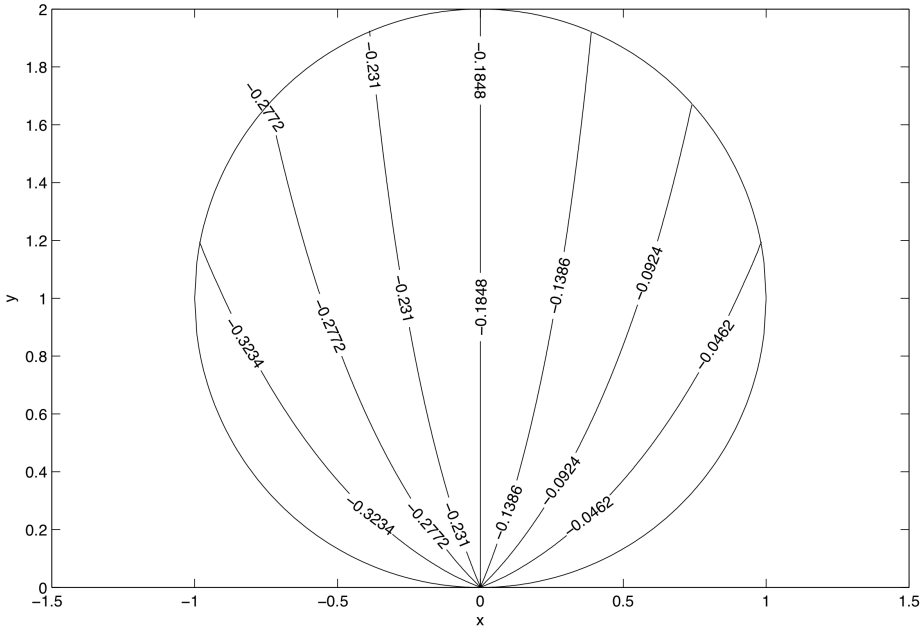

(a)

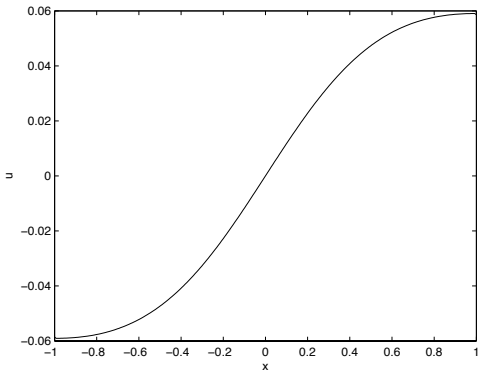

(b)

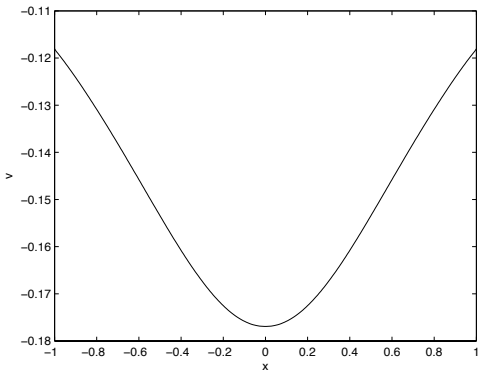

(c)

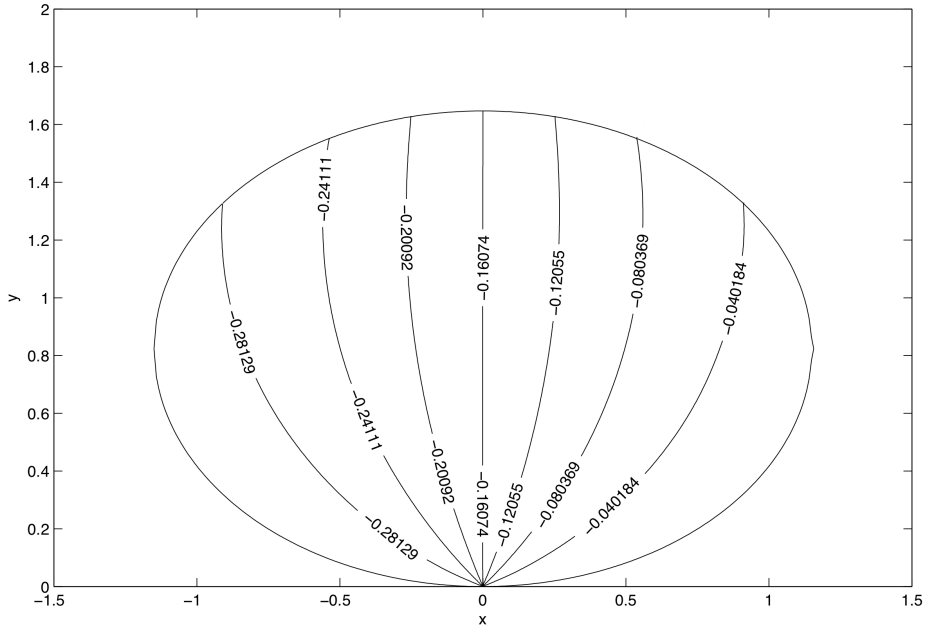
x
y
−0.28129
−0.24111
−0.20092
−0.16074
−0.12055
−0.080369
−0.040184

(d)

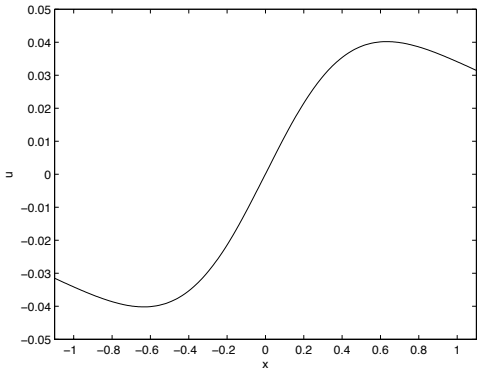
u
x

(e)

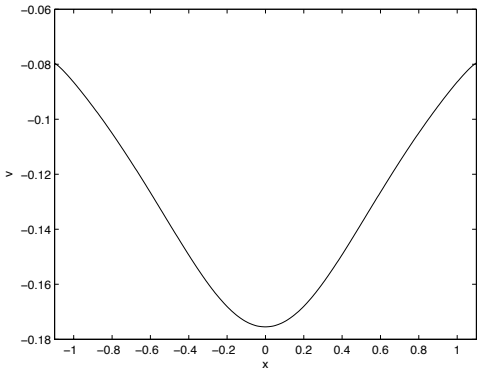
v
x

(f)

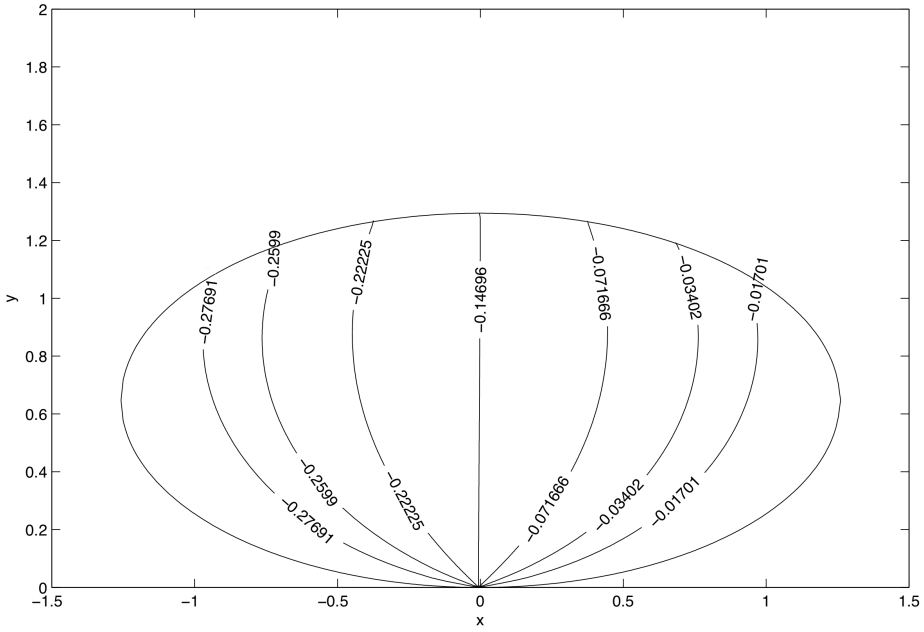

(g)

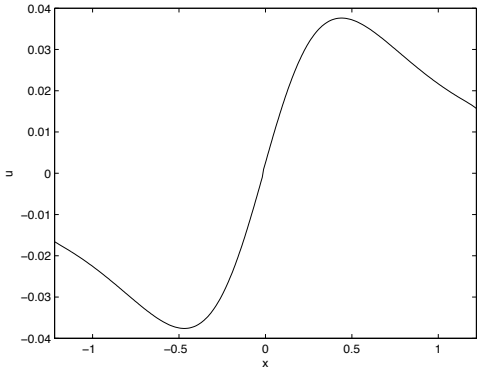

(h)

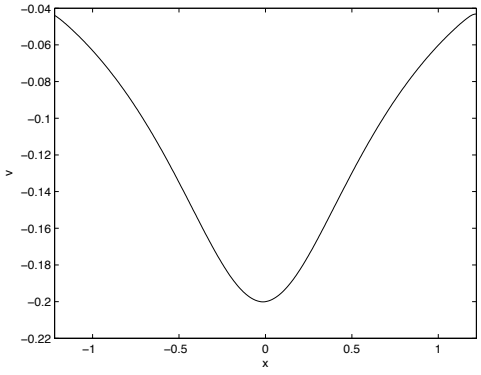

(i)

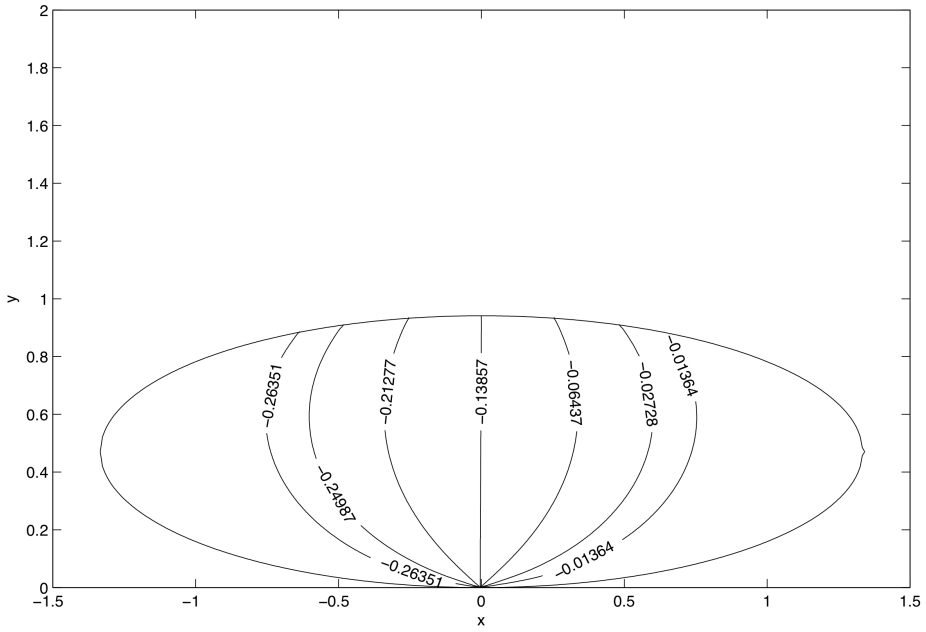
−0.26351
−0.24987
−0.21277
−0.13857
−0.06437
−0.02728
−0.01364
−0.26351
−0.01364
x
y

(j)

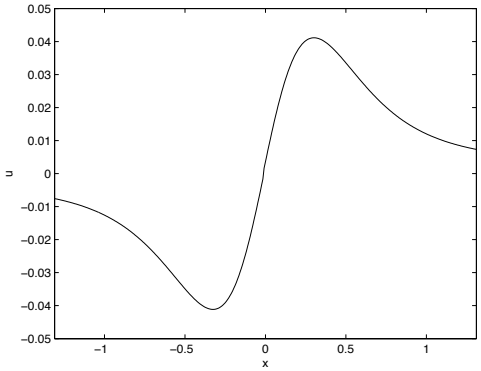
u
x

(k)

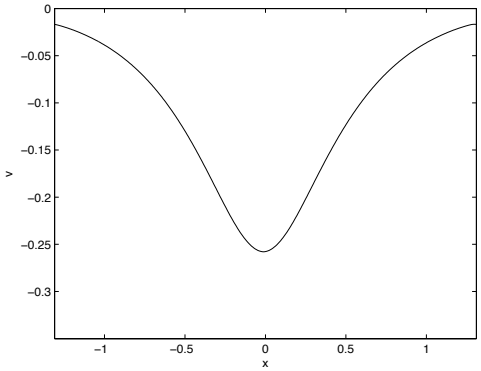
v
x

(l)

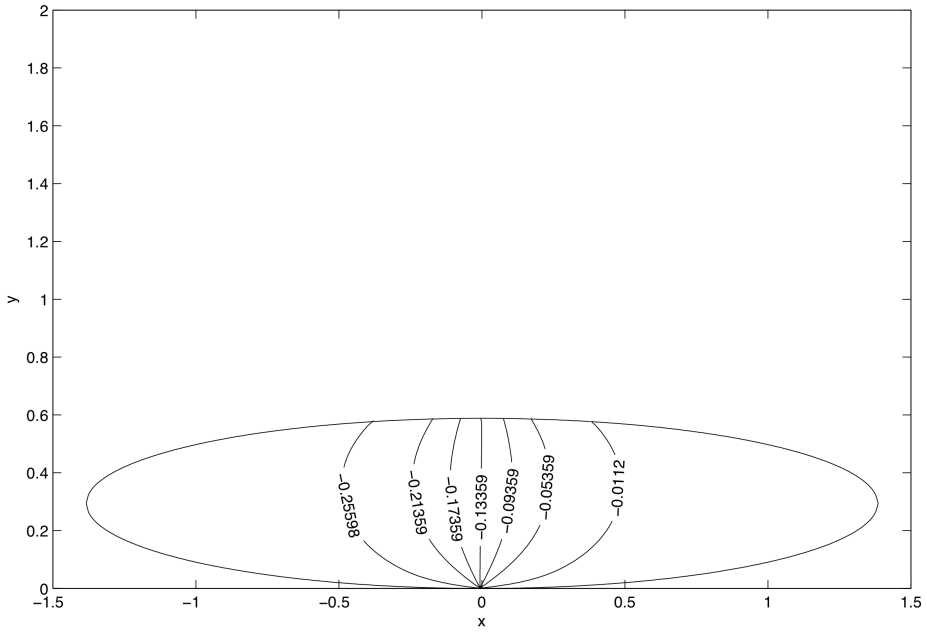

(m)

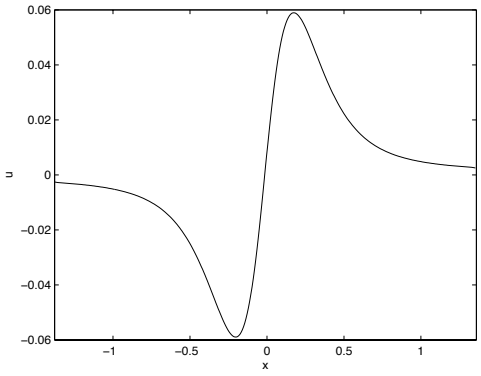

(n)

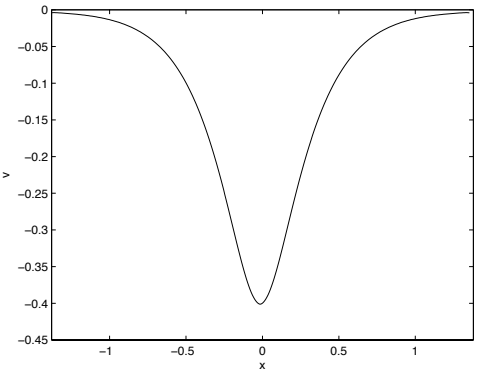

(o)

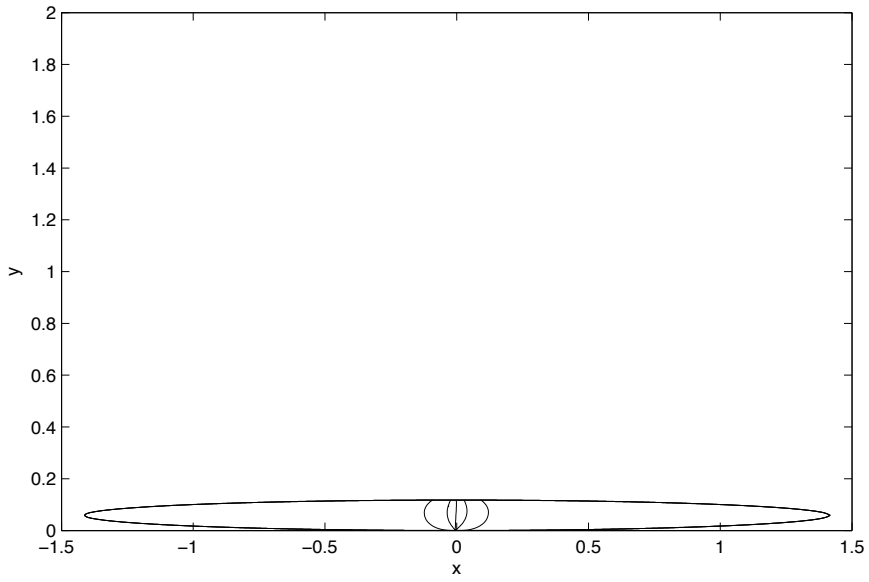

(p)

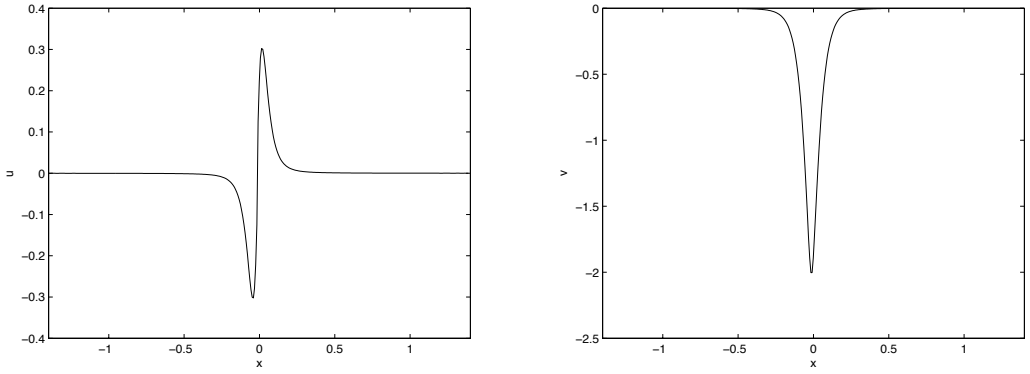

(q) (r)

Figure 4.13: Contour plots of the flow inside the collapsing bladder described in section 4.3. Also plotted are the horizontal and vertical velocity along the horizontal centreline. Times for the parts are 0 (contour plot (a), horizontal velocity (b) and vertical velocity (c)), then 3((d)-(f)), 6((g)-(i)), 9((j)-(l)), 12((m)-(o)) and 16((p)-(r)) respectively.

4.4 Circular Shape using Boundary Element Method

4.4.1 Boundary Integral Formulation

As mentioned in section 4.1, this method can also be used to tackle the bladder collapse. A short overview with results is presented in this section. We need to compute the solution of (2.0.1) at any point inside a two-dimensional circle given a known value of Ψ on the boundary. We will be applying a Dirichlet boundary condition. Everything described here in section 4.4.1 is the standard formulation of the Boundary Element Formulation and is shown as a background.

Using a Green's function, we formulate the solution in terms of two integral equations that we can solve using the Boundary Element Method. Green's function for Laplace's equation in two dimensions is represented by [91] $G(\underline{x}, \underline{x}_0)$ satisfying

$$\nabla^2 G(\underline{x}, \underline{x}_0) + \delta(\underline{x} - \underline{x}_0) = 0, \tag{4.4.1}$$

where:

- $\underline{x} = (x, y)$ is the variable "field point".
- $\underline{x}_0 = (x_0, y_0)$ is the fixed location of the "singular point" or "pole".
- $\delta(\underline{x} - \underline{x}_0) = \delta(x - x_0, y - y_0)$ is Dirac's delta function in two dimensions.

Let us also remind ourselves of Green's theorem. One form of the theorem can be derived to link two variables in the volume V. Assume the existence of two variables G and Ψ with continuous first and second derivatives within the volume V. It can be

readily shown [10] that the following integral transformation is valid

$$\int_V \left(\Psi\nabla^2 G - G\nabla^2\Psi\right)\, dV = \int_S \left(\Psi\frac{\partial G}{\partial n} - G\frac{\partial \Psi}{\partial n}\right)\, dS, \tag{4.4.2}$$

where $\frac{\partial}{\partial n}$ is the derivative of a function in the direction of the outward normal vector. This equation is Green's second identity and is used in Boundary Element applications in order to reduce the dimensionality of a problem by one. The mathematical functions are not arbitrarily chosen; Ψ is the unknown potential, or the streamfunction in our case while G is the known fundamental solution of Laplace's equation,

$$G(\underline{x}, \underline{x}_0) = -\frac{1}{2\pi}\ln\left(\sqrt{(x-x_0)^2 + (y-y_0)^2}\right), \tag{4.4.3}$$

applicable to any solution domain geometry. Applying Green's second identity to these two functions results in the following transformation from an area integral in dA to a line integral in $d\Gamma$,

$$\int_A \left(\Psi\nabla^2 G - G\nabla^2\Psi\right)\, dA = \int_\Gamma \left(\Psi\frac{\partial G}{\partial n} - G\frac{\partial \Psi}{\partial n}\right)\, d\Gamma, \tag{4.4.4}$$

where $\frac{\partial}{\partial n}$ is as defined above, A is the arbitrary area that we are interested in and Γ is the closed lines bounding the area A. The streamfunction Ψ satisfies Laplace's equation $\nabla^2\Psi = 0$ everywhere in the solution domain. The fundamental solution G however satisfies $\nabla^2 G = 0$ everywhere except at the point $\underline{x}_0$ itself where it is singular. To deal with this singularity, we can surround the point $\underline{x}_0$ by a very small circle of radius ϵ and examine the solution in the limit $\epsilon \to 0$. By excluding this small circle, the new area is $A - A_\epsilon$ and the new surface is $\Gamma + \Gamma_\epsilon$, and then equation (4.4.4) becomes

$$\int_{A-A_\epsilon} \left(\Psi\nabla^2 G - G\nabla^2\Psi\right)\, dA = \int_{\Gamma+\Gamma_\epsilon} \left(\Psi\frac{\partial G}{\partial n} - G\frac{\partial \Psi}{\partial n}\right)\, d\Gamma, \tag{4.4.5}$$

where A_ϵ is the area of the circle of radius ϵ surrounding the singular point $\underline{x}_0$ and Γ_ϵ is the closed line bounding the area A_ϵ. We know that within the area $A - A_\epsilon$, $\nabla^2\Psi = 0$ and $\nabla^2 G = 0$ everywhere. This makes the left hand side of (4.4.5) equal to zero and the surface integral $\Gamma + \Gamma_\epsilon$ can then be split into two line integrals as follows:

$$0 = \int_\Gamma \left(\Psi\frac{\partial G}{\partial n} - G\frac{\partial \Psi}{\partial n}\right) d\Gamma + \int_{\Gamma_\epsilon} \left(\Psi\frac{\partial G}{\partial n} - G\frac{\partial \Psi}{\partial n}\right) d\Gamma. \tag{4.4.6}$$

We now need to evaluate the Γ_ϵ integral in the above equation. It is convenient to use the angle α measured anticlockwise from the x-axis at point $\underline{x}_0$ and substitute $d\Gamma = \epsilon\, d\alpha$. The following substitution can also be used

$$\frac{\partial G}{\partial n} = \frac{\partial G}{\partial r}\frac{\partial r}{\partial n} = -\frac{1}{2\pi r}(-1) = \frac{1}{2\pi r}. \tag{4.4.7}$$

Taking the Γ_ϵ integral to the limit as $r \to \epsilon$ within the limits of α from 0 to 2π, the second integral of (4.4.6) becomes

$$\begin{aligned}\int_{\Gamma_\epsilon} \left(\Psi\frac{\partial G}{\partial n} - G\frac{\partial \Psi}{\partial n}\right) d\Gamma &= \frac{1}{2\pi}\int_0^{2\pi} \left(\Psi\left(\frac{1}{\epsilon}\right) - \ln\left(\frac{1}{\epsilon}\right)\frac{\partial \Psi}{\partial n}\right)\epsilon\, d\alpha \\ &= \frac{1}{2\pi}\int_0^{2\pi} \left(\Psi + (\epsilon\ln(\epsilon))\frac{\partial \Psi}{\partial n}\right) d\alpha = \frac{1}{2\pi}(2\pi\Psi) = \Psi, \end{aligned} \tag{4.4.8}$$

with Ψ evaluated at $\underline{x}_0$.

Substituting this result in (4.4.6) and rearranging the terms, results in the following equation,

$$\Psi = \int_\Gamma \left(G\frac{\partial \Psi}{\partial n} - \Psi\frac{\partial G}{\partial n}\right) d\Gamma. \tag{4.4.9}$$

The above equation is called the Boundary Integral Equation [10], [15], [25], [87] and forms the starting point for the subsequent numerical formulation.

In order to make the Boundary Integral Equation a truly "boundary only" one, we must move the interior fixed location $\underline{x}_0$ to the boundary. This results in the following equation [10], [15], [25], [87],

$$\frac{1}{2}\Psi = \int_\Gamma \left(G\frac{\partial \Psi}{\partial n} - \Psi \frac{\partial G}{\partial n} \right) d\Gamma. \tag{4.4.10}$$

4.4.2 Numerical Implementation

Up to this point, numerical approximations have not been used in arriving at the boundary integral formulation of (4.4.9), (4.4.10). If the closed boundary of the domain can be represented by a simple equation (a circular curve for example), then an analytical solution of the boundary integral equation may be possible. However, to be able to cover any geometry, there seems no option but to perform the integration of the boundary integral equation numerically [5], [10], [11], [15], [25], [87]. As in most forms of numerical integration, the integral is divided into small segments called the boundary elements. These elements can be straight lines, quadratic curves or cubic splines. The accuracy of the boundary element approach is critically dependent on the accuracy of the numerical integration performed.

The boundary is divided into elements and each element is defined by nodal points. Assume that we have N nodal points on the boundary; each node has two variables

Ψ and $\frac{\partial \Psi}{\partial n}$ associated with it so there is a total of $2N$ variables. Any problem with a unique solution must have either Ψ or $\frac{\partial \Psi}{\partial n}$ prescribed on every nodal point. Therefore, we have N unknowns and we need N equations to solve the problem. Assume now a hypothetical case: a potential placed at node 1. Using the fundamental solution, we can calculate potentials and potential gradients at every node from 1 to N, yielding our first linear equation using the boundary integral equation (4.4.9). In producing the second linear equation, we now place the potential at node 2 and repeat the use of the fundamental solution to calculate all variables at the other nodes. This operation is repeated until the potential is placed at the last node N, which will give us the final (Nth) equation. Therefore we end up with N equations for N unknowns which produce (we assume) a unique solution.

We then divide the boundary of the solution domain into a number of connected elements. The variation of the geometry and the variables must be described over each element. These variations can be constant, linear, quadratic, cubic or higher order. Furthermore, it is possible to allow the geometry variation to be different from the variation of the variables (e.g. a linear geometry description with a quadratic variation potential.) Increasing the order of variation of an element should produce more accurate solutions but the penalty of higher CPU time must be paid.

The boundary is described using continuous rectilinear elements and the collocation points are taken at the middle of the elements (a, b). We take the natural co-ordinate to be ξ along the elements with ξ having values ± 1 at the edges. As such,

$$x_i(\xi) = N_j(\xi) x_{ij}(\xi), \quad i = 1, 2 \quad j = a, b, \tag{4.4.11}$$

where $x_i\,(i=1,2)$ is the co-ordinate at the intermediate point defined by ξ. $N_j(\xi)$ is the shape function associated to the extremes $j=a,b$ given by

$$N_a=-\frac{1}{2}(\xi-1),\quad N_b=\frac{1}{2}(\xi+1), \tag{4.4.12}$$

with x_{ij} representing the i^{th} co-ordinate of the j^{th} extreme.

The functions involved in the formulation are $\Psi(\xi)$ and $\frac{\partial\Psi(\xi)}{\partial n}$ and are represented discretely by

$$\Psi(\xi)=N_j(\xi)\Psi_j,\quad \frac{\partial\Psi(\xi)}{\partial n}=N_j\left(\frac{\partial\Psi}{\partial n}\right)_j, \tag{4.4.13}$$

ending up with

$$\Psi^k(\xi)=\left(\begin{array}{c|c} N_1(\xi) & N_2(\xi) \end{array}\right)\left(\Psi^k(k)\right),\quad \frac{\partial\Psi^k(\xi)}{\partial n}=\left(\begin{array}{c|c} N_1(\xi) & N_2(\xi) \end{array}\right)\left(\frac{\partial\Psi^k(k)}{\partial n}\right), \tag{4.4.14}$$

where k is the number of the node, and $\left(\begin{array}{c|c} A & B \end{array}\right)$ is a matrix consisting of two matrix blocks $[A]$ and $[B]$, both together.

Discretisation of Integral Equations

We now discretise the integral equations (4.4.9), (4.4.10) leading to the following form for each equation respectively

$$\Psi(l)=\sum_{k=1}^{K}\left(\begin{array}{c|c} A_1(l,k) & A_2(l,k) \end{array}\right)\left(\frac{\partial\Psi^k(k)}{\partial n}\right)-\sum_{k=1}^{K}\left(\begin{array}{c|c} B_1(l,k) & B_2(l,k) \end{array}\right))\left(\Psi^k(k)\right), \tag{4.4.15}$$

and for the boundary equation

$$\frac{1}{2}\Psi_B(l)=\sum_{k=1}^{K}\left(\begin{array}{c|c} A_1(l,k) & A_2(l,k) \end{array}\right)\left(\frac{\partial\Psi^k(k)}{\partial n}\right)-\sum_{k=1}^{K}\left(\begin{array}{c|c} B_1(l,k) & B_2(l,k) \end{array}\right))\left(\Psi^k(k)\right). \tag{4.4.16}$$

Here, A_1, A_2, B_1, B_2 are constants arising when the equation is applied at node l associated to each element k along which integration is performed. Hence, we end up with the following values for the constants

$$A_j(l,k) = \int_{\partial D_k} N_j(\xi) G(l,\xi) \frac{L_k}{2} d\xi, \text{ for } j = 1, 2\,, \tag{4.4.17}$$

and also

$$B_j(l,k) = \int_{\partial D_k} N_j(\xi) \frac{\partial G(l,\xi)}{\partial n} \frac{L_k}{2} d\xi, \text{ for } j = 1, 2\,, \tag{4.4.18}$$

with l being the collocation point, k the k^{th} node and L_k the length of the k^{th} element.

We will compute these constants using numerical integration based on a trapezoidal rule.

Computation of the Normal Derivatives on the Boundary

We now move on to calculate $\frac{\partial \Psi}{\partial n}$ on the boundary using (4.4.16). Since we know the function describing the streamfunction on the boundary (i.e. Ψ_B which is calculated using the kinematic boundary condition), we arrive at a linear system of k equations and k unknowns which upon rearranging gives a system of the form

$$\underline{A}\,\underline{X} = \underline{B}, \tag{4.4.19}$$

where $\underline{A}$ is a kxk matrix and $\underline{X}$, $\underline{B}$ are both kx1 matrices. Thus, $\underline{X}$ is the solution to the above equation computed by Gaussian elimination and hence we end up with the values of $\frac{\partial \Psi}{\partial n}$ on the boundary.

Computation of Streamfunctions at Internal Points

Finally, we use the results calculated above and apply the discrete equation (4.4.15) to calculate the value of Ψ at all of the internal points. We evaluate the constants of integration as before to obtain our solution.

4.4.3 Numerical Solutions

We now use the method described in section 4.4 to develop a numerical scheme on *MatLab* [14], [24], [28], [37], [58], [105]. The scheme can be used to examine numerical solutions for different shapes and different rates of collapse of the vessel.

We start by validating the scheme in the case where the condition on the boundary is

$$\Psi_B = \sin(\theta), \tag{4.4.20}$$

and the shape of the bladder is circular. We compare the numerical results with the analytical solution

$$\Psi = r\sin(\theta), \tag{4.4.21}$$

where r is the radius of the circle and θ the polar angle at any point.

Giving the contour plots for both the exact and numerical results for a number of internal points, as shown in Figure 4.15, we see that the two are virtually identical. This suggests that the code is working satisfactorily. For this particular results, a boundary with 128 nodes was used to replicate the computational results.

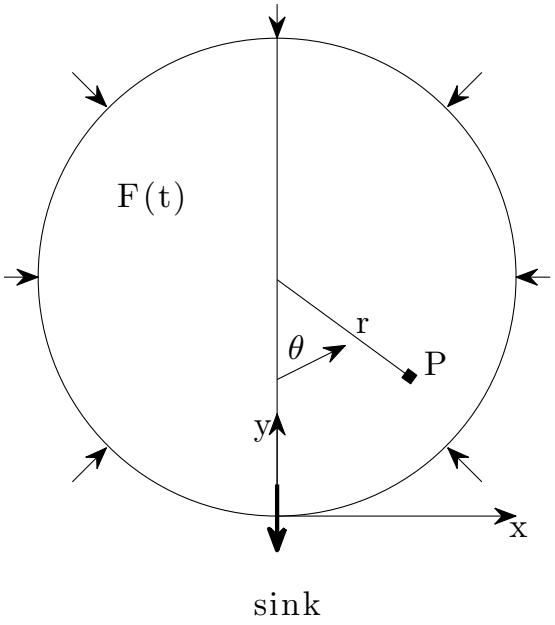

Figure 4.14: The collapsing circle model showing the sink, general internal point P and polar coordinates r and θ based at the centre of the vessel of diameter F(t). Cartesian coordinates x and y are horizontal and vertical in turn with the sink as the origin.

We then continue our validation by examining the numerical solutions found when solving the problem within a circle with a sink at the bottom. We use a more appropriate boundary condition that creates a point discontinuity at the origin representing the sink (associated with the opening of the urethra). We use the following boundary condition

$$\Psi_B = aa'(\theta - \sin(\theta)), \tag{4.4.22}$$

where Ψ_B is the boundary stream function as calculated in equation (2.1.16).

This condition comes from the kinematic boundary condition representing both inward

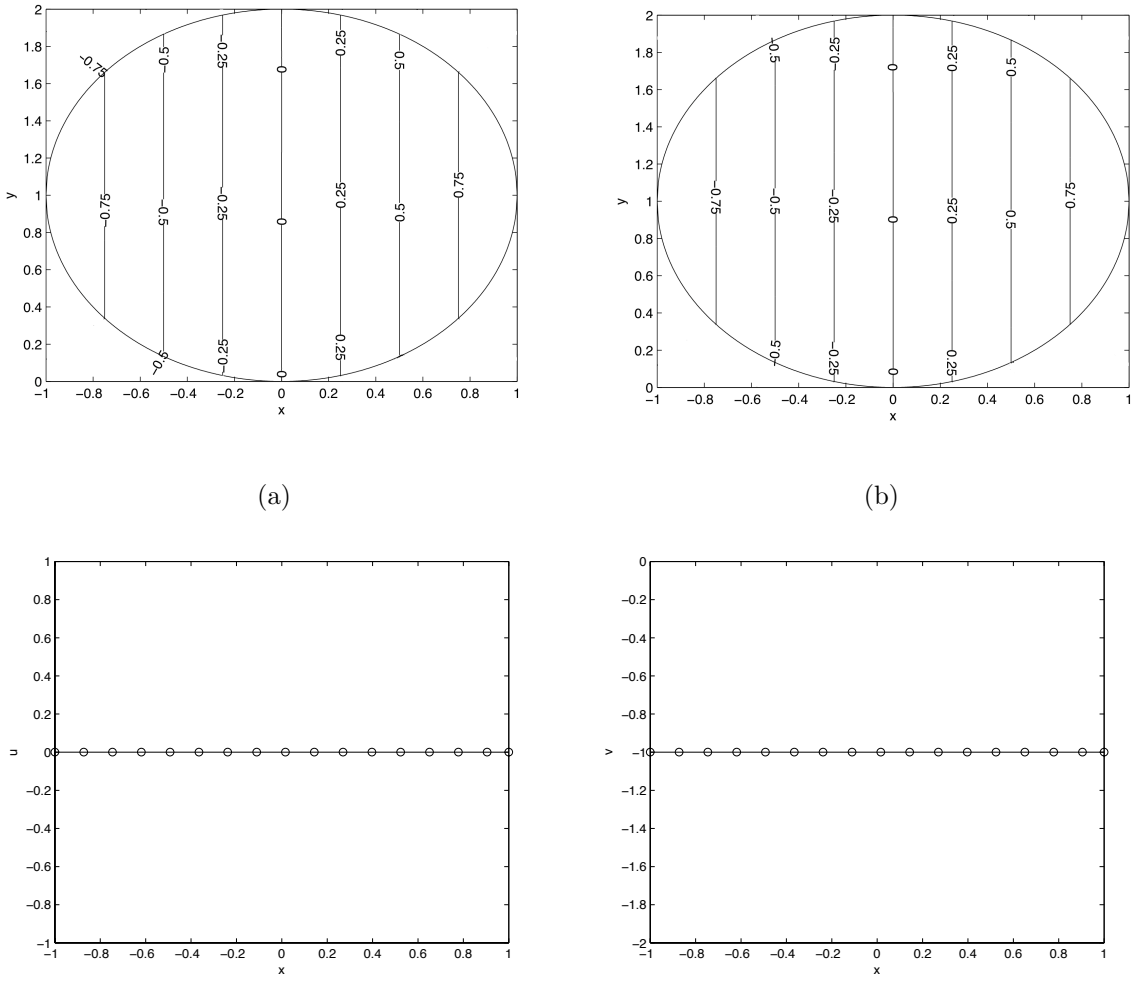

Figure 4.15: A basic test. Contour plot of exact streamfunction values (a) and numerical values (b) in a circle. Also plotted are the horizontal (c) and vertical velocity (d) along the horizontal centreline.

and downward movement in order to keep the bottom fixed and potentially be more realistic. Additionally, the jump of 2π in Ψ_B is located at the bottom and represents a sink strength of 2π.

We validate this using the following analytical solution

$$\Psi = \theta - r\sin(\theta) - 2\arctan\left(\frac{(1+r)\tan\left(\frac{\theta}{2}\right)}{(1-r)}\right) + \pi, \qquad 0 < \theta < \pi, \tag{4.4.23}$$

and

$$\Psi = \theta - r\sin(\theta) - 2\arctan\left(\frac{(1+r)\tan\left(\frac{\theta}{2}\right)}{(1-r)}\right) - \pi, \qquad \pi < \theta < 2\pi, \tag{4.4.24}$$

with r and θ as above.

We now adjust our numerical scheme, compute as above and plot the solution contours for both the exact and numerical results for a number of internal points as shown in Figure 4.16. Once again, for this particular example, we have used a boundary of 128 nodes resulting in a very good accuracy.

The analytical results of (4.4.23), (4.4.24) are matched by our numerical ones. This is promising for the progress of the numerical modeling of the research. It is clear that the results in both the simple case (4.4.20) and the more realistic (4.4.22) are quite accurate. In fact, the errors are less than one percent.

4.4.4 Results & Comments

It is seen in this section (4.4) that it is also possible to tackle our problem with boundary-detailing methods such as the boundary element method. The boundary

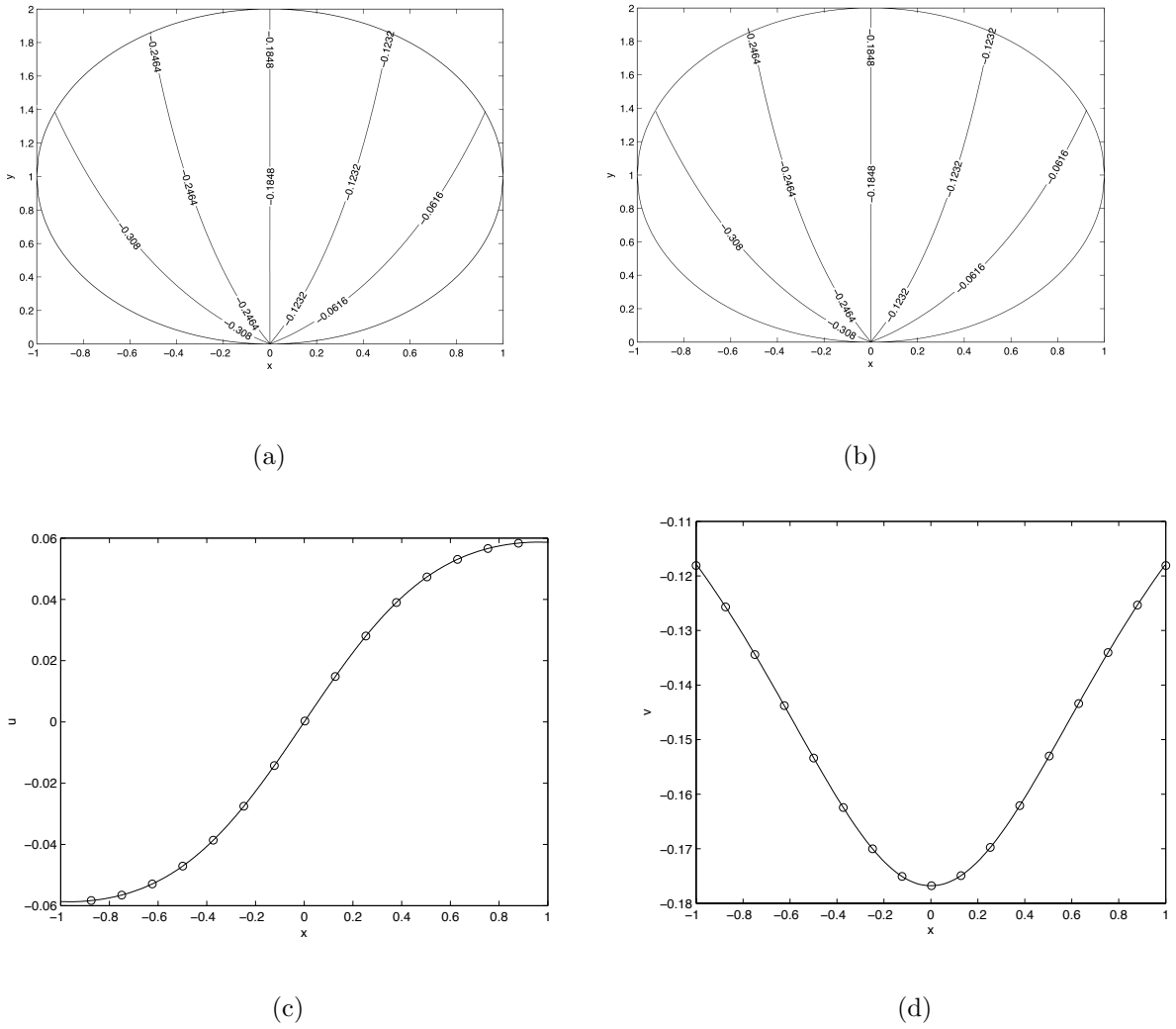

Figure 4.16: Contour plot of exact streamfunction values (a) and numerical values (b) in a circle with a point discontinuity at the base. Also plotted are the horizontal (c) and vertical velocity (d) along the horizontal centreline.

element method is a very powerful tool that can tackle the current problem as it is seen here. The similarity in the results in terms of accuracy of both the modified iterative finite difference method described in section 4.2 and the boundary element method described in section 4.4 lead us to favour the simpler and perhaps easier-to-modify iterative finite difference method in order to further develop the numerical scheme.

4.5 Summary

The apparent reliability of the numerical scheme developed in this chapter gives us some confidence as the results seem reasonable, make physical sense but most of all agree with the results obtained from the earlier analysis. This tends to give us the confidence to further develop the numerical scheme in order to tackle more complex vessels. That can be done mostly by making further developments concerning the boundary condition. The trend required is to make our model more realistic. Even though these shapes are very simple, and in two dimensions, they approximate fairly well shapes that the bladder might take: see for example Figure 1.5 in chapter 1. The circle is taken here throughout as the starting point of the bladder. Further developments though have to be made in order to incorporate more realistic shapes that match better with the clinical results.

Chapter 5

Numerical Solutions for More Complex Two-Dimensional Shapes

5.1 Cardioidal Shapes

We will now use the method from section 4.2 in order to tackle more complex (or complicated) situations. A problem with this method is that calculating the boundary condition for Ψ can be rather awkward. We can do somewhat better and avoid such awkward calculations by working with the boundary condition on the tangential derivative of the stream function. In other words, $\frac{\partial \Psi}{\partial s}$ where $\partial s = \sqrt{(}\partial x^2 + \partial y^2)$ is the distance element along the boundary. Working with the tangential derivative of

the stream function is helpful especially because the new boundary condition now only depends on the shape function $F(x, y, t)$. This gives us more flexibility to tackle more complex shapes. At the same time, we will construct (or rather model) below (see Figure 5.2) some of those complex shapes that the vessel can have at any point during micturition in the case of human bladder evacuation.

5.1.1 Analysis of Boundary Condition

For completeness, we now simplify the form of our input boundary condition which is significant in analytical and computational terms.

Let $F = y - f(x, t)$ and so $F_y = 1$, $F_x = -f_x$, $F_t = -f_t$, where F_y is the differential of F with respect to y and similarly for the rest. Now, using the result of (2.1.5) for the kinematic condition

$$F_t - F_y\Psi_x + F_x\Psi_y = 0, \tag{5.1.1}$$

and substituting the above results in it, we have

$$-\Psi_x = f_x\Psi_y + f_t, \tag{5.1.2}$$

and upon rearranging and dividing both sides by $(1 + f_x^2)^{\frac{1}{2}}$, we obtain

$$\frac{\Psi_x + f_x\Psi_y}{(1 + f_x^2)^{\frac{1}{2}}} = \frac{-f_t}{(1 + f_x^2)^{\frac{1}{2}}}. \tag{5.1.3}$$

Using triangle (a) in Figure 5.1 to help our mathematical construction, we can clearly see that

$$\frac{dx}{ds} = \cos\alpha = \frac{1}{(1 + f_x^2)^{\frac{1}{2}}} \quad \text{and} \quad \frac{dy}{ds} = \sin\alpha = \frac{f_x}{(1 + f_x^2)^{\frac{1}{2}}}. \tag{5.1.4}$$

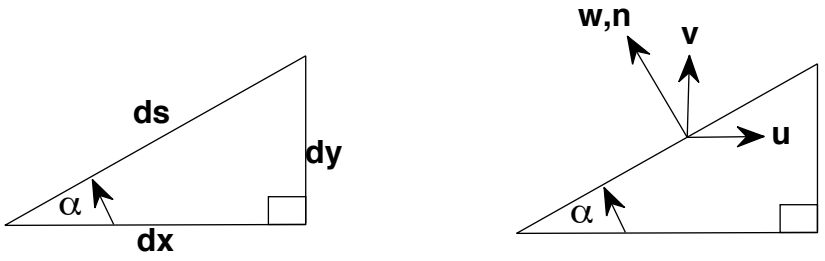

(a) (b)

Figure 5.1: Constructions of basic triangles used for the calculations.

Now using triangle (b) from the same figure we arrive at the equation for the normal velocity component w,

$$w = v\cos\alpha - u\sin\alpha = -\Psi_x\cos\alpha - \Psi_y\sin\alpha = -\frac{\partial\Psi}{\partial s}, \tag{5.1.5}$$

as might be expected, where $u = \Psi_y$ and $v = -\Psi_x$. Using equation (5.1.4), we see that (5.1.5) becomes

$$\frac{\partial\Psi}{\partial s} = \frac{\Psi_x}{(1+f_x^2)^{\frac{1}{2}}} + \frac{f_x\Psi_y}{(1+f_x^2)^{\frac{1}{2}}}, \tag{5.1.6}$$

and thus we have

$$\frac{\partial\Psi}{\partial s} = \frac{f_t}{(1+f_x^2)^{\frac{1}{2}}}. \tag{5.1.7}$$

Generalizing the formula now, we let $F = \mathscr{G}(y - f(x,t))$ and therefore its differentials with respect to x, y and t are $F_t = -f_t\mathscr{G}'$, $F_x = -f_x\mathscr{G}'$, $F_y = \mathscr{G}'$. We then use equation (5.1.7) and substitute the above results yielding

$$\frac{\partial\Psi}{\partial s} = \frac{f_t}{(1+f_x^2)^{\frac{1}{2}}} = -\frac{\frac{F_t}{\mathscr{G}'}}{(1+(\frac{F_x}{\mathscr{G}'})^2)^{\frac{1}{2}}} = -\frac{F_t}{(\mathscr{G}'^2+F_x^2)^{\frac{1}{2}}} = -\frac{F_t}{(F_y^2+F_x^2)^{\frac{1}{2}}}. \tag{5.1.8}$$

Therefore we end up with the tidy general equation for $\frac{\partial \Psi}{\partial s}$ in terms of F

$$\frac{\partial \Psi}{\partial s} = -\frac{F_t}{(F_y^2 + F_x^2)^{\frac{1}{2}}}. \tag{5.1.9}$$

5.1.2 Validation

We establish whether equation (5.1.9) works by comparing it in detail with the elliptical-shape case of equation (2.1.14), i.e. with

$$\frac{\partial \Psi}{\partial \theta} = ba'(\sin(\theta))^2 - ab'\cos(\theta) + b'a(\cos(\theta))^2, \tag{5.1.10}$$

and we also use the exact same function to calculate it; hence

$$F(x, y, t) = \frac{x^2}{a^2} + \frac{(y-b)^2}{b^2} - 1, \tag{5.1.11}$$

with $a = a(t)$ and $b = b(t)$ denoting the lengths of the semi major and semi minor axis respectively for the ellipse. Now, differentiating F with respect to t, we have

$$\frac{\partial F}{\partial t} = -\frac{2x^2 a'}{a^3} - \frac{2b'(y-b)}{b^2} - \frac{2b'(y-b)^2}{b^3}, \tag{5.1.12}$$

and similarly, with respect to x and then for y, we obtain

$$\frac{\partial F}{\partial x} = \frac{2x}{a^2} \quad \text{and} \quad \frac{\partial F}{\partial y} = \frac{2(y-b)}{b^2}. \tag{5.1.13}$$

We also use parametric co-ordinates to describe our ellipse with the urethra at the bottom, namely, $\frac{x}{a} = r\sin(\theta)$ and $\frac{y-b}{b} = -r\cos(\theta)$. We substitute these in F_t, F_x and F_y, and we end up with the following equations:

$$\frac{\partial F}{\partial x} = \frac{2r\sin\theta}{a}, \tag{5.1.14}$$

$$\frac{\partial F}{\partial y} = -\frac{2r\sin\theta}{a}, \tag{5.1.15}$$

$$\frac{\partial F}{\partial t} = -\frac{2a'r^2\sin^2\theta}{a} - \frac{2b'r^2\cos^2\theta}{b} + \frac{2b'r\cos\theta}{b}. \tag{5.1.16}$$

Substituting equations (5.1.14)-(5.1.16) into equation (5.1.9), we find after tidying up that

$$\frac{\partial \Psi}{\partial s} = \frac{ba'(\sin(\theta))^2 - ab'\cos(\theta) + b'a(\cos(\theta))^2}{\left(a^2\cos^2\theta + b^2\sin^2\theta\right)^{\frac{1}{2}}}. \tag{5.1.17}$$

Once again, using triangle (a) from Figure 5.1 and of course from Pythagoras's theorem, we know that

$$ds^2 = dx^2 + dy^2. \tag{5.1.18}$$

Switching to parametric and using the same definitions as above for x and y, namely, $\frac{x}{a} = r\sin(\theta)$ and $\frac{y-b}{b} = -r\cos(\theta)$, we then have

$$ds^2 = a^2\left(dr\sin\theta + rd\theta\cos\theta\right)^2 + b^2\left(dr\cos\theta - rd\theta\sin\theta\right)^2. \tag{5.1.19}$$

Since an ellipse has $r = 1$ in the present cases, and hence $dr = 0$, we find after substituting these that

$$ds = d\theta\left(a^2\cos^2\theta + b^2\sin^2\theta\right)^{\frac{1}{2}}. \tag{5.1.20}$$

Replacing ds in equation (5.1.17) with this, we end up with (5.1.10)

$$\frac{\partial \Psi}{\partial \theta} = ba'(\sin(\theta))^2 - ab'\cos(\theta) + b'a(\cos(\theta))^2. \tag{5.1.21}$$

This validates equation (5.1.9).

5.1.3 Construction of Shapes

It is seen that equation (5.1.9) reduces the analytical calculations involved in the boundary condition. It becomes even more noticeable if the shape description is more complicated than a circle or ellipse. Once again, we let our vessel collapse in time using the three-dimensional steady flow equation from [17] but in two spatial dimensions and time: time here replaces the third spatial dimension of [17]. (The feature being recognised here is that the partial collapse spatially to a carina in the setting in [17] is similar to the full collapse in temporal terms to a zero-volume vessel in the present setting.) With the necessary alterations the function that describes the present collapse becomes

$$F_u(x,y,t) = y - \left(1-x^2\right)^{\frac{1}{2}} + \sum_{m=1}^{n} h_m t^2 e^{-8(x-k_m)^2}, \tag{5.1.22}$$

where h_m is the collapsing factor at the $x = k_m$ position of the vessel, of the m out of n movements. This represents the upper half of the function, and we similarly have a lower one given as

$$F_l(x,y,t) = y + \left(1-x^2\right)^{\frac{1}{2}} - \sum_{p=1}^{q} h_p t^2 e^{-8(x-k_p)^2}, \tag{5.1.23}$$

where h_p is the collapsing factor at the $x = k_p$ position for the bladder, of the p out of q movements. Using (5.1.9) and differentiating $F = F_u$ with respect to x, y and t, we derive

$$F_x = \frac{x}{(1-x^2)^{\frac{1}{2}}} - \sum_{m=1}^{n} 16 h_m t^2 (x-k_m) e^{-8(x-k_m)^2}, \tag{5.1.24}$$

$$F_y = 1, \tag{5.1.25}$$

and

$$F_t = \sum_{m=1}^{n} 2h_m t e^{-8(x-k_m)^2}. \tag{5.1.26}$$

Substituting these results in equation (5.1.9), after some manipulation, we obtain

$$\begin{aligned} \frac{\partial \Psi_u}{\partial s} &= -\frac{F_t}{(F_y^2 + F_x^2)^{\frac{1}{2}}} \\ &= -\frac{(1-x^2)^{\frac{1}{2}} \sum_{m=1}^{n} 2h_m t e^{-8(x-k_m)^2}}{\left(1 - 2x(1-x^2)^{\frac{1}{2}}\alpha + (1-x^2)\alpha^2\right)}, \end{aligned} \tag{5.1.27}$$

where $\alpha = \sum_{m=1}^{n} 16h_m t^2 (x-k_m) e^{-8(x-k_m)^2}$. In a similar way, we end up with a corresponding equation for the lower surface

$$\begin{aligned} \frac{\partial \Psi_l}{\partial s} &= -\frac{F_t}{(F_y^2 + F_x^2)^{\frac{1}{2}}} \\ &= \frac{(1-x^2)^{\frac{1}{2}} \sum_{v=1}^{c} 2h_v t e^{-8(x-k_v)^2}}{\left(1 - 2x(1-x^2)^{\frac{1}{2}}\alpha + (1-x^2)\alpha^2\right)}, \end{aligned} \tag{5.1.28}$$

where $\alpha = \sum_{v=1}^{c} 16h_v t^2 (x-k_v) e^{-8(x-k_v)^2}$.

5.1.4 Implementation of the Numerical Scheme

The numerical scheme performed here uses the same five-point modified iterative finite difference method described in Chapter 4. In this case though, the boundary condition is treated by means of equation (5.1.9). More precisely, the method also incorporates the shape construction and hence the boundary conditions used are the ones described in equations (5.1.27) and (5.1.28). We then apply the conditions all around our boundary by means of the length of the element ds between two points. We then

apply Laplace's equation inside the boundary using also our boundary interpolation simultaneously.

We would also like to mention or recap here that the shape of the collapsing vessel of Figure 5.2 is motivated by actual bladders collapsing similarly to those in Figures 1.5 and 1.6. Of course the real-world bladder can take many other shapes during its collapse but often of a similar structure. The numerical scheme can cope with many kinds of bladder collapse and shapes.

This particular example displayed in Figure 5.2 uses five collapsing factors for the upper structure of equation (5.1.22) and three for the lower structure displayed in equation (5.1.23). Hence, we place the collapsing effect at $x = 0$ (i.e. $k_1 = 0$) with a collapsing factor $h_1 = 1.3$, similarly, we have $k_2 = -k_3 = 0.4$ with a collapsing factor $h_2 = h_3 = 1.2$ and finally $k_4 = -k_5 = 0.9$ with a collapsing factor $h_4 = h_5 = 1.1$. In the same manner the lower half of the vessel is constructed. A collapsing effect is placed at $x = 0$ (i.e. $k_1 = 0$) with a collapsing factor $h_1 = 0.01$. Also, we have $k_2 = -k_3 = 0.75$ with a collapsing factor of $v_2 = v_3 = -0.1$. The same structure is also used in Chapter 6 for the same case but in an axisymmetric configuration.

5.2 Results

The results plotted in Figure 5.3 have many interesting features. First of all, it is important to repeat that these sorts of shapes are what is expected for a real-world collapsing bladder. These can be compared quite favourably with the cystourethrograms

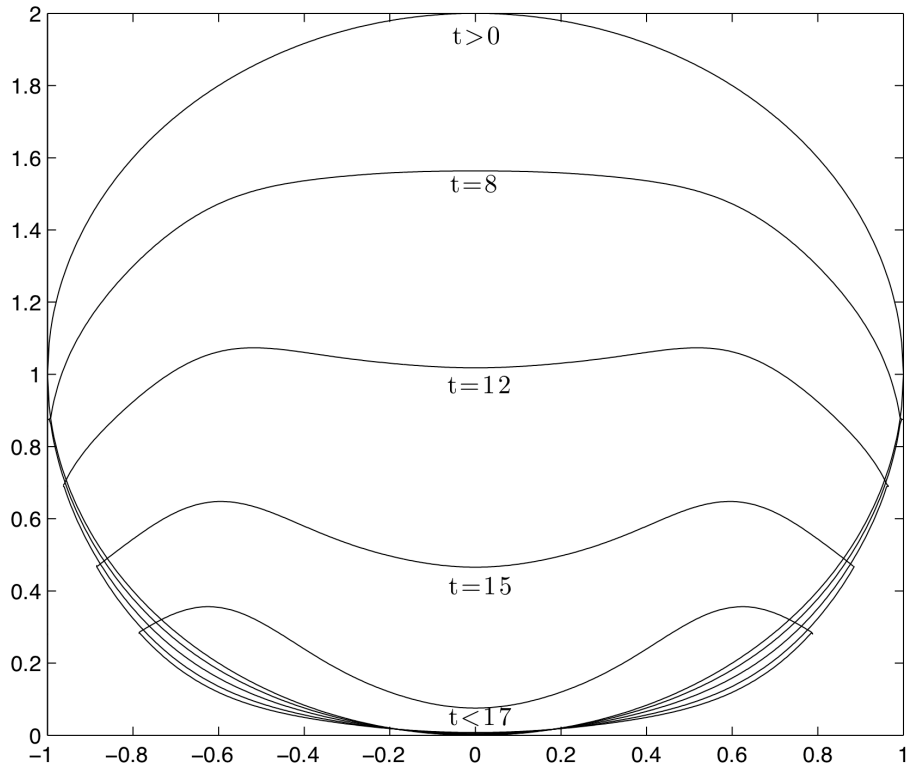

Figure 5.2: Shapes that the vessel takes at different times as it collapses with a cardioidal-like shape, in the model of section 5.1. Horizontal x, vertical y.

described in the introduction and shown in Figures 1.5 and 1.6. The shape the collapse takes here is perhaps a candidate to be taken into consideration for possible transplants of the bladder. It seems that most of the squeeze velocity is vertical from those scans. This is seen from the fact that the bladder starts off as a sphere and turns into an elliptical or thin cardioidal vessel as it collapses, making minimum movement from the sides. Contrary to Figure 4.12 where the vessel opens outwards and its horizontal

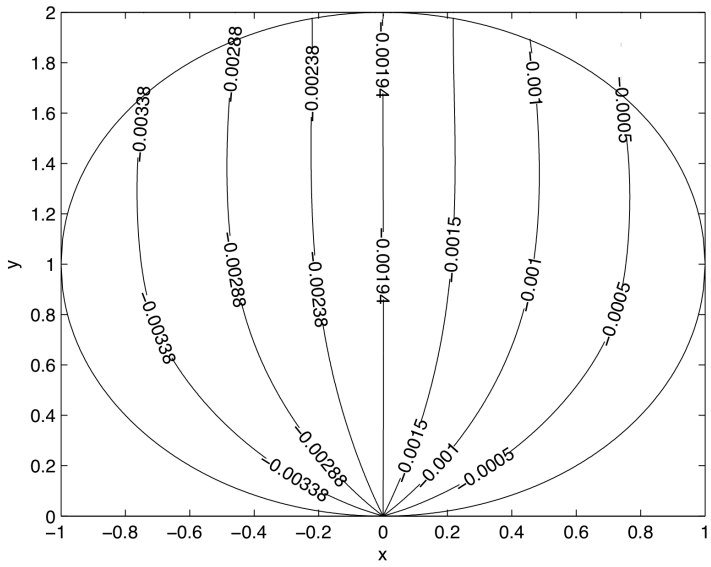
x
y
-0.00338
-0.00288
-0.00238
-0.00194
-0.0015
-0.001
-0.0005

(a)

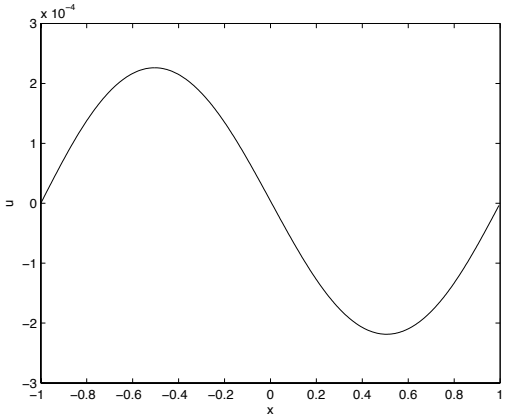
x 10^-4
u
x

(b)

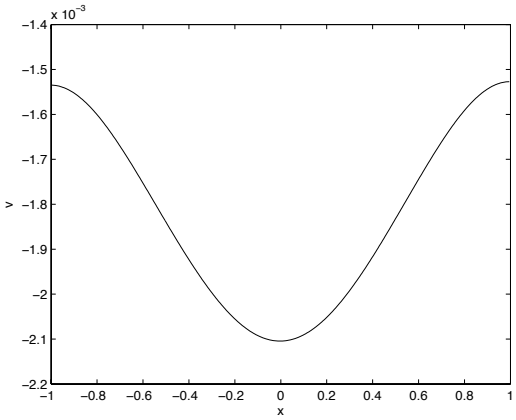
x 10^-3
v
x

(c)

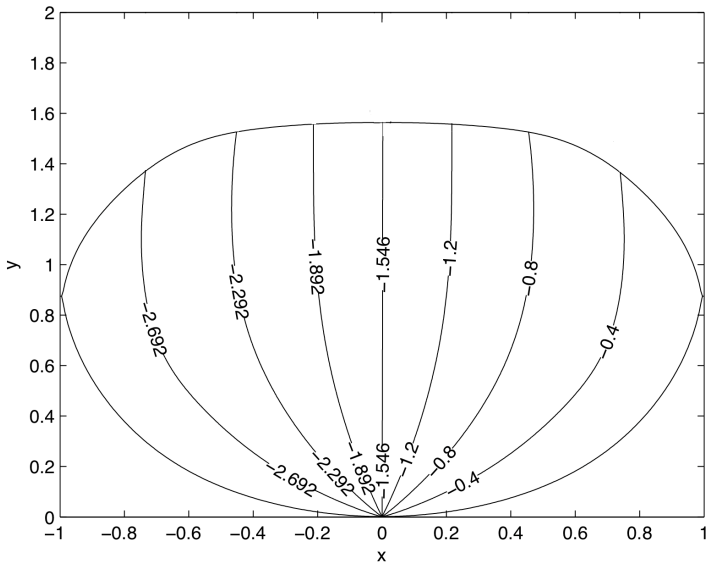
2
1.8
1.6
1.4
1.2
1
0.8
0.6
0.4
0.2
0
y
−1
−0.8
−0.6
−0.4
−0.2
0
0.2
0.4
0.6
0.8
1
x
2.692
2.292
1.892
1.546
1.2
0.8
0.4

(d)

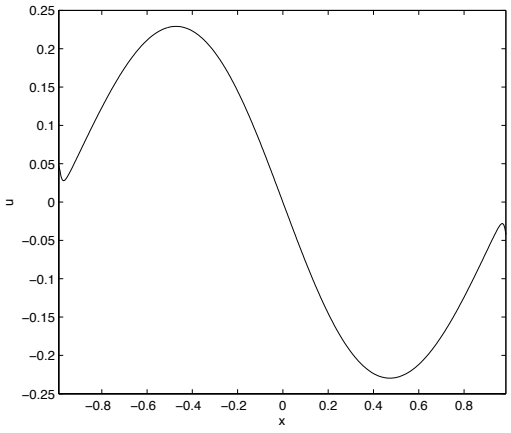
0.25
0.2
0.15
0.1
0.05
0
−0.05
−0.1
−0.15
−0.2
−0.25
u
−0.8
−0.6
−0.4
−0.2
0
0.2
0.4
0.6
0.8
x

(e)

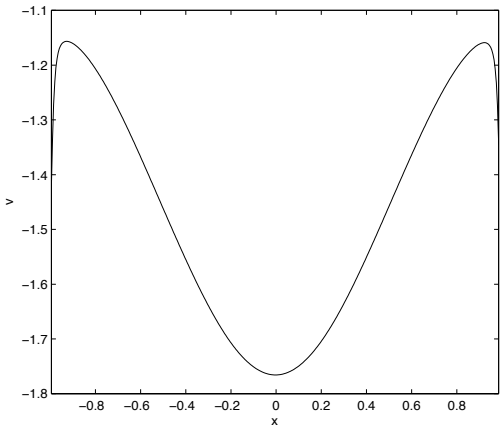
−1.1
−1.2
−1.3
−1.4
−1.5
−1.6
−1.7
−1.8
v
−0.8
−0.6
−0.4
−0.2
0
0.2
0.4
0.6
0.8
x

(f)

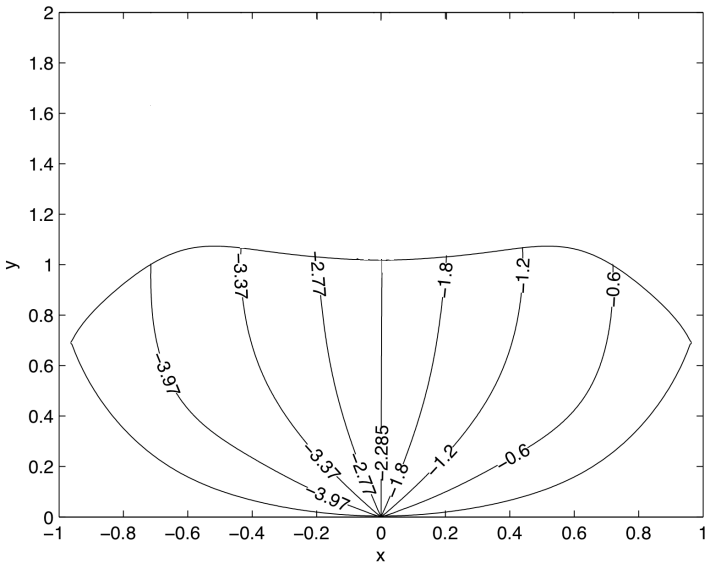

(g)

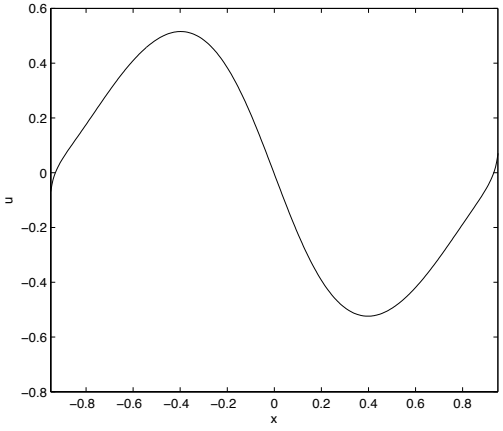

(h)

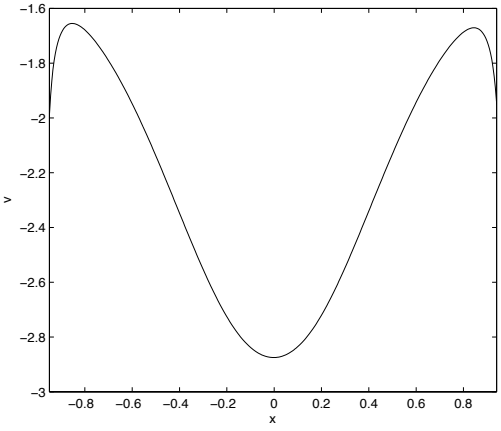

(i)

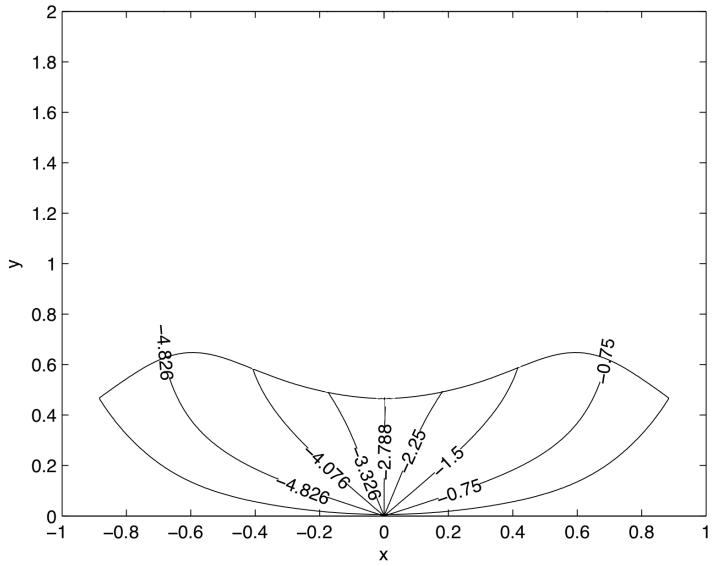

(j)

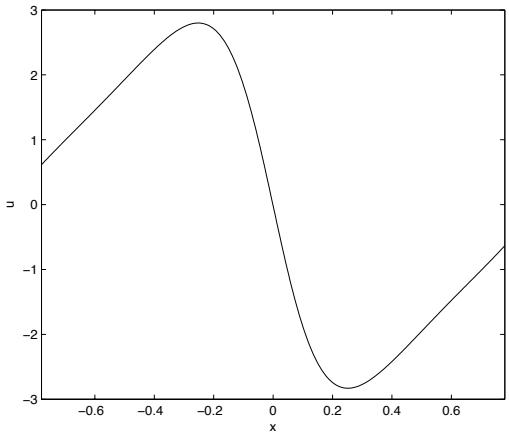

(k)

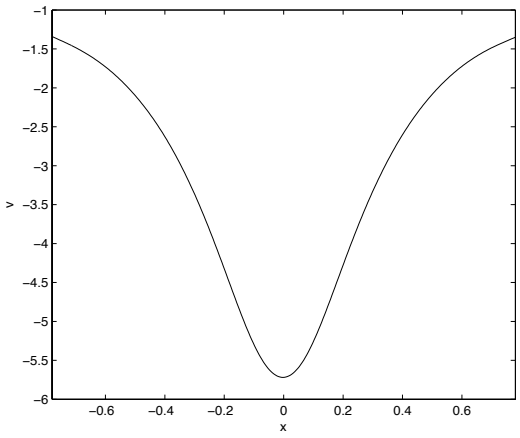

(l)

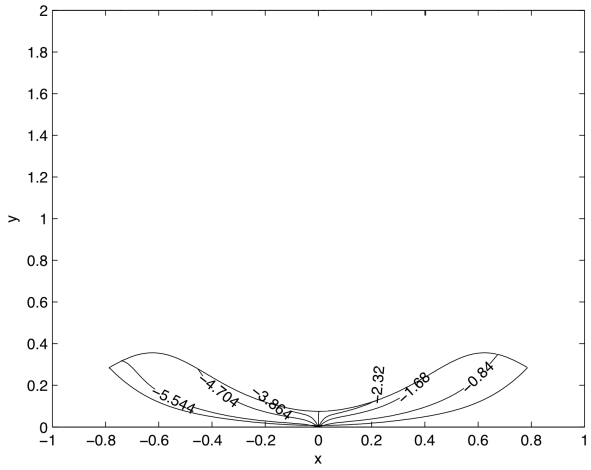

(m)

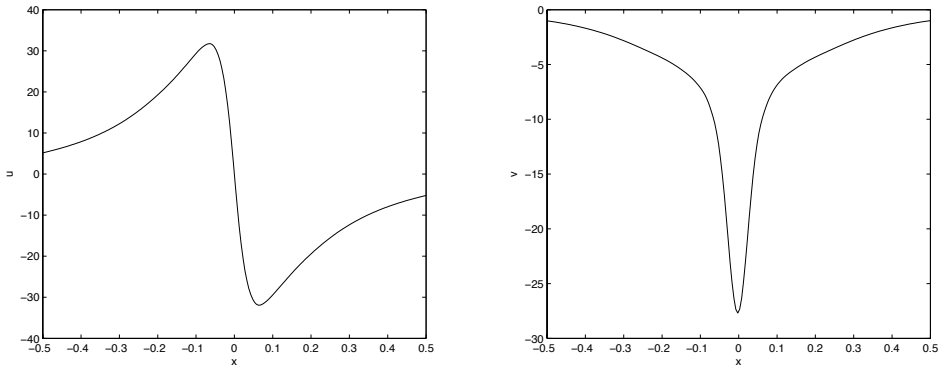

(n) (o)

Figure 5.3: Contour plots of the fluid motion within the modeled collapsing vessel. Also plotted are the horizontal and vertical velocity along the horizontal centreline. Times for the parts are 0.01 - just after the start of micturition - (contour plot (a), horizontal velocity (b) and vertical velocity (c)), then 8((d)-(f)), 12((g)-(i)), 15((j)-(l)) and 16.8 - just before the end of micturition - ((m)-(o)) respectively.

length increases, the vessel shapes from Figure 5.2 have reduction (squeeze) in horizontal length (size). This is what is expected from a normal bladder during micturition as described in the introduction. It is also useful here to notice and compare the thin case (streamlines and velocities) during the end of the collapse. As we see in Figure 4.13 (p)-(r), the horizontal and vertical velocity away from the urethra has a near zero velocity. This can be potentially risky, causing high urine volumes to remain in the bladder and can have negative effects or cause problems in the bladder. The shape and collapse of Figure 5.3 (m)-(o), which is more realistic, shows a non-zero velocity value on the sides and the areas away from the urethra in general, thus avoiding this slow movement and potential problems. Thus, the shape the vessel takes during its collapse is seen to substantially affect the flow. Possible changes in the shapes, such as the one in Figure 4.13, can cause problems including stagnant regions or even eddies, and therefore have medical implications on the bladder. In chapters 2 and 4 and more precisely in Figure 2.3 we addressed the analytical shape where the circular vessel collapses proportionally from all sides and finishes as a very small circle during its full collapse. In contrast, we now have quite a different case as we can see with Figure 5.3 and this is more similar to the human bladder collapse in general. In particular, we can see in Figure 5.3 (b) that at the start of micturition the horizontal velocity at the sides is effectively zero.

It is also appropriate to mention here that the streamfunction is time dependent as is seen in equations (5.1.27) and (5.1.28). All the plots of the horizontal velocity along the centre line in Figure 5.3 are odd about $x = 0$ and similarly the vertical velocity of the centre line is even about $x = 0$. The horizontal velocity is zero along $x = 0$. This makes physical sense as the urethra is right underneath in a sense and the velocity

is mainly vertical at that point close to the axis $x = 0$. We can also see that as the vessel collapses and becomes thinner, the horizontal velocity appears to approach the earlier thin-vessel analysis results. This becomes obvious in Figure 5.3 (k) near the range $-0.3 \leq x \leq 0.3$ and even more in Figure 5.3 (n) where the velocity (horizontal) has its Laplace/Euler region in the range near $-0.08 \leq x \leq 0.08$ in effect. Therefore, Figures 5.3 (n) and (o) (near the range $-0.08 \leq x \leq 0.08$) resemble those from the Euler/Laplace analysis seen in Figure 2.15 (c), (d). This is encouraging even though the shape of this vessel is different. Away from these regions the thin horizontal analysis of section 2.2.1 applies. Also, in Figure 5.3 (e) we can see a small feature near the wall which is attributed to the definition of the shape (the separation of the upper and the lower half). A similar comment can be made about the vertical velocity as we can see in Figure 5.3 (f) and (i). Even though in the horizontal velocity case (Figure 5.3 (e)) it is not a large effect, the vertical velocity cases (Figure 5.3 (f) and (i)) seem to have a larger effect which is most probably affected by the general collapse and shape rather than what is specifically happening at that point. The largest velocity is at the $x = 0$ axis in all case. Finally, if we see the vertical velocity values of Figure 5.3 (o), we see the very high values that occur near the urethra.

5.3 Summary

The treatment of the kinematic boundary condition here means that we can now tackle the whole numerical task in a more efficient way. The combination of it with the shape construction means that a substantial number of shapes can be tackled now with

minimal effort in principle. The demonstration in Figure 5.3 is just for one possible shape that the numerical scheme can tackle. Non-symmetrical shapes can also be covered in the same way as the symmetric example in Figure 5.3.

Chapter 6

Numerical Solutions for Axisymmetric Shapes

The natural progression of the current work is to tackle numerically axisymmetric shapes. Obviously, the analytical model described in chapter 3 was fairly simple both in terms of the shape and also the fact that it was axisymmetric. It is nonetheless a step forward. The modified iterative finite difference numerical scheme that we have also described earlier in chapters 4 and 5 tackles two dimensions but is capable of being extended readily to the axisymmetric behaviour of current concern. This tends to confirm that the method is very flexible especially compared with other methods such as conformal mapping which is confined to two-dimensional problems. The simplicity of the present model as well as the methodology makes it capable of adapting to all sorts of vessel shapes. This is very important when we are dealing with a substantially

distorting vessel such as the bladder.

6.1 Numerical Solution for Axisymmetric Sphere

We now aim to first tackle numerically the axisymmetric sphere. This will be a good check for the altered numerical method that aims at tackling axisymmetric shapes for our vessels. A stream function can be defined for axisymmetric flows because the continuity equation reduces to two terms only. When working in axisymmetric coordinates, it is always convenient to move back and forth from spherical coordinates to cylindrical and vice versa. In order to keep the present account as clear as possible, we will keep for spherical coordinates the same notation that was used in chapter 3 (r, θ), and use for cylindrical coordinates the notation (R, z) with R being the horizontal coordinate (radius) and z the vertical (distance up the axis).

The continuity equation in cylindrical coordinates can be written as

$$\frac{\partial}{\partial R}(Ru_R) + \frac{\partial}{\partial z}(Ru_z) = 0, \tag{6.1.1}$$

yielding

$$u_R = -\frac{1}{R}\frac{\partial \Psi}{\partial z}, \quad u_z = \frac{1}{R}\frac{\partial \Psi}{\partial R}. \tag{6.1.2}$$

The axisymmetric stream function has units m^3/s in contrast to the stream function for plane flow which has units m^2/s. In addition, since our flow is also irrotational,

$$\frac{\partial u_R}{\partial z} - \frac{\partial u_z}{\partial R} = 0. \tag{6.1.3}$$

Now, substituting (6.1.2) into (6.1.3), we obtain

$$\frac{\partial^2 \Psi}{\partial R^2} - \frac{1}{R}\frac{\partial \Psi}{\partial R} + \frac{\partial^2 \Psi}{\partial z^2} = 0, \tag{6.1.4}$$

or $E^2\Psi = 0$, as it is sometimes known where $E^2 = \frac{\partial^2}{\partial R^2} - \frac{1}{R}\frac{\partial}{\partial R} + \frac{\partial^2}{\partial z^2} = 0$. This is different from the Laplace equation, $\nabla^2\Phi = 0$, satisfied by the velocity potential.

6.1.1 Numerical Scheme using Finite Difference Method

As with Laplace's equation in two dimensions, so it goes with equation (6.1.4). Once again, we approximate the equation (in this case (6.1.4)) into a set of linear simultaneous equations and write them in matrix notation. A standard iterative approach is used to solve the problem. We proceed in the exact same way as before and we retain the definition of our stencil as in Figure 6.1. Moreover, we use the standard iterative finite difference results for the R-direction, namely,

$$\frac{\partial^2 \psi_{(i,j)}}{\partial R^2} = \frac{\psi_{(i+1,j)} - 2\psi_{(i,j)} + \psi_{(i-1,j)}}{h^2} + O(h^2). \tag{6.1.5}$$

Now for the vertical or z-direction we have

$$\frac{\partial^2 \psi_{(i,j)}}{\partial z^2} = \frac{\psi_{(i,j+1)} - 2\psi_{(i,j)} + \psi_{(i,j-1)}}{h^2} + O(h^2), \tag{6.1.6}$$

and also

$$\frac{\partial \psi_{(i,j)}}{\partial R} = \frac{\psi_{(i+1,j)} - \psi_{(i-1,j)}}{2h} + O(h^2). \tag{6.1.7}$$

Superimposing both the R and z directions and substituting (6.1.5), (6.1.6), (6.1.7) in

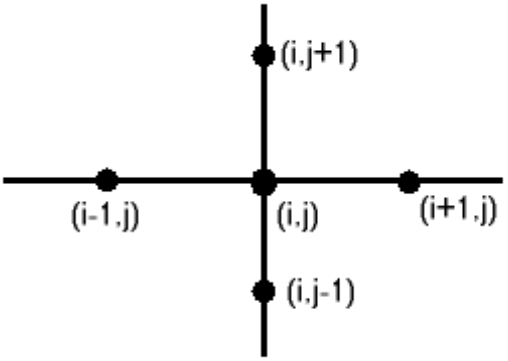

Figure 6.1: Example of 5-point stencil on our grid.

(6.1.4) after tidying up, we have

$$E^2\psi = 2R\left(-4\psi_{(i,j)} + \psi_{(i,j-1)} + \psi_{(i,j+1)} + \psi_{(i+1,j)} + \psi_{(i-1,j)}\right) + h\left(\psi_{(i-1,j)} - \psi_{(i+1,j)}\right) = 0. \tag{6.1.8}$$

Upon rearranging we obtain the following iterative formula

$$\psi_{(i,j)} = \frac{1}{4}\left(\psi_{(i+1,j)} + \psi_{(i-1,j)} + \psi_{(i,j+1)} + \psi_{(i,j-1)}\right) + \frac{h}{8R}\left(\psi_{(i-1,j)} - \psi_{(i+1,j)}\right), \tag{6.1.9}$$

which is the resulting iterative equation for calculating the stream function at any point inside our vessel. The method is then as in the two-dimensional case in the sense that a shape is defined on our grid. We define the boundary conditions using an in -or out-sense (see section 6.1.2) and/or interpolation as before and we let the code calculate the flow inside the vessel or approximated vessel.

Similarly to section 4.2.3, we use successive over-relaxation to accelerate the method. The overall process is as described in section 4.2.3.

6.1.2 Boundary Interpolation

Similarly to section 4.2.4, we briefly describe here this non-standard aspect of the numerical scheme. Since accuracy on the boundary is very important due to the complexity of the shapes, we adhere to the scheme of chapter 4. The boundary is where most of the error is and we therefore aim to reduce that. In order to minimise the error, we embed into our code a boundary interpolation. The interpolation is done by relatively accurate means at the boundary.

In Figure 6.2 which shows an elliptical vessel in a grid, we can clearly see that most of those nodes that are just inside the boundary have part of their stencil outside the boundary but still within the total grid. Now, since we are only interested in solution values inside and on the boundary and not outside, this feature needs to be tackled. Boundary interpolation is adopted. The general formula for the nodes described and shown in Figure 6.2 satisfies the following equation

$$\begin{aligned}\left(\frac{2}{h_{i+1}h_{i-1}}+\frac{(h_{i-1}-h_{i+1})}{r_{i,j}h_{i+1}h_{i-1}}+\frac{2}{h_{j+1}h_{j-1}}\right)\Psi(i,j)= \\ \frac{2\Psi_{j+1}}{h_{j+1}(h_{j+1}+h_{j-1})}+\frac{2\Psi_{i+1}}{h_{i+1}(h_{i+1}+h_{i-1})} \\ +\frac{2\Psi_{j-1}}{h_{j-1}(h_{j-1}+h_{j+1})}+\frac{2\Psi_{i-1}}{h_{i-1}(h_{i-1}+h_{i+1})} \\ +\frac{h_{i-1}\Psi_{i+1}}{r_{i,j}h_{i+1}(h_{i+1}+h_{i-1})}-\frac{h_{i+1}\Psi_{i-1}}{r_{i,j}h_{i-1}(h_{i-1}+h_{i+1})},\end{aligned} \quad (6.1.10)$$

with h_{i+1}, h_{i-1}, h_{j+1}, h_{j-1} denoting the distances between the nodes. Each of these distances can have a value of either h or smaller depending on the boundary and as depicted in Figure 6.2. In addition $r_{i,j}$ is the value of R at point (i,j).

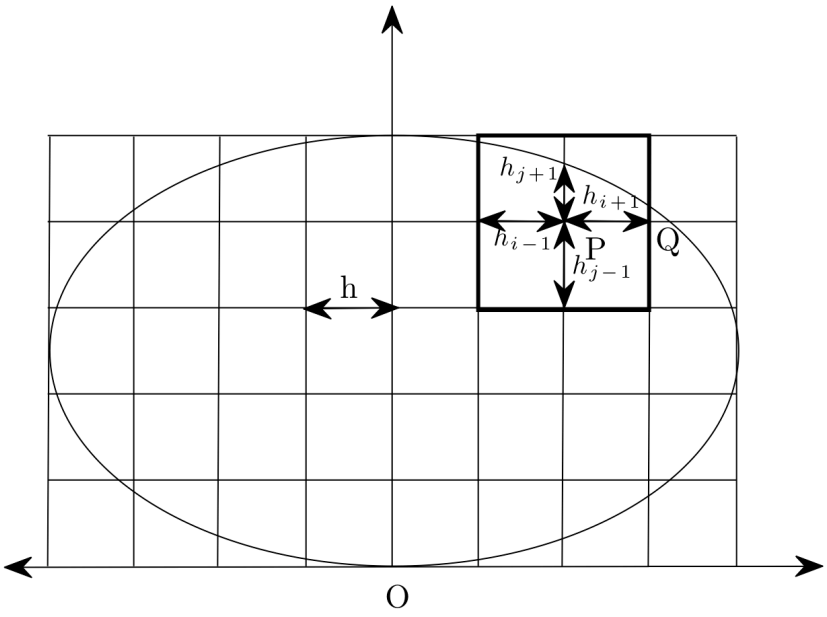

Figure 6.2: Example of a possible elliptical boundary within our grid. The nodes are generally separated by a distance h. Near the boundary though this is not always the case. As you can see in the figure, $h_{i+1} = h_{i-1} = h_{j-1} = h$. This is not the case with h_{j+1} which is smaller. We therefore employ formula (6.1.10) for this point P. In the case of the point Q on its right, we have two points which are smaller than h. The formula (6.1.10) tackles this case as well. Horizontal R(t), vertical z(t).

Once again, it is possible to have one or two or even three points of our stencil outside the grid. Hence, depending on the positioning of the stencil inside the shape, different points of the stencil will be outside and hence the above formula will vary accordingly.

For the case where we have one point of the stencil outside the shape, and more specif-

ically the point $(i+1, j)$ outside, the iterative equation is as follows:

$$\Psi_0 = \frac{r_{i,j}h^2 D_{i+1}}{2r_{i,j}(D_{i+1}+h)+h(D_{i+1}-h)} \left(\frac{(2r_{i,j}-h)}{r_{i,j}D_{i+1}(D_{i+1}+h)}\Psi_B + \frac{1}{h^2}\Psi_{j-1} + \frac{(2r_{i,j}+D_{i+1})}{r_{i,j}h(D_{i+1}+h)}\Psi_{i-1} + \frac{1}{h^2}\Psi_{j+1}\right), \quad (6.1.11)$$

where h is the distance between stencil points, D_{i+1} the new distance between Ψ_0 and the boundary in the $(i+1)$ direction, and Ψ_B the value of Ψ on the boundary. Similarly, for the other three directions, we derive the following three equations. For the bottom one we have

$$\Psi_0 = \frac{h^2 D_{j-1}}{2(D_{j-1}+h)} \left(\frac{(2r_{i,j}-h)}{2r_{i,j}h^2}\Psi_{i+1} + \frac{2}{D_{j-1}(D_{j-1}+h)}\Psi_B + \frac{(2r_{i,j}+h)}{2r_{i,j}h^2}\Psi_{i-1} + \frac{2}{h(D_{j-1}+h)}\Psi_{j+1}\right); \quad (6.1.12)$$

for the left one we have

$$\Psi_0 = \frac{r_{i,j}h^2 D_{i-1}}{2r_{i,j}(D_{i-1}+h)-h(D_{i-1}-h)} \left(\frac{(2r_{i,j}-D_{i-1})}{r_{i,j}h(D_{i-1}+h)}\Psi_{j+1} + \frac{1}{h^2}\Psi_{j-1} + \frac{(2r_{i,j}+h)}{r_{i,j}D_{i-1}(D_{i-1}+h)}\Psi_B + \frac{1}{h^2}\Psi_{j+1}\right); \quad (6.1.13)$$

and for the right one

$$\Psi_0 = \frac{h^2 D_{j+1}}{2(D_{j+1}+h)} \left(\frac{(2r_{i,j}-h)}{2r_{i,j}h^2}\Psi_{i+1} + \frac{2}{h(D_{j+1}+h)}\Psi_{j-1} + \frac{(2r_{i,j}+h)}{2r_{i,j}h^2}\Psi_{i-1} + \frac{2}{D_{j+1}(D_{j+1}+h)}\Psi_B\right); \quad (6.1.14)$$

is the appropriate iterative form. Similarly, for the case where we have two points of the stencil outside our shape, and more specifically $(i+1, j)$ and $(i, j-1)$, the iterative equation is as follows:

$$\Psi_0 = \frac{r_{i,j} D_{i+1} D_{j-1} h}{2r_{i,j}(D_{i+1} + D_{j-1}) + D_{j-1}(D_{i+1} - h)} \left(\frac{(2r_{i,j} - h)}{r_{i,j} D_{i+1}(D_{i+1} + h)} \Psi_B + \frac{2}{D_{j-1}(D_{j-1} + h)} \Psi_B + \frac{(2r_{i,j} + D_{i+1})}{r_{i,j} h (D_{i+1} + h)} \Psi_{i-1} + \frac{2}{h(D_{j-1} + h)} \Psi_{j+1} \right), \quad (6.1.15)$$

where the notation is, as in the previous case of one stencil point, outside the shape. In a similar way, there are three more cases with two points of the stencil outside the shape. For the case where the points $(i-1, j)$ and $(i, j-1)$ are outside the stencil, we have

$$\Psi_0 = \frac{r_{i,j} D_{j-1} D_{i-1} h}{2r_{i,j}(D_{j-1} + D_{i-1}) - D_{j-1}(D_{i-1} - h)} \left(\frac{(2r_{i,j} - D_{i-1})}{r_{i,j} h (D_{i-1} + h)} \Psi_{i+1} + \frac{2}{D_{j-1}(D_{j-1} + h)} \Psi_B + \frac{(2r_{i,j} + h)}{r_{i,j} D_{i-1}(D_{i-1} + h)} \Psi_B + \frac{2}{h(D_{j-1} + h)} \Psi_{j+1} \right); \quad (6.1.16)$$

for $(i, j+1)$ and $(i-1, j)$ we have

$$\Psi_0 = \frac{r_{i,j} D_{i-1} D_{j+1} h}{2r_{i,j}(D_{i-1} + D_{j+1}) - D_{j+1}(D_{i-1} - h)} \left(\frac{(2r_{i,j} - D_{i-1})}{r_{i,j} h (D_{i-1} + h)} \Psi_{i+1} + \frac{2}{h(D_{j+1} + h)} \Psi_{j-1} + \frac{(2r_{i,j} + h)}{r_{i,j} D_{i-1}(D_{i-1} + h)} \Psi_B + \frac{2}{D_{j+1}(D_{j+1} + h)} \Psi_B \right); \quad (6.1.17)$$

and finally for $(i+1,j)$ and $(i,j+1)$

$$\Psi_0 = \frac{r_{i,j}D_{j+1}D_{i+1}h}{2r_{i,j}(D_{j+1}+D_{i+1})+D_{j+1}(D_{i+1}-h)} \left(\frac{(2r_{i,j}-h)}{r_{i,j}D_{i+1}(D_{i+1}+h)}\Psi_B + \frac{2}{h(D_{j+1}+h)}\Psi_{j-1} + \frac{(2r_{i,j}+D_{i+1})}{r_{i,j}h(D_{i+1}+h)}\Psi_{i-1} + \frac{2}{D_{j+1}(D_{j+1}+h)}\Psi_B\right), \quad (6.1.18)$$

following the same pattern. There is also the case where we have three points outside the vessel shape. In the event that $(i+1,j)$, $(i,j-1)$ and $(i,j+1)$ are outside

$$\Psi_0 = \frac{r_{i,j}D_{j+1}D_{i+1}hD_{j-1}}{2r_{i,j}D_{j+1}D_{j-1}+(h-D_{i+1})D_{j+1}D_{j-1}+2r_{i,j}D_{i+1}h)} \left(\frac{2\Psi_B}{D_{j+1}(D_{j+1}+D_{j-1})} + \frac{2\Psi_B}{D_{i+1}(D_{i+1}+h)} + \frac{2\Psi_B}{D_{j-1}(D_{j-1}+D_{j+1})} + \frac{2\Psi_{i-1}}{h(h+D_{i+1})} + \frac{h\Psi_B}{r_{i,j}D_{i+1}(D_{i+1}+h)} - \frac{D_{i+1}\Psi_{i-1}}{r_{i,j}h(h+D_{i+1})}\right), \quad (6.1.19)$$

for $(i,j-1)$, $(i-1,j)$ and $(i+1,j)$ we have

$$\Psi_0 = \frac{r_{i,j}D_{i-1}D_{i+1}hD_{j-1}}{2r_{i,j}hD_{j-1}+(D_{i-1}-D_{i+1})hD_{j-1}+2r_{i,j}D_{i-1}D_{i+1})} \left(\frac{2\Psi_{j+1}}{h(h+D_{j-1})} + \frac{2\Psi_B}{D_{i+1}(D_{i+1}+D_{i-1})} + \frac{2\Psi_B}{D_{j-1}(D_{j-1}+h)} + \frac{2\Psi_B}{D_{i-1}(D_{i-1}+D_{i+1})} + \frac{D_{i-1}\Psi_B}{r_{i,j}D_{i+1}(D_{i+1}+D_{i-1})} - \frac{D_{i+1}\Psi_B}{r_{i,j}D_{i-1}(D_{i-1}+D_{i+1})}\right), \quad (6.1.20)$$

for $(i,j-1)$, $(i-1,j)$ and $(i,j+1)$ we have

$$\Psi_0 = \frac{r_{i,j}D_{j+1}D_{i-1}hD_{j-1}}{2r_{i,j}D_{j+1}D_{j-1}+(D_{i-1}-h)D_{j+1}D_{j-1}+2r_{i,j}D_{i-1}h)} \left(\frac{2\Psi_B}{D_{j+1}(D_{j+1}+D_{j-1})} + \frac{2\Psi_{i+1}}{h(D_{i-1}+h)} + \frac{2\Psi_B}{D_{j-1}(D_{j-1}+D_{j+1})} + \frac{2\Psi_B}{D_{i-1}(h+D_{i-1})} + \frac{D_{i-1}\Psi_{i+1}}{r_{i,j}h(D_{i-1}+h)} - \frac{h\Psi_B}{r_{i,j}D_{i-1}(h+D_{i-1})}\right), \quad (6.1.21)$$

and for $(i-1,j)$, $(i+1,j)$ and $(i,j+1)$ we have

$$\Psi_0 = \frac{r_{i,j}D_{i-1}D_{i+1}hD_{j+1}}{2r_{i,j}hD_{j+1}+(D_{i-1}-D_{i+1})hD_{j+1}+2r_{i,j}D_{i-1}D_{i+1})} \left(\frac{2\Psi_B}{D_{j+1}(h+D_{j+1})}+\frac{2\Psi_B}{D_{i+1}(D_{i+1}+D_{i-1})}+\frac{2\Psi_{j-1}}{h(D_{j+1}+h)} + \frac{2\Psi_B}{D_{i-1}(D_{i-1}+D_{i+1})}+\frac{D_{i-1}\Psi_B}{r_{i,j}D_{i+1}(D_{i+1}+D_{i-1})}-\frac{D_{i+1}\Psi_B}{r_{i,j}D_{i-1}(D_{i-1}+D_{i+1})}\right). \quad (6.1.22)$$

As with the two dimensional case, equation (6.1.10) and the twelve conditions that are derived from it and have been employed (equations (6.1.11)-(6.1.22)) make the numerical scheme more memory intensive than without them, but a lot more accurate around the boundary.

6.1.3 Numerical Results

We now apply the numerical scheme described in sections 6.1.1 and 6.1.2. The aim is to develop a numerical scheme capable of examining numerical solutions for many different shapes and different rates of collapse of the vessel.

For the sphere, in particular, we will use the boundary condition for a spherical vessel with a sink at its lowest point. This can be worked out by letting $r = a$ in equation (3.1.18), then Ψ on the boundary of our axisymmetric sphere satisfies

$$\Psi_{r=a} = a^2V(1+\cos\theta) - \frac{a^2V}{2}\sin^2\theta. \quad (6.1.23)$$

For simplicity we let $V = 1$ and also use a circle of radius one, hence $a = 1$. We therefore have the boundary condition

$$\Psi_{r=a} = (1+\cos\theta) - \frac{1}{2}\sin^2\theta. \quad (6.1.24)$$

This equation will be used to test the validity of our Cartesian-based code in the present axisymmetric setting. We will use this as the boundary condition for our numerical scheme to see if the analytical result is reproduced. It is known from Butler's theorem in chapter 3, and more specifically equation (3.1.18), that the analytical solution with this condition at any point inside the vessel is

$$\Psi = r\left(1+\cos\theta\right) + \left(1 + \frac{\frac{1}{r}+\cos\theta}{\left(\frac{1}{r^2}+\frac{2}{r}\cos\theta+1\right)^{\frac{1}{2}}}\right) - r\left(1+\frac{r+\cos\theta}{\left(r^2+2r\cos\theta+1\right)^{\frac{1}{2}}}\right) - \frac{r^2}{2}\sin^2\theta, \qquad 0<\theta<2\pi \;\&\; 0<r<1. \quad (6.1.25)$$

Once again, for simplicity, we let $a = 1$ and also $V = 1$. In addition, r and θ are as defined previously in this thesis.

Plotting the results of both the numerical and the analytical approaches, we obtain the results of Figure 6.3. It can be seen that both the plots look very similar and they are in fact virtually identical proving the accuracy of the computational method. The grid used here is a 128x128. We also demonstrate in Figure 6.4 the efficiency of the code through more coarse grids. As we increase the grid points though, the code becomes even more efficient especially at the urethral point. We see that even with the 4x4 grid, most of the flow in the vessel is captured.

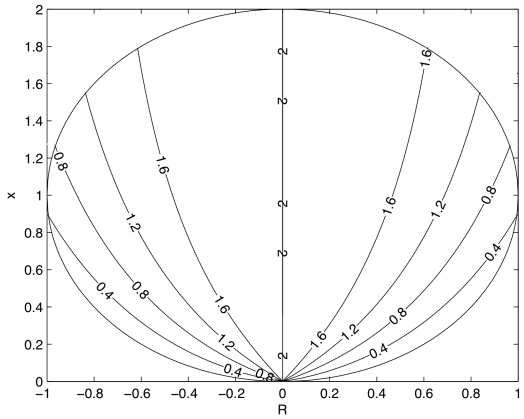

(a)

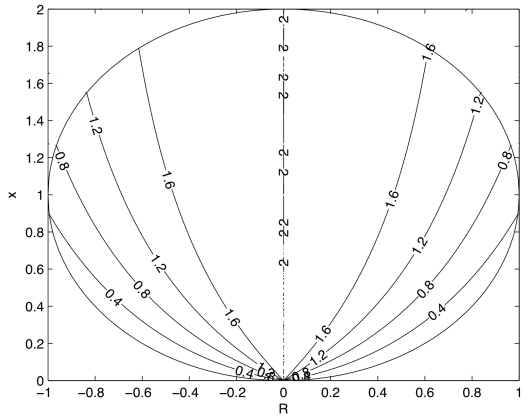

(b)

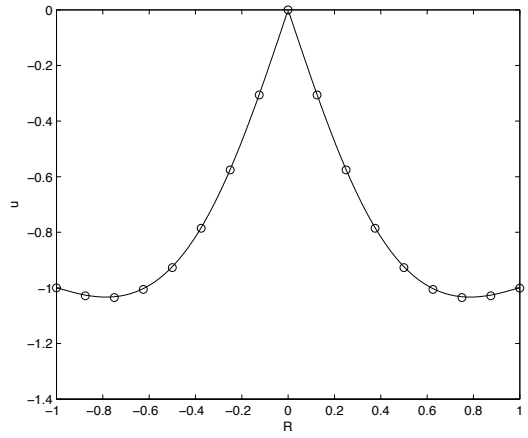

(c)

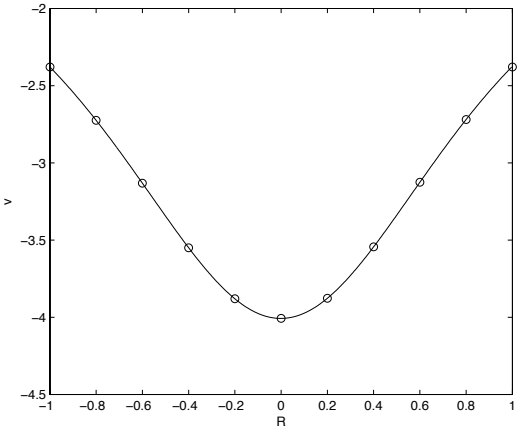

(d)

Figure 6.3: Contour plot of exact streamfunction values (a) and numerical values (b) for the sphere using the boundary condition $\Psi = (1 + \cos\theta) - \frac{1}{2}\sin^2\theta$. Also plotted are the horizontal (c) and vertical (d) velocity along the horizontal centreline.

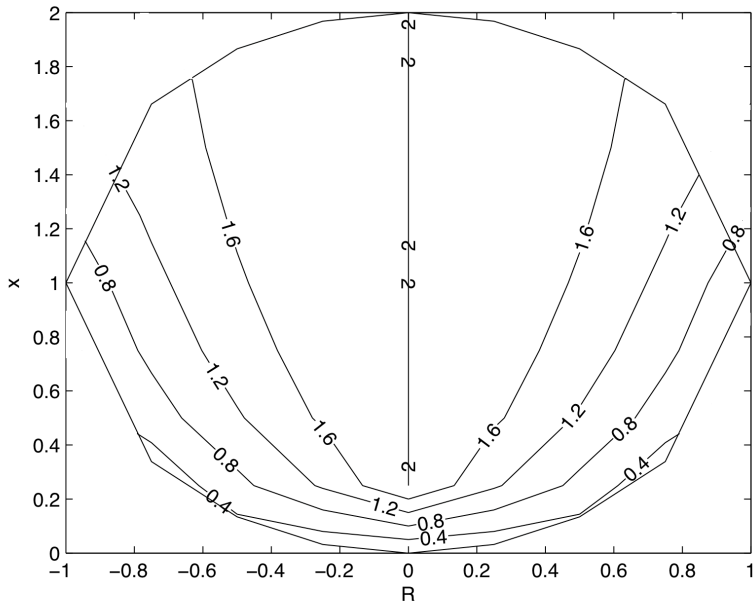

(a)

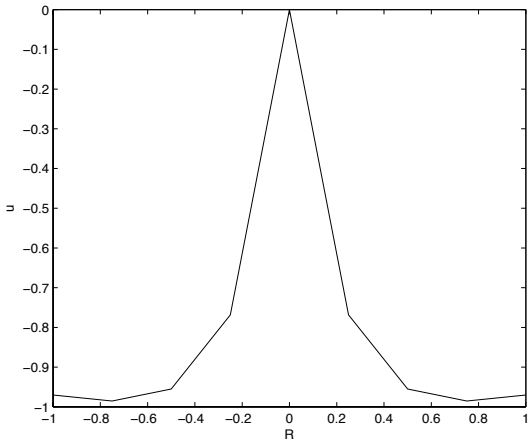

(b)

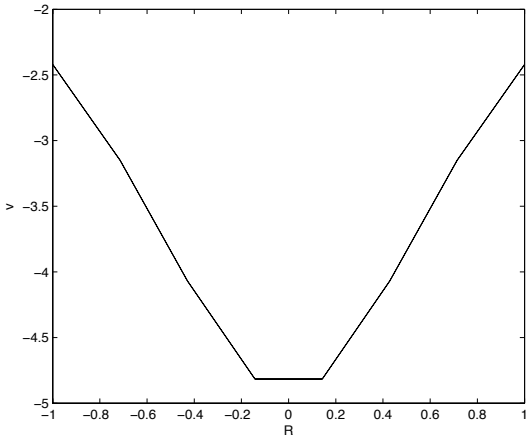

(c)

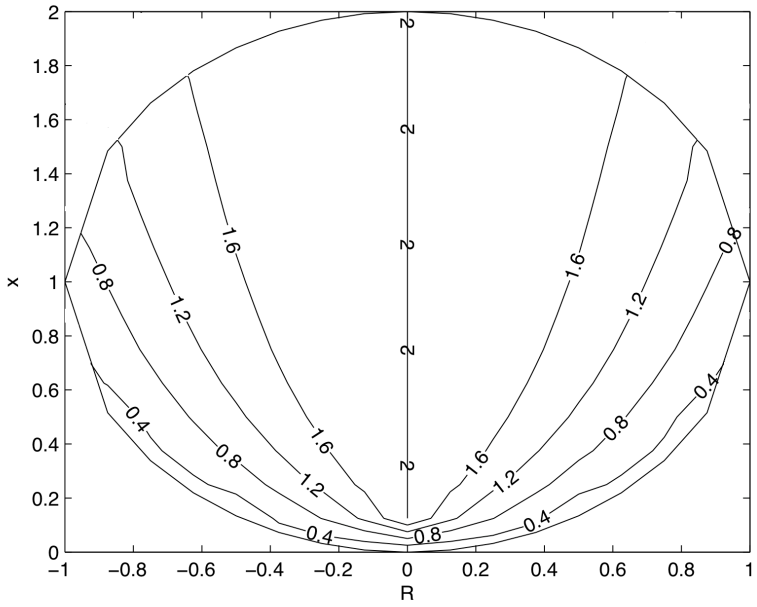
x
R
2
1.8
1.6
1.4
1.2
1
0.8
0.6
0.4
0.2
0
−1
−0.8
−0.6
−0.4
−0.2
0
0.2
0.4
0.6
0.8
1
0.4
0.8
1.2
1.6
2

(d)

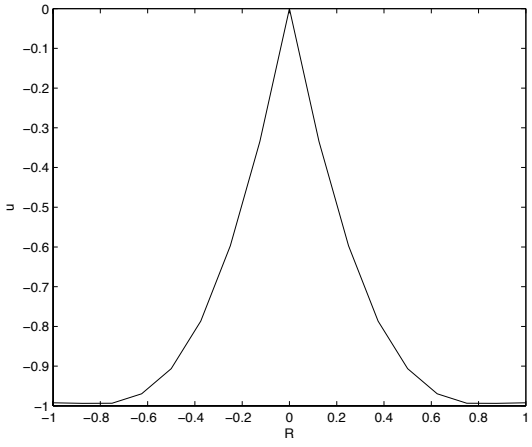
u
R
0
−0.1
−0.2
−0.3
−0.4
−0.5
−0.6
−0.7
−0.8
−0.9
−1
−1
−0.8
−0.6
−0.4
−0.2
0
0.2
0.4
0.6
0.8
1

(e)

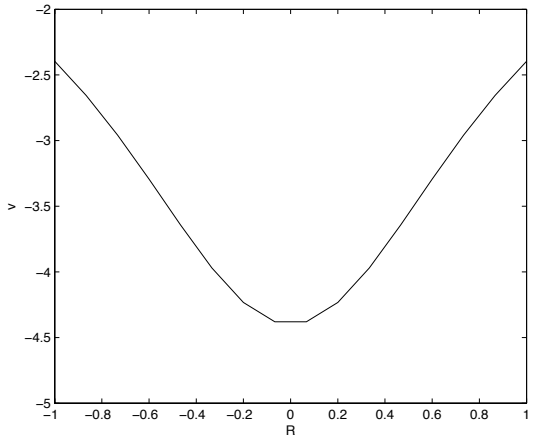
v
R
−2
−2.5
−3
−3.5
−4
−4.5
−5
−1
−0.8
−0.6
−0.4
−0.2
0
0.2
0.4
0.6
0.8
1

(f)

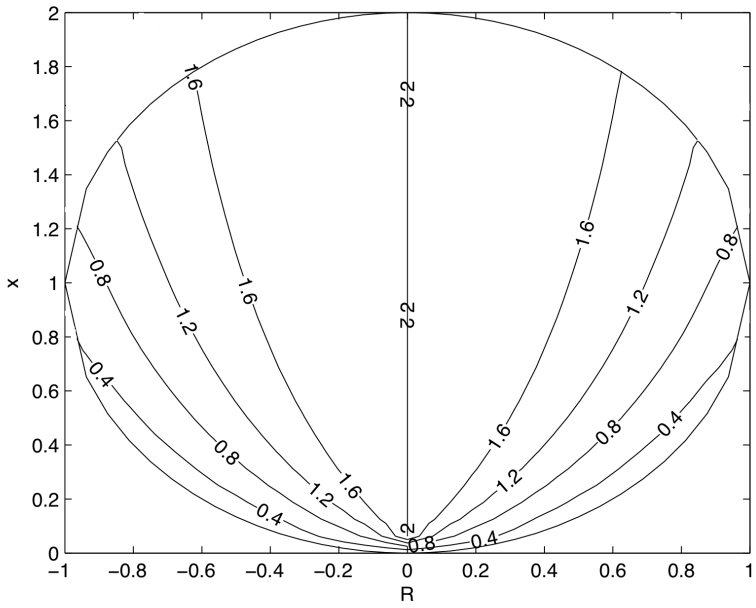

(g)

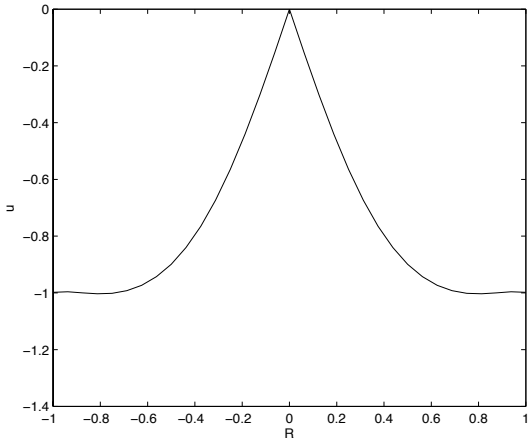

(h)

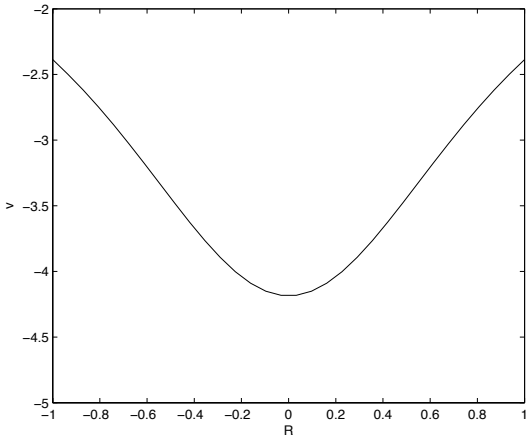

(i)

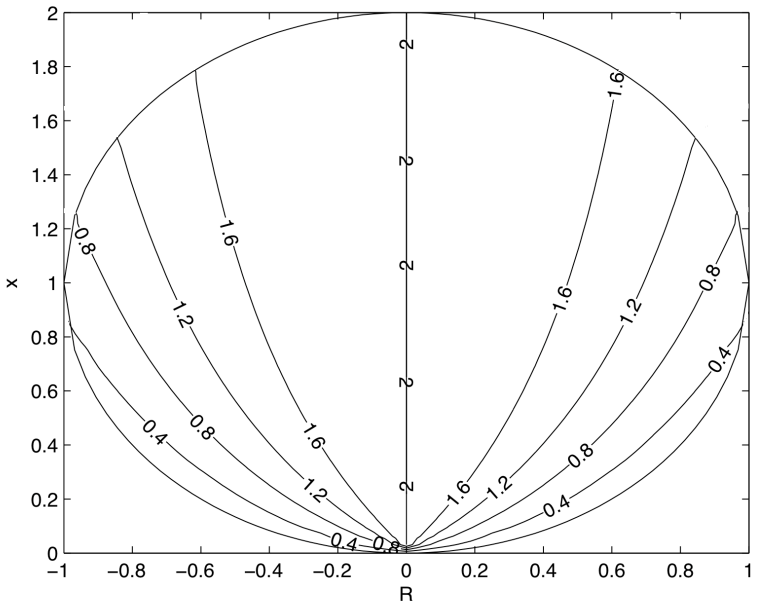
x
R
2
1.8
1.6
1.4
1.2
1
0.8
0.6
0.4
0.2
0
−1
−0.8
−0.6
−0.4
−0.2
0
0.2
0.4
0.6
0.8
1
0.4
0.8
1.2
1.6
2

(j)

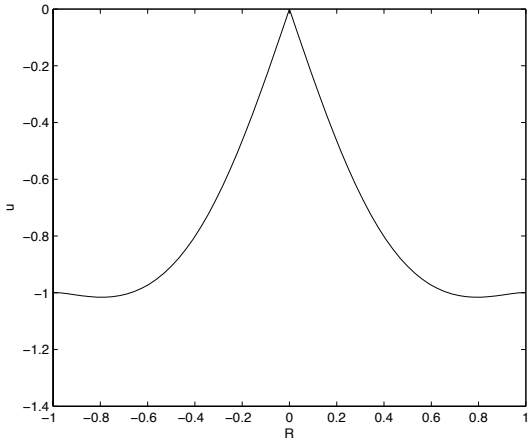
u
R
0
−0.2
−0.4
−0.6
−0.8
−1
−1.2
−1.4
−1
−0.8
−0.6
−0.4
−0.2
0
0.2
0.4
0.6
0.8
1

(k)

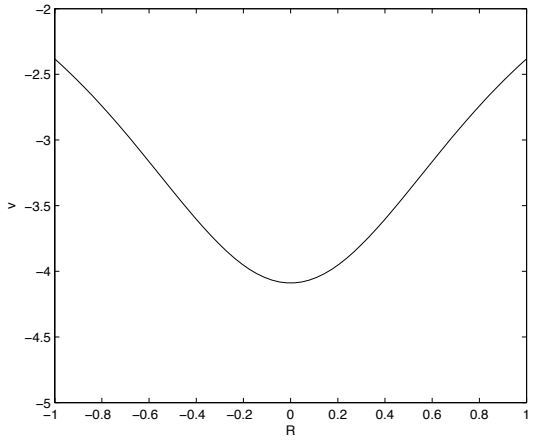
v
R
−2
−2.5
−3
−3.5
−4
−4.5
−5
−1
−0.8
−0.6
−0.4
−0.2
0
0.2
0.4
0.6
0.8
1

(l)

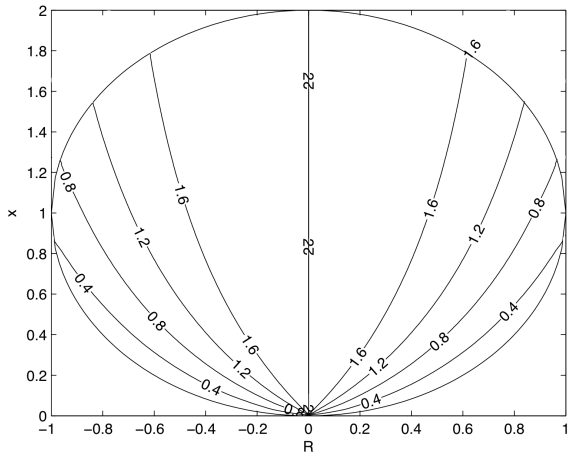

(m)

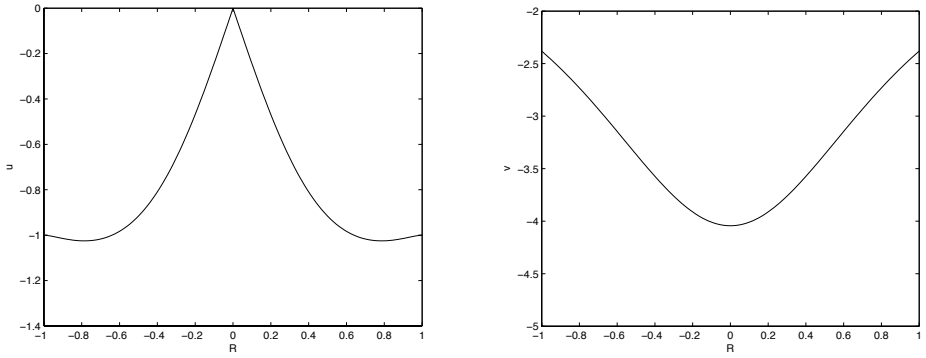

(n) (o)

Figure 6.4: Contour plot for computational results for the sphere using the boundary condition $\Psi = (1 + \cos\theta) - \frac{1}{2}\sin^2\theta$. Here, the demonstration of the code efficiency is through the showing of more coarse grids. Also plotted are the horizontal and vertical velocity along the horizontal centreline. First a 4x4 grid (contour plot (a), horizontal velocity (b) and vertical velocity (c)), then we have an 8x8 ((d)-(f)), 16x16 ((g)-(i)), 32x32 ((j)-(l)) and 64x64 ((m)-(o)) grid respectively. Again the urethra is at the origin.

6.2 Numerical Solutions for More Complex Axisymmetric Shapes

6.2.1 Axisymmetric Cardioidal Shapes

The method described in section 6.1 will now be used to tackle more complex shapes. The method is also an extension of chapter 5. Once again, the issue of the method used in section 6.1 is that it can be quite awkward to calculate. We will therefore once again treat it by working with the tangential derivative of the stream function. More precisely, $\frac{\partial \Psi}{\partial s}$ where $\partial s = \sqrt{(\partial R^2 + \partial z^2)}$ is the distance element along the boundary. The fact that the boundary condition now depends solely on the shape function makes this very helpful. The flexibility to tackle even more complex shapes, especially in an axisymmetric configuration, is rather useful in making our model have increased applicability.

Analysis of Boundary Condition

A simplification of our input boundary condition is significant both in analytical and computational terms and is considered here.

Let $F = z - f(R,t)$ and therefore $F_z = 1$, $F_R = -f_R$, $F_t = -f_t$, where F_z is the differential of F with respect to z and similarly for the other terms. Now, using the result of equation (2.1.5) for the kinematic condition, gives

$$F_t = \frac{1}{R} F_R \Psi_z - \frac{1}{R} F_z \Psi_R. \tag{6.2.1}$$

After substituting the above results in it and upon rearranging and dividing both sides by $(1+f_R^2)^{\frac{1}{2}}$, we obtain

$$\frac{\Psi_R + f_R\Psi_z}{(1+f_R^2)^{\frac{1}{2}}} = \frac{Rf_t}{(1+f_R^2)^{\frac{1}{2}}}. \tag{6.2.2}$$

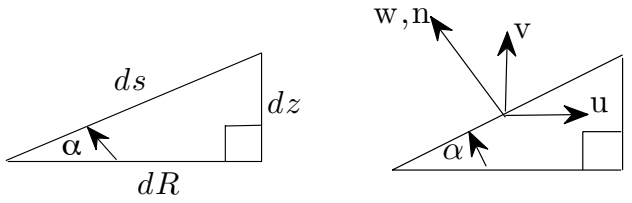

(a) (b)

Figure 6.5: Constructions of triangles used for the calculations.

Using triangle (a) in Figure 6.5 to help our mathematical construction, we can clearly see that

$$\frac{dz}{ds} = \sin\alpha = \frac{1}{(1+f_R^2)^{\frac{1}{2}}} \quad \text{and} \quad \frac{dR}{ds} = \cos\alpha = \frac{f_R}{(1+f_R^2)^{\frac{1}{2}}}. \tag{6.2.3}$$

Now, using triangle (b) from the same figure, we arrive at the equation for the normal velocity component w. After substituting $u_R = \frac{1}{R}\Psi_z$ and $u_z = -\frac{1}{R}\Psi_R$ and also using equation (6.2.3), we obtain

$$\frac{\partial\Psi}{\partial s} = \frac{1}{R}\frac{\Psi_x}{(1+f_R^2)^{\frac{1}{2}}} + \frac{1}{R}\frac{f_R\Psi_R}{(1+f_R^2)^{\frac{1}{2}}}, \tag{6.2.4}$$

and thus we have

$$\frac{\partial\Psi}{\partial s} = \frac{f_t}{(1+f_R^2)^{\frac{1}{2}}}. \tag{6.2.5}$$

Once again, for generalizing the formula, we let $F = \mathscr{G}(z - f(R,t))$ and therefore its differentials with respect to R, z and t are $F_t = -f_t\mathscr{G}'$, $F_R = -f_R\mathscr{G}'$, $F_z = \mathscr{G}'$. We then

use equation (6.2.5), substitute the above results and simplify to end up with

$$\frac{\partial \Psi}{\partial s} = -\frac{F_t}{(F_R^2 + F_z^2)^{\frac{1}{2}}}, \tag{6.2.6}$$

as the appropriate boundary condition.

6.2.2 Construction of shapes

As we have seen in effect in chapter 5, equation (6.2.6) reduces the analytical calculations involved in the boundary condition. This is more apparent if the shape description is more complex than a sphere. Once again, the three-dimensional flow equation from [17] is used but in this context there are two spatial dimensions of an axisymmetric structure and time: this again replaces the third spatial dimension of [17]. With the necessary alterations, the function describing the present collapse becomes

$$F_u(R, z, t) = z - \left(1 - R^2\right)^{\frac{1}{2}} + \sum_{m=1}^{n} h_m t^2 e^{-8(R-k_m)^2}, \tag{6.2.7}$$

where h_m is the collapsing factor at the $R = k_m$ position of the vessel, of the m out of n movements. This represents the upper half of the function, and we similarly have a lower half given as

$$F_l(R, z, t) = z + \left(1 - R^2\right)^{\frac{1}{2}} - \sum_{p=1}^{q} h_p t^2 e^{-8(R-k_p)^2}, \tag{6.2.8}$$

where h_p is the collapsing factor at the $R = k_p$ position for the bladder, of the p out of q movements. Using (6.2.6) and differentiating $F = F_u$ with respect to R, z and t, we

derive after some manipulation to the condition

$$\begin{aligned}\frac{\partial \Psi_u}{\partial s} &= -\frac{F_t}{(F_R^2 + F_z^2)^{\frac{1}{2}}} \\ &= -\frac{(1-R^2)^{\frac{1}{2}} \sum_{m=1}^{n} 2h_m t e^{-8(R-k_m)^2}}{\left(1 - 2R(1-R^2)^{\frac{1}{2}}\alpha + (1-R^2)\alpha^2\right)},\end{aligned} \tag{6.2.9}$$

where $\alpha = \sum_{m=1}^{n} 16h_m t^2 (R - k_m) e^{-8(R-k_m)^2}$. In a similar way, we end up with a corresponding condition for the lower surface

$$\begin{aligned}\frac{\partial \Psi_l}{\partial s} &= -\frac{F_t}{(F_R^2 + F_z^2)^{\frac{1}{2}}} \\ &= \frac{(1-R^2)^{\frac{1}{2}} \sum_{v=1}^{c} 2h_v t e^{-8(R-k_v)^2}}{\left(1 - 2R(1-R^2)^{\frac{1}{2}}\alpha + (1-R^2)\alpha^2\right)},\end{aligned} \tag{6.2.10}$$

where $\alpha = \sum_{v=1}^{c} 16h_v t^2 (R - k_v) e^{-8(R-k_v)^2}$.

6.2.3 Implementation of the Numerical Scheme

The numerical scheme performed here is similar to chapter 5. In this case though, the boundary conditions (equations (6.2.9) and (6.2.10)) are only applied in the positive radius side ($\phi = 0$) and we use a constant value as a boundary condition at the line $R = 0$. This is because on the axis we require the radial velocity $u_R = 0$ and hence $\frac{\partial \Psi}{\partial z} = 0$ which means that Ψ is constant along the vertical axis. The outer wall boundary condition (equations (6.2.9) and (6.2.10)) is then multiplied by the boundary length of the boundary ds between two points. We then apply equation (6.1.9) inside our boundary. The boundary interpolation performed in section 6.1.2 is also used. The

structure in Figure 6.6 is the same as that used in Chapter 5 motivated by medical cystourethrograms.

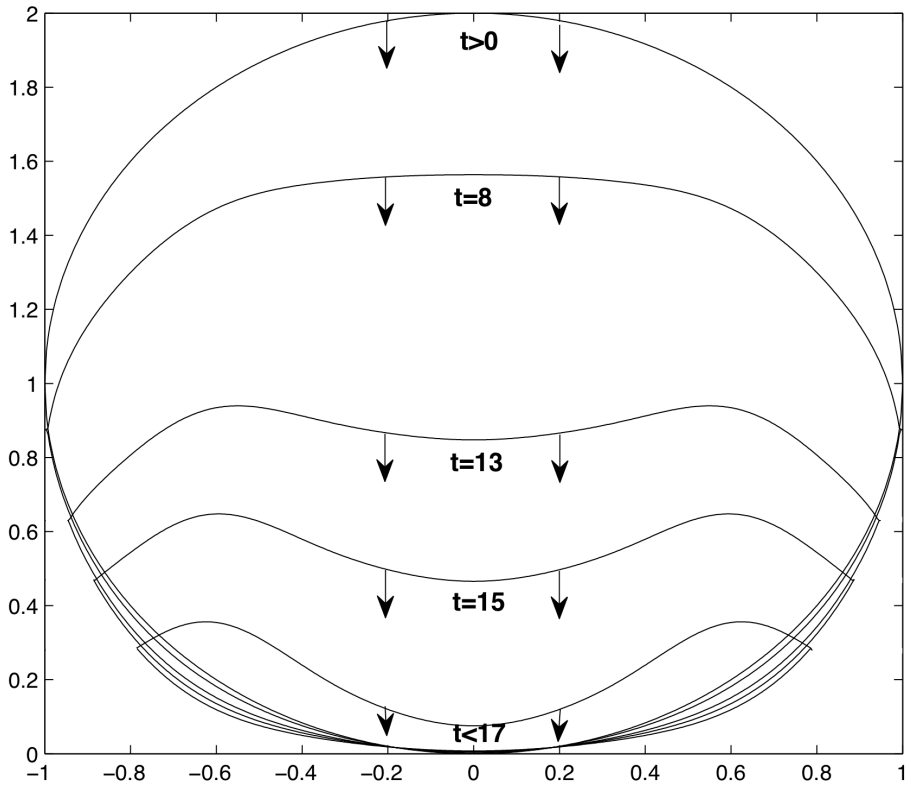

Figure 6.6: Shapes that the axisymmetric vessel takes at different times as it collapses with a cardioidal-like shape. Horizontal axis is R, vertical is z.

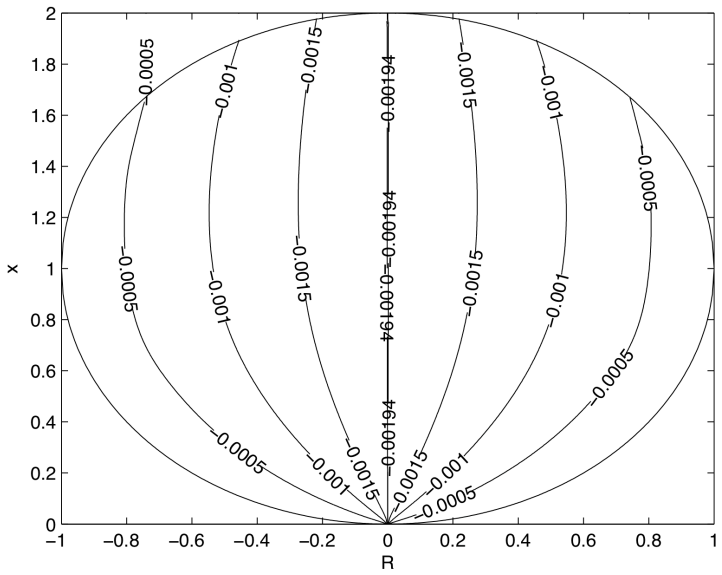

(a)

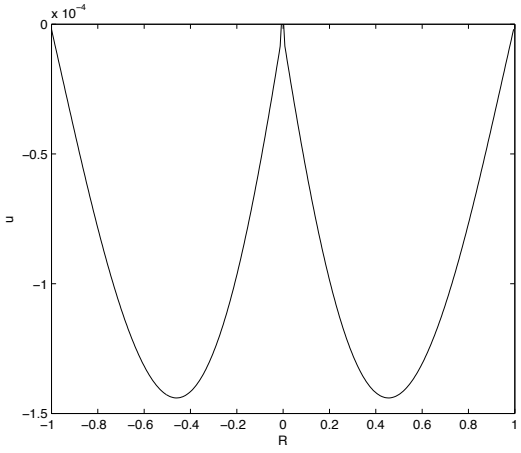

(b)

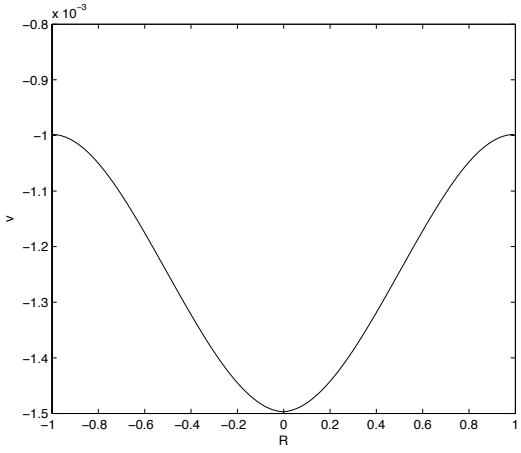

(c)

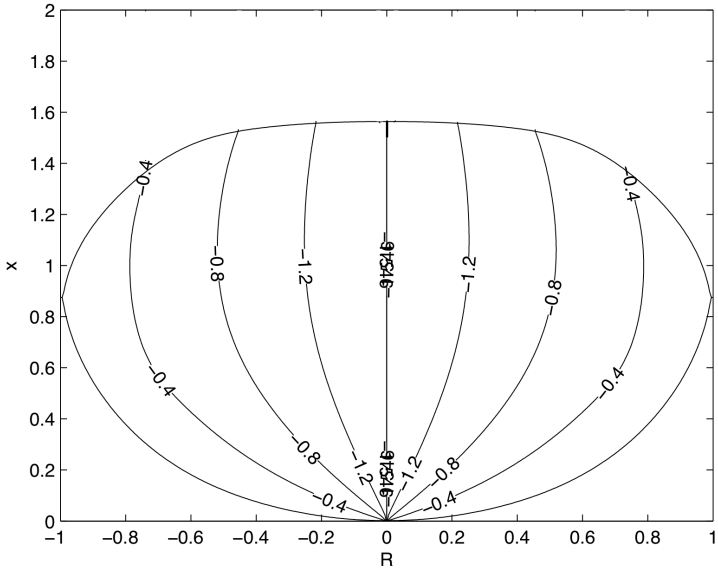

(d)

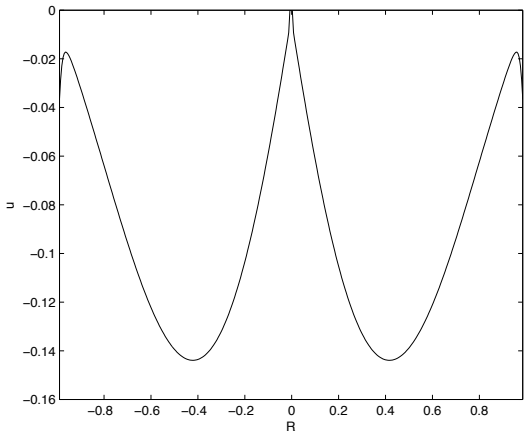

(e)

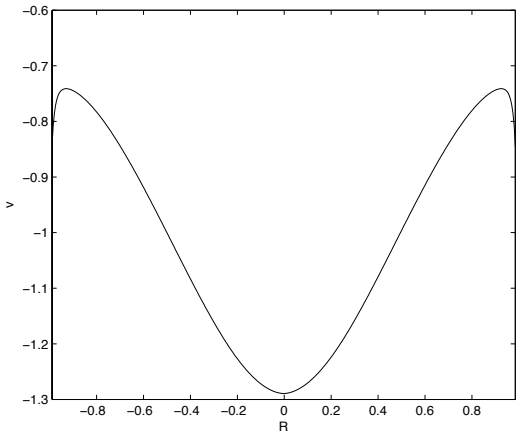

(f)

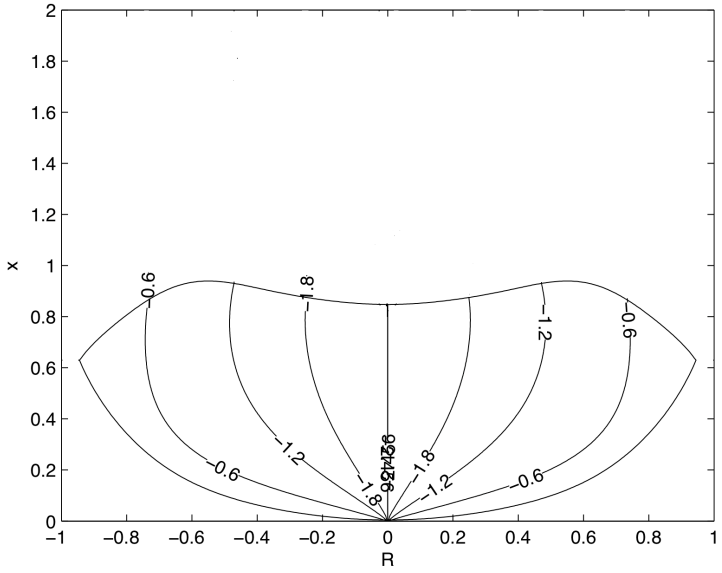

(g)

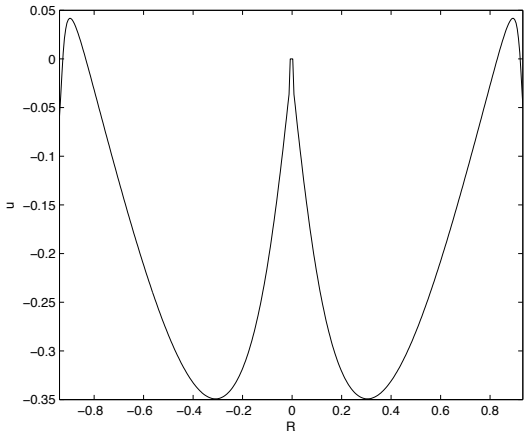

(h)

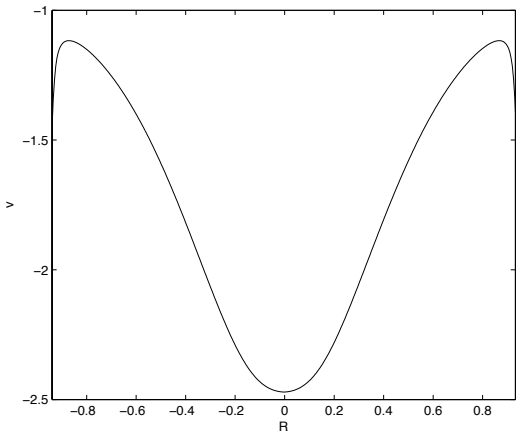

(i)

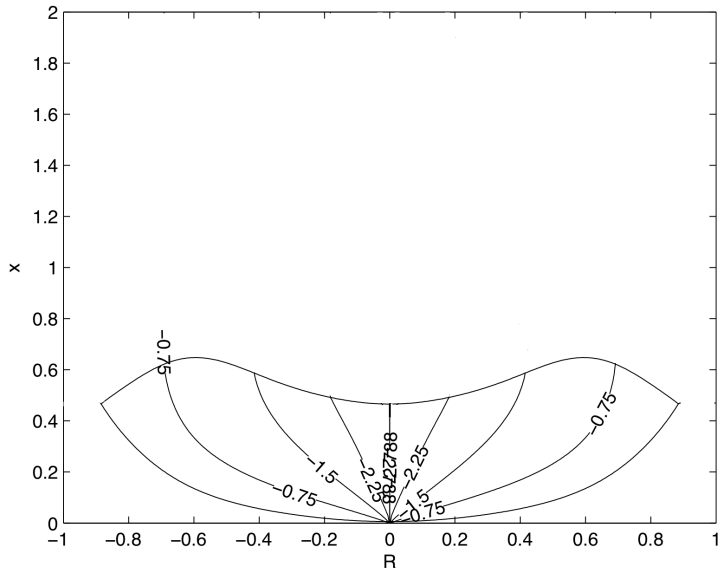

(j)

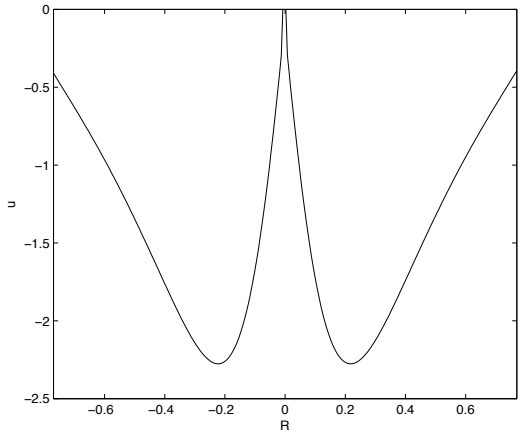

(k)

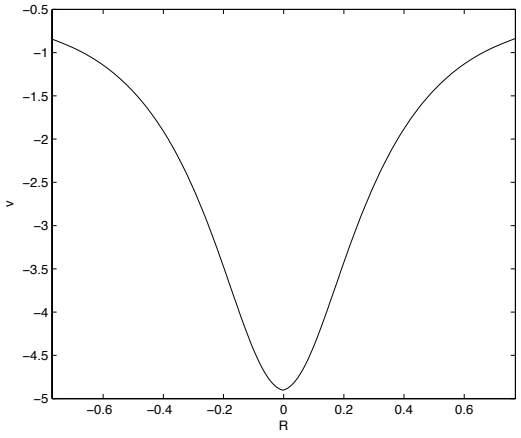

(l)

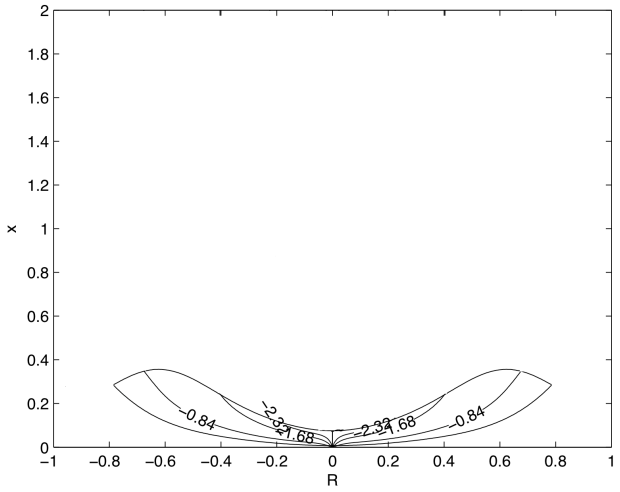

(m)

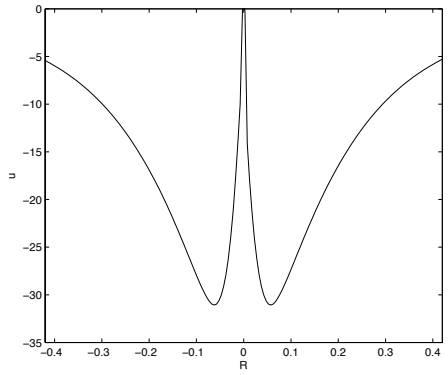

(n)

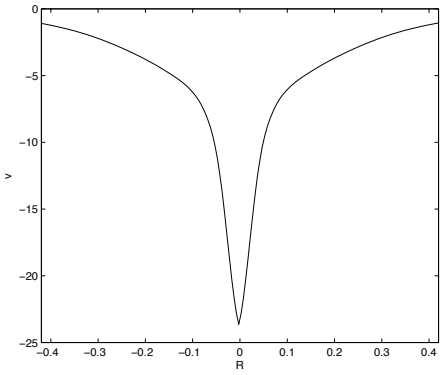

(o)

Figure 6.7: Contour plots of the fluid motion within the modeled collapsing vessel. Also plotted are the horizontal and vertical velocity along the horizontal centreline. Times for the parts are 0.01 -just after the start of micturition- (contour plot (a), horizontal velocity (b) and vertical velocity (c)), then 8((d)-(f)), 13((g)-(i)), 15((j)-(l)) and 16.8 -just before the end of micturition- ((m)-(o)) respectively.

6.3 Results

As described previously in the two-dimensional results in chapter 5, the shapes that are described here are fairly representative of what we expect from a normal bladder during micturition (collapse). Axisymmetric shapes such as these are also very useful potentially for real comparisons as we can see from the cystourethrograms in Figures 1.5 and 1.6 (b) and (c). As described earlier in chapter 5 and more precisely in section 5.2 most of the squeeze velocity is vertical. Hence, the analytical result from Figure 6.3 (c) shows that we have a high horizontal velocity. Similarly to the circle, the sphere described in Figure 6.3 collapses proportionally from all sides keeping the urethra fixed and the shape spherical. This is not the case of course in reality as most of the squeeze is vertical. Thus we can see in the Figure 6.7 (b) that at the start of micturition the horizontal velocity at the sides is zero. The streamfunction here is also time dependent as we can see in equations (6.2.9) and (6.2.10).

All the plots of the horizontal and vertical velocity of the centre line in Figure 6.7 are even about $x = 0$. The horizontal velocity is zero along $x = 0$ as required. We can also see that as the vessel collapses and becomes thinner, the horizontal velocity tends to approach the thin-vessel analysis results. This is once again obvious in Figure 6.7 (k) near the range $-0.3 \leq x \leq 0.3$ and even more in Figure 6.7 (n) where the velocity (horizontal) has its Laplace/Euler region in the range $-0.08 \leq x \leq 0.08$ effectivelly. Away from this region once again the thin-layer analysis applies as in section 3.2 and also 2.2.1.

Also in Figure 6.7 (h) we can see once again a small feature on the sides which is

attributed to the definition of the shape (the separation of the upper and the lower half). A similar point can be made about the vertical velocity near the edges in Figure 6.7 (f) and (i); even though in the horizontal velocity cases (see Figure 6.7 (e) and (h)) it is not a big effect, the vertical velocity cases seem to have a larger effect which is most probably affected by the general collapse and shape rather than by what is happening specifically at that point. It is also worth mentioning that the vertical velocity of the analytical result of the sphere in Figure 6.3 (d) and Figure 6.7 (c) exhibits a different behaviour in the middle.

It is also interesting to compare the streamlines between the two dimensional and axisymmetric cases. We can see similarities especially in the thin cases but in the spherical or near-spherical shapes the lines are more curved in the axisymmetric cases (the differences also apply for their respective horizontal and vertical velocities). Finally, if we once again examine the vertical velocity values of Figure 6.7 (o), we see the very high values that occur near the urethra.

6.4 Summary

In summary, we see in this chapter that the numerical results for the axisymmetric cases are very similar to those in two dimensions. That is overall encouraging as it means that the axisymmetric flow structure resembles to a significant extent that of the two-dimensional case.

Chapter 7

Concluding Remarks

7.1 Overview

In this thesis, we have developed a first mathematical model for the mechanical or fluid dynamical characteristics of the human bladder. The research was done in cooperation with the pharmaceutical industry (Astellas Pharma Ltd) through a Cooperative Award in Science and Engineering (CASE) for the present project and with several linkages with the UCL medical modelling group. The current models used in practice are mostly based on statistical results from previous patients rather than the actual mechanical issues of the bladder and its contained fluid. After all, its shape is different from individual to individual and it changes based on the sex, the size of the cavity in which it is contained [71], et cetera. Due to its elasticity (modulus of elasticity of about 0.05 MPa [21]) depending on the reasons mentioned and also its filling capacity, the huge

changes and deformations of the bladder shape make it rather challenging to tackle, as regards detailed modelling.

We suggest tentatively that our approach of tackling the modelling of this vessel depending on its shape may prove to be rather practical in the long run since it can be put into a clinical context (after vessel construction), in principle, and also be more precise depending on the case of each individual. Lack or delay in mathematical modelling of the urinary bladder may have slowed medical progress in this area. Yet, developing an understanding for the mechanical and dynamical functions of the vessel, including its fluid, can open new doors for further clinical and pharmaceutical research.

In particular, a main feature in this thesis has been the simplification of the input boundary condition. Having a boundary condition that satisfies the kinematic boundary condition which only depends on the shape of the vessel makes it potentially really useful and user friendly. At the same time, the use of the function used in [17] for the shape of the vessel means that we can alter our code to virtually model many different shapes just by means of one equation or just by altering the parameters. These features appear to have been particularly advantageous.

With regard to the numerical scheme, effort has been put in to make it overall as time efficient as possible. Using a numerical scheme based simply on a modified finite difference method meant that this was possible. Hence, almost all of the figures from this thesis take only a few seconds to obtain. Time efficiency was an aspect of the model that we wanted due to the perceived need for combining this model with others (like [43]) modelling other parts of the lower urinary tract.

The appendix of the thesis has a chapter on the possibility of extending all the work in order to cover the Navier-Stokes equations and not just Laplace's equation. In essence, a possible relationship on the boundary for the streamfunction and vorticity can lead the way in further expanding the current work as it is.

7.2 Summary Discussions for Each Section

Presented here is a brief discussion for each chapter and its results. Chapter 2 started with the analysis of two-dimensional vessel shapes and more specifically a circle with a point discontinuity at the lowest point. This shape was tackled in three ways, numerically and analytically in terms of the Poisson integral formula and also with respect to complex functions. All three results agreed with each other and so provided a first guidance for this simple shape. This chapter was the backbone of the thesis. The complex function result could be applied in a similar way to the axisymmetric model later on. At the same time, analysis of thin vessels took place in this chapter. Apart from the fact that it is possible in reality to have vessels with such thin shapes it also provided for a limiting case for our numerical results when tackling elliptical configurations in particular. The small Euler/Laplace region of nonuniformity with enhanced fluid velocities for these cases was also studied complementing these results.

The axisymmetric analysis was outlined in chapter 3. This chapter was only presented for an axisymmetric spherical shape. Nevertheless it was important when it cames to justifying our numerical scheme. It also provided significant results with respect to the flow validity. We also prepared the scene for subsequent numerical work. This chapter

concluded all the analytical results with regard to the vessel. More analytical work followed in later chapters with respect to the numerical scheme.

Chapter 4 introduced the beginning of the numerical work. A simple and accurate modified iterative finite difference scheme was used. The boundary element method was also used to demonstrate that other methods could also tackle the problem. The modified iterative finite difference scheme was further extended in the next chapters.

The analysis performed with respect to the boundary condition in chapter 5 was a central part of the thesis. This meant that we could still apply the kinematic condition on our vessels with minimal work compared with the previous boundary condition when we were just using the full kinematic boundary condition. This work became even more elegant when it was coupled with the involved shape structure from Bowles et al [17]. Even though we only presented symmetric shapes in this thesis, it is worth remarking that the numerical scheme also covered non-symmetric vessel shapes. The symmetrical results were presented because they could show the accuracy of the scheme in a visual way.

Chapter 6 describes the numerical scheme for the axisymmetric configuration. This is done in a similar way to the two-dimensional case but obviously it does not satisfy Laplace's harmonic equation. The fact that the axisymmetric scheme agrees well with the complex function analysis is very encouraging. It is also worth mentioning here that the results of the axisymmetric scheme are very similar qualitatively to those in two dimensions. This is encouraging for a view that the two-dimensional work is a reasonable foundation when it comes down to modelling the flow in the vessel.

The work that incorporated Navier-Stokes equations in appendix A was in essence the beginning of a further extension on the current research. A numerical scheme was developed in a similar way to the previous ones. Using the standard streamfunction/vorticity equations, we solved the coupled equations numerically. The scheme was verified by means of the classical driven cavity problem. Work can be done on extending the developments in this appendix as our results appear to be quite encouraging.

7.3 Suggestions for Future Work

Completing the main body now, it is only relevant to make some suggestions for future work.

The first extension that would make some considerable sense to cover is to solve the contained-flow problem using the Navier-Stokes equations in two dimensions. This could potentially be tricky when it comes to handling the boundary conditions with accuracy combined with flexibility.

Another extension would be to further develop the numerical scheme in order to make it more accurate. Although this is possible, it will obviously come at the expense of computational time. Schemes with more stencil points offer a potential way to approach this.

Another possible extension would be to include more characteristics of the bladder. We have modelled the bladder wall throughout as a thin smooth vessel but this is not strictly accurate compared with reality. Even though the outside surface is smooth,

the bladder wall inside is rough. Hence, the wall is thicker at some places than others. Another assumption that we took was with regard to the urethra. We have assumed throughout this work that the urethra is in effect a point. Further developments can be made in order to allow for the urethral neck to be increased in size depending on each individual's case.

The ideal setup for this case would be to have a fully working three-dimensional collapsible-vessel Navier-Stokes scheme calculating pressures at all points in the human bladder. There is still a long way to go for that but to start with a two-dimensional collapsible model might be a sensible way forward, especially if we read more into our two-dimensional and axisymmetric results. This will be very interesting and it will be particularly intriguing to compare in great detail the two-dimensional Laplace results and the Navier-Stokes ones.

Appendices

Appendix A

Navier-Stokes Effects

A.1 Ideas/Notation

The purpose here is to extend or begin extending the range of the study in order to cover fluid flow equations that have more generality. Thus we abandon some of the restrictions, on viscosity in particular, which were required for the earlier work.

Ideas similar to those of the previous chapters are now to be investigated in the context of the Navier-Stokes equations rather than the Laplace or Laplace-like systems. We will use the same type of complex geometry as before, namely, vessel shapes which deform substantially. The application to fluid behaviour within the human bladder is again very much in mind here including its large deformations and possible folding of the vessel. Very little quantitative work has been done, as far as we know, on the folding of the vessel.

A.2 Numerical Scheme

A.2.1 Finite Difference Scheme

Similarly to Laplace's equation, that was treated earlier in the thesis, we convert the coupled streamfunction-vorticity version of the Navier-Stokes equations into finite-difference form. For this, we use the following equations

$$\nabla^2 \Psi = -\zeta, \tag{A.2.1}$$

and

$$\nabla^2 \zeta = Re \left(u \frac{\partial \zeta}{\partial x} + v \frac{\partial \zeta}{\partial y} \right), \tag{A.2.2}$$

where Re is the Reynolds number, ζ the vorticity and u, v, Ψ, x and y are as described in the previous chapters. We approximate the equations into a set of linear simultaneous equations and write them in matrix notation. Once again, the problem is solved in a standard iterative way. We use the same stencil as before (Figure A.1) and for simplicity, we treat the equations in a similar manner as in section 4.2.2. We obtain for equation (A.2.1)

$$\psi(i,j) = \frac{1}{2\left(\frac{1}{h^2} + \frac{1}{k^2}\right)} \left(\frac{\psi_{(i+1,j)} + \psi_{(i-1,j)}}{h^2} + \frac{\psi_{(i,j+1)} + \psi_{(i,j-1)}}{k^2} + \zeta(i,j) \right), \tag{A.2.3}$$

and similarly for equation (A.2.2)

$$\zeta(i,j) = \frac{1}{2\left(\frac{1}{h^2}+\frac{1}{k^2}\right)} \left(\frac{\zeta_{(i+1,j)}+\zeta_{(i-1,j)}}{h^2} + \frac{\zeta_{(i,j+1)}+\zeta_{(i,j-1)}}{k^2} - \frac{Re}{4hk}\left((\psi_{(i,j+1)}-\psi_{(i,j-1)})(\zeta_{(i+1,j)}-\zeta_{(i-1,j)})\right) + \frac{Re}{4hk}\left((\psi_{(i+1,j)}-\psi_{(i-1,j)})(\zeta_{(i,j+1)}-\zeta_{(i,j-1)})\right)\right). \quad \text{(A.2.4)}$$

These are the discrete finite-difference equations for calculating the streamfunction and vorticity at any point inside our vessel. As one can clearly see here, the horizontal and vertical velocity u and v respectively are treated in terms of the stream function, namely,

$$u = \frac{\partial \psi}{\partial y} = \frac{\psi_{(i,j+1)}-\psi_{(i,j-1)}}{2k} \quad \text{and} \quad v = -\frac{\partial \psi}{\partial x} = \frac{\psi_{(i-1,j)}-\psi_{(i+1,j)}}{2h}, \quad \text{(A.2.5)}$$

in turn.

Once again, the method is standard and relatively straightforward, at least in principle. We define the required vessel shape on a Cartesian grid and approximate it simply on that grid. We also define the boundary conditions in a manner similar to that in the previous chapters. The code then calculates the flow inside the vessel or approximated vessel satisfying the Navier-Stokes equations.

A.2.2 Applications

The two applications on which we focus in sections A.3 and A.4 below are, respectively, a classical one and a novel one relevant to the main thrust of the thesis.

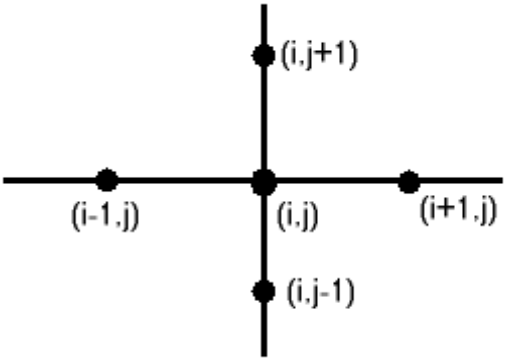

Figure A.1: Example of 5-point stencil on our grid.

A.3 Verification through Driven Cavity

To test the overall approach and the code development for the flow system itself, we address the well studied numerical problem of the flow in a driven cavity. We will try to keep it as simple as possible but at the same time we will try not to compromise on accuracy. Most of the weight though is on the time efficiency of the code.

An incompressible fluid revolves steadily in a square-shaped cavity under the influence of a sliding upper wall, which moves from left to right, and imparts motion to the fluid via the no-slip boundary condition. This wall moves with a uniform velocity in its own plane. The tangential velocity on all other boundaries is zero, while the normal velocity on all boundaries is also zero. This classical problem has served over time as a model problem for testing and evaluating numerical techniques. In order to evaluate accuracy, we will be using several papers to check our the results [42], [75].

We will be solving the driven cavity problem in terms of the vorticity/stream function formulation described above incorporating equations (A.2.3) and (A.2.4). We try to keep things basic with the boundary condition of this problem. We therefore implement Thom's formula [109], [110], on the sides and specifically,

$$\zeta_{(0,j)} = \frac{2}{h^2}\psi_{(1,j)} \quad \text{with} \quad \psi_{(-1,j)} = \psi_{(1,j)}, \tag{A.3.1}$$

with ζ and ψ as previously described and $\psi_{(-1,j)}$ the ghost grid point outside the computational domain. This is a very simple way to describe the boundary requirement. It is an old and well known formula which is in fact second order accurate even though it was thought to be first order. Another very popular formula that could be used is Wood's formula [124] but since it is third order accurate and we are working with a second order accuracy, it would not be appropriate or necessary.

Now, applying the iterative numerical scheme on *MatLab*, we aim to produce results for the relatively low Reynolds numbers that we are most interested in. In order to keep it more direct, we will be comparing results for Reynolds numbers of 1, 100 and 400. These results are well established and are in the range of interest. Plotting these, we have Figures A.2, A.3 and A.4.

Close comparisons with [42], [75], [94], [121], [123] indicate that these results are very accurate suggesting that the scheme can work well for the relatively low values of Reynolds number that we have examined. As a matter of fact, the plots are virtually indistinguishable from those in [42] and [75].

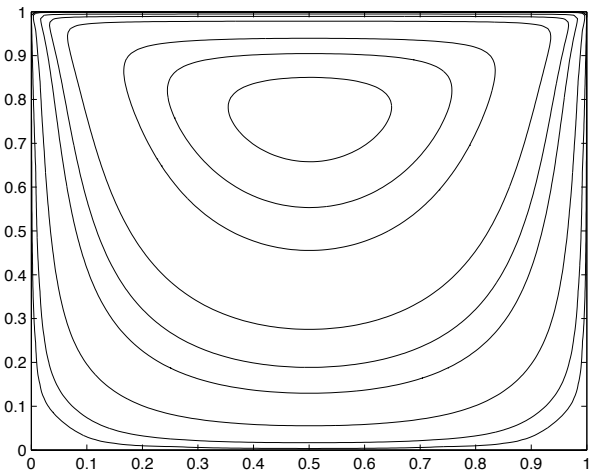

(a)

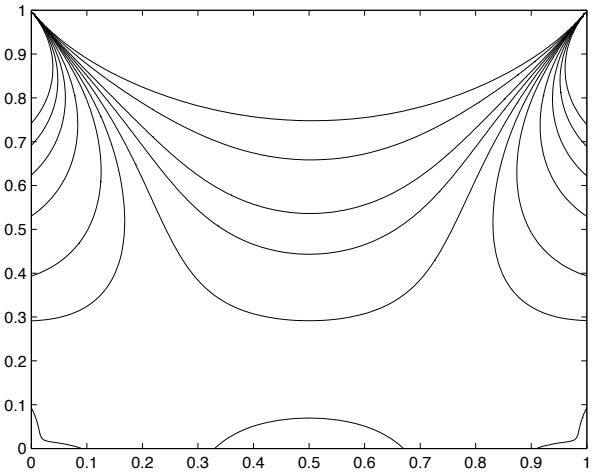

(b)

Figure A.2: Contour plot of numerical streamfunction plots (a) and numerical vorticity plots (b) for the driven cavity problem with the scheme developed for Reynolds number of 1. The upper wall has a velocity of unity from left to right.

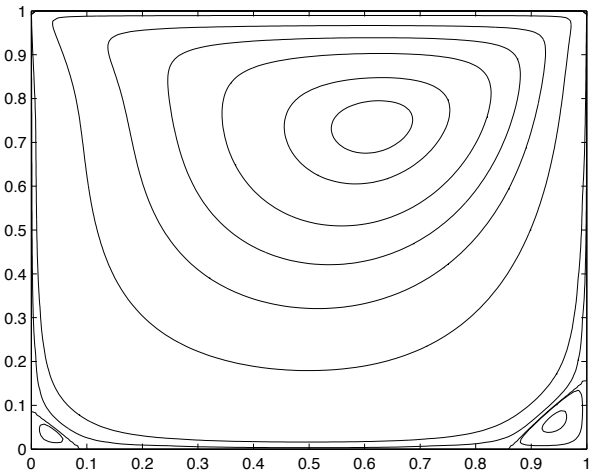

(a)

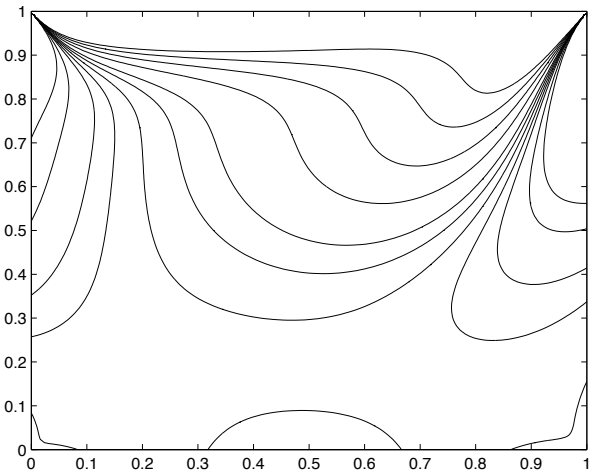

(b)

Figure A.3: Contour plot of numerical streamfunction plots (a) and numerical vorticity plots (b) for the driven cavity problem with the scheme developed for Reynolds number of 100.

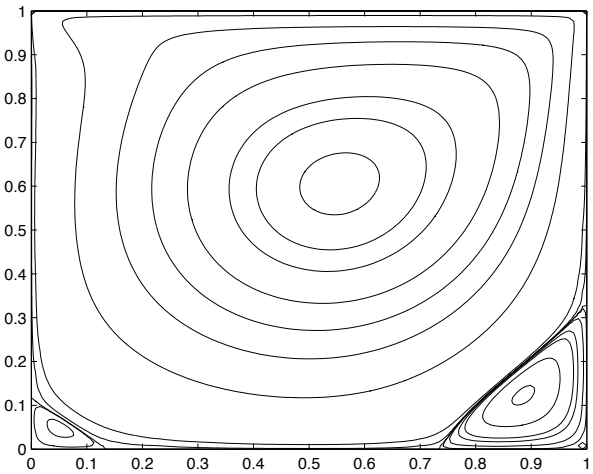

(a)

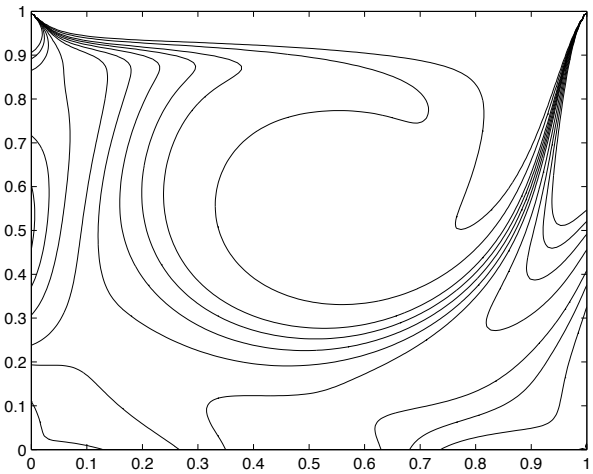

(b)

Figure A.4: Contour plot of numerical streamfunction plots (a) and numerical vorticity plots (b) for the driven cavity problem with the scheme developed for Reynolds number of 400.

A.4 More Complex Two-Dimensional Shapes

The problem of fluid motion inside a significantly deformable vessel, as governed by the Navier-Stokes equations, is now tackled. This is based partly on the approach of the previous section and partly on an approach developed recently by Bowles et al [17]. Their study is on a three-dimensional steady flow concerned with branching vessels and centering on the longitudinal vortex equations, namely,

$$u\frac{\partial u}{\partial X} + V\frac{\partial u}{\partial y} + W\frac{\partial u}{\partial z} = -\pi_1'(X) + \Gamma\triangle u, \tag{A.4.1}$$

$$u\frac{\partial V}{\partial X} + V\frac{\partial V}{\partial y} + W\frac{\partial V}{\partial z} = -\frac{\partial \pi_2}{\partial y} + \Gamma\triangle V, \tag{A.4.2}$$

$$u\frac{\partial W}{\partial X} + V\frac{\partial W}{\partial y} + W\frac{\partial W}{\partial z} = -\frac{\partial \pi_2}{\partial z} + \Gamma\triangle W, \tag{A.4.3}$$

where the parameter $\Gamma = \frac{1}{\alpha^2 Re}$, ∇ is the usual gradient vector operator $(\partial_X, \partial_y, \partial_z)$ in scaled form and also $\triangle$ is the two-dimensional Laplacian operator $(\partial_y^2 + \partial_z^2)$. This is because the longitudinal diffusion is negligible over the axial length scales used in their branching-flow application. We also have the continuity equation

$$\frac{\partial u}{\partial X} + \frac{\partial V}{\partial y} + \frac{\partial W}{\partial z} = 0, \tag{A.4.4}$$

with the parameters et cetera as defined below. It is also necessary to mention the length scales of the problem as defined in the paper [17]. The three-dimensional geometry is taken to have a dimensional axial length scale L_0^* which is much larger than the cross-sectional length based on the typical vessel radius R_0^*. The geometrical aspect ratio is defined as $\alpha = \frac{R_0^*}{L_0^*} \ll 1$, with the typical angles of divergence of the daughter branches assumed to be small and of order α. The dimensional Cartesian coordinates x^*, y^*, z^* are

used with x^* being the axial coordinate. At the same time, we have the corresponding axial components to be u^*, v^*, w^* with the dimensional pressure represented as p^*. The Reynolds number Re is based on the longer axial length scale and is given by

$$Re = \frac{U_0^* L_0^* \rho_0^*}{\mu_0^*}, \tag{A.4.5}$$

where U_0^* is a representative dimensional axial in-flow velocity and ρ_0^* and μ_0^* are the fluid density and viscosity respectively. The non-dimensinalization of the variables is as follows:

$$[x^*, y^*, z^*] = [L_0^* X, R_0^* y, R_0^* z], \quad [u^*, v^*, w^*] = [U_0^* u, U_0^* \alpha V, U_0^* \alpha W], \tag{A.4.6}$$

with $p^* = \rho_0^* U_0^{*2}(\pi_1(X) + \alpha^2 \pi_2(X, y, z))$. The scalings on velocity are implied by the continuity balance while those involved in the pressure response stem from the axial momentum balance as far as the $O(1)$ term π, independent of y and z is concerned and from the cross-section momentum equations for the $O(\alpha)$ contribution which depends on y, z as well as X. The model wall shapes used for the work of [17] are similar to the ones we have used earlier in chapters 5 and 6 provided allowance is made for the switch from (X, y, z) coordinates for three-dimensional steady motion to (t, x, y) coordinates for our two dimensional unsteady cases of concern. Hence, there is an 'upper' z value dependent on X and y given by

$$z_{upper}(X, y) = b_h(X) \left(1 - \left(\frac{y}{a_h(X)}\right)^2\right)^{\frac{1}{2}} - \sum_{m=1}^{M} H_m(X) G_m(y - y_m(X)), \tag{A.4.7}$$

and similarly the lower one being z_{lower} given by $-z_{upper}$. Here, $H_1(X) = h_1 F(X)$ with the constant h_1 being specified for each case while the functions $H_2(X)$, $H_3(X)$ and so on vary depending on the case along with the number of carinas M in the

geometry of [17]. The function $F(X)$ is $(X/X_2)^2$ for $X < X_2$ but $(2X - X_2)/X_2$ for $X > X_2$ where X_2 is a station downstream of $X_{-\infty}$, taken to be unity. Furthermore, $[a_h(X), b_h(X)] = [a_1, b_1](1 - rF(X))$ with the constants r, a_1, b_1 constants. A shift in the centreline of the vessels is also incorporated in equation (A.4.7). The parameters G_m are responsible for that along with the alterations of the branching geometry.

All the work above in [17] has been done in three dimensions. However, we recognise that we can convert the above system to the configuration of a two-dimensional unsteady flow of current concern. This can be done by effectively setting the axial velocity component, u in this case, identically equal to unity, replacing the axial pressure gradient π_1' by zero and regarding the coordinate X as representing time in our case, leading from (A.4.1)-(A.4.3) to the following

$$\frac{\partial V}{\partial X} + V\frac{\partial V}{\partial y} + W\frac{\partial V}{\partial z} = -\frac{\partial \pi_2}{\partial y} + \Gamma \triangle V, \tag{A.4.8}$$

$$\frac{\partial W}{\partial X} + V\frac{\partial W}{\partial y} + W\frac{\partial W}{\partial z} = -\frac{\partial \pi_2}{\partial z} + \Gamma \triangle W, \tag{A.4.9}$$

while the continuity equation (A.4.4) becomes

$$\frac{\partial V}{\partial y} + \frac{\partial W}{\partial z} = 0, \tag{A.4.10}$$

here.

For our cases, together with the switch $(X, y, z) \rightarrow (t, x, y)$, we keep the shape functions as defined specifically in chapters 5 and 6, namely,

$$F_u(x, y, t) = y - \left(1 - x^2\right)^{\frac{1}{2}} + \sum_{m=1}^{n} h_m t^2 e^{-8(x-k_m)^2}, \tag{A.4.11}$$

where h_m is the collapsing factor at the $x = k_m$ position of the vessel of the m out of n movements. This represents the upper half of the shape function, and we similarly have a lower one given as

$$F_l(x, y, t) = y + \left(1 - x^2\right)^{\frac{1}{2}} - \sum_{p=1}^{q} h_p t^2 e^{-8(x-k_p)^2}, \tag{A.4.12}$$

where h_p is the collapsing factor at the $x = k_p$ position for the bladder, of the p out of q movements.

The shape starts off at time zero ($t = 0$) as a circle and hence there is some immediate interest in what happens to the starting flow. The results from Figure A.5 show that indeed the majority of the decay which is seen in the amplitude of the flow solution occurs quite rapidly, in fact, while the cross sectional shape is still more or less circular. A helpful comparison is possible with the results of an analysis for the temporal decay inside our circular shape.

The analysis is basically for, or related to, the stopping rotation of a fluid-filled circular cylinder, as in Batchelor [8] for example, and it proceeds as follows:

The main governing equations written for convenience in polar coordinates r, θ with corresponding velocity components $u_r (= \bar{V}$ say$), u_\theta$ are

$$\frac{\partial \bar{V}}{\partial \theta} = 0, \tag{A.4.13}$$

for continuity from (A.4.10), implying that $\bar{V} = \bar{V}(r, t)$ depends only on r, t and for the azimuthal momentum balance

$$\frac{\partial \bar{V}}{\partial t} = \nu \left(\bar{V}_{rr} + \frac{\bar{V}_r}{r} - \frac{\bar{V}}{r^2} \right). \tag{A.4.14}$$

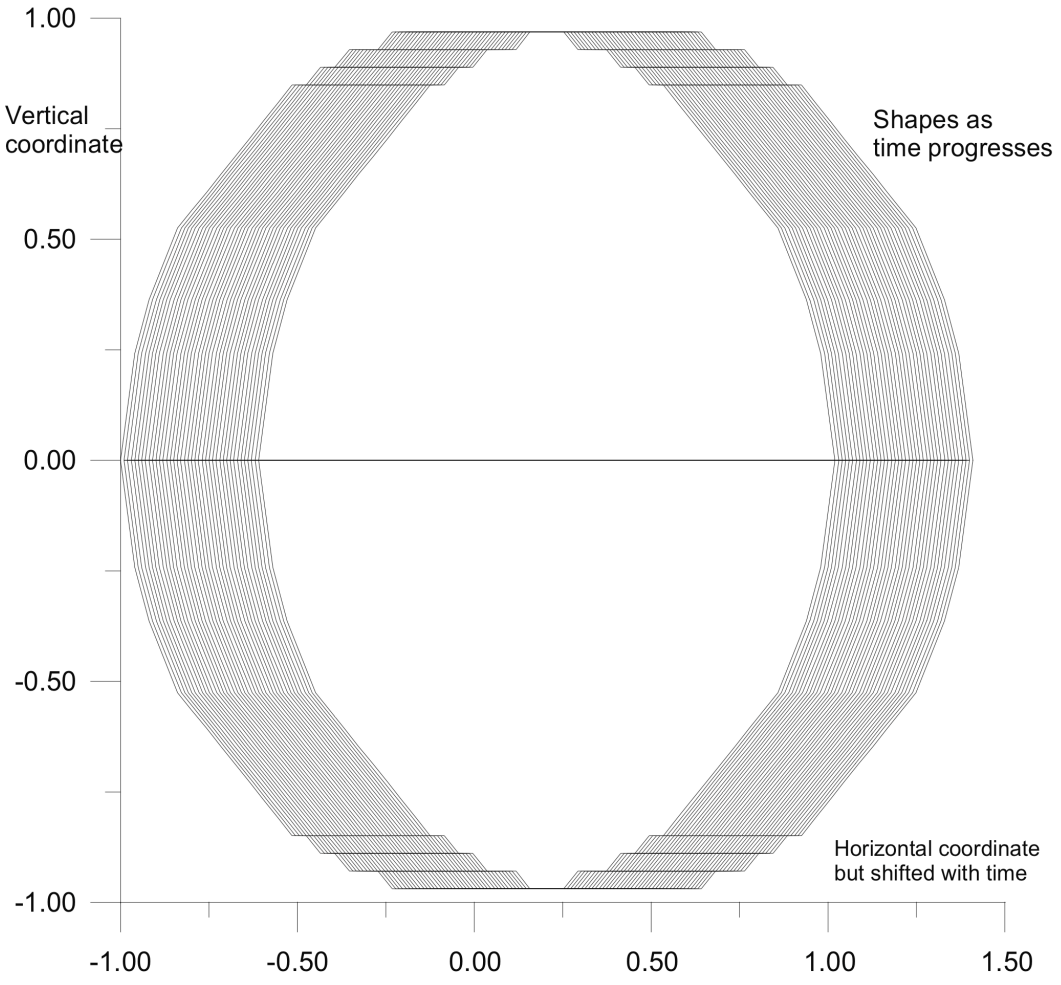
1.00
Vertical
coordinate
0.50
0.00
-0.50
-1.00
-1.00
-0.50
0.00
0.50
1.00
1.50
Shapes as
time progresses
Horizontal coordinate
but shifted with time

(a)

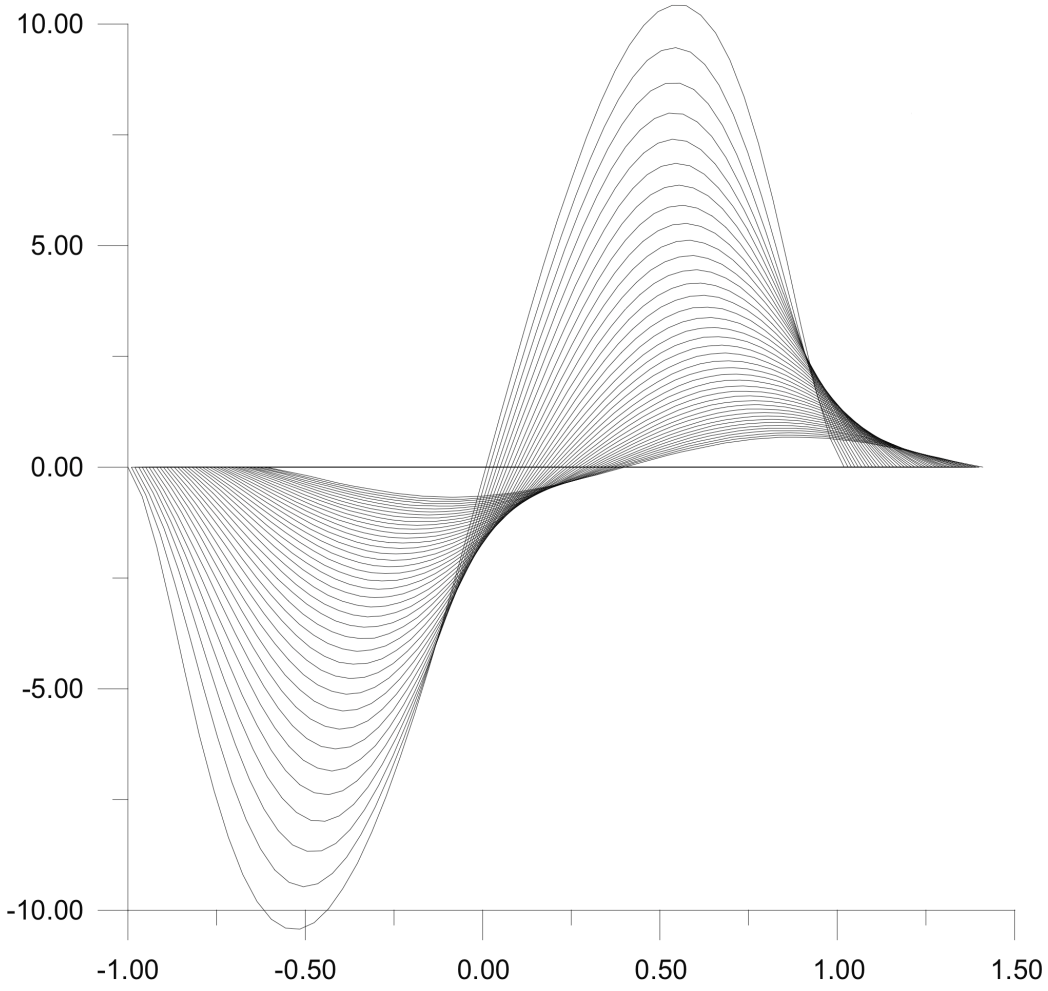

(b)

Figure A.5: Plot of the shapes the vessel takes near time zero (a) and also the velocity profiles of v (b). Here, y, v are in the vertical direction and x, u (or shifted x as time increases) are in the horizontal direction.

The equations are consistent with the Cartesian version above. All these assume that the description for decaying motion is dominated by the mode independent of θ which means in particular that the component u_θ is effectively zero and the pressure p is independent of θ. The pressure in fact satisfies $\frac{\partial p}{\partial r} = \frac{\bar{V}^2}{r}$ from the radial momentum balance. The appropriate boundary conditions are to account for a singularity-free behaviour at the origin and no slip at the circular surface of radius a say. As such,

$$\bar{V} = 0 \quad \text{at} \quad r = 0, a, \tag{A.4.15}$$

while the initial condition would take $\bar{V}$ as a multiple of r for the rotation stopping scenario. Otherwise it can be left arbitrary here. The response for large times t is expected to take the form

$$\bar{V} = f(r) \exp^{\frac{-\lambda^2 \nu t}{a^2}}, \tag{A.4.16}$$

with λ being an unknown constant giving the square root of the temporal decay rate in effect. The function $f(r)$ is to be determined. Substitution into (A.4.14), (A.4.15) then shows that more precisely $f(r)$ must be proportional to the Bessel function of the first kind J_1 giving

$$\bar{V} = A_n J_1 \left(\frac{\lambda_n r}{a} \right) \exp^{\frac{-\lambda^2 \nu t}{a^2}} . \tag{A.4.17}$$

Here, A_n remains an unknown constant of proportionality but λ_n is a root of J_1. The first root, λ_1, is the most likely to arise in practice and it has the value $\lambda_1 = 3.83$ approximately. The second root is $\lambda_2 = 7.02$ approximately. The ratio $\frac{\lambda_2^2}{\lambda_1^2}$ is in the range 3-4 and so the first root contribution can dominate for a long duration.

To compare quantitatively the analytical result (A.4.17) with the computational results in which the coefficients ν, a can be taken as unity, we address the issue of tempo-

ral decay. The analysis with n taken as 1 suggests a decay factor of approximately $\exp(-14.67t)$ from (A.4.17) indicating a factor close to 0.053 over a time duration of 0.2. This is found to agree fairly well with the Cartesian-based computational results in Figure A.7 (c). For instance, here an early-time value of about 8 for the maximum of the velocity component is seen to reduce to below 0.8 over the time scale of 0.2 even for the comparatively low values of t involved here. This trend continues throughout the flow solution at later times. The time intervals of the presentation in that figure are 0.02. Furthermore, the shape of the Bessel function J_1 is also in line with the velocity profile shapes observed in the numerical work.

The results from the three grids in Figure A.7 are seen to be fairly in agreement when the overall accuracy of the methodology is taken into account, certainly in qualitative terms and to a large extent also in quantitative terms. Coupled with the analytical comparison described above, the grid effect provides some assurance about the accuracy as well as the feasibility of applying in full the present approach to the Navier-Stokes-based behaviour.

Thus far in the work of this chapter we have explored the evolution of the flow inside the substantially deforming vessel when the effects of the initial conditions dominate over those of the kinematic boundary conditions. We believe that the inclusion of the latter would represent a further extension of much value.

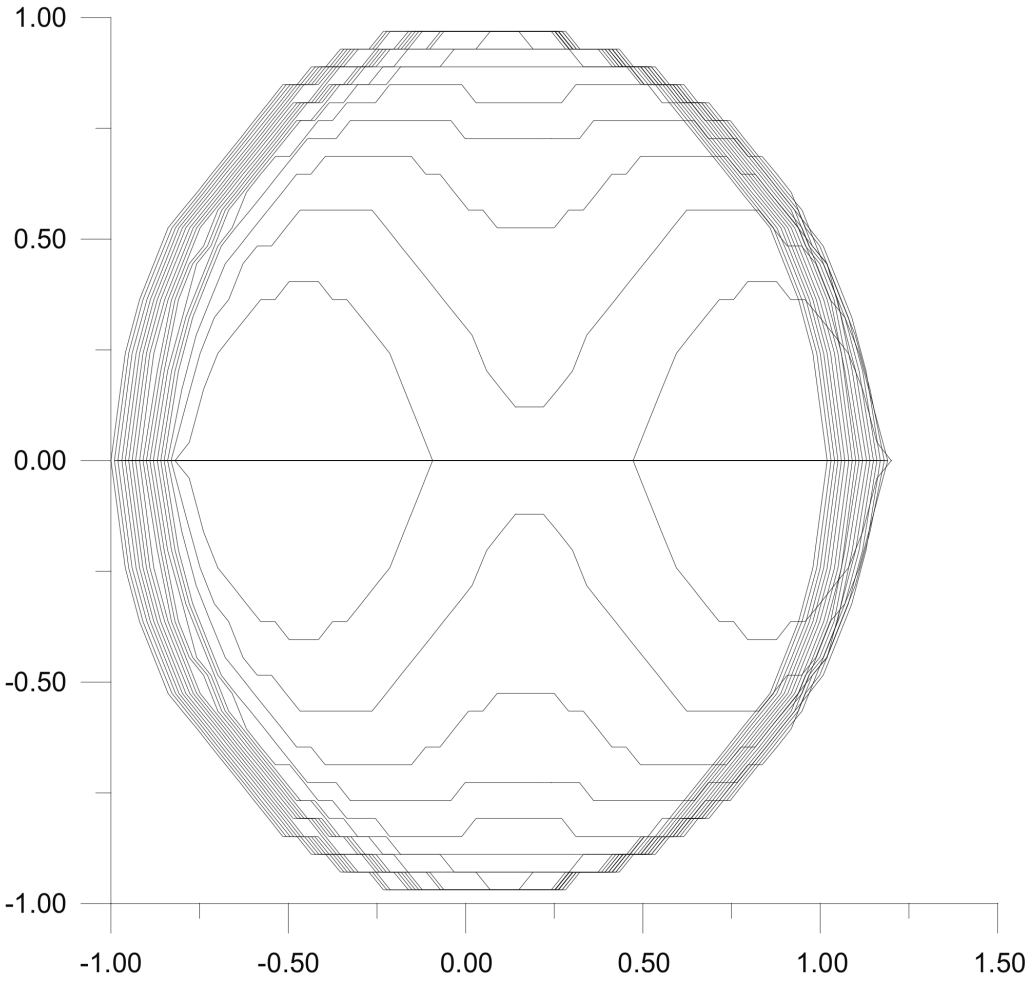

(a)

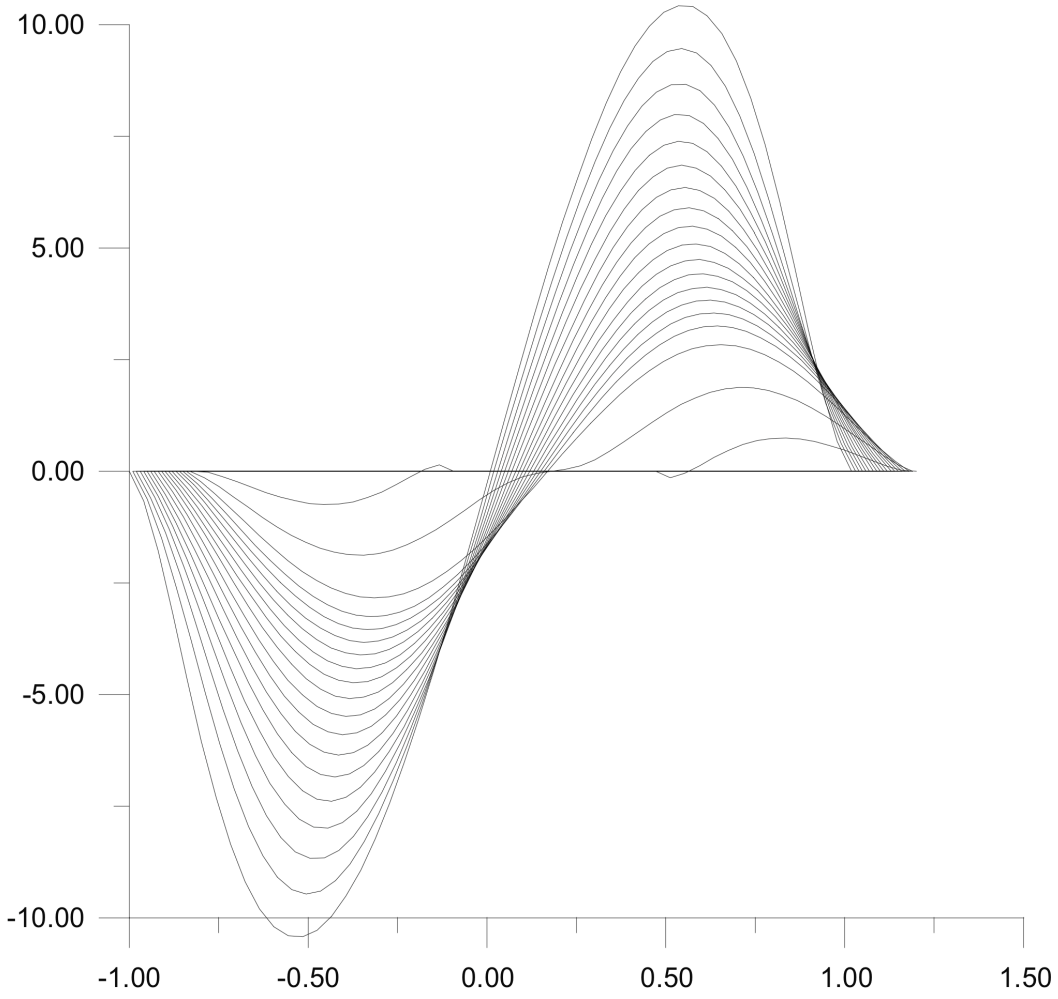

(b)

Figure A.6: Plot for a shape which evolves slightly faster in time towards a non-circular form. Here, the corresponding velocity profiles v are again presented and are somewhat more involved than the previous ones of Figure A.5. The temporal decay is nevertheless quite similar to that observed in the previous figure.

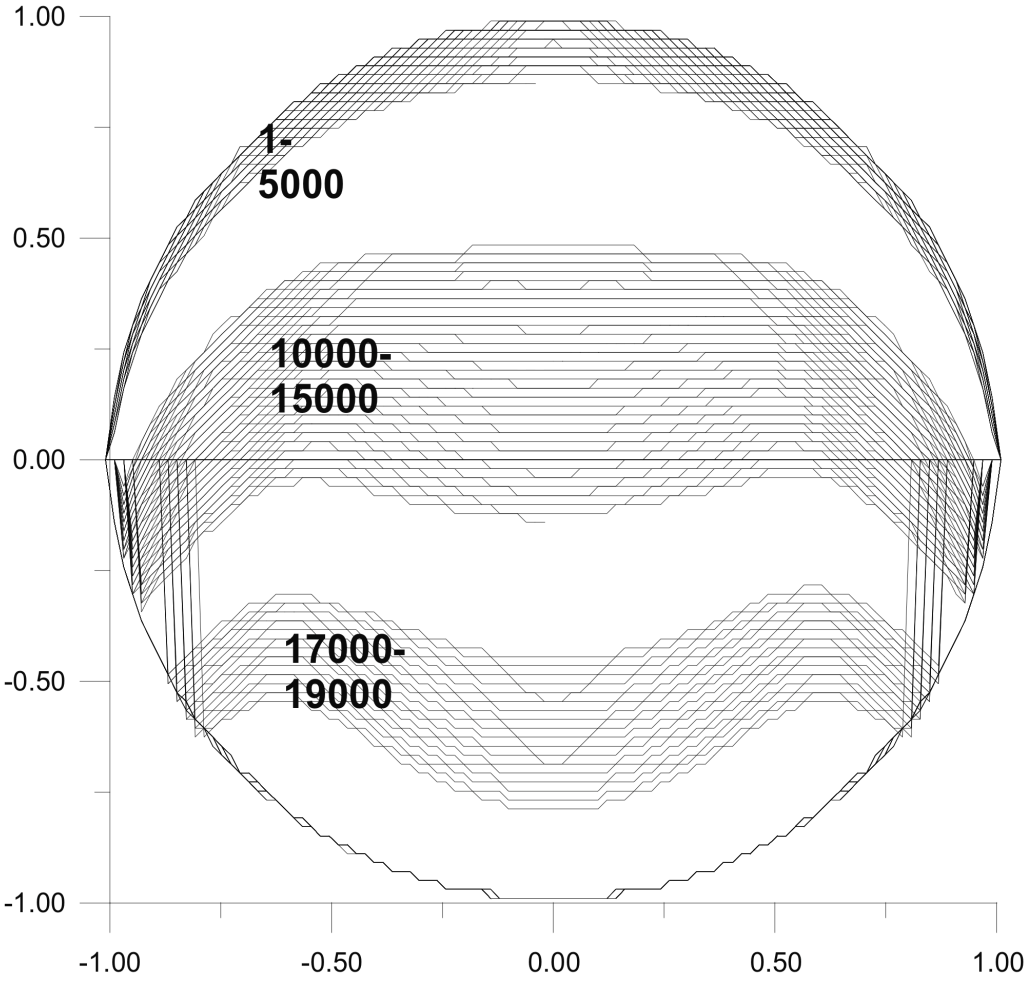
1.00
0.50
0.00
-0.50
-1.00
-1.00
-0.50
0.00
0.50
1.00
1-
5000
10000-
15000
17000-
19000

(a)

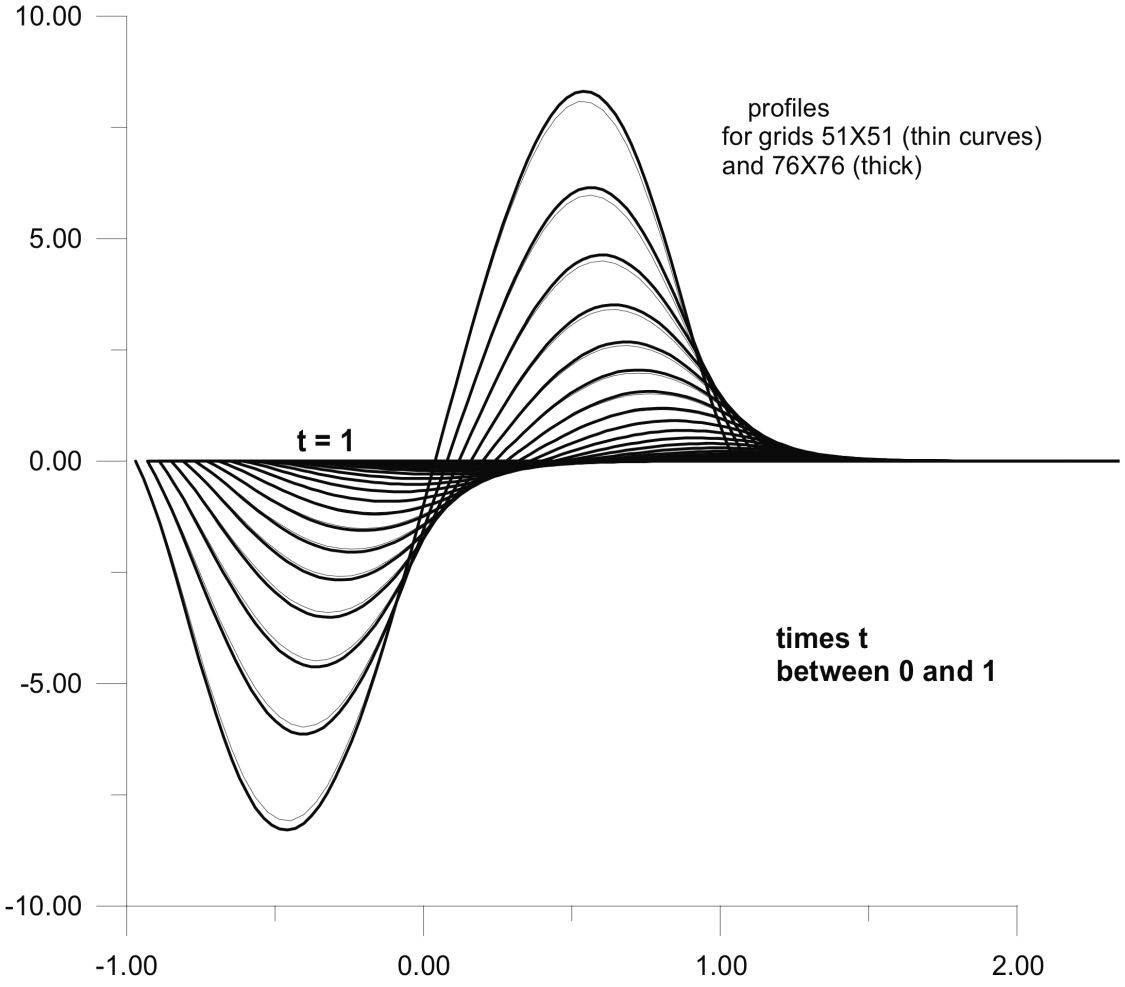
10.00
5.00
0.00
-5.00
-10.00
-1.00
0.00
1.00
2.00
profiles
for grids 51X51 (thin curves)
and 76X76 (thick)
t = 1
times t
between 0 and 1

(b)

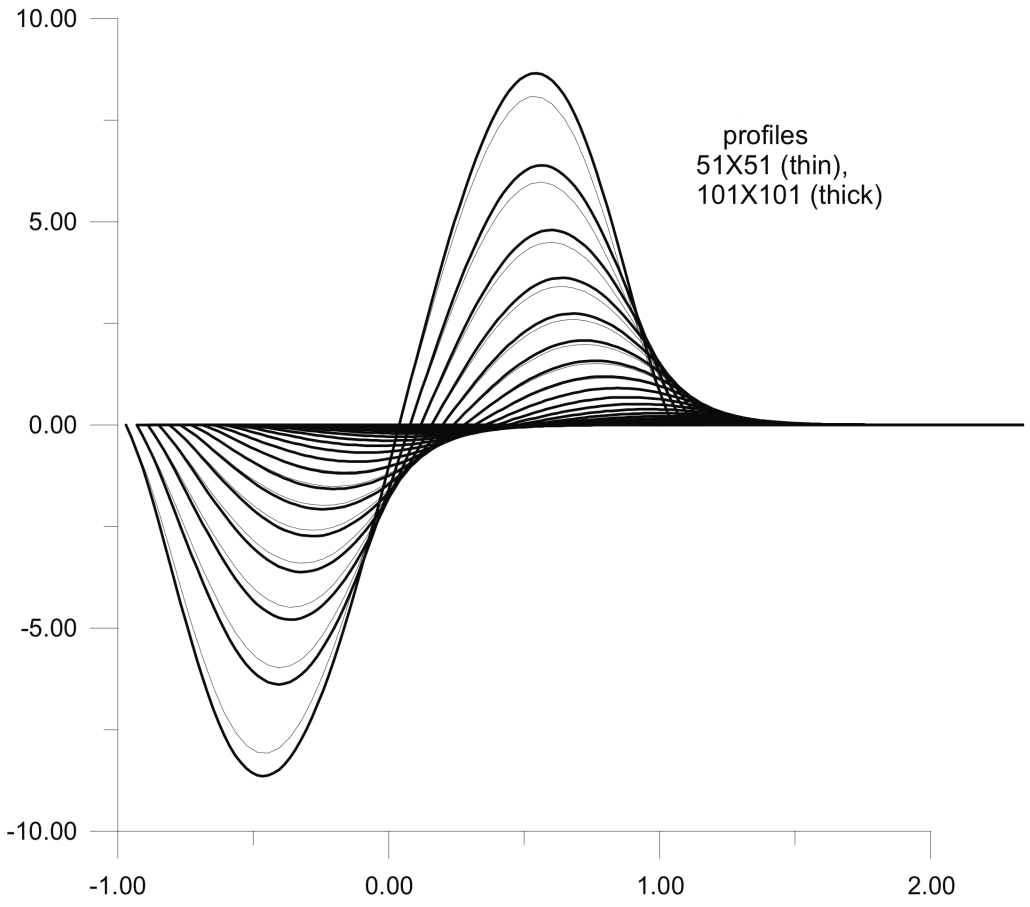

(c)

Figure A.7: Plot (a) shows a more bladder-like evolution of the cross-sectional shape which is in keeping with those studied in earlier chapters of the thesis. The numbers shown on the shapes in the figure refer to entry numbers in the associated time-marching data file and hence are a scaled measure of time t. The velocity results v for the case of (a) are given in (b) and (c) and these include results for different grids, namely, 51x51, 76x76 and 101x101 in terms of $x \,\mathrm{x}\, y$.

A.5 Summary

In this chapter, the Navier-Stokes equations are put into use to develop the modelling of the bladder. The numerical scheme is developed and we verify it through the driven cavity. The development of velocities in the vessel for different shapes and times is then compared.

Appendix B

Evaluation of Poisson Integral

A more detailed step by step solution of (2.1.2) is shown here. This determines the solution for the circular vessel. To start with, we split the integral in two parts such that

$$\frac{1-r^2}{2\pi}\int_0^{2\pi}\frac{\hat{\theta}-\sin(\hat{\theta})}{1-2r\cos(\hat{\theta}-\theta)+r^2}d\hat{\theta}$$
$$=\frac{1-r^2}{2\pi}\left(\underbrace{\int_0^{2\pi}\frac{\hat{\theta}}{1-2r\cos(\hat{\theta}-\theta)+r^2}d\hat{\theta}}_{\text{(A)}}-\underbrace{\int_0^{2\pi}\frac{\sin(\hat{\theta})}{1-2r\cos(\hat{\theta}-\theta)+r^2}d\hat{\theta}}_{\text{(B)}}\right). \quad \text{(B.0.1)}$$

We first attempt to integrate part (A) of (B.0.1),

$$A=\int_0^{2\pi}\frac{\hat{\theta}}{1-2r\cos(\hat{\theta}-\theta)+r^2}d\hat{\theta}, \quad \text{(B.0.2)}$$

and we substitute $\hat{\theta} - \theta = \varphi$ to give the following

$$A = \int_{-\theta}^{2\pi-\theta} \frac{\theta + \varphi}{1 - 2r\cos(\varphi) + r^2} d\varphi$$
$$= \underbrace{\int_{-\theta}^{2\pi-\theta} \frac{\theta}{1 - 2r\cos(\varphi) + r^2} d\varphi}_{\text{(C)}} + \underbrace{\int_{-\theta}^{2\pi-\theta} \frac{\varphi}{1 - 2r\cos(\varphi) + r^2} d\varphi}_{\text{(D)}}. \quad \text{(B.0.3)}$$

We consider

$$C = \int_{-\theta}^{2\pi-\theta} \frac{\theta}{1 - 2r\cos(\varphi) + r^2} d\varphi. \quad \text{(B.0.4)}$$

This can be calculated by means of the complex plane by substituting the following $z = e^{i\varphi} \Rightarrow d\varphi = \frac{dz}{iz}$. We end up with

$$C = \frac{-\theta}{i} \oint_C \frac{dz}{r(z - r)(z - r^{-1})}. \quad \text{(B.0.5)}$$

This result gives two poles for z. The only one inside the circle is at point r, with r^{-1} outside. It therefore yields the contribution

$$C = \frac{2\pi\theta}{1 - r^2}. \quad \text{(B.0.6)}$$

We now integrate part (D) of equation (B.0.3) which can be split once again into

$$\int_{-\theta}^{2\pi-\theta} \frac{\varphi}{1 - 2r\cos(\varphi) + r^2} d\varphi$$
$$= \underbrace{\int_{-\theta}^{\pi-\theta} \frac{\varphi}{1 - 2r\cos(\varphi) + r^2} d\varphi}_{\text{(E)}} + \underbrace{\int_{\pi-\theta}^{2\pi-\theta} \frac{\varphi}{1 - 2r\cos(\varphi) + r^2} d\varphi}_{\text{(F)}}. \quad \text{(B.0.7)}$$

Making the substitution $\varphi = 2\pi - B$ in part (F) of equation (B.0.7) gives

$$\int_{\pi+\theta}^{\theta} \frac{-(2\pi - B)}{1 - 2r\cos(B) + r^2} dB = \int_{\theta}^{\pi+\theta} \frac{2\pi}{1 - 2r\cos(B) + r^2} dB - \int_{\theta}^{\pi+\theta} \frac{B}{1 - 2r\cos(B) + r^2} dB, \quad \text{(B.0.8)}$$

and we now substitute $B = \varphi$ into (B.0.8) and add (E) of equation (B.0.7) to equation (B.0.8). As such, we now have

$$\int_{-\theta}^{2\pi-\theta} \frac{\varphi}{1 - 2r\cos(\varphi) + r^2} d\varphi = \underbrace{\int_{-\theta}^{\pi-\theta} \frac{\varphi}{1 - 2r\cos(\varphi) + r^2} d\varphi}_{(\alpha)} + \underbrace{\int_{\theta}^{\pi+\theta} \frac{2\pi}{1 - 2r\cos(\varphi) + r^2} d\varphi}_{(\beta)} - \underbrace{\int_{\theta}^{\pi+\theta} \frac{\varphi}{1 - 2r\cos(\varphi) + r^2} d\varphi}_{(\gamma)}. \quad \text{(B.0.9)}$$

If we now look carefully at (α) and (γ), we can see that we have the same integral over a different range. Yet, part of it overlaps. Hence, we can cancel the overlapping parts (from θ to $\pi - \theta$) and we are therefore left with

$$\underbrace{\int_{-\theta}^{\theta} \frac{\varphi}{1 - 2r\cos(\varphi) + r^2} d\varphi}_{(\delta)} - \underbrace{\int_{\pi-\theta}^{\pi+\theta} \frac{\varphi}{1 - 2r\cos(\varphi) + r^2} d\varphi}_{(\epsilon)} + \underbrace{\int_{\theta}^{\pi+\theta} \frac{2\pi}{1 - 2r\cos(\varphi) + r^2} d\varphi}_{(\zeta)}. \quad \text{(B.0.10)}$$

The two remaining integrals now need to be tackled, one for a range of $-\theta$ to θ and another for $\pi - \theta$ to $\pi + \theta$. (β) is also left to be solved. The (δ) part of equation (B.0.10) is odd therefore,

$$\int_{-\theta}^{\theta} \frac{\varphi}{1 - 2r\cos(\varphi) + r^2} d\varphi = 0. \quad \text{(B.0.11)}$$

We now tackle part (ϵ) and we will do that by means of a substitution. Let $\varphi = \pi + V$ yielding to

$$-\int_{\pi-\theta}^{\pi+\theta} \frac{\varphi}{1-2r\cos(\varphi)+r^2}d\varphi = -\int_{-\theta}^{\theta} \frac{\pi+V}{1-2r\cos(V)+r^2}dV$$
$$= \underbrace{-\int_{-\theta}^{\theta} \frac{\pi}{1-2r\cos(V)+r^2}dV}_{(\eta)} \underbrace{-\int_{-\theta}^{\theta} \frac{V}{1-2r\cos(V)+r^2}dV}_{(\kappa)}. \quad \text{(B.0.12)}$$

Since (κ) is the same with (δ), it also vanishes. Hence, we end up having to integrate only

$$-\int_{-\theta}^{\theta} \frac{\pi}{1-2r\cos(V)+r^2}dV, \quad \text{(B.0.13)}$$

which is achieved by the substitution of $t = \tan(\frac{V}{2})$. In other words, $V = 2\arctan(t)$ and hence differentiating V with respect to t gives

$$\frac{dV}{dt} = \frac{2}{1+t^2} \Rightarrow \frac{2dt}{1+t^2} = dV,$$

and also follows that

$$\cos(V) = \frac{1-t^2}{1+t^2}.$$

Substituting into the integrand, making some cancelations and adjusting the limits, we have

$$-\int_{-\theta}^{\theta} \frac{\pi}{1-2r\cos(V)+r^2}dV = \frac{-2\pi}{(1-r)^2}\int_{\tan(\frac{-\theta}{2})}^{\tan(\frac{\theta}{2})} \frac{dt}{t^2+\frac{(1+r)^2}{(1-r)^2}}. \quad \text{(B.0.14)}$$

The fact that the function is even yields to

$$\frac{-4\pi}{(1-r)^2}\int_{0}^{\tan(\frac{\theta}{2})} \frac{dt}{t^2+\frac{(1+r)^2}{(1-r)^2}}. \quad \text{(B.0.15)}$$

Integrating this gives us the answer to (ϵ) and hence,

$$-\int_{\pi-\theta}^{\pi+\theta}\frac{\varphi}{1-2r\cos(\varphi)+r^2}d\varphi=\frac{-4\pi}{(1-r^2)}\arctan\left(\frac{(1-r)\tan(\frac{\theta}{2})}{(1+r)}\right). \tag{B.0.16}$$

So we are now done with (α) and (γ) and are only left with (β) (or (ζ)) of equation (B.0.9) to evaluate. It is worked out in the same way as the above (i.e. by substituting $t=\tan(\frac{\varphi}{2})$) giving

$$\begin{aligned}\int_{\theta}^{\pi+\theta}&\frac{2\pi}{1-2r\cos(\varphi)+r^2}d\varphi\\&=\frac{4\pi}{(1-r^2)}\left(\arctan\left(\frac{(1+r)\tan(\frac{\pi+\theta}{2})}{(1-r)}\right)-\arctan\left(\frac{(1+r)\tan(\frac{\theta}{2})}{(1-r)}\right)\right).\end{aligned} \tag{B.0.17}$$

Adding together (B.0.16),(B.0.17) gives us the result for (D) in equation (B.0.3)

$$\begin{aligned}\int_{-\theta}^{2\pi-\theta}&\frac{\varphi}{1-2r\cos(\varphi)+r^2}d\varphi\\&=\frac{4\pi}{(1-r^2)}\left(\arctan\left(\frac{(1+r)\tan(\frac{\pi+\theta}{2})}{(1-r)}\right)\right.\\&\left.-\arctan\left(\frac{(1+r)\tan(\frac{\theta}{2})}{(1-r)}\right)+\arctan\left(\frac{(1-r)\tan(\frac{\theta}{2})}{(1+r)}\right)\right).\end{aligned} \tag{B.0.18}$$

We then simplify our result by means of

$$\cot\left(\frac{-\theta}{2}\right)=-\cot\left(\frac{\theta}{2}\right),\ \tan\left(\frac{\pi}{2}+\frac{\theta}{2}\right)=\cot\left(\frac{-\theta}{2}\right),\ \cot\left(\frac{\theta}{2}\right)=\frac{1}{\tan\left(\frac{\theta}{2}\right)},$$

and hence equation (B.0.18) becomes

$$\begin{aligned}\frac{4\pi}{(1-r^2)}&\left(\arctan\left(\frac{(1+r)\cot(\frac{-\theta}{2})}{(1-r)}\right)\right.\\&\left.-\arctan\left(\frac{(1+r)\tan(\frac{\theta}{2})}{(1-r)}\right)-\arctan\left(\frac{(1-r)}{(1+r)\cot(\frac{\theta}{2})}\right)\right).\end{aligned} \tag{B.0.19}$$

Now, using the convenient definition that

$$\arctan(x) = \begin{cases} -\frac{\pi}{2} - \arctan\left(\frac{1}{x}\right), & \text{for } x < 0 \ , \\ \frac{\pi}{2} - \arctan\left(\frac{1}{x}\right), & \text{for } x > 0 \ , \end{cases}$$

substituting into the equation above and doing the necessary algebra, we find that

$$\frac{1-r^2}{2\pi}\int_{-\theta}^{2\pi-\theta} \frac{\varphi}{1-2r\cos(\varphi)+r^2}d\varphi = \begin{cases} \pi - 2\arctan\left(\frac{(1+r)\tan(\frac{\theta}{2})}{(1-r)}\right) & \text{for } 0 \leqslant \theta < \pi \ , \\ -\pi - 2\arctan\left(\frac{(1+r)\tan(\frac{\theta}{2})}{(1-r)}\right) & \text{for } \pi \leqslant \theta < 2\pi \ . \end{cases} \tag{B.0.20}$$

So, we finally add (C) of equation (B.0.3). Adding up with (A) of (2.1.17) we end up with

$$\frac{1-r^2}{2\pi}\int_{0}^{2\pi} \frac{\hat{\theta}}{1-2r\cos(\hat{\theta}-\theta)+r^2}d\hat{\theta} = \begin{cases} \theta + \pi - 2\arctan\left(\frac{(1+r)\tan(\frac{\theta}{2})}{(1-r)}\right) & \text{for } 0 \leqslant \theta < \pi \ , \\ \theta - \pi - 2\arctan\left(\frac{(1+r)\tan(\frac{\theta}{2})}{(1-r)}\right) & \text{for } \pi \leqslant \theta < 2\pi \ . \end{cases} \tag{B.0.21}$$

Next, we attempt to integrate part (B) of equation (2.1.17), namely,

$$-\int_{0}^{2\pi} \frac{\sin(\hat{\theta})}{1-2r\cos(\hat{\theta}-\theta)+r^2}d\hat{\theta}. \tag{B.0.22}$$

Once again, we substitute $\varphi = \hat{\theta} - \theta$. Forgetting for simplicity the negative sign for now, we end up with

$$\int_{-\theta}^{2\pi-\theta} \frac{\sin(\varphi+\theta)}{1-2r\cos(\varphi)+r^2}d\varphi = \underbrace{\int_{-\theta}^{2\pi-\theta} \frac{\sin(\varphi)\cos(\theta)}{1-2r\cos(\varphi)+r^2}d\varphi}_{\text{(AA)}} + \underbrace{\int_{-\theta}^{2\pi-\theta} \frac{\sin(\theta)\cos(\varphi)}{1-2r\cos(\varphi)+r^2}d\varphi}_{\text{(BB)}}, \tag{B.0.23}$$

using the double angle formula. Now, tackling first integral (AA) by substituting $u = \cos(\varphi)$ and $du = -\sin(\phi)d\varphi$ gives the following result:

$$-\cos(\theta)\int_{\cos(-\theta)}^{\cos(2\pi-\theta)}\frac{du}{1-2ru+r^2}=0, \tag{B.0.24}$$

since $\cos(-\theta)=\cos(2\pi-\theta)$. Therefore, we are left with (BB)

$$\sin(\theta)\int_{-\theta}^{2\pi-\theta}\frac{\cos(\varphi)}{1-2r\cos(\varphi)+r^2}d\varphi. \tag{B.0.25}$$

Now, we write $\cos(\varphi) = -\frac{1}{2r}\left(1+r^2-2r\cos(\varphi)\right)+\frac{1+r^2}{2r}$ and substitute this in our integral. Hence,

$$\underbrace{-\frac{\sin(\theta)}{2r}\int_{-\theta}^{2\pi-\theta}d\varphi}_{\text{(CC)}}+\underbrace{\frac{(1+r^2)\sin(\theta)}{2r}\int_{-\theta}^{2\pi-\theta}\frac{d\varphi}{1+r^2-2r\cos(\varphi)}}_{\text{(DD)}}. \tag{B.0.26}$$

We first integrate (CC) which is quite simple

$$-\frac{\sin(\theta)}{2r}\int_{-\theta}^{2\pi-\theta}d\varphi=-\frac{\pi\sin(\theta)}{r}. \tag{B.0.27}$$

Then, we move on to (DD) which is the the same as integral (B.0.4) apart from the constant yielding to

$$\frac{(1+r^2)\sin(\theta)}{2r}\int_{-\theta}^{2\pi-\theta}\frac{d\varphi}{1+r^2-2r\cos(\varphi)}=\frac{\pi\sin(\theta)}{r(1-r^2)}+\frac{\pi r\sin(\theta)}{1-r^2}. \tag{B.0.28}$$

Hence,

$$\int_{-\theta}^{2\pi-\theta}\frac{\sin(\varphi+\theta)}{1-2r\cos(\varphi)+r^2}d\varphi=-\frac{\pi\sin(\theta)}{r}+\frac{\pi\sin(\theta)}{r(1-r^2)}+\frac{\pi r\sin(\theta)}{1-r^2}, \tag{B.0.29}$$

and, after multiplying by the constant, we obtain

$$\frac{1-r^2}{2\pi}\int_{-\theta}^{2\pi-\theta}\frac{\sin(\varphi+\theta)}{1-2r\cos(\varphi)+r^2}d\varphi=r\sin(\theta). \tag{B.0.30}$$

Therefore, adding together parts (A) and (B) from equation (2.1.17), we have

$$\begin{aligned}\psi(r,\hat{\theta}) &= \frac{1-r^2}{2\pi}\int_0^{2\pi}\frac{\hat{\theta}-\sin(\hat{\theta})}{1-2r\cos(\hat{\theta}-\theta)+r^2}d\hat{\theta} \\ &= \begin{cases} \theta - r\sin(\theta) + \pi - 2\arctan\left(\frac{(1+r)\tan(\frac{\theta}{2})}{(1-r)}\right) & \text{for } 0 \leqslant \theta < \pi \ , \\ \theta - r\sin(\theta) - \pi - 2\arctan\left(\frac{(1+r)\tan(\frac{\theta}{2})}{(1-r)}\right) & \text{for } \pi \leqslant \theta < 2\pi \ . \end{cases}\end{aligned} \tag{B.0.31}$$

Bibliography

[1] Abrams, P. (2006) *Urodynamics*. Springer.

[2] Abrams, P. (1997) The urodynamics of lower urinary tract symptoms (LUTS). *Proceedings of the 4th International Consultation on BPH.*, 11. France.

[3] Abrams, P., Cardozo, L., Fall, M., Griffiths, D., Rosier, P., Ulmsten, U., van Kerrebroek, P., Victor, A., & Wein, A. (2002) The Standardisation of the Terminology of Lower Urinary Tract Function: Report from the Standardisation Sub-committee of the International Continence Society. *Neurology and Urodynamics*, 21, 167-178.

[4] Alexandre, F., Sayed, E., & Rania, F. (2008) 3D reconstruction of pelvic floor for numerical simulation purpose. *Vipimage-Eccomas*, 359-362.

[5] Aliabadi, M.H., & Wrobel, L. (2002) *The Boundary Element Method*, Volume 1 and 2. John Wiley.

[6] Band, L.R., Cummings, L.J., Waters, S.L., & Wattis, J.A.D. (2009) Modelling crystal aggregation and deposition in the catheterised lower urinary tract. *Journal of Mathematical Biology*, 59, 809-840.

[7] Barry, M.J., Fowler, F.J., O'Leary, M.P., Bruskewitz, R.C., Haltgrewe, H.L., & Mebust, W.K. (1992) The American urological association symptom index for benign prostatic hyperplasia. *Journal of Urology*, 48, 1549-1557.

[8] Batchelor, G.K. (1964) Axial Flow in trailing line vortices. *Journal of Fluid Mechanics*, 20(4), 645-658.

[9] Batchelor, G.K. (1991) *An Introduction to Fluid Dynamics*. Cambridge University Press.

[10] Becker, A.A. (2001) *The Boundary Element Method in Engineering: a complete course*. McGraw-Hill.

[11] Beer, G. (2001) *Programming the Boundary Element Method, an introduction for engineers*. Wiley.

[12] Beyer, R.P., & Leveque, R.J. (1992) Analysis of a one dimensional model for the immersed boundary method. *Society for Industrial and Applied Mathematics*, 29(2), 332-364.

[13] Bhatti, M.A. (2006) *Advanced Topics in Finite Element Analysis of Structures, with Mathematica and MatLab Computations*. John Wiley.

[14] Biran, A., & Breiner, M. (2002) *MATLAB 6 for Engineers*. Pearson Education.

[15] Bonnet, M. (1995) *Boundary Integral Equation Methods for Solids and Fluids*. Wiley.

[16] Boos, K., Cardozo, L., Anders, K., & Malone-Lee, J.G. (1996) The calculations of detrusor muscle velocity to explain voiding difficulties after Burch colposuspension. *Proceedings of the International Continence Society Annual Meeting*, Abstract 281.

[17] Bowles, R.I., Ovenden, N.C., & Smith, F.T. (2008) Multi-branching three-dimensional flow with substantial changes in vessel shapes. *Journal of Fluid Mechanics*, 614, 329-354.

[18] Boyanov, T., Dimova, S., Georgiev, K., & Nikolov, G. (2006) *Numerical Methods and Applications: 6th international conference*. Springer.

[19] Capecchi, V. (2010) *Applications of Mathematics in Models, Artificial Neural Networks and Arts: Mathematics and Society*. Springer.

[20] Carrrier, G.F., Krook, M., & Pearson, C.E. (2005) *Functions of a Complex Variable, Theory and Technique*. SIAM.

[21] Celik, I.B., Bayrak, C., Varol, A., & Nanduri, J.R. (2007) A one-dimensional mathematical model for urodynamics. *Proceedings of FEDSM2007 5th Joint ASME/JSME Fluids Engineering Conference*, 2, 765-771.

[22] Chan, J.C.L., & Kepert, J.D. (2010) *Global Perspectives on Tropical Cyclones: From Science to Mitigation*. World Scientific.

[23] Chapple, C.R., MacDiarmid, S.A., & Patel, A. (2010) *Urodynamics Made Easy*. Elsevier Health Sciences.

[24] Chapra, S.C. (2008) *Applied Numerical Methods with MATLAB for Engineers and Scientists*. McGraw-Hill Education.

[25] Chen, G. & Zhou, J. (1992) *Boundary Element Methods*. Academic Press.

[26] Chitode, J.S. (2010) *Numerical Methods*. Technical Publications.

[27] College of Radiology, *Academy of Medicine of Malaysia*.

[28] Cooper, J. (1998) *Introduction to Partial Differential Equations with MATLAB*. Springer.

[29] Croitoru, S., Gross, M., & Barmeir, E. (2007) Duplicated Ectopic Ureter with Vaginal Insertion: 3D CT Urography with IV and Percutaneous Contrast Administration. *American Journal of Roentgenology*, 189, w272-w274.

[30] Cummings, L.J., Waters, S.L., Wattis, J.A.D., & Graham, S.J. (2004) The effect of ureteric stents on urine flow: reflux. *Journal of Mathematical Biology*, 49, 56-82.

[31] Cushman-Roisin, B. (1994) *Introduction to Geophysical Fluid Dynamics*. Prentice Hall.

[32] Damaser, M.S., & Lehman, S.L. (1995) The effect of urinary bladder shape on its mechanics during filling, *Journal of Biomechanics* 28, (6), 725-732.

[33] Delancet, J.O. (1993) Anatomy and biomechanics of genital prolapsed. *Clinical Obstetrics and Gynaecology*, 36(4), 897-909.

[34] Doctors Gate, *Medical diagrams and articles*.

[35] Engeln-Mullges, G., & Uhlig, F. (1996) *Numerical Algorithms with C*, Volume 1. Springer.

[36] Farrashkhalvat, M., & Miles, J.P. (2003) *Basic Structured Grid Generation with an Introduction to Unstructured Grid Generation*. Butterworth-Heinemann.

[37] Fausett, L.V. (1999) *Applied Numerical Analysis using MATLAB*. Prentice Hall.

[38] Fornberg, B. (1998) *A Practical Guide to Pseudospectral Methods*. Cambridge University Press.

[39] Forsythe, G.E., & Wason, W.R. (1960) *Finite-Difference Methods for Partial Differential Equations*. Wiley.

[40] Frankel, S.T. (1950) Convergence Rates of Iterative Treatments of Partial Differential Equations. *Mathematical Tables and Other Aids to Computation*, 4, 65-75.

[41] Gaul, L., Kogl, M., & Wagner, M. (2003) *Boundary Element Methods for Engineers and Scientists: an Introductory Course with Advanced Topics*. Springer.

[42] Ghia, U., Ghia, K.N., & Shin, C.T. (1982) High-Re solutions for incompressible flow using the Navier-Stokes equations and a multigrid method. *Journal of Computational Physics*, 48, 387-411.

[43] Glavin, S. (2011) *Mathematical modelling of urethral and other similar flows*. Unpublished PhD thesis.

[44] Gosling, J.A. (1979) The structure of the bladder and urethra in relation to function. *Urologic Clinics of North America*, 6, 31-38.

[45] Gray, H. (1918) *Anatomy of the Human Body*. Lea & Febiger.

[46] Greene, R.E., & Krantz, S.G. (2006) *Function Theory of One Complex Variable*. AMS Bookstore.

[47] Griffiths, D.J. (1977) Urodynamic assessment of bladder function. *British Journal of Urology*, 49, 29-36.

[48] Griffiths, D.J. (1980) *Urodynamics - The Mechanics and Hydrodynamics of the Lower Urinary Tract*. Hilger.

[49] Griffiths, D.J. (1982) The mechanism of micturition. In Chisholm, G.D., & Innes Williams D. (Eds.), *Scientific Foundations of Urology*, 411-420. Heinemann.

[50] Griffiths, D.J., Constantinou, C.E., & Van Mastrigt, R. (1986) Urinary bladder function and its control in healthy females. *American Journal of Physiology* (Regulatory Integrative and Comparative Physiology 20), 251, R225-R230.

[51] Griffiths, D.J. (1988) Mechanics of micturition. In Yalla, S.V. McGuire, E.J., Elbadawi, E., & Blaivas, J.G. (Eds.), *Neurourology and urodynamics: principles and practice*, 96-105. Macmillan.

[52] Griffiths, D.J. (1994) Hydrodynamics and mechanics of the bladder and urethra. In Mundy, A.R., Stephenson, T.P., & Wein, A.J. (Eds.), *Urodynamics: Principles Practice and Application*, 2nd ed, 71-81. Churchill Livingstone.

[53] Griffiths, D.J. , Harding, C., Blake, C., McIntosh, S., Drinnan, M.J., Robson, W.A., Abrams, P., Ramsden, P.D., & Pickard, R.S. (2004) A nomogram to classify men with lower urinary tract symptoms using urine flow and noninvasive measurement of bladder pressure. *Journal of Urology*, 174(4), 1323-1326.

[54] Gu, Y.T., & Liu, G.R. (2001) A coupled element free Galerkin boundary element method for stress analysis of two-dimensional solids. *Computer Methods in Applied Mechanics and Engineering*, 190(34), 4405-4419.

[55] Gufler, H., Ohde, A., Grau, G., & Grossmann, A. (2004) Colpocystoproctography in the upright and supine positions correlated with dynamic MRI of the pelvic floor. *European Journal of Radiology*, 51(1), 41-47.

[56] Hakenberg, O.W., Linne, C., Manseck, A., & Wirth, M.P. (2000) Bladder wall thickness in normal adults and men with mild lower urinary tract symptoms and benign prostatic enlargement. *Neurourology and Urodynamics*, 19, 585-593.

[57] Hald, T., Nielsen, K.K., & Nordling, J. (1993) Clinical urodynamics in benign hyperplasia. *European Urology Update Series*, 2, 74-79.

[58] Hanselman, D., & Littlefield, B. (2001) *Mastering MATLAB 6, a comprehensive tutorial and reference*. Prentice Hall.

[59] David, A., & Hatch, M.D. *Loyola University Stritch School of Medicine*.

[60] Hicks, P.D., & Smith, F.T. (2010) Skimming impacts and rebounding from shallow liquid-layers. *Proceedings of the Royal Society*, A 467(2127), 653-674.

[61] Hoffman, J.D. (2001) *Numerical Methods for Engineers and Scientists*. Marcel Dekker.

[62] Hoppensteadt, F.C. & Peskin, C.S. (2002) *Modelling and Simulation in Medicine and Life Sciences*. Springer.

[63] Hullfish, K.L. (2008) Pelvic floor dysfunction–what do women really want? *Journal of Urology*, 179(6), 2092-2093.

[64] Jeffrey, A., & Dai, H.H. (2008) *Handbook of Mathematical Formulas and Integrals*. Academic Press.

[65] Jin, Q., Zhang, X., Li, X., & Wang, J. (2010) Dynamics of bladder-urethra system based on CFD. *Frontiers Mechanical Engineering in China*, 5(3), 336-340.

[66] Jin, Y.M., & Kim, T.K. (2002) The usefulness of bladder wall thickness measurement using ultrasound in patients with benign prostatic hyperplasia. *Korean Journal of Urology*, 43, 598-604.

[67] Johnson, R.W. (1998) *Handbook of Fluid Dynamics*. Springer.

[68] Kageyama, A., & Sato, T. (2004) The "Yin-Yang Grid": An overset grid in spherical geometry. *Geochemistry Geophysics Geosystems*, 5 (Q09005).

[69] Kahle, W., Leonhardt, H., & Platzer, W. (1993) *Color Atlas and Textbook of Human Anatomy - Internal Organs*. Thieme.

[70] Klevmark, B. (1980) Motility of the urinary bladder in cats during filling at physiological rates. *Scandinavian Journal of Urology and Nephrology*, 14, 219-224.

[71] Knight, C. (2010) *English Cyclopedia*. Bibliolife.

[72] Kuo, H.C., Chen, Y.C., Chen, C.Y., & Chancellor, M.B. (2009) Transabdominal ultrasound measurement of detrusor wall thickness in patients with overactive bladder. *Tzu Chi Medical Journal*, 21(2), 129-135.

[73] Lai, M.C., &. Peskin, C.S. (2000) An Immersed boundary method with formal second-order accuracy and reduced numerical viscosity. *Journal of Computational Physics*, 160, 705-719.

[74] Sir Lamb, H. (1895) *Hydrodynamics*. Cambridge University Press.

[75] Li, M., Tang, T., & Fornberg, B. (1995) A compact fourth-order finite difference scheme for the steady incompressible Navier-Stokes equations. *International Journal for Numerical Methods in Fluids*, 20, 1137-1151.

[76] Li, X., Chen, D., Peng, X., Takahashi, K., & Xiao, F. (2007) A multimoment finite-volume shallow-water model on the YinYang overset spherical grid. *Monthly Weather Review*, 136, 3066-3086.

[77] Lynoudis, P.S., & Roos, R. (1970) The fluid mechanics of the ureter from a lubrication theory point of view. *Journal of Fluid Mechanics*, 43(4), 661-674.

[78] Manieri, C., Carter, S.S.C., Romano, G., Trucchi, A., Valenti, M., & Tubaro, A. (1998) The diagnosis of bladder outlet obstruction in men by ultrasound measurement of bladder wall thickness. *Journal of Urology*, 159, 761-775.

[79] Marsden, J.E. (1984) *Fluids and Plasmas: geometry and dynamics*. AMS Bookstore.

[80] Marshall, J.S. (2001) *Inviscid Incompressible Flow*. Wiley - IEEE.

[81] Mei, R., & Plotkin, A. (1986) A finite-difference scheme for the solution of the steady Navier-Stokes equations. *Computers & Fluids*, 14(3), 239-251.

[82] Milne-Thomson, L.M. (1996) *Theoretical Hydrodynamics*. Courier Dover Publications.

[83] Ney, C., & Friedenberg, R.M. (1981) *Radiographic Atlas of the Genitourinary System*, Volume 2. J.B. Lippencott Company.

[84] Niu, Y.Y., & Chang, D.Y. (2007) CFD simulation of shear stress and secondary flows in urethra. *Biomedical Engineering: Applications Basis and Communications*, 19(2), 117-127.

[85] NorthWest Radiology Associates: *Radiology Services, Imaging Services and Teleradiology Services*.

[86] Osswald, T.A., Turng, L.S., & Gramann, P.J. (2007) *Injection Molding Handbook*, Hanser Verlag.

[87] Paris, F., & and Canas, J. (1997) *Boundary Element Method, fundamentals and applications*. Oxford University Press.

[88] Pasipoularides, A. (2009) *Heart's Vortex - Intracardiac Blood Flow Phenomena*. PMPH-USA.

[89] Pel, J.J., & van Mastrigt, R. (2007) Development of a CFD urethral model to study flow-generated vortices under different conditions of prostatic obstruction. *Physiological Measurement*, 28(1), 13-23.

[90] Peskin, C.S. (2002) The immersed boundary method. *Acta Numerica*, 11, 479-517.

[91] Pozrikidis, C. (2002) *A Practical Guide to Boundary Element Methods with the Software Library BEMLIB*. Chapman & Hall/CRC.

[92] *Princeton University*, images and scans.

[93] Rosar, M.E., & Peskin, C.S. (2001) Fluid flow in collapsible elastic tubes: A three-dimensional numerical model. *New York Journal of Mathematics*, 7, 281-302.

[94] Runchal, A.K., Spalding, D.B., & Wolfshtein, M. (1969) Numerical Solution of the Elliptic Equations for Transport of Vorticity, Heat, and Matter in Two-Dimensional Flow. *Physics of Fluids*, 12(II), 22-28.

[95] Salmon, R. (1998) *Lectures on geophysical fluid dynamics*. Oxford University Press.

[96] Salmond, D.J. (1983) *Calculation of Aerodynamic Forces on an oscillating aerofoil in transonic flow*. Unpublished PhD Thesis.

[97] Schinzinger, R., & Laura, P.A.A. (2003) *Conformal Mapping: Methods and Applications*. Courier Dover Publications.

[98] Schmidt, F., Shin, P., Jorgensen, T.M., Djurhuus, J.C., & Constantinou, C. E. (2002) Urodynamic patterns of normal male micturition influence of water consumption on urine production and detrusor function. *Journal of Urology*, 168(4 Pt 1), 1458-63.

[99] Shapiro, A.H., Jaffrin, M.Y., & Weinberg, S.L. (1969) Peristaltic pumping with long wavelengths at low Reynolds number. *Journal of Fluid Mechanics*, 37(4), 799-825.

[100] Smith, F.T., & Ellis, A.S. (2010) On interaction between falling bodies and the surrounding uid. *Mathematika*, 56, 140-168.

[101] Smith, F.T.: *Private communication from Professor Frank T. Smith.*

[102] Snell, R.S. (2004) *Clinical Anatomy: an illustrated review with questions and explanations*. Lippincott Williams & Wilkins.

[103] Snell, R.S. (2007) *Clinical Anatomy by regions*. Lippincott Williams & Wilkins.

[104] Snooks, S.J., Swash, M., Mathers, S.E., & Henry, M.M. (1990) Effect of vaginal delivery on the pelvic floor: a 5-year follow-up. *British Journal of Surgery*, 77(12), 1358-1360.

[105] Stanoyevitch, A. (2005) *Introduction to Numerical Ordinary and Partial Differential Equations using MATLAB*. Wiley-Interscience.

[106] Surhone, L.M., Timpledon, M.T., & Marseken, S.F. (2010) *Volume of Fluid Method*. VDM AG & Co. Kg.

[107] Suri, J.S. & Farag, A.A. (2007) *Deformable Models: biomedical and clinical applications*. Springer.

[108] Tadjfar, M., & Smith, F.T. (2004) Direct simulations and modelling of basic three-dimensional bifurcating tube flows. *Journal of Fluid Mechanics*, 519, 1-32.

[109] Thom, A. (1928) *An investigation of fluid flow in two dimensions, Technical Report 1194*. Aerospace Research Center. United Kingdom.

[110] Thom, A. (1933) The flow past circular cylinders at low speeds. *Proceedings of Royal Society*. Section A. 141, 651-669.

[111] Tuck, E.O., & Dixon, A. (1989) Surf-skimmer planning hydrodynamics. *Journal of Fluid Mechanics*, 205, 581-592.

[112] *U.S. National Cancer Institute*, SEER training programs.

[113] Valentini, F.A., Besson, G.R., Nelson, P.P., & Zimmern, P.E. (2000) A mathematical micturition model to restore simple flow recordings in healthy and symptomatic individuals and enhance uroflow interpretation. *Neurourology and Urodynamics*, 19, 153-176.

[114] Valentini, F.A., Mazieres, L., & Nelson, P.P. (2010) Can modelled analysis of urodynamic recordings help to demonstrate the nervous control of the bladder and urethra during micturition? *UroToday International Journal*, 3(4), (Online journal).

[115] van de Vosse, F.N., de Hart, J., van Oijen, C.H.G.A., Bessems, D., Segal, A., Wolters, B.J.B.M., Stijnen, J.M.A., & Baaijens F.P.T. (2003) Finite-element-based computational methods for cardiovascular fluid-structure interaction. *Journal of Engineering Mathematics*, 47, 335-368.

[116] van de Vosse, F.N. (2003) Mathematical modelling of the cardiovascular system. *Journal of Engineering Mathematics*, 47, 175-183.

[117] van Duin, F., Rosier, P.F., Benelmans, B.L., Wijkstra, H., Debruyne, F.M., & van Oosterom, A. (2000) Comparison of different computer models of the neural

control system of the lower urinary tract. *Neurourology and Urodynamics*, 19(3), 289-310.

[118] van Mastrigt, R., & Pel, J.J.M. (1999) Toward a non-invasive urodynamic diagnosis of infravesical obstruction. *British Journal of Urology International*, 84, 195-203.

[119] Venegas, J.G., Woll, J.P., Woolfson, S.B., Cravalho, E.G., Resnick, N., & Yalla, S.V. (1991) Viscoelastic properties of the contracting detrusor, Volume II. Experimental approach. *American Journal of Physiology*, 261, C364-C375.

[120] Vowles, J.E., & Wagg, A.S. (1999) The Pressure-Flow plot in the evaluation of female incontinence. *BJU International*, 84(9), 948-952.

[121] Wang, J., Zhong, W., & Zhang, J. (2006) High order compact computation and nonuniform grids for streamfunction vorticity equations. *Applied Mathematics and Computation*, 179, 108-120.

[122] Waters, S.L., Heaton, K., Siggers, J.H., Bayston, R., Bishop, M., Cummings, L.J., Grant, D.M., Oliver, J.M., &. Wattis, J.A.D. (2008) Ureteric stents: investigating flow and encrustation, Proceedings IMechE. *Journal of Engineering in Medicine*, 222(H), 551-561.

[123] Weinan, E., & Liu, J.G. (1996) Vorticity Boundary Condition and Related Issues for Finite Difference Schemes. *Journal of Computational Physics*, 124, 368-382.

[124] Woods, L.C. (1954) A note on the numerical solution of fourth order differential equations. *Aeronautical Quarterly*, 5, 176-184.

[125] Zhang, Y., Kim, S., Erdman, A.G., Roberts, K.P., & Timm, G.T. (2009) Feasibility of using a computer modelling approach to study SUI induced by landing a jump. *Annals of Biomedical Engineering*, 37(7), 1425-1433.

[126] Zimmerman, W.B.J. (2004) *Process Modelling and Simulation with Finite Element Methods*. World Scientific.

[127] Zumbal, G.I., Harrell, C.R., Smith, E.O., Rattner, Z., Gindi, G., & Hoffer, P.B. (1994) Computerized three-dimensional segmented human anatomy. *Medical Physics*, 21 (2), 299-302.